

AD-A273 097



2

4

# FINAL TECHNICAL REPORT

**S** DTIC  
ELECTE  
NOV 24 1993  
**A**

## Growth, Characterization and Device Development in Monocrystalline Diamond Films

Supported by the Innovative Science and Technology Office  
Strategic Defense Initiative Organization  
Office of Naval Research  
under Contract #N00014-90-J-1604  
for the period January 10, 1990–October 31, 1993

R. F. Davis, J. T. Glass, R. J. Nemanich\* and R. J. Trew\*\*  
North Carolina State University  
c/o Materials Science and Engineering Department  
\*Department of Physics  
\*\*Electrical and Computer Engineering  
Raleigh, NC 27695

This document has been approved  
for public release and sale; its  
distribution is unlimited.

October 31, 1993

15405

93-28695



93 11 23 07 8

# REPORT DOCUMENTATION PAGE

Form Approved  
OMB No. 0704-0188

Public reporting burden for this collection of information is estimated to average 1 hour per response, including the time for reviewing instructions, searching existing data sources, gathering and maintaining the data needed, and completing and reviewing the collection of information. Send comments regarding this burden estimate or any other aspect of this collection of information, including suggestions for reducing this burden to Washington Headquarters Services, Directorate for Information Operations and Reports, 1215 Jefferson Davis Highway, Suite 1204, Arlington, VA 22202-4302, and to the Office of Management and Budget Paperwork Reduction Project (0704-0188), Washington, DC 20503

1. AGENCY USE ONLY (Leave blank)	2. REPORT DATE October 31, 1993	3. REPORT TYPE AND DATES COVERED FINAL TECHNICAL (1/10/90-10/31/93)
----------------------------------	------------------------------------	--

4. TITLE AND SUBTITLE Growth, Characterization and Device Development in Monocrystalline Diamond Films	5. FUNDING NUMBERS s400003srr08 1114SS N00179 N66005 4B855
6. AUTHOR(S) Robert F. Davis	

7. PERFORMING ORGANIZATION NAME(S) AND ADDRESS(ES) North Carolina State University Hillsborough Street Raleigh, NC 27695	8. PERFORMING ORGANIZATION REPORT NUMBER N00014-90-J-1604
---	--

9. SPONSORING/MONITORING AGENCY NAMES(S) AND ADDRESS(ES) Sponsoring: ONR, Code 1513:CMB, 800 N. Quincy, Arlington, VA 22217-5000 Monitoring: Office of Naval Research Resider The Ohio State University Research Center 1960 Kenny Road Columbus, OH 43210-1063	10. SPONSORING/MONITORING AGENCY REPORT NUMBER
--	--

11. SUPPLEMENTARY NOTES

12a. DISTRIBUTION/AVAILABILITY STATEMENT Approved for Public Release; Distribution Unlimited	12b. DISTRIBUTION CODE
---	------------------------

13. ABSTRACT (Maximum 200 words)

The effects of hydrogen on cluster binding energy and resulting growth mode during chemical vapor deposition of diamond, the process parameters and the effect of substrates during bias enhanced nucleation, the growth of textured diamond films, the characterization of these films using transmission electron microscopy, Raman spectroscopy and photo-luminescence comprise the growth and thin film characterization research conducted during this grant. Additional work included determination of the surface properties including the negative electron affinity, the growth and characterization of SiGe contacts, and the modeling and characterization of electronic devices. The nucleation of diamond grains on unscratched Si(100) wafer is enhanced by four order of magnitude relative to scratched substrates by using negative bias-enhanced microwave plasma CVD in a 2% methane/hydrogen plasma for an initial period. *In vacuo* surface analysis has revealed that the actual nucleation occurs on the amorphous C coating present on the thin SiC layer which forms as the product of the initial reaction with the Si surface. It is believed that the C forms critical clusters which are favorable for diamond nucleation. TEM of nucleation of diamonds on single crystal SiC showed that approximately half of the diamond nuclei were in epitaxial alignment with the SiC substrate. UV photoemission spectroscopy have revealed Schottky barrier heights of  $1.0 \pm 0.2$  eV and  $1.5 \pm 0.2$  for the Ti-diamond (111) and (100) interfaces. Upon Ti deposition on the (111) surface, a sharp (0.5 eV FWHM) peak developed at the position of the conduction band edge indicative of a negative electron affinity surface. I-V measurements at room temperature demonstrated the formation of a ohmic contact using SiGe layers. The results of modeling research to determine the electronic properties of semiconducting diamond, the microwave- and millimeter-wave potential of MESFET devices, operative in DC and rf environments are also presented. Finally, pure c-BN has been achieved on both Si (100) and diamond (100) substrates. The growth of c-BN on diamond and vice versa have also been modeled geometrically.

14. SUBJECT TERMS diamond, bias-enhanced nucleation, microwave plasma CVD, transmission electron microscopy, Raman spectroscopy, photoluminescence, negative electron affinity, metal-diamond interfaces, SiGe contacts, electronic properties, modeling, MESFETs, c-BN-diamond system	15. NUMBER OF PAGES 152
	16. PRICE CODE

17. SECURITY CLASSIFICATION OF REPORT UNCLAS	18. SECURITY CLASSIFICATION OF THIS PAGE UNCLAS	19. SECURITY CLASSIFICATION OF ABSTRACT UNCLAS	20. LIMITATION OF ABSTRACT SAR
---	--	---	-----------------------------------

## Table of Contents

- I. Introduction
- II. The Effects of Hydrogen on Cluster Binding Energy and Resulting Growth Mode During Chemical Vapor Deposition of Diamond
- III. Process Parameter and Substrate Effect of Bias-enhanced Nucleation
- IV. Characterization of Bias-enhanced Nucleation of Diamond on Silicon by *in vacuo* Surface Analysis and Transmission Electron Microscopy
- V. Textured Diamond Growth on (100)  $\beta$ -SiC Via Microwave Plasma Chemical Vapor Deposition
- VI. Analysis of the Diamond/SiC Interface Via Cross Sectional Transmission Electron Microscopy
- VII. *In-Situ* Growth Rate Measurement and Nucleation Enhancement for Microwave Plasma CVD of Diamond
- VIII. Analysis of the Composite Structures in Diamond Thin Films by Raman Spectroscopy
- IX. Microphotoluminescence and Raman Scattering Study of Defect Formation in Diamond Films
- X. Effects of Hydrogen and Argon Plasma Exposure on the Diamond (111) Surface
- XI. Properties of Interfaces of Diamond
- XII. Growth and Characterization of SiGe Contacts on Semiconducting Diamond Substrates
- XIII. Characterization of the Electronic Properties of Diamond
- XIV. Modeling and Characterization of Electronic Devices Fabricated from Semiconducting Diamond Thin Films
- XV. Modeling of Microwave MESFET Electronic Devices Fabricated from Semiconducting Diamond Thin Films—Part I
- XVI. Modeling of Microwave MESFET Electronic Devices Fabricated from Semiconducting Diamond Thin Films—Part II
- XVII. The Role of Geometric Considerations in the Diamond-cubic Boron Nitride Heteroepitaxial System
- XVIII. Cubic Boron Nitride Thin Film Growth
- XIX. Phase Evolution in Boron Nitride Thin Films
- XX. Distribution List

## I. Introduction

Diamond as a semiconductor in high-frequency, high-power transistors has unique advantages and disadvantages. Two advantages of diamond over other semiconductors used for these devices are its high thermal conductivity and high electric-field breakdown. The high thermal conductivity allows for higher power dissipation over similar devices made in Si or GaAs, and the higher electric field breakdown makes possible the production of substantially higher power, higher frequency devices than can be made with other commonly used semiconductors.

In general, the use of bulk crystals severely limits the potential semiconductor applications of diamond. Among several problems typical for this approach are the difficulty of doping the bulk crystals, device integration problems, high cost and low area of such substrates. In principal, these problems can be alleviated via the availability of chemically vapor deposited (CVD) diamond films. Recent studies have shown that CVD diamond films have thermally activated conductivity with activation energies similar to crystalline diamonds with comparable doping levels. Acceptor doping via the gas phase is also possible during activated CVD growth by the addition of diborane to the primary gas stream.

The recently developed activated CVD methods have made feasible the growth of polycrystalline diamond thin films on many non-diamond substrates and the growth of single crystal thin films on diamond substrates. More specifically, single crystal epitaxial films have been grown on the {100} faces of natural and high pressure/high temperature synthetic crystals. Crystallographic perfection of these homoepitaxial films is comparable to that of natural diamond crystals. However, routes to the achievement of rapid nucleation on foreign substrates and heteroepitaxy on one or more of these substrates has proven more difficult to achieve. This area of study has been a principal focus of the research of this contract.

At present, the feasibility of diamond electronics has been demonstrated with several simple experimental devices, while the development of a true diamond-based semiconductor materials technology has several barriers which a host of investigators are struggling to surmount. It is in this latter regime of investigation that the research described in this report has and continues to address.

Boron nitride is similar to carbon in having three crystalline structures: a layered hexagonal structure (*h*-BN) corresponding to graphite, the cubic structure (*c*-BN) analogous to diamond, and a rare hexagonal wurtzite structure (*w*-BN) corresponding to Lonsdaleite. The last two phases are metastable under normal environmental conditions. An amorphous phase (*a*-BN) is also common in films and coatings.

The extreme mechanical and thermal properties of *c*-BN make it useful for wear-resistant tools for the machining of steels, for corrosion resistant and electrically insulating parts, and for heat sinks for electronic devices. It has also recently been shown that bulk single crystals

of this wide bandgap ( $E_g \approx 6.4$  eV) semiconductor can be doped with both n- and p-type impurities and that light emitting p-n junctions can be produced. This phase combined with other BN phases, has also been achieved in thin film form via physical vapor deposition and chemical vapor deposition methods.

Most researchers growing BN films use FTIR spectroscopy for phase identification. The cubic phase of BN has a distinct absorption peak at about  $1080 \text{ cm}^{-1}$ . The hexagonal, turbostratic (disordered hexagonal), and amorphous phases have primary and secondary absorption peaks at  $1370$  and  $780 \text{ cm}^{-1}$ , respectively. Thus, these non-cubic phases cannot be distinguished using FTIR. A commonly reported feature of these spectra obtained from analyses of the total thickness of the films wherein the presence of *c*-BN is apparent is the indication of various amounts of the hexagonal and/or amorphous phases. However, the actual evolution of these phases must be determined by HRTEM.

The research of this grant has included the studies of the process parameters and substrate effects on bias-enhanced nucleation, the effects of hydrogen on cluster binding energy and resulting growth mode, the characterization of diamond and diamond metal interfaces via TEM, laser reflection interferometry, Raman spectroscopy, photoluminescence, and angle-resolved ultraviolet photoelectron spectroscopy. The property of negative electron affinity has been discerned for this work. Modeling and characterization of electronic devices particularly MESFETs have been studied from the standpoint of bulk and thin film diamond materials. And finally, *c*-BN has been achieved as the final phase in a growth sequence involving the growth of *a*BN and *h*BN on Si (100) and diamond (100) surfaces. The deposition of diamond on *c*-BN has been both modeling and experimentally realized.

The following subsections detail the experimental procedures for each of the aforementioned studies, discuss the results and provide conclusions and references for these studies. Note that each major section is self-contained with its own figures, tables and references.

## II. The Effects of Hydrogen on Cluster Binding Energy and Resulting Growth Mode During Chemical Vapor Deposition of Diamond

B. R. Stoner and J.T. Glass

Department of Materials Science and Engineering,  
North Carolina State University, Raleigh, NC 27695-7907

### Abstract

Capillarity and atomistic formulations for determining diamond thin film growth modes are compared. Arguments are presented based on simple atomistic cluster binding energy calculations that suggest hydrogen should play an important role in stabilizing the 2-dimensional cluster configuration and thus promote layered diamond growth, assuming that the interfacial strain and misfit energies are not too high. Assumptions which may cause this model to break down experimentally are also discussed.

DTIC QUALITY INSPECTED 8

Accession For	
NTIS	CRAM <input checked="" type="checkbox"/>
DTIC	TAB <input type="checkbox"/>
Unannounced	<input type="checkbox"/>
Justification	
By	
Distribution /	
Availability Codes	
Dist	Avail and/or Special
A-1	

It is generally agreed that in order for diamond to be fully utilized as an electronic material, single crystal diamond thin-films over large areas must be realized<sup>1-4</sup>. Ideally one would prefer to grow the single crystal diamond two-dimensionally (Frank-van der Merwe growth) on economic, easily obtained non-diamond substrates. However, due to diamonds high surface energy it is often considered that CVD diamond should grow in a 3-D, or Volmer-Webber, mode on most foreign substrates, and this is in fact what has been observed. Justifications for the 3-D growth mode are based on Youngs Equation;

$$\cos(\theta) = (\gamma_s - \gamma_i) / \gamma_c \quad (1)$$

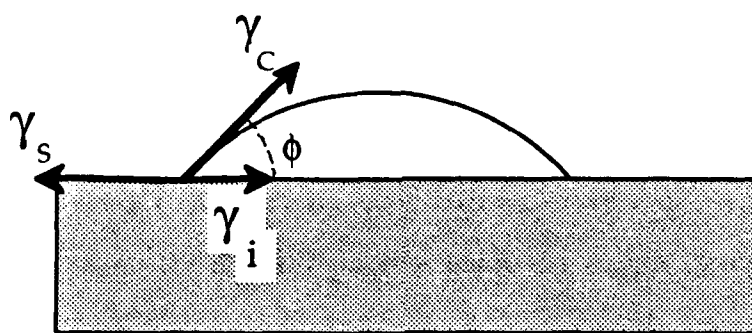


Figure 1. Capillarity model, showing the relationship between surface energies and condensate contact angle,  $\theta$ .

Where  $\gamma_s$ ,  $\gamma_c$ , and  $\gamma_i$  are the surface free energies of the substrate, condensate (diamond), and the interface between the two respectively (Refer to figure 1).

From this relationship, in order to obtain 2-D growth ( $\theta = 0$ ) the following inequality must occur;

$$\gamma_s \geq \gamma_i + \gamma_c$$

Since diamond has a surface energy higher than all other known materials,  $\gamma_s$  should always be  $< (\gamma_i + \gamma_c)$ , and therefore 3-D growth should always be the

preferred mode. This is not surprising when one considers the high bond strength of diamond.

However, the previous statement, that ' $\gamma_s$  should always be  $< (\gamma_i + \gamma_c)$ ', assumes that  $\gamma_c$  is equal to that of a freshly cleaved diamond surface and, in the case of vapor phase diamond the surface energies are not affected or altered during the chemical vapor deposition process. Surface energies are often determined by measuring the cleavage energy on a particular plane. The high energy associated with that surface is due to the unaccommodated bonds created as a result of the cleaving process. If some of those bonds are subsequently satisfied, either by forming a C=C double bond with another carbon or by bonding with a foreign atom on the surface, the result is a lowering of the overall free energy associated with that diamond surface. In this article the authors will present arguments based on cluster binding energy calculations that suggest 2-D growth of diamond on foreign substrates should be possible under certain conditions.

The following is concerned with cluster binding energy calculations and how they relate to the equilibrium shape and resulting growth mode of small diamond clusters. For more general discussions on thin film nucleation and growth several excellent reviews are recommended.<sup>5-8</sup> There are two formulations typically used in the determination of the equilibrium shape of a cluster of atoms, or nuclei, on the surface. The first and most commonly used, is referred to as the capillarity method, and the second is the atomistic method. In the present arguments, the atomistic formulation will be utilized because it has been shown to be more accurate in the determination of the equilibrium shapes of microscopic clusters of atoms<sup>9</sup>.

The atomistic formulation is used to calculate the binding energy of a cluster of atoms. For a given cluster size, the configuration with the highest binding energy will be the most stable<sup>9, 10</sup>. So while the capillarity method<sup>9</sup> looks at the nuclei macroscopically as a droplet on a surface, the atomistic method will sum the binding energies of every atom in the cluster in order to determine the most stable configuration. For the following formulation, the energy changes due to relaxation of interfacial strain are neglected. Thus, the binding energy of the cluster is approximated as the sum of all bond energies in that cluster, including those between cluster and substrate atoms.

Consider clusters of atoms on a hexagonal close packed plane (see figure 2). If  $E_a$  and  $E_b$  represent the adsorption energy of a single atom on the substrate, and the bond strength of two cluster atoms, respectively, then the binding energy ( $E_i$ ) for a cluster of  $i$ -atoms may be expressed as follows;

$$E_i = \sum(E_a) + \sum(E_b) . \quad (2)$$

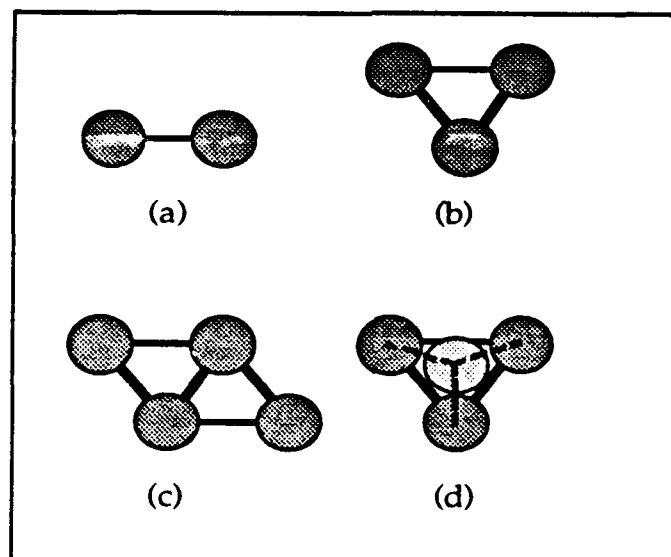


Figure 2. Clusters of atoms on a hexagonally closed packed plane: (a) two, (b) three, (c) four 2-D, and (d) four 3-D atom clusters.

For example, if there are 2 atoms on the substrate (figure 2-a) which have a single bond to each other and one bond each to the substrate, the binding energy for that 2-atom cluster would be  $E_2 = 2E_a + E_b$ . For 3 atoms on the surface (figure 2-b), the cluster would still be planar and the binding energy would equal  $3E_a + 3E_b$ . A cluster of 4 atoms may either be planar (figure 2-c) or three dimensional (figure 2-d), depending upon the respective binding energies for each case. The binding energies for these two cases may be calculated as follows;

$$E_4 = 4E_a + 5E_b \quad (2-D), \quad (3)$$

and  $E_4 = 3E_a + 6E_b \quad (3-D). \quad (4)$

If  $E_{i(2-D)} > E_{i(3-D)}$  then the 2-dimensional cluster configuration should be more energetically favorable.

So based on the above formulation, one may calculate the most favorable cluster configuration as a function of cluster size,  $i$ , and thus be able to determine the expected growth mode for a given condensate/substrate system. For the above example of a 4-atom cluster, the relationship;  $E_a \geq E_b$  should be sufficient to promote 2-D growth. For slightly larger clusters ( $i \geq 6$ )  $E_a$  must be  $\geq 2E_b$  for 2-D growth to be favored, which is similar to the condition predicted for small clusters by the capillarity model<sup>9</sup>.

The above discussion covers only the simplest of models. Second nearest neighbor interactions, bond relaxation and distortion, and atom vibrations were not considered. Others have performed more elaborate calculations of the structure and stability of small clusters of atoms of various sizes<sup>11-13</sup>. Allpress and Sanders<sup>11</sup>, and Hoare and Pal<sup>13</sup> in particular, have performed calculations on the stability of multiply twinned particle clusters.

To apply the atomistic binding energy calculations to small clusters of diamond, one must simply utilize the correct covalent bonding configurations. The following results and discussion will be based on diamond growth under typical CVD conditions. All carbon bonding will be assumed to be  $sp^3$  in nature. It will also be assumed that both substrate and diamond cluster surface bonds will be hydrogen terminated (as expected due to the atomic hydrogen growth environment for most CVD), and strain energy due to interfacial lattice misfit is negligible (i.e. assume growth on a closely lattice matched substrate). Simple cluster binding energies will be calculated under these conditions for diamond growth on a (100) surface.

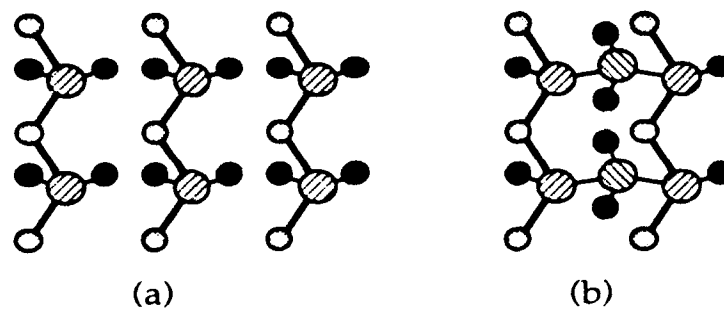
Consider first, a single carbon atom on the (100) surface that is hydrogen terminated with two hydrogens attached to every substrate atom. Since it was stipulated that all carbon atoms will be  $sp^3$  bonded, there should be two bonds attached to the substrate atoms, and two that are hydrogen terminated for each surface carbon atom. The binding energy for this single carbon-atom cluster will be;

$$E_1 = 2E_a - 2E_{S-H} + 2E_{C-H} \quad (5)$$

Where  $E_{C-H}$  and  $E_a$  are the bond strengths of a C-H bond and a C-substrate bond respectively.  $E_{S-H}$  represents the bond strength of a substrate-hydrogen bond. The quantity  $2(E_a - E_{S-H})$  therefore represents the energy required to remove two hydrogens atoms from the substrate surface and replace them with a single carbon atom. Now consider a six atom cluster of 2-D (figure 3-a) and 3-D (figure 3-b) configurations. The corresponding binding energies for these two clusters are calculated to be;

$$E_{6(2-D)} = 12(E_a - E_{S-H}) + 12E_{C-H} \quad (6)$$

$$\text{and } E_{6(3-D)} = 8(E_a - E_{S-H}) + 4E_{C-C} + 8E_{C-H} \quad (7)$$



- ⊗ Carbon(bottom layer)
- ⊙ Carbon(top layer)
- Hydrogen
- Substrate Atom

Figure 3. Diamond cluster of six atoms on (100) plane in (a) 2-D and (b) 3-D configurations.

Since the C-H bond is stronger than a single C-C bond (100 vs 85 kcal/mol at R.T.), when one substitutes these numbers into the previous equations, it is evident that the binding energy of the 2-D cluster will always be higher than that of the 3-D cluster, for  $(E_a - E_{S-H}) \geq 0$ . The 2-D growth mode may still be favored for  $(E_a - E_{S-H}) < 0$  if the following inequality is maintained;

$$(E_a - E_{S-H}) + (E_{C-C} - E_{C-H}) > 0. \quad (8)$$

In other words if equation (8) holds true, 2-D growth is expected on any lattice matched substrate to which the diamond can bond when the film is hydrogen terminated. The hydrogen termination therefore appears to lower the surface energy of the diamond nuclei enough to promote layered growth. If one continues to increase the size of the cluster ( $i \gg 6$ ), calculations show that layered growth should continue to dominate. A similar formulation for growth on a (111) surface yields a similar result where;

$$E_{6(2-D)} = 6(E_a - E_{S-H}) + 18E_{C-H}, \quad (9)$$

$$\text{and } E_{6(3-D)} = 4(E_a - E_{S-H}) + 6E_{C-C} + 8E_{C-H} . \quad (10)$$

Obtaining a triply hydrided (111) diamond surface such as this in reality may be difficult, though, due to steric hindrances between hydrogens. Even though the data above suggest strongly that layered growth should be favored under the given conditions, in reality, it is not observed except in homoepitaxial growth. The possible explanations for this are discussed below.

The above example is that of an ideal experiment. The following non-idealities may enhance 3-D growth and thus explain why layered growth has not yet been obtained on non-diamond substrates. First, it was assumed that the interfacial strain and/or misfit relaxation energy was negligible. Strain and misfit dislocations at the interface will increase the interfacial energy, and therefore decrease the binding energy of the cluster. This implies that a new atom being added to the cluster would prefer to go to second or higher levels and thereby avoid the added interfacial strain associated with an atom addition onto the surface level. By making it more energetically favorable for atoms to join to the upper layers of the cluster, 3-D growth becomes more likely.

The second assumption, that all surface carbon bonds are both tetrahedrally coordinated and hydrogen terminated, may also be in error thus resulting in a lower binding energy for the 2-D cluster. The fact that the C-H bond is stronger than the C-C bond effectively stabilizes the 2-D configuration by maximizing the number of C-H bonds in the cluster. Tsuno and coworkers have shown, via STM analysis, that the surface of homoepitaxial diamond films grown at higher surface temperatures ( $\geq 800$  °C) are in a mono-hydride configuration<sup>14, 15</sup>. Films grown at 600 °C, however, appeared to be in an

ideal di-hydride arrangement. In the case of a mono-hydride diamond cluster, the binding energy of a 2-D cluster would be greatly reduced due to the removal of half of the C-H bonds. If one assumes that the now unsatisfied bonds on the mono-hydride surface reconstruct and form distorted  $\sigma$ -bonds (or dimer chains) with neighboring carbon atoms as suggested by Tsuno et al.<sup>14, 15</sup> and Hamza et al.<sup>16</sup> (figure 4a & b), then the binding energy for this configuration of a 6-atom cluster may be calculated as follows;

$$E_6 = 12(E_a - E_{S-H}) + 6E_{C-H} + 3E_{\sigma} \quad (2-D, \text{ mono-hydride}), \quad (11)$$

and  $E_6 = 8(E_a - E_{S-H}) + 6E_{C-H} + 4E_{C-C} + E_{\sigma} \quad (3-D, \text{ mono-hydride}). \quad (12)$

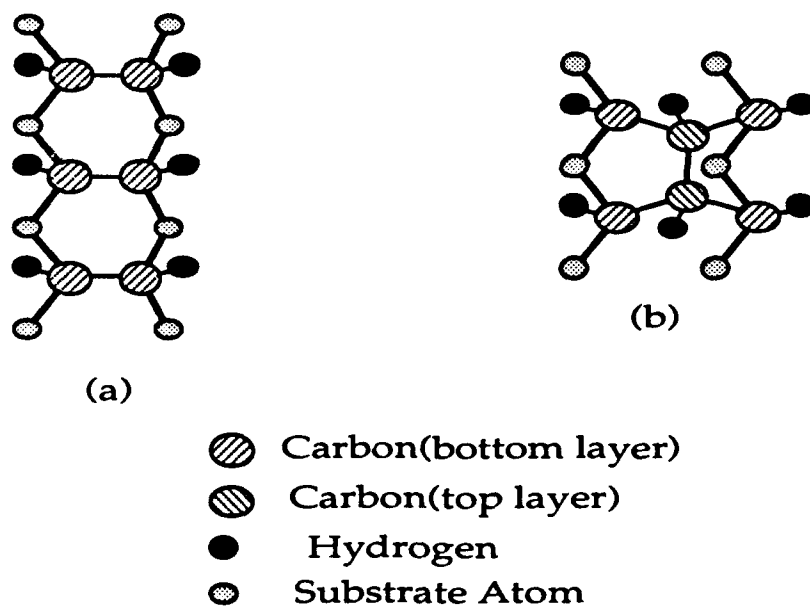


Figure 4. Reconstructed mono-hydride configuration of a six atom cluster in (a) 2-D and (b) 3-D configurations.

It is evident from figures 4-a & b that the  $\sigma$ -bonds associated with the reconstruction are slightly distorted. This implies that  $E_{\sigma}$  will be less than  $E_{C-C}$  because of this distortion. So if one assumes that  $E_{\sigma} < 85$  kcal/mol and

substitutes this and the other bond energies into the above equations the resulting decrease in cluster binding energies due to the de-hydrogenation and corresponding reconstruction will be;

$\geq 345$  kcal/mol for the 2-D cluster,

and  $\geq 115$  kcal/mol for the 3-D cluster.

From these calculations, it is clear that when de-hydrogenation occurs, the binding energy of a 2-D cluster is decreased by significantly more than that of a 3-D cluster thus suggesting that the mono-hydride terminated case will favor 3-D growth more so than the di-hydride case. It is impossible to determine the exact cluster binding energies without proper knowledge of the interfacial quantity ( $E_a - E_{S-H}$ ), however based on the above equations for a mono-hydride surface, 3-D growth will be favored if  $(E_a - E_{S-H}) \leq 60$  kcal/mol. Thus suggesting that island growth is highly favored under growth conditions where the diamond surface is only mono-hydrated. Since the di-hydride case is more promising for potential 2-D growth, the low temperature homoepitaxial experiments performed by Tsuno et al.<sup>14, 15</sup>, in which di-hydride surfaces were observed on films grown at 600 °C, suggest that layered growth should be more favored at lower temperatures assuming surface mobilities are kept sufficiently high.

By using an atomistic approach it was possible to determine the most stable growth mode for diamond deposited by chemical vapor deposition by maximizing the binding energy for a cluster of a given size. During typical CVD conditions, it was found that the diamond surface free energy may be greatly reduced by full hydrogenation of the diamond surface, thus improving the chances for 2-D growth. However, interfacial strain, misfit energy, and incomplete hydrogenation during deposition are believed to

create strong driving forces towards 3-D growth by increasing both the interfacial and surface free energy and thus decreasing the binding energy of a 2-D cluster. These are the most probable explanations for why 2-D growth on non-diamond substrates has not yet been achieved. By obtaining near complete hydrogenation of the diamond surface during growth, possibly through lower deposition temperatures, as well as decreasing the interfacial energy, the chances for layered growth of diamond are expected to be improved.

Valuable technical discussions with Dr. Robert Johnson of the University of Virginia were greatly appreciated. This work was financially supported in part by SDIO/IST through ONR and the Kobe Steel, Ltd. Professorship at NCSU.

### References

1. S. Kurita, Japan New Diamond Forum, 113 (1990).
2. M. Seal, *First International Conf. on the Applications of Diamond Films and Related Materials, Auburn, Alabama, U.S.A., Aug. 17-22, 1991*, edited by Y. Tzeng, M. Yoshikawa, M. Murakawa and A. Feldman, Elsevier, p. 3 (1991).
3. W. A. Yarbrough, *J. Vac. Sci. Technol. A*, 9(3), 1145 (1991).
4. M. N. Yoder, *First International Conf. on the Applications of Diamond Films and Related Materials, Auburn, Alabama, U.S.A., Aug. 17-22, 1991*, edited by Y. Tzeng, M. Yoshikawa, M. Murakawa and A. Feldman, Elsevier, p. 287 (1991).
5. R. Kern, G. L. Lay and J. J. Metois, "Basic Mechanisms in the Early Stages of Epitaxy," in *Current Topics in Materials Science*, edited by E. Kaldis, North-Holland Publishing Company, Amsterdam, p. 134 (1979).
6. J. L. Robins, *Applied Surface Science*, 33/34, 379 (1988).

7. J. A. Venables, G. D. T. Spiller and M. Hanbucken, *Rept. Progr. Phys.*, **47**, 399 (1984).
8. K. Reichelt, *Vacuum*, **38**(12), 1083 (1988).
9. B. Lewis, *Thin Solid Films*, **1**, 85 (1967).
10. J. A. Venables and G. L. Price, "Nucleation of Thin Films," in *Epitaxial Growth*, edited by J. W. Matthews, Academic Press., New York, p. (1975).
11. J. G. Allpress and J. V. Sanders, *Aust. J. Phys.*, **23**, 23 (1970).
12. J. V. Dave and F. F. Abraham, *Surface Sci.*, **26**, 557 (1971).
13. M. R. Hoare and P. Pal, *J. Crystal Growth*, **17**, 77 (1972).
14. T. Tsuno, T. Imai, Y. Nishibayashi, K. Hamada and N. Fujimori, *Jap. J. of Appl. Phys.*, **30**(5), 1063 (1991).
15. T. Tsuno, T. Imai, Y. Nishibayashi and N. Fujimori, *MRS Fall Meeting*, Boston, MA (1991).
16. A. V. Hamza, G. D. Kubiak and R. H. Stulen, *Surface Science*, **237**, 35 (1990).

### III. Process Parameter and Substrate Effect of Bias-enhanced Nucleation

#### A. Introduction

Bias-enhanced nucleation (BEN) via microwave plasma chemical vapor deposition (MPCVD) was utilized to investigate the influence of this process on various substrate materials. In addition, a statistical experimental design (SED) has been implemented to optimize the process parameters associated with BEN. Negatively biasing the substrate as an in-situ pretreatment has been attributed to greatly enhancing the nucleation density of diamond on silicon [1] and has also been utilized to epitaxially nucleate diamond on  $\beta$ -SiC [2].

#### B. Results and Discussion

The initial findings of this study revealed that it was essential that the substrate holder be diamond coated while performing BEN as shown in Figure 1. It was discovered that the uncoated molybdenum substrate holder resulted in little or no observable diamond nucleation during the biasing process. To determine the importance of the diamond coating, both alumina and graphite substrate holder coatings were tested. Neither were successful in enhancing the diamond nucleation via biasing, suggesting that some unique property of diamond is responsible for the increased nucleation densities. There does appear to be a critical amount of diamond on the substrate holder that is essential for reproducible results. This is shown in Figure 2 which indicates that as more diamond is coated on the substrate holder the biasing time for the formation of a continuous film becomes constant. Also of interest in this plot is the observation of an increase in current with diamond coating thickness. Furthermore, it was found that when other materials surrounded the substrate, including metals, the bias current decreased by up to 80%. This suggests that the diamond is acting as an electron emission source.

After obtaining a greater understanding of the BEN process various substrates were chosen for study based on their affinity for carbon. In a previous work it was observed that silicon was much more influenced by the negative substrate bias than was copper [3]. This reveals that the carbide forming nature of silicon compared to the non-carbide forming nature of copper may give an indication of the class (i.e. carbide or non-carbide forming) of substrate material which may yield the optimum results. For this reason the carbide forming refractory elements, Ti, Nb, W, and Ta, were chosen to study in greater detail. In Figure 3 a plot of the nucleation density versus bias time is shown for the different refractory elements in addition to silicon, copper, and germanium. This plot indicates that, among the various carbide forming substrates, silicon shows a dramatically higher nucleation efficiency. All the refractory elements tended to nucleate more rapidly than the non-carbide forming germanium and copper substrates thus strongly suggesting that the carbide forming nature of the substrate may play an

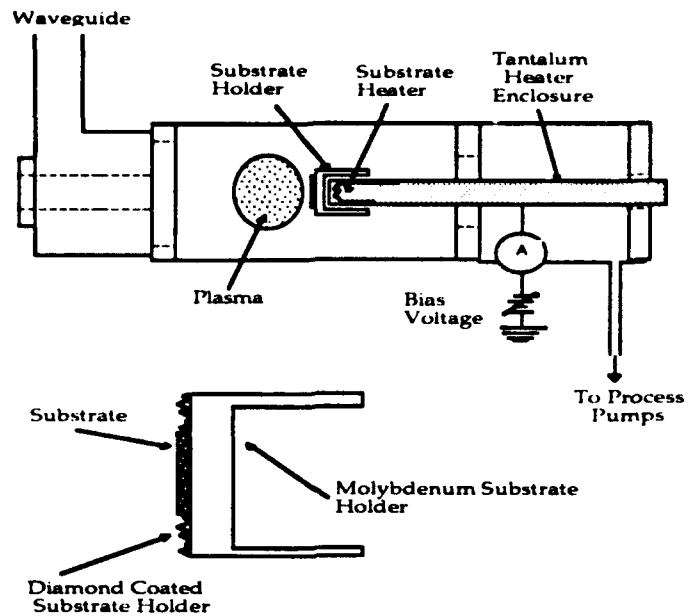


Figure 1. Microwave Plasma Chemical Vapor Deposition chamber and diamond coated substrate holder.

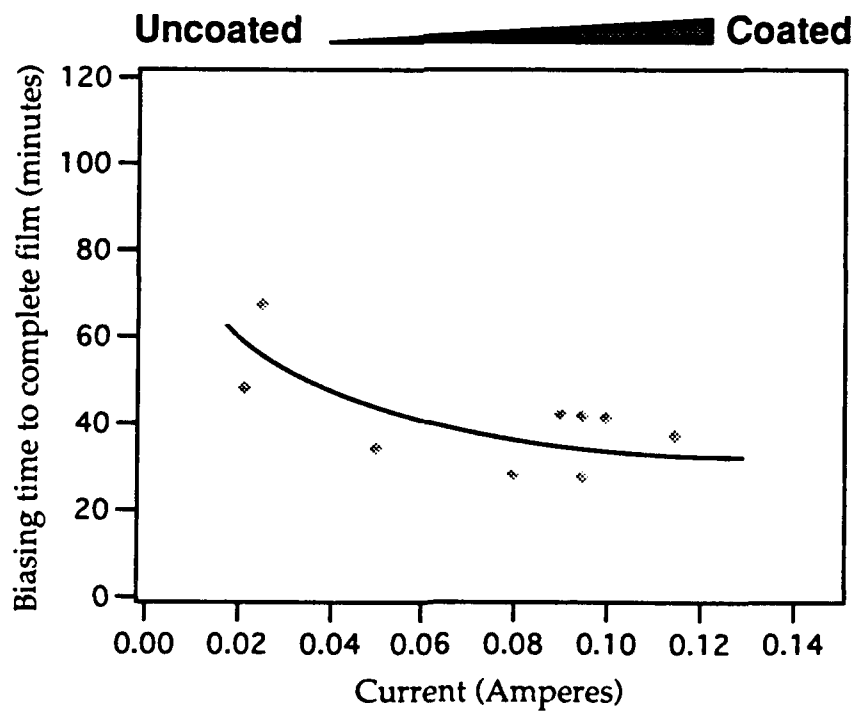


Figure 2. Time for the formation of a continuous diamond film versus the amount of coated substrate diamond.

important role in the BEN process. Several possible explanations were considered for the trends established between the various substrate materials. These being the carbon diffusivity, the heat of formation of the carbide, and the heat of sublimation. Joffreau et al. [4] proposed a relationship between the nucleation kinetics and the diffusivity values of the refractory elements. There was an indication in this experimentation that the nucleation kinetics were consistent with the diffusivity values of the refractory carbides. However, there is still no conclusive evidence that relates this material property as well as the other suggested material properties to the trends established in Figure 3.

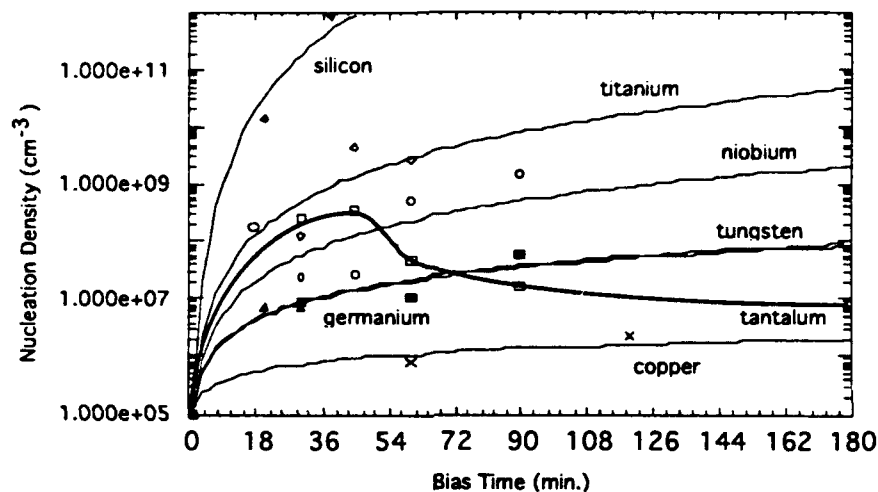


Figure 3. Nucleation density versus bias time for the refractory elements in relation to silicon and the non-carbide forming copper and germanium substrates.

The process parameters associated with BEN were studied to optimize the conditions under which this process was performed utilizing the SED. These process parameters being the substrate bias voltage, pressure, and methane concentration. In this respect, the parametric space may be isolated deriving the highest nucleation density, best film uniformity, highest diamond particle quality, and lowest bias time required for the formation of a diamond film. In addition to optimizing the parametric space of BEN these responses may also offer an insight into a better understanding of BEN in general. It was observed that under a high bias voltage and/or low pressure regime the diamond was noted to have etched from the substrate holder. In addition, no diamond was observed to have nucleated on the silicon substrates under these same conditions. Likewise, at lower bias voltages and/or higher pressures the bias current was observed to be reduced and much longer bias times were required to nucleate diamond.

### C. Conclusion

In summary, a better general understanding of BEN was obtained. The SED was implemented to observe the relative influence of the process parameters for obtaining the optimum diamond films on silicon substrates. In addition, this study has explored the possibility of utilizing BEN on substrate materials other than silicon; these being the refractory elements. Silicon was observed to obtain the highest nucleation densities with respect to bias time, followed by the refractory substrates and finally the non-carbide forming germanium and copper substrates.

### D. Acknowledgment

The authors wish to thank M. Veil for her assistance during experimentation. The financial support of this research was provided in part by SDIO/IST through ONR and the Kobe Steel, Ltd. Professorship at NCSU.

### E. References

1. B. R. Stoner, G.-H. M. Ma, S. D. Wolter and J. T. Glass, *Phys. Rev. B*, **45**, 11067 (1992).
2. W. Zhu, B. R. Stoner, G.-H. M. Ma, H. S. Kong, M. W. H. Brawn and J. T. Glass, *Phys. Rev. B* **15**, (1992) (submitted).
3. S. D. Wolter, B. R. Stoner, G.-H. M. Ma and J. T. Glass, in *Materials Research Society Symposium Proceedings*, (in press), MRS, San Francisco, Ca, Vol. 270.
4. P. O. Joffreau, R. Haubner, and B. Lux, *Int. J. Refract. Hard Met.* December, 186 (1988).

#### IV. Characterization of bias-enhanced nucleation of diamond on silicon by *in vacuo* surface analysis and transmission electron microscopy

B. R. Stoner, G.-H. M. Ma, S. D. Wolter, and J. T. Glass

*Department of Materials Science and Engineering, North Carolina State University, Raleigh, North Carolina 27695-7919*

(Received 15 October 1991)

An in-depth study has been performed of the nucleation of diamond on silicon by bias-enhanced microwave plasma chemical vapor deposition. Substrates were pretreated by negative biasing in a 2% methane-hydrogen plasma. The bias pretreatment enhanced the nucleation density on unscratched silicon wafers up to  $10^{11}$  cm<sup>-2</sup> as compared with  $10^7$  cm<sup>-2</sup> on scratched wafers. *In vacuo* surface analysis including x-ray photoelectron spectroscopy (XPS), Auger electron spectroscopy, and combined XPS and electron-energy-loss spectroscopy were used to study systematically both the initial-nucleation and growth processes. High-resolution cross-sectional transmission electron microscopy (TEM) was used to study the physical and structural characteristics of the diamond-silicon interface as well as to complement and enhance the *in vacuo* surface-analytical results. Raman spectroscopy confirmed that diamond was actually nucleating during the bias pretreatment. Scanning electron microscopy has shown that once the bias is turned off, and conventional growth is conducted, diamond grows on the existing nuclei and no continued nucleation occurs. If the bias is left on throughout the entire deposition, the resulting film will be of much poorer quality than if the bias had been turned off and conventional growth allowed to begin. Intermittent surface analysis showed that a complete silicon carbide layer developed before diamond could be detected. High-resolution cross-sectional TEM confirmed that the interfacial layer was amorphous and varied in thickness from 10 to 100 Å. A small amount of amorphous carbon is detected on the surface of the silicon carbide and it is believed to play a major role in the nucleation sequence. A model is proposed to help explain bias-enhanced nucleation on silicon, in hopes that this will improve the understanding of diamond nucleation, in general, and eventually result in the nucleation and growth of better-quality diamond films.

#### I. INTRODUCTION

With its large band gap and a unique combination of properties, diamond is regarded as the most suitable candidate for many applications, ranging from wear-resistant coatings and optical windows for visible and infrared (ir) transmission to high-temperature electronic devices. Currently, diamond synthesis from the vapor phase under low pressure is routinely achieved by more than ten different methods. However, despite rapid progress, the mechanism(s) for diamond nucleation onto nondiamond substrates remains unknown. The understanding of nucleation phenomena appears to be essential for achieving heteroepitaxy of diamond, which is necessary for exploiting the potential of diamond electronic devices. It would also be extremely beneficial in controlling the microstructure and surface morphology of diamond coatings for various applications.

Since the time when diamond growth from the vapor phase was achieved at reasonable growth rates,<sup>1-4</sup> it has been a subject of argument as to whether diamond nucleation occurs in the gas phase (homogeneous nucleation) or on the substrate surface (heterogeneous nucleation). Fedoseev *et al.*<sup>5-7</sup> presented theoretical arguments, based on the classical nucleation theory, that homogeneous nucleation is possible. Furthermore, diamond powders have been collected directly from the gas

phase,<sup>8-12</sup> which provides proof that such a nucleation process does exist. Nevertheless, the number of diamond particles collected from the gas phase was very small compared with the usual nucleation density (number of particles/cm<sup>2</sup>) observed on a substrate surface. Furthermore, homogeneous-nucleation mechanisms cannot solely account for the large variety of nucleation densities observed on different substrate materials and that result from various surface pretreatments.

Several hypotheses for heterogeneous diamond nucleation onto foreign substrates have also been made, most of them based on experimental observation. It is well known that the diamond-nucleation density may be increased by several orders of magnitude by simply scratching or abrading the substrate surface prior to placing it into the growth chamber. Bachmann *et al.*<sup>13,14</sup> postulated that residual diamond particles left on the surface from the scratching medium acted as diamond-nucleation sites. This is based on the fact that diamond will tend to nucleate preferentially on the diamond seeds, thus resulting in discrete homoepitaxy of diamond. Recently, Iijima, Aikawa, and Baba<sup>15,16</sup> provided direct observation by high-resolution transmission electron microscopy (HRTEM) of diamond nucleation on "diamond seeds" left from the scratching process. However, abrading the substrate with nondiamond abrasives such as cubic boron nitride (cubic BN),<sup>17</sup> silicon carbide,<sup>18</sup> and

stainless steel<sup>19</sup> has also yielded high nucleation densities. Furthermore, the diamond-nucleation density may be enhanced by nonabrasive surface pretreatments, such as the predeposition of carbonaceous layers of diamondlike carbon<sup>20-22</sup> (DLC) or even oil residue.<sup>23,24</sup> Another technique for nucleation enhancement, which has been employed in the experiments presented here and will be discussed in greater detail in a later section, is to simply bias the substrate negatively while immersed in a methane-hydrogen plasma.<sup>25,26</sup> Based on the variety of techniques used for the nucleation enhancement of diamond, presented above, it is the belief of the authors that the "diamond-seeding" hypothesis, although it has its merit and experimental evidence, is not the dominant mechanism for diamond nucleation from the gas phase.

Diamond nucleation is also favored on prominent features of the substrate surface, that is, surface morphologies that protrude with sharp edges or points, as opposed to valleys or flats. Such features are created by scratching or etching before or during the growth. Denig and Stevenson<sup>27,28</sup> observed selected growth on chemically etched surfaces, and Kirkpatrick, Ward, and Economou<sup>29</sup> used sputtered crater arrays as a means of selected-area nucleation. It has been speculated that the total free energy of a diamond embryo is lowered by securing some minimized contact area with the substrate, thereby favoring a nucleation event at these morphological features. Since high diamond-nucleation densities can also be achieved with pretreatments that result in macroscopically smooth surfaces, such as with oil residues, it is believed that the "sharp-edge" mechanism should play a relatively minor role. Scratching is also believed to create a high surface-defect density, which will in turn act as favorable nucleation sites. However, despite extensive TEM work, to date there has been no direct observation to support this defect-related nucleation theory.

Experimental data suggest that diamond nucleation on nondiamond substrates is promoted by a stable carbonaceous precursor. This speculation is based on the fact that higher surface carbon concentration has been observed via both surface<sup>21,22,30,31</sup> and bulk-sensitive techniques<sup>32,33</sup> on substrate surfaces pretreated with many of the nucleation-enhancing processes discussed above. The understanding of the nature and origin of such carbonaceous nucleation promoters created during a bias pretreatment is one of the major goals of the current research.

Interface chemistry was thought to play an important role in the diamond-nucleation process. Williams, Asbury, and Glass<sup>34,35</sup> observed an interfacial  $\beta$ -SiC layer between the silicon substrate and diamond film grown at 0.3% methane by cross-sectional TEM (XTEM) and again by x-ray photoelectron spectroscopy (XPS). Since then, carbide formation on various substrates has been observed prior to diamond nucleation and growth by many other researchers with electron and x-ray diffraction, as well as *in vacuo* surface-analytical techniques.<sup>32-38</sup> Joffreau, Haubner, and Lux<sup>39,40</sup> performed a systematic study of diamond growth on refractory metals (all are carbide formers) and observed that diamond nucleation occurred only after the formation of a thin car-

bide layer. They subsequently postulated that the difference in diamond-nucleation density, as observed on the various substrates, was related to the diffusivity of carbon in the respective carbide. However, attempts in the authors' laboratory to grow diamond on untreated bulk SiC substrates did not yield high nucleation densities, thus suggesting that carbide formation may only play an intermediate or secondary role. Others have reported favorable growth on SiC,<sup>22,41</sup> with nucleation densities only a few times greater than on untreated silicon. The importance of the carbide surface condition (order or disorder, stoichiometric or nonstoichiometric?) and the exact role that it plays in the promotion of diamond nucleation are thus unclear, although data presented in this study should help to alleviate some of this uncertainty.

Other noncarbide carbonaceous nucleation promoters have been postulated as well. Belton and co-workers observed, via *in vacuo* surface-analytical techniques, that diamond nucleation on platinum occurred on a surface that was mostly covered with a thin (1-3-monolayer) layer of hydrocarbons.<sup>42,43</sup> They also found that disordered graphite formed prior to diamond nucleation on a nickel substrate.<sup>44</sup> Angus *et al.* have also speculated that graphite may act as a diamond-nucleation precursor based on experiments where diamond nucleation was enhanced by the sprinkling of nonoriented graphite powders onto unscratched substrates.<sup>45</sup> Rudder *et al.* achieved a similar result from treating the surface with graphite fibers.<sup>46</sup> Ravi *et al.* observed that diamond nucleation could be enhanced by predepositing a layer of DLC in both combustion-flame and dc glow-discharge plasmas.<sup>20,21</sup> However, the actual nature of this DLC layer was never defined or well characterized, and other attempts to grow diamond on sputtered amorphous carbon and DLC have been unsuccessful in promoting high nucleation densities.<sup>41,47</sup> The discrepancy and diversity in the possible nucleation mechanisms presented above point to the need for a better understanding of the diamond-nucleation process. If the nature (structure and chemistry) and formation mechanism of this nucleation precursor can be identified, the nucleation of diamond from the vapor phase may then be more easily controlled and the deposition processes better tailored toward specific applications.

The purpose of the current research was to study systematically the nucleation of diamond on silicon enhanced via a predeposition biasing. To simplify and possibly reduce the number of active nucleation mechanisms, no *ex situ* pretreatments were employed. High nucleation densities on mirror-finished silicon were obtained via an *in situ* pretreatment that involves the deposition of an intermediate carbon layer by negatively biasing the substrate. Such a pretreatment method is very suitable for the study of diamond nucleation since it does not involve any scratching by diamond abrasives, therefore avoiding the confusion caused by the possibility of residual diamond seeds acting as nucleation sites. The chemical composition and structure of this intermediate carbon layer was characterized thoroughly via several *in vacuo* surface-analytical techniques including XPS, Auger electron spectroscopy (AES), and surface electron-energy-loss

spectroscopy (EELS), as well as high-resolution XTEM, scanning electron microscopy (SEM), and Raman spectroscopy. The information presented in this study should significantly improve the current understanding of the diamond-nucleation process by providing strong evidence of a dominant diamond-nucleation mechanism under the conditions employed.

## II. EXPERIMENTAL DETAILS

### A. *In vacuo* chemical-vapor-deposition and analytical chambers

All samples used in this study were both grown and analyzed in the *in vacuo* chemical-vapor-deposition (CVD) and surface-analytical chamber shown in Fig. 1. This apparatus consists of a microwave plasma CVD reactor (A in Fig. 1) and a multitechnique surface-analytical chamber (B in Fig. 1) that are joined via a transfer tube (C in Fig. 1). All samples are initially introduced into the system via a central load lock (D in Fig. 1), which is isolated from the transfer tube via a gate valve and may be evaluated to  $5 \times 10^{-8}$  Torr by a separate turbopump. With this arrangement the samples may be transferred back and forth between the CVD and analytical chambers without being exposed to atmospheric contamination.

The microwave plasma CVD reactor (A in Fig. 1) consists of a 6-in.-inner-diameter stainless-steel chamber made by Applied Science Technology, Inc. (ASTeX) (A in Fig. 1). The power supply used was an ASTeX S-1000, 2.45-GHz microwave supply with a rectangular waveguide that is coupled to the cylindrical growth cavity. The substrate holder is a fully retractable, differentially pumped tantalum heater that may be used to control the substrate temperature independently of the plasma power. During processing, the growth chamber is pumped by a roots blower followed by a process mechanical pump. The chamber is ultrahigh vacuum (UHV) compatible and can be evacuated to a base pressure of  $1 \times 10^{-7}$  Torr by the attached turbopump. The substrate temperature is measured by an infrared pyrom-

eter through a viewpoint normal to the substrate. The growth rate as well as the initial-nucleation process may be monitored *in situ* via laser-reflection interferometry (LRI).<sup>25</sup>

The analytical chamber (B in Fig. 1) is equipped with a Riber Mac2, semidispersive, electron analyzer which is used for both x-ray photoelectron spectroscopy and Auger electron spectroscopy. The x-ray source is a Riber dual-anode, Mg and Al, source. The electron source used for AES is a VG LEG61 electron gun, which is typically run at 3 kV and 200  $\mu$ A emission. Acquisition of the XPS and AES spectra was achieved via an IBM PC/AT microcomputer. The XPS spectra for this study, obtained using Mg  $K\alpha$ , were acquired in the pulse-counting mode using a Riber pulse counter. For AES the analyzer was modulated at 8 kHz and the differential spectra were obtained using a lock-in amplifier.

### B. Test of biasing effects on nucleation

The *in situ* biasing pretreatment is performed while the substrate is immersed in a methane-hydrogen plasma. Under standard growth conditions the holder-heater arrangement is isolated from ground (floating). The biasing pretreatment simply involves placing a negative dc bias (approximately 250 V) on the substrate relative to ground (Fig. 2). The substrate holder is approximately 1.5 in. in diameter, and the resulting current ranges from 100 to 200 mA. For a 1-cm<sup>2</sup> substrate, the resulting current flux is calculated to be approximately 15 mA/cm<sup>2</sup>. The heater is a tantalum filament surrounded by, and isolated from, a welded 0.04-in.-thick tantalum can that is differentially pumped as described above. The sample holder is made of molybdenum and is designed to fit on the end of the tantalum can. The tantalum can is connected to a single feedthrough to which the dc bias is connected (Fig. 2).

### C. Surface-analytical series versus bias time

This series was designed to observe systematically the nucleation process by intermittently stopping the bias pretreatment to study the chemical species on the surface. It has been previously documented that biasing

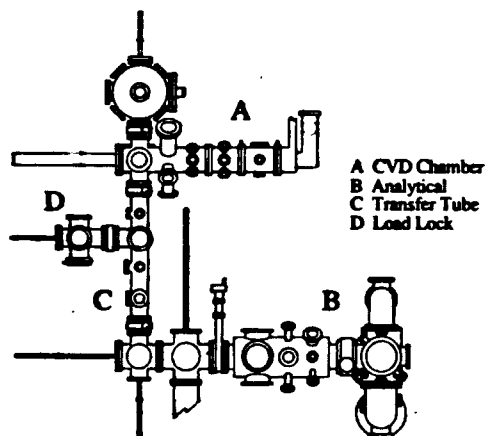


FIG. 1. *In vacuo* chemical-vapor-deposition and surface-analytical chamber.

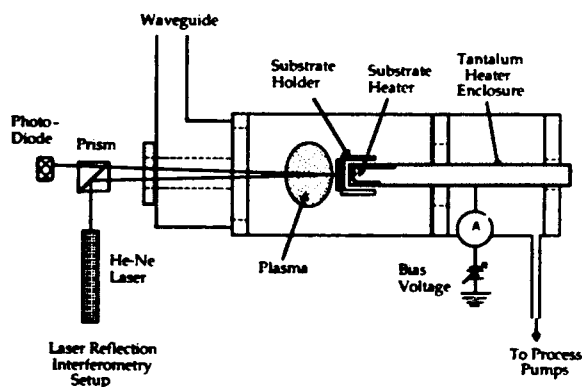


FIG. 2. CVD chamber showing *in situ* laser-reflection interferometry and substrate-biasing arrangements.

enhances the nucleation of diamond on silicon, yet the actual mechanism for this enhancement was not clearly understood. For this study a series of biasing pretreatments was interrupted at set intervals and then analyzed *in vacuo* to observe the changes in the surface chemistry that result. Table I outlines the experiments run and analyses performed for this pretreatment series.

From undoped silicon wafers, 1-cm<sup>2</sup> samples were prepared. They were subsequently ultrasonically cleaned in trichloroethylene (TCE), acetone, methanol, and 2-propanol and then rinsed in de-ionized (DI) water. Just prior to insertion into the load lock, they were dipped for 1 min into a 1:10 mixture of hydrofluoric acid in DI water to remove any existing native oxide, rinsed in DI water, and then blown dry with nitrogen. This procedure was designed to ensure minimal surface oxidation and hydrocarbon contamination on each of the samples used for this series.

The surface-analytical and biasing series was performed as follows. The substrates were biased at -250 V, immersed in a 2% methane in hydrogen plasma. The total flow rate was 1000 sccm, the net microwave power was maintained at 600 W, and the pressure was 15 Torr. Separate samples were biased for 1, 5, 15, 30, 60, 90, and 120 min. The plasma and bias were then shut off, the growth chamber was rapidly evacuated to  $1 \times 10^{-7}$  Torr, and the sample was subsequently transferred to the surface-analytical chamber. In the analytical chamber, XPS, XPS EELS, and AES were performed on each of the samples in this series. An as-inserted sample was also analyzed to observe the species present on the surface before the biasing pretreatment was initiated.

#### D. Analytical series versus growth time (after a 1-h bias)

The previous experimental series was designed to study the creation of nucleation sites. The present series was intended to observe and distinguish between the development of the nuclei and the growth of diamond on the existing sites. Table II outlines the experiments and analysis performed for this growth and analytical series.

The substrates were prepared identically to those in the preceding section. The samples were then biased for 1 h under the conditions described above. At the end of the biasing, the voltage was turned off, the bias leads were

disconnected, leaving the substrate floating, the methane concentration was reduced to 1% at 1000 sccm of hydrogen, the pressure was increased to 25 Torr, and the substrate was moved to a distance of about 0.5 cm from the plasma. These experimental conditions are those that have been proven in the past to grow high-quality diamond films.<sup>38</sup> Samples were grown under these conditions for 0.75, 1.0, 2.0, and 5 h, the plasma was then turned off, the chamber pumped down, and the samples were transferred into the analytical chamber for surface analysis as described above.

#### E. Transmission electron microscopy

Cross-sectional transmission-electron-microscopy imaging in both conventional and high-resolution modes was used to confirm and expand on observations made by surface analysis via direct observation of nucleation sites and the resulting interface between the diamond and silicon. XTEM was performed on the samples that were biased for 1 and 2 h and then further grown for 5 h. Therefore the interface observed would represent that which was intermittently analyzed using XPS, AES, and XPS EELS during the growth series outlined above. It has been difficult to observe the actual nuclei in TEM because of low diamond-nucleation densities even by scratching pretreatments. Past observations may be inconclusive because the actual nucleation sites may not be included in the region of the TEM thin specimen examined. However, the present biasing pretreatment has made it possible to obtain very high nucleation densities; thus the probability of observing an actual diamond nucleus has been dramatically increased.

XTEM specimens were prepared by special mechanical thinning and ion-milling methods, described elsewhere.<sup>48,49</sup> The specimens were examined in a Philips EM 430 T analytical electron microscope (AEM) operated at 300 kV and in a Philips EM 400 AEM, which is equipped with a field-emission gun (FEG) and Gatan parallel-detection electron-energy-loss spectroscope, operated at 100 kV. High-resolution transmission electron microscopy was performed on a JEOL 4000 EX electron microscope operated at 400 kV, with a resolution of 1.8 Å.

TABLE I. Sample bias times and analysis performed during analytical series of nucleation during the biasing pretreatment.

Bias time	XPS or AES	XPS EELS	Analysis performed		
			Raman spectroscopy	SEM	TEM
Before bias	X				
1 min	X				
5 min	X	X			
15 min	X	X			
30 min	X	X		X	
1 h	X	X		X	
1.5 h	X	X	X	X	
2.0 h	X	X	X	X	

TABLE II. Sample bias or growth times and analysis performed during the analytical series study of growth after a bias pretreatment.

Bias or growth time (h/h)	Analysis performed				
	XPS or AES	XPS EELS	Raman spectroscopy	SEM	TEM
1.0/0.0	X	X		X	
1.0/0.75	X	X			
1.0/1.0	X	X		X	
1.0/2.0	X	X		X	
1.0/5.0	X	X	X	X	X

### III. RESULTS

#### A. Biasing results

Figure 3 shows SEM micrographs of diamond grown by microwave plasma CVD on (a) a Si wafer that was scratched with 0.25- $\mu\text{m}$  diamond paste and (b) a pristine Si wafer that was pretreated by biasing. Both samples were further grown for 5 h under identical conditions.

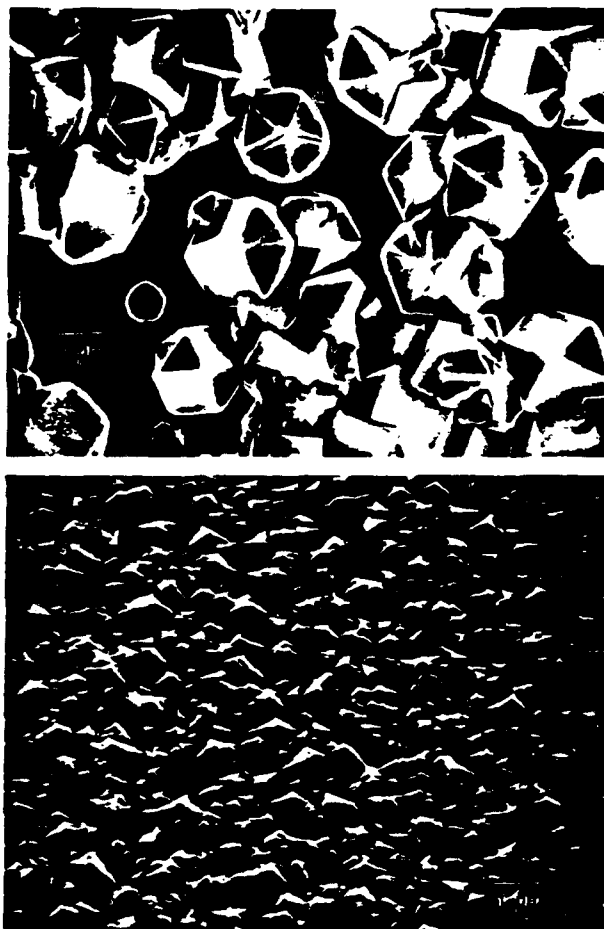


FIG. 3. SEM micrographs of samples grown under various pretreatments: (a) silicon wafer scratched with 0.25- $\mu\text{m}$  diamond powder and (b) pristine silicon wafer biased on a (2% methane)-in-hydrogen plasma at -250 V for 1 h.

The Raman spectra from both the scratched and biased samples are shown in Fig. 4. The smaller diamond peak and larger background observed from the biased sample are indicative of films with higher nucleation densities and a larger number of grain boundaries.<sup>50,51</sup> The samples prepared by biasing were found to produce nucleation densities up to  $10^{11} \text{ cm}^{-2}$ , depending upon pretreatment time. This is contrasted with the scratched Si and pristine Si nucleation densities of  $10^7$  and  $10^4 \text{ cm}^{-2}$ , respectively. Nucleation on the untreated Si wafer was too low to measure, but a comparison with published nucleation densities of  $10^3$ – $10^5 \text{ cm}^{-2}$  (Refs. 23 and 41) shows that the biasing technique has a pronounced effect on nucleation and is thus deserving of a more in-depth study.

#### B. Surface-analytical series versus bias time

The carbon 1s core-level peak [Fig. 5(a)] was observed using XPS, as a function of bias time, of which the quantitative analysis is shown in Table III. The silicon substrate was found to have a small amount of carbon contamination on it before biasing began. This carbon contamination has been observed previously by other researchers<sup>36–38</sup> and was found, in the present experiments, to either be removed or converted into SiC in the first 5 min of biasing. From 5 min to 1 h the majority of

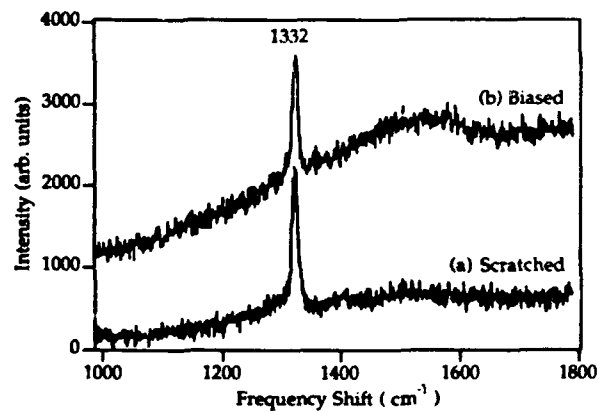


FIG. 4. Raman spectra of diamond grown on (a) scratched and (b) biased substrates shown in Figs. 3(a) and 3(b), respectively.

the carbon on the surface has a binding energy of 282.8 eV and is assigned to Si-C bonding. Deconvolution of the C 1s peaks shows that a smaller peak, approximately 20%, exists at 284.3 eV, which is characteristic of C-C bonding. The origin and structure of this excess C-C bonding is unclear as is its effect on the nucleation density.

It is unlikely that the C-C peak could represent diamond since such a large difference in nucleation density is observed (spanning several orders of magnitude) for biases of 5 min to 1 h. The fact that the relative per-

TABLE III. Quantification of species on the surface at various bias times as calculated from XPS peak-area ratios and relative sensitivity factors.

Bias time	Carbon 1s	Silicon 2p	Concentration ratios [C]/[Si]
	peak ratios $I_{C-C}:I_{Si-C}$	peak ratios $I_{Si-Si}:I_{Si-C} (I_{Si-O})$	
0.0 h	( $C_xH_yO_z$ )	100:0	16:84
5 min	22:78	44:43:(13)	26:74
15 min	22:78	26:74	32:68
30 min	20:80	20:80	33:67
1 h	20:80	1:99	37:63
1.5 h	54:46	12:88	48:52
2.0 h	90:10	11:89	92:08

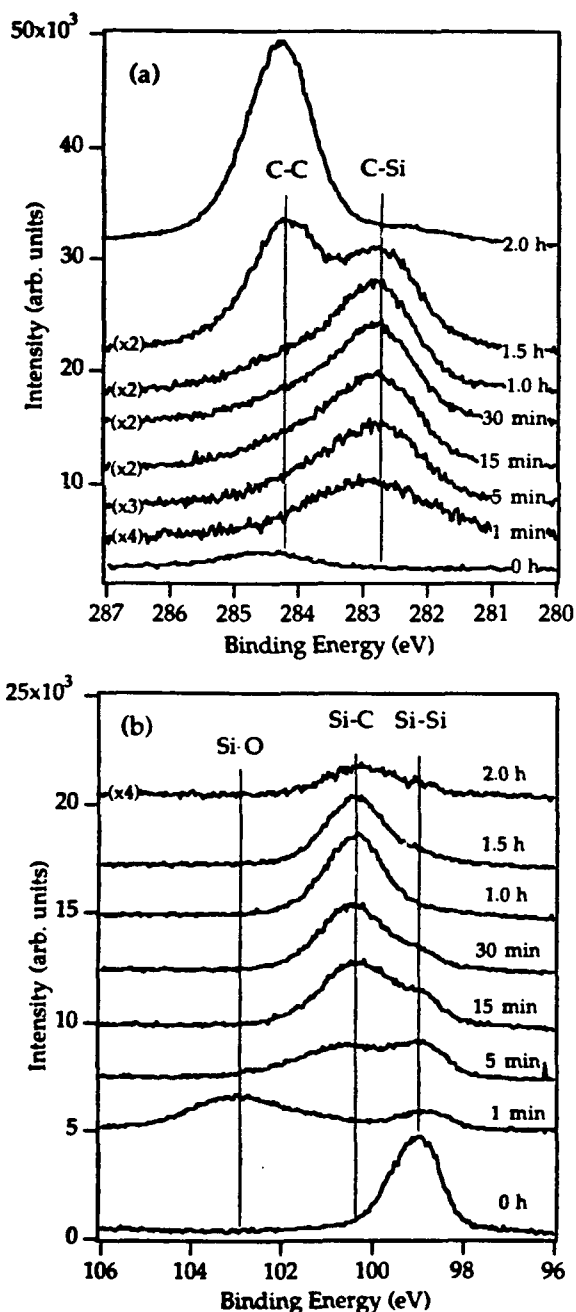


FIG. 5. XPS analysis as a function of bias-pretreatment time: (a) carbon 1s and (b) silicon 2p peak progressions.

tage of this peak to the total C 1s is fairly constant at 20% for 5 min to 1 h suggests that it could be on the surface. In fact, a post-biasing sputter with argon in the analytical chamber was successful in removing the C-C, resulting in a single Si-C peak at 282.8 eV, thus confirming that this carbon was confined to the surface. The possible sources of this carbon could be any one or a combination of the following: (i) condensation of carbon from the hydrocarbon species in the gas phase when the plasma was turned off, (ii) carbon contamination from the walls of the CVD chamber, or (iii) an excess amount of carbon on the surface that is a direct result of the biasing process. The following experiments were performed to help determine the source of this surface carbon.

When the plasma power is turned off, it is possible that carbon from the various hydrocarbon species present in the gas phase may then condense onto the substrate surface. To make sure that this condensation was not responsible for the excess carbon observed on the carbide surface, the methane flow was turned off following a 30-min bias, and the sample was exposed to a hydrogen plasma for 15 min. Surface analysis performed on this sample revealed that the substrate still contained elemental carbon in addition to silicon carbide, thus excluding the condensation of amorphous carbon from the gas phase as a possible source. Regarding item (ii), if contamination from the CVD chamber were a possible source of this carbon, an increase in the observed C-C contamination would be expected with increased exposure to the CVD chamber prior to analysis. For the samples observed in this study, the waiting time before analysis ranged from 15 min to 2 h and no dependence on this time was observed. This suggests that chamber contamination should be ruled out as a possible source. From these observations the authors propose that this small amount of carbon on the surface is caused by the biasing process, such as excess etching or sublimation of the Si from the Si-C or an increased flux of hydrocarbon ions to the surface. By exposing SiC to elevated temperatures, van Brommel, Crombeen, and Tooren showed, using low-energy electron diffraction (LEED) and AES, that the surface became carbon rich.<sup>52</sup> They speculated that this was due to the preferential evaporation of Si from SiC. In a hydrogen-rich plasma, it is possible that this process may be accelerated, resulting in the observed supersaturation of carbon on the substrate surface. This will be

discussed further in Sec. IV A.

The Si 2p peak [Fig. 5(b)] was used to observe the chemical transformation of the silicon substrate as a function of bias time. Before biasing begins there exists only a single peak at 99.0 eV, which is representative of elemental silicon. After just 1 min of biasing, a majority of the silicon observed has been converted into silicon oxide (102.7 eV). By 15 min of biasing, however, the oxide has been totally removed and the resulting peak is a mixture of elemental silicon (99.0 eV) and Si-C (100.3 eV). From 15 min to 1 h of biasing, the Si-C peak steadily increases to nearly 100%, suggesting that it is covering the silicon substrate. At 1.5 h, corresponding to the sharp increase in the C 1s peak at 284.3 eV in Fig. 5(a), there is a reemergence of the elemental silicon signal at 99.0 eV. This suggests that etching of the interfacial SiC layer may be occurring, thereby bringing Si closer to the surface and causing an increase in the Si signal. By 2 h the C 1s peak shows over 90% C-C bonding, and the carbon-to-silicon ratio is up to over 90% as well, indicating that the surface is nearly covered with some elemental form of carbon. This elemental carbon is shown to be diamond by AES, XPS EELS, and Raman spectroscopy as presented in the following paragraphs.

The XPS series showed that a silicon film develops before the surface becomes covered with some elemental form of carbon. Overlayer calculations were performed on this carbide layer to determine its approximate thickness as a function of bias time. Calculations are based on an inelastic electron mean free path of 20 Å (Ref. 53) and assume a layer-by-layer growth model<sup>54,55</sup> of the silicon carbide overlayer for simplicity. The results of these calculations are shown in Table IV. Before biasing there exists a clean silicon substrate with approximately 4 Å of the amorphous and hydrogenated carbon on the surface. From 5 min to 1 h, the carbide thickness increases from approximately 10 to 90 Å, while the surface carbon increases slightly from 5 to 10 Å. At 1.5 h, concurrent with the observed increase in the elemental silicon peak, the carbide thickness drops drastically back down to approximately 45 Å and remains relatively unchanged by 2 h. Some preliminary biasing experiments performed on single-crystal SiC, in the authors' laboratory, have confirmed that SiC may be etched under the above conditions.

TABLE IV. Overlayer calculations for the biasing pretreatment, assuming an inelastic electron mean free path of 20 Å and a layered growth mode for the overlayer.

Bias time	Si-C layer thickness (Å)	C-C thickness (Å)	Si-O thickness (Å)
0.0 h		4	0
5 min	12	6	4
15 min	27	8	0
30 min	32	8	0
1 h	90	9	0
1.5 h	42	(diamond)	0
2.0 h	44	(diamond)	0

The layer-by-layer approximation used above may result in a low calculated value for the interfacial carbide thickness. If the carbide film at 1 h had a uniform thickness of 90 Å and the subsequent etching was nonuniform (i.e., islandlike), then the actual average thickness would be higher than the 45 Å calculated above. There would still be a decrease in the overall thickness from 1 to 1.5 h, but not as drastic. To calculate more accurately the actual layer thicknesses, one would have to assume a model that involved both layer-by-layer and island growth. One also would have to assume a fraction of the surface covered by the islands and a ratio of layered to island growth. So, in the above thickness calculations as well as those to follow, it is important to observe the qualitative trends and not the absolute thicknesses reported. A good review of overlayer-thickness calculations for electron spectroscopy may be found in Feldman and Mayer.<sup>55</sup>

Since the XPS core-level shifts can only provide chemical bonding information, C EELS and AES were implemented to help provide information as to the crystalline structure of the different forms of carbon observed on the surface during this series. Figures 6(a) and 6(b) display both standard AES and XPS-EELS spectra taken from natural type-IIA diamond, sputtered amorphous carbon, silicon carbide, and highly oriented pyrolytic graphite (HOPG). The AES fine structure from the bias-time series [Fig. 7(a)] indicates a transition from hydrogenated and amorphous carbon that exists on the surface before biasing begins to SiC by 30 min and then to diamond by 2 h of biasing. There is a subtle change from the 1-h-bias sample to the 1.5-h case, but without elaborate curve fitting the exact nature of this change is unclear.

From the XPS-EELS data [Fig. 7(b)], the transition from SiC to diamond is much more evident. From the standards shown in Fig. 6(b) and from previously published data,<sup>37,56-58</sup> silicon carbide has a characteristic bulk plasmon peak at 23 eV and diamond has both bulk and surface plasmon peaks at 35 and 25 eV, respectively. Diamond has also been shown to have a weak peak in the energy range from 14 to 17 eV, which is said to be due to interband transitions.<sup>56,57</sup> At 0.5 h the spectra clearly resembles that of SiC, with a single bulk-plasmon peak at 23 eV, and at 2 h resembles diamond with both bulk- and surface-plasmon peaks at 35 and 25 eV, respectively. However, at 1.5 h the spectra is a clear mixture of both diamond and SiC, thus suggesting that some diamond is present on the surface after 1.5 h of biasing. From this data it can be concluded that the sharp rise in the C 1s peak at 284.3 eV after 1.5 h of bias, shown in Fig. 5(a), was due to an increase in the number of diamond nuclei on the surface.

To further assure ourselves that the carbon observed after 1.5 and 2 h of bias was diamond, Raman spectroscopy was performed. Because of the relatively low Raman cross section for diamond, ten scans were performed and then subsequently superimposed in order to improve the signal-to-noise ratio. The carbon concentration on the 1.5-h sample was still too low to observe with this technique; however, the 2.0-h sample (Fig. 8) did produce a small characteristic diamond peak at 1332 cm<sup>-1</sup>. No graphitic peaks were observed near 1580 cm<sup>-1</sup>. Since

graphite has about a 50 times higher Raman cross section than does diamond, it is highly improbable that the diamond could have nucleated on graphite. If it had nucleated on graphite, a Raman peak at  $1580\text{ cm}^{-1}$  would have been observed for a nucleation density as high as that obtained here.

SEM micrographs were taken (Fig. 9) at 1-, 1.5-, and 2.0-h bias to see if the diamond could be observed. The 2-h sample showed that the surface was about 90%

covered with diamond particles ranging in sizes from 10 to 60 nm in diameter (within the resolution of the Hitachi H-5000 field-emission microscope). The nucleation density from this sample was observed to be roughly  $5 \times 10^{10}\text{ cm}^{-2}$ , with the understanding that there could be particles less than 10 nm in diameter that could not be observed because of the resolution limit of the microscope used. The 1.5- and 1.0-h samples showed decreasing nucleation densities, of particles within this same size range, of  $5 \times 10^9$  and  $5 \times 10^8\text{ cm}^{-2}$ , respectively.

The 30-min sample had a very small number of observ-

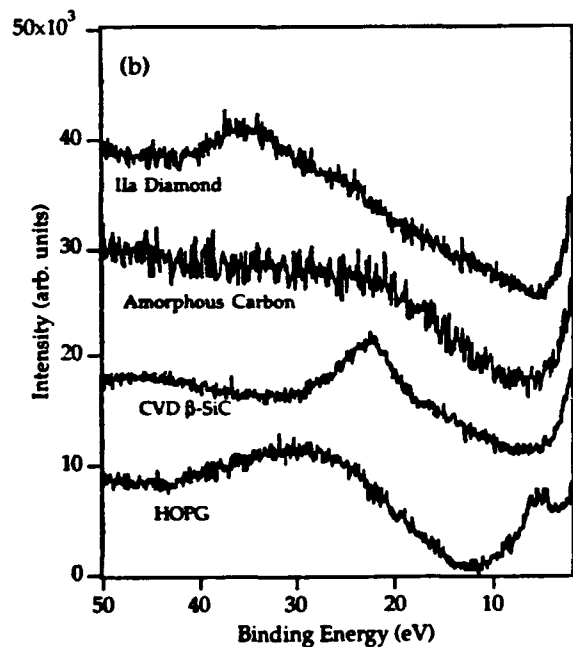
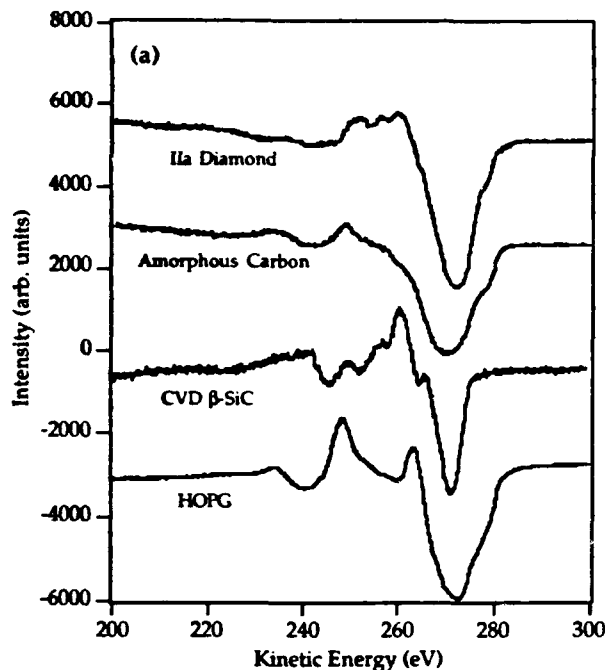


FIG. 6. Standard (a) AES and (b) XPS-EELS spectra from single-crystal diamond, amorphous carbon, single-crystal SiC, and highly ordered pyrolytic graphite (HOPG).

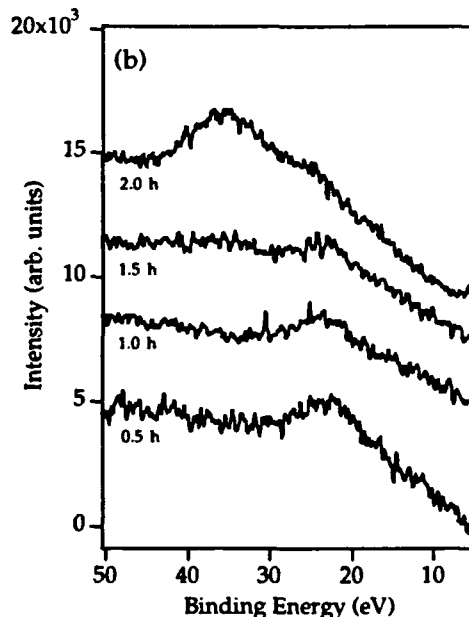
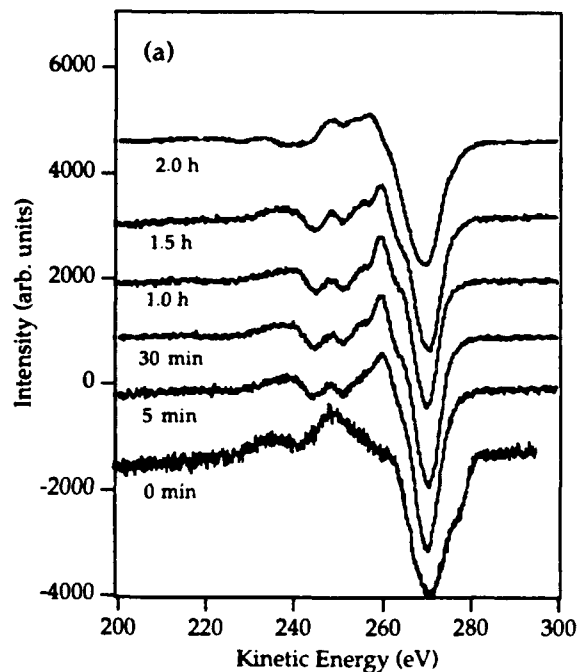


FIG. 7. Auger electron spectra and (b) XPS EELS taken at various bias times.

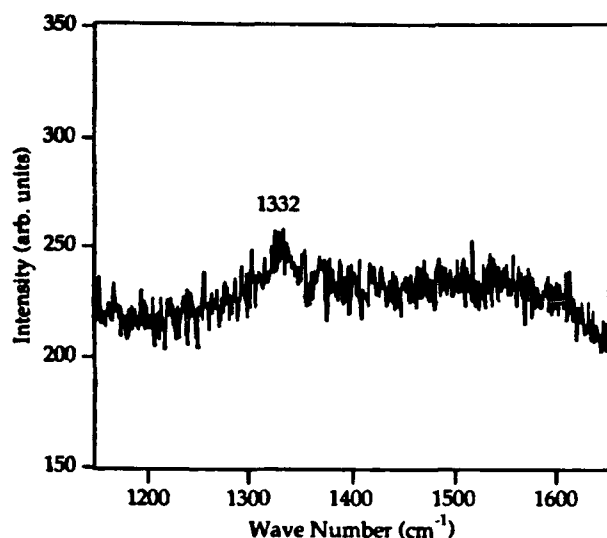


FIG. 8. Raman spectra from sample after 2 h of the bias pretreatment.

able nuclei present on the surface; thus it was difficult to obtain an accurate measure of the nucleation density. Therefore the nucleation density for the 30-min sample was determined based on a 30-min bias followed by a 10-h growth, which produced an approximately 75% complete diamond film. The density of particles on this sample was measured to be  $1 \times 10^7 \text{ cm}^{-2}$ . Figure 10 shows a plot of resulting nucleation density as a function of bias time. The 0-min-bias sample is based on average values obtained from the literature for growth on untreated Si wafers. From these data it is evident that the nucleation density may be controlled over six orders of magnitude by varying the length of the bias pretreatment.

Data from AES, XPS EELS, Raman spectroscopy and SEM, obtained from the bias series, confirm that diamond is nucleating during the biasing pretreatment. Diamond particles may be observed by SEM at as early as 30 min of biasing. Nucleation continues for up to 2 h, at which time the surface is nearly covered with nuclei no larger than 80 nm in diameter. This confirms that the biasing process is actually creating the diamond nuclei, as opposed to just creating sites that are favorable for diamond nucleation. It is also important to note that if the bias pretreatment is allowed to continue long after the nominal 2-h limit, a much poorer-quality diamond film results, thus suggesting that conditions favorable for nucleation are not so for diamond growth.

In summary of the present section, the *in vacuo* surface-analytical series revealed several important stages in this diamond-nucleation process. First, there existed an amorphous nondiamond carbon on the surface before biasing began. This carbon layer was, within the first 5 min, either etched away or converted into Si-C as a thin Si-O layer was also formed. By 15 min of biasing, the Si-O layer was completely removed and the majority of the carbon on the surface was in the form of Si-C. From 5 min to 1 h of biasing, there existed a small surface layer of carbon, presumably on top of the Si-C. Overlayer cal-

culations revealed that the carbide thickness reached a maximum of approximately 90 Å by 1 h of biasing and then decreased to near 50 Å by 2 h. The surface carbon was calculated to be approximately 5 Å thick at 5 min and increased to 10 Å by 1 h. XPS-EELS and Raman-

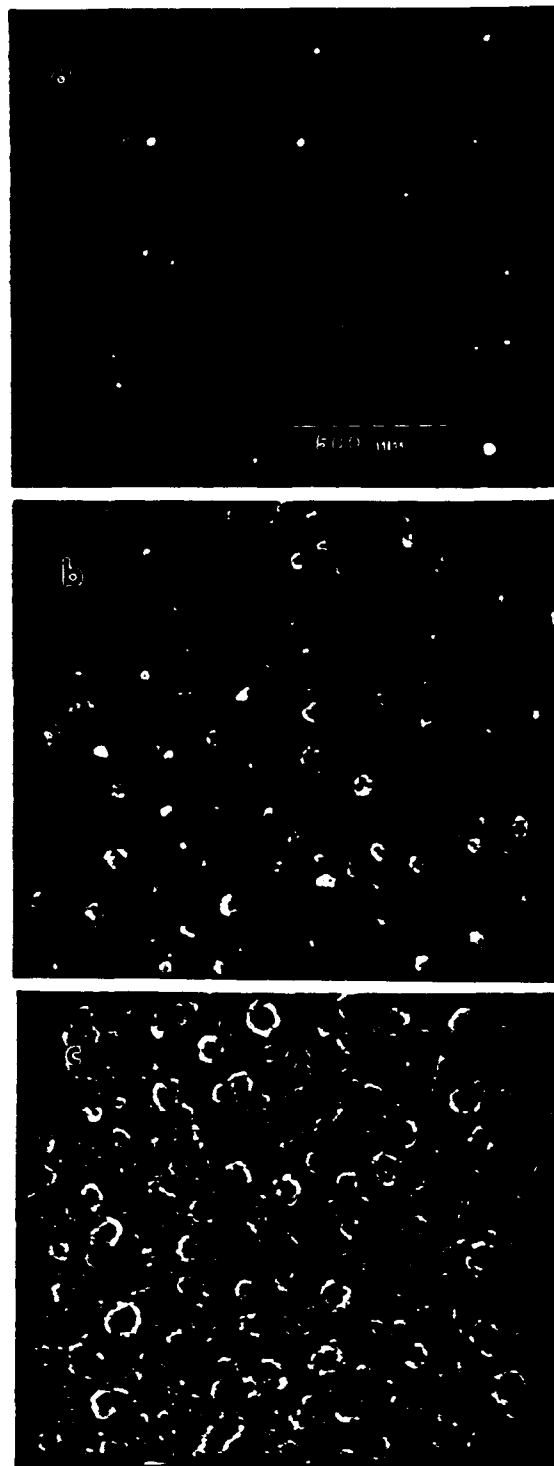


FIG. 9. SEM micrograph of the bias pretreatment after (a) 1.0 h, (b) 1.5 h, and (c) 2.0 h. Magnification scale is the same for all three.

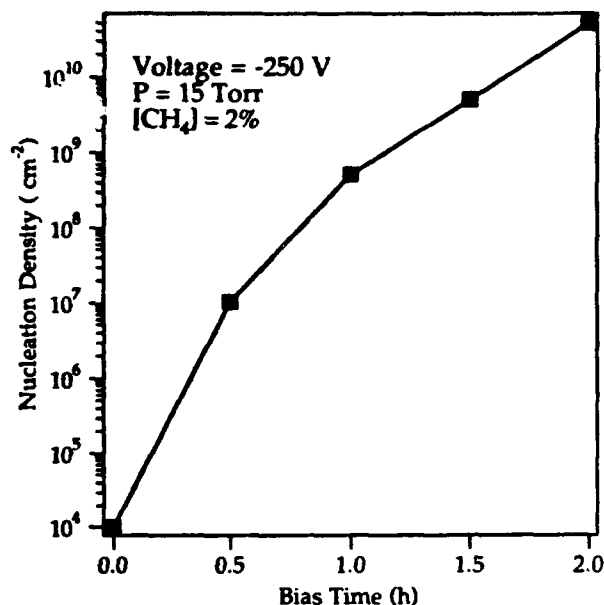


FIG. 10. Plot of nucleation density as a function of bias time. Nucleation density for 0.0-h-bias time taken from average literature values for growth on unscratched silicon.

spectroscopy data suggest that it is not graphitic and nucleation results exclude it from being diamond. It is believed that the Si-C is covered with a thin layer of amorphous carbon that has accumulated on the surface as a result of the biasing environment and that this carbon may play an important role in the nucleation of diamond during the bias-pretreatment process as discussed later.

### C. Analytical series versus growth time (after a 1-h bias)

The data presented below were obtained by first biasing for 1 h and then intermittently performing surface analysis on the sample after periods of diamond growth with no biasing, as outlined in Sec. II. The diamond-growth times are defined as the period of time after the bias pretreatment has ended. The purpose of this series was to study the growth of diamond on the pretreated samples analyzed and discussed above. Table V displays

TABLE V. Quantification of species on the surface at various growth times for the 1-h-bias pretreatment, as calculated from XPS peak-area ratios.

Bias or growth time (h/h)	Carbon 1s peak ratios $I_{C-C}:I_{Si-C}$	Silicon 2p peak ratios $I_{Si-Si}:I_{Si-C} (I_{Si-O})$	Concentration ratios [C]/[Si]
0.0/0.0	(C, H, O <sub>2</sub> )	100:0	16:84
0.08/0.0	22:78	44:43:(13)	26:74
0.25/0.0	22:78	26:74	32:68
0.5/0.0	20:80	20:80	33:67
1.0/0.0	20:80	1:99	37:63
1.0/0.75	43:57	10:90	35:65
1.0/1.0	50:50	14:86	41:59
1.0/2.0	76:24	35:65	52:48
1.0/5.0	100:0		100:0

the results from surface analysis for this series.

From observing the carbon 1s peak as a function of growth time [Fig. 11(a)], one notes a steady increase in C-C bonding (284.3 eV) from when the bias voltage is turned off and official growth begins, until the substrate is totally covered with diamond at the 5-h mark. Of special interest is the progression of the Si 2p peak [Fig. 11(b)]. When the bias is turned off at 1 h, the surface has been almost totally converted to SiC. After just 45 min of growth on this surface, the relative contribution of reduced Si to the total Si 2p peak has increased to 10%, while the carbon-to-silicon ratio has remained nearly con-

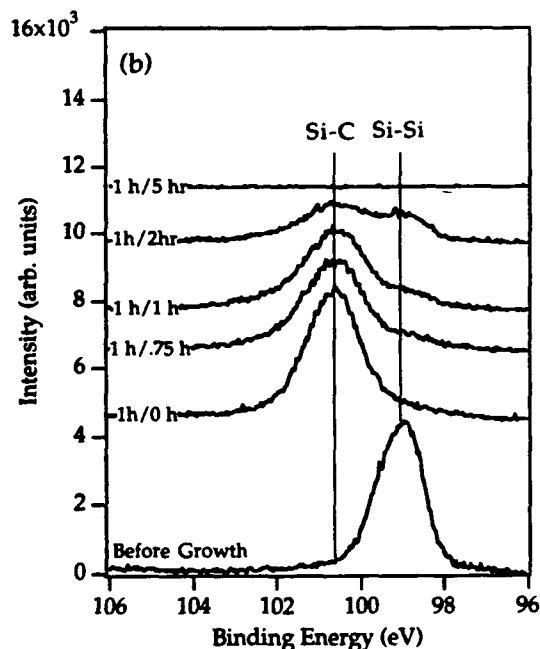
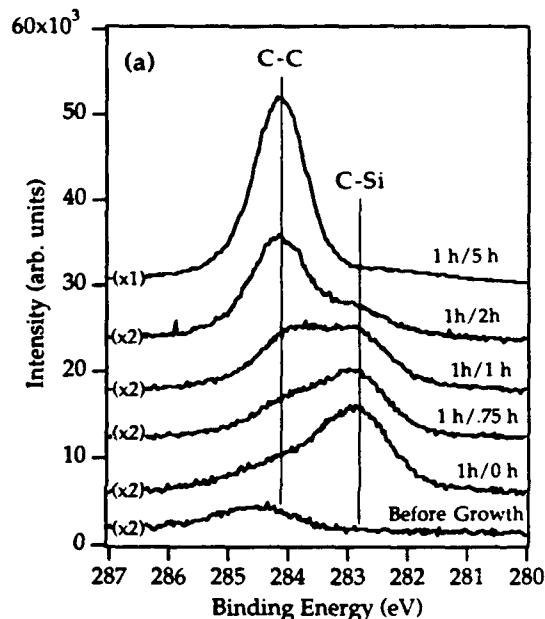


FIG. 11. XPS at various growth times after a 1-h-bias pretreatment: (a) carbon 1s and (b) silicon 2p peak progressions.

stant. This suggests that as the individual diamond particles are growing, as indicated by the increase in the C 1s peak at 284.3 eV, etching of the SiC surface or interfacial layer may be exposing silicon from the original substrate. It should be mentioned that it is not necessary to totally expose the silicon in order to observe it by XPS. Given the theoretical escape depth for Si, it should still be possible to observe the signal if it is covered by as much as 80–100 Å of SiC. If the SiC is amorphous, the escape depth may be slightly longer. After 2 h of growth following the biasing, the carbon-to-silicon ratio has increased to over 50%, with 76% of the C 1s signal originating from C-C bonding. The contribution from Si-Si bonding to the Si 2p peak has now increased to 35%, further suggesting that etching of the SiC interfacial layer may be continuing as the diamond particles continue to grow.

Overlayer calculations, similar to those performed for the previous series, indicate that once the bias is turned off, the silicon carbide layer begins to diminish rapidly. The interfacial layer reduces in average thickness, from 90 Å at the end of the biasing to 40 Å by 1 h and 20 Å by 2 h of growth. These data suggest again more convincingly that the silicon carbide layer is being etched, or removed, once significant diamond growth occurs. As mentioned in the previous section, the actual decrease in carbide thickness will not be as sharp if the etching, or removal of the carbide, is nonuniform.

As in the previous series, the AES spectra [Fig. 12(a)] continue to show a strong contribution from the SiC and do not resemble diamond until after 5 h of growth. The XPS-EELS series, on the other hand [Fig. 12(b)], shows that the contribution from diamond begins to become significant by 1.0 h of growth and continues until the film is complete at 5 h. Figure 13 displays SEM micrographs taken from sample (a) right after the 1-h bias and (b) after 1 h of growth. The micrographs show that after the bias is turned off, no more significant nucleation occurs and that the diamond growth continues primarily on the nuclei that existed at the end of the biasing period. The nucleation density remains roughly unchanged throughout the growth, and the average particle diameter increases in size.

It is important here to comment on the sensitivity of XPS EELS in observing diamond nucleation on, in this case, silicon carbide. Based on SEM data discussed above for the 1-h-biased sample (Fig. 13), the nucleation density of diamond particles on the surface was approximately  $5 \times 10^8 \text{ cm}^{-2}$  and they were 10–50 nm in diameter. This concentration may be too insignificant to be detected by XPS EELS. If one were to perform a rough area calculation based on an average particle diameter of 20 nm, the percentage of the sampling area covered by the diamond particles would be only 0.2%. For the sample that was grown for 1 h after biasing, the average particle diameter is near 100 nm. From this the average sampling area occupied by the diamond has increased to over 4%. Based on these calculations and the data presented above, the XPS core-level measurements are an effective means of determining the amount of specific phases on the surface during the nucleation process, but XPS EELS may only be used to obtain structural information for surface con-

centrations in excess of 2–4%.

From the bias and growth series, the data suggest that diamond grows primarily on the diamond particles that existed on the surface after the initial biasing. SEM micrographs at different post-biasing growth times show that the initial particles just increase in size and develop better crystal habits with time. The discontinuation of nucleation once biasing ceases suggests again that ideal growth conditions may not be favorable for nucleation. As the diamond particles grow, there appears to be etch-

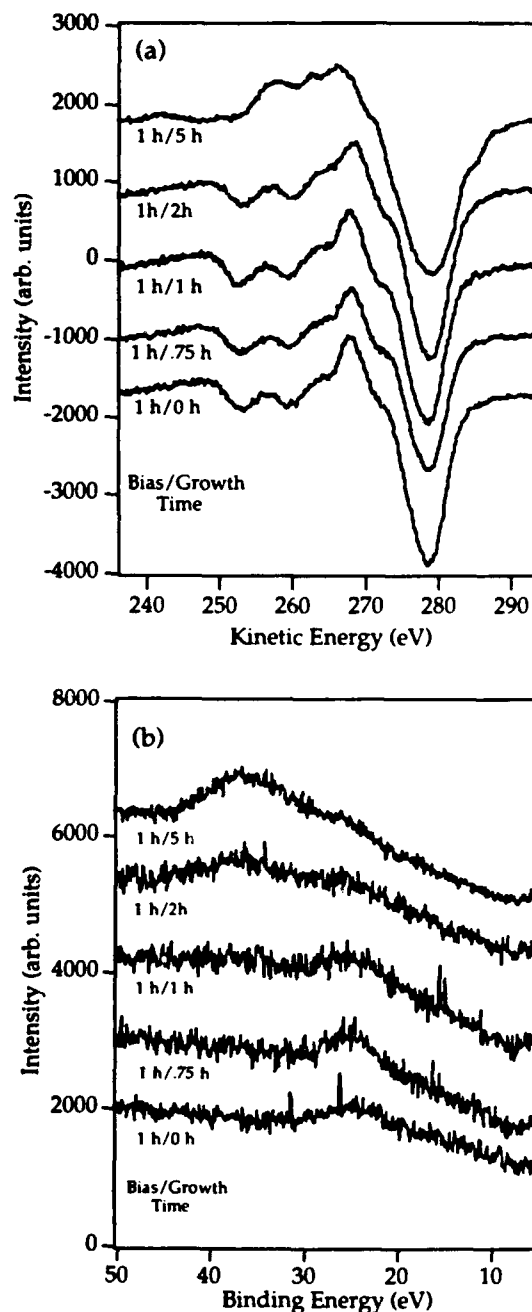


FIG. 12. (a) Auger electron spectra and (b) XPS EELS taken at various growth times on a sample bias pretreated for 1 h.

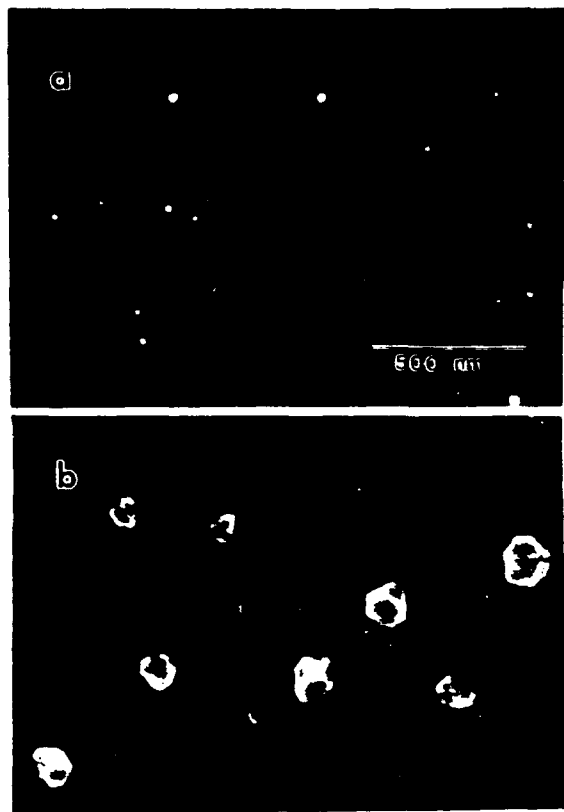


FIG. 13. SEM micrographs as a function of growth time on samples that were biased for 1 h, showing no new significant nucleation once the bias was turned off: (a) 1-h bias only and (b) 1-h growth after bias.

ing of the SiC layer as suggested by the increase in the Si-Si bonding observed in the XPS Si 2*p* series.

#### D. Cross-sectional transmission electron microscopy

Figure 14 displays an XTEM micrograph from a sample that was biased for 1 h and then further grown for 5 h. The electron-beam direction was parallel to the Si(110) direction, such that the sample was viewed in an exact edge-on condition. An interfacial layer is readily observed between the silicon substrate and diamond film. Several diamond nuclei are seen to be emerging from this interfacial layer, and none were observed to be in direct contact with the Si substrate. This divergence of the initial nuclei reconfirms that CVD diamond undergoes three-dimensional growth once the stable nuclei has formed. Twin lamellae, prominent defects in diamond, were also observed just above where the nuclei begin to coalesce, as shown by the arrows in Fig. 14.

High-resolution TEM images were also obtained in the same region, as shown in Fig. 15. The grainy appearance of this interfacial layer under optimum focusing conditions revealed its noncrystalline, or amorphous, character. This was then confirmed by electron microdiffraction and optical diffractogrammetry. EELS was not performed in this region since its thickness was below the spatial resolution limit required for microanalysis in

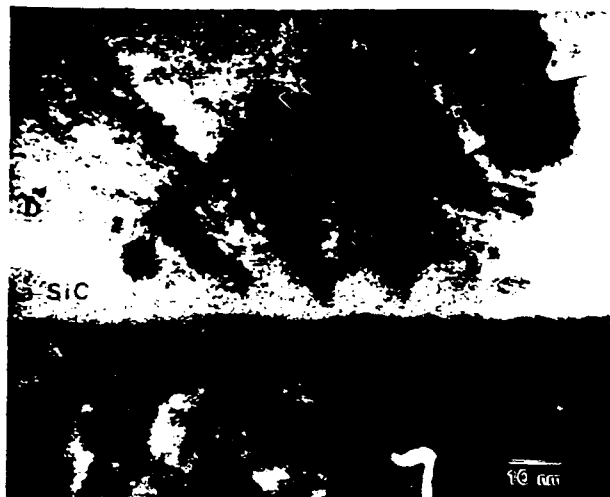


FIG. 14. Low-magnification high-resolution XTEM micrograph showing several nucleation sites and an interfacial layer between silicon and diamond.

TEM. However, transmission EELS was performed on a separate sample that had a much thicker interfacial layer, and the spectra obtained were identical to a spectrum collected from single-crystal  $\beta$ -SiC under similar operating conditions. No other elements were found in these EELS spectra. Combined with the *in vacuo* surface analysis presented earlier, it is reasonable to assume that this interfacial layer is predominantly amorphous silicon carbide. The interfacial layer for the 1-h-bias sample appears to have an average thickness of approximately 60 Å, with some areas as thick as 100 Å.

It is important to determine whether the nuclei actually formed on top of this amorphous layer or on the surface of the silicon. Because the sample is viewed in cross section and because of the limited depth of field, the nuclei may only appear to have formed within the interfa-

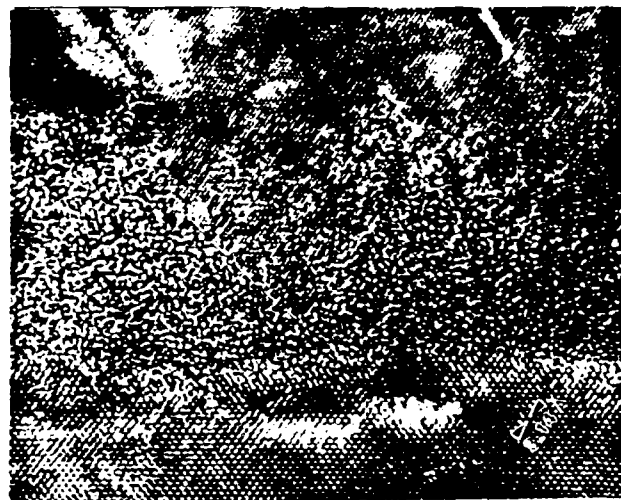


FIG. 15. High-magnification high-resolution XTEM micrograph showing an amorphous interfacial layer between the diamond and silicon substrates.

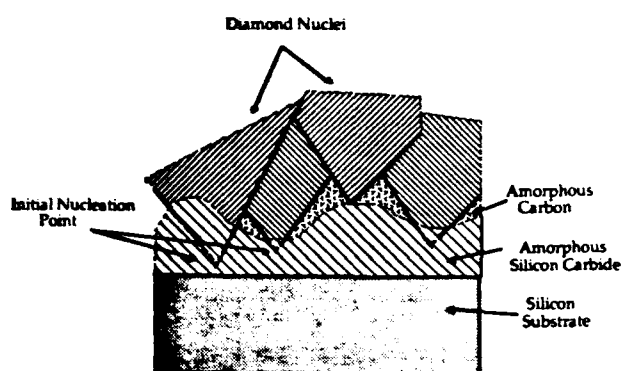


FIG. 16. Model of a diamond nuclei showing how nucleation may have occurred closer to the substrate than it appears.

cial layer, when, in fact, they may have formed on the silicon. If one models the nucleus as an inverted pyramid, it is easy to envision how a cross-sectional slice, not made in the exact center of the nucleus, can make it appear to have originated in the interfacial layer. However, by tracing the boundaries of the nuclei to a converging point, it appears that the nuclei originate within the interfacial layer and above the silicon substrate. This is shown schematically in Fig. 16 and may also be seen in Fig. 15. Furthermore, in all the samples examined, none of the diamond crystals were observed to be in direct contact with the Si substrate. Therefore it was concluded that nucleation did not occur on the silicon substrate directly, but rather on top of the interfacial layer.

#### IV. DISCUSSION

Based on the data presented above, as well as published studies on diamond nucleation, the authors have compiled a list of nucleation models or possible explanations for the enhancement of diamond nucleation resulting from a bias pretreatment. Since the emphasis of the present research involves this bias pretreatment, some nucleation mechanisms, although they may be valid under other experimental conditions, are not mentioned here. Listed below are four possible explanations for nucleation data presented in this study, and each will be discussed in greater detail in later sections: (a) diamond nucleation on adventitious carbon that existed on the surface before the biasing pretreatment, (b) diamond nucleation directly on an interfacial layer of either (i) crystalline silicon carbide or (ii) amorphous silicon carbide, (c) diamond nucleation on some stable nondiamond carbon that has accumulated on the surface during the biasing pretreatment, (d) diamond nucleation enhancement caused by the removal and suppression of a surface oxide.

##### A. Potential nucleation models

###### 1. Nucleation on surface contamination present before biasing pretreatment

Williams,<sup>30</sup> in a study of the effect of various surface pretreatments on nucleation, has shown that a trend ex-

ists between the amount of carbon observed on the surface before growth and the resulting nucleation density. Samples that had higher amounts of carbon on the surface resulted, qualitatively, in higher nucleation densities. One possible source of nucleation enhancement could have been from the adventitious carbon found on the substrate prior to biasing. However, a problem with this model is that similar concentrations of adventitious carbon were found on the surfaces of unscratched silicon wafers in Williams's study and the resulting nucleation densities were very low. One might then argue that, during the biasing, this carbon is converted into a form suitable for nucleation. From the surface-analytical series versus bias time discussed in Sec. III B, it was found that within the first 5 min of biasing the adventitious carbon had either been replaced by or converted into a mixture of C-C and Si-C. If the conversion of the adventitious carbon, via biasing, is the explanation for increased nucleation, then one would expect a significantly higher nucleation density after just 5 min of biasing. This suggests that the surface contamination alone does not account for the observed increase in nucleation density.

###### 2. Nucleation directly on silicon carbide

Silicon carbide was observed in this study to have formed on the silicon surface before the diamond particles could be detected. Both Belton *et al.*<sup>36</sup> and Williams *et al.*,<sup>38</sup> in similar *in vacuo* studies, also observed the formation of Si-C during the early stages of diamond growth. Polycrystalline silicon carbide has also been observed by many other researchers<sup>32-35,59</sup> to have formed between the diamond and silicon substrate. Badzian and Badzian<sup>60</sup> have suggested that the development of a  $\beta$ -SiC buffer layer is first required before diamond nucleates on silicon. These arguments were made based on a partial lattice matching observed on the (110) when the (100) direction of  $\beta$ -SiC is parallel to the (112) direction of diamond. Hartnett *et al.*<sup>41</sup> reported 3 times higher diamond-nucleation densities on (220)-textured CVD-grown  $\beta$ -SiC films than on untreated silicon, but no enhancement for growth on ion-sputtered SiC and (111)-textured  $\beta$ -SiC films.

The authors believe that the formation of silicon carbide plays a role in diamond nucleation on silicon, but that it is not alone sufficient for nucleation to occur. The focus of this discussion should not be on whether diamond can be grown on a SiC substrate or whether an interfacial SiC layer forms before diamond growth on silicon, but rather on the actual steps by which diamond forms on the SiC. Does the nucleation occur directly on the silicon carbide, or is there another intermediate step that must occur?

One of the first problems with the hypothesis that diamond nucleation occurs directly on SiC is the relatively small increase in nucleation density observed when SiC substrates are used. The reports show as much as 3 times higher nucleation density on SiC substrates,<sup>41</sup> but the biasing pretreatment used in this study increased nucleation by several orders of magnitude beyond that. Furthermore, if the presence of silicon carbide is the sole

requirement for nucleation to occur, then one would expect much higher nucleation densities for the shorter bias times since a SiC layer forms immediately. It could be argued that it is the amorphous character of the SiC layer in the present research that promotes higher nucleation rates. An amorphous surface has a higher surface free energy, and it is thus more energetically favorable for nucleation to occur on such a surface. However, this alone cannot explain the large change observed in nucleation density as a function of bias time since this amorphous layer essentially forms immediately. Furthermore, as mentioned previously, on sputtered SiC no significant increase in nucleation was observed.<sup>41</sup>

Another problem with the theory that diamond nucleates directly on the carbide is expressed in reports of nucleation-enhancement techniques that do not involve carbide formation. Angus *et al.* have achieved high nucleation densities by sprinkling graphite powder on the substrate surface,<sup>45</sup> while Morrish *et al.*<sup>23,24</sup> were equally successful with pump oil as a nucleation promoter. Furthermore, one of the present authors has also observed in a separate study<sup>61</sup> that under some conditions amorphous carbon interfacial layers exist between the diamond film and silicon substrate rather than a SiC layer. Finally, scratching a Si substrate is not expected to modify the formation of SiC significantly, yet it has a major impact on nucleation density.

These data suggest that some type of a carbonaceous precursor may be involved and that the carbide formation only plays an intermediate role. Recall that the XPS data for the bias series (Table III and Fig. 5) showed that from 5 min to 1 h of biasing there existed an excess concentration of elemental carbon on the SiC surface. This excess carbon again suggests that the nucleation of diamond directly on silicon carbide may not be the primary explanation for the increased density from biasing and is the topic of the next section (Sec. IV A 3).

### 3. Nucleation of a non-diamond carbonaceous precursor

The majority of the data from the literature as well as from this study suggest that some intermediate nucleation step exists between the carbide formation and actual diamond nucleation. In the data presented here, amorphous silicon carbide was immediately formed (1–5 min) on the surface of the silicon. There also existed a small amount of amorphous carbon (it was determined to be neither graphite nor diamond) on the surface of the Si-C. This "excess" carbon may have resulted from (1) increased flux of positively charged carbon and hydrocarbon ions to the surface or (2) nonuniform etching or sublimation of the silicon carbide. Van Bommel, Crombeen, and Tooren,<sup>52</sup> found that silicon could preferentially evaporate from SiC thus leaving the surface carbon rich. In the present work, as the carbide layer continues to grow from 5 min to 1 h, the concentration of this amorphous layer relative to the carbide remains fairly constant. After 1 h of bias the amorphous carbon can no longer be distinguished from the diamond nuclei on the surface using XPS core-level shifts. It is hypothesized that this surface carbon contributes significantly to the

nucleation of diamond and that the silicon carbide merely acts as a temporary but critical host on which the carbon can accumulate until clusters of the appropriate size and structure required for diamond nucleation develop.

Before attacking the specific problem of diamond nucleation, one should first consider the basic steps involved in the nucleation of three-dimensional clusters. General cluster-nucleation phenomena may be simplified and explained as a series of the following steps.<sup>62</sup>

(i) Atoms impinge upon the substrate from the vapor phase and become adsorbed onto the surface.

(ii) At standard CVD temperatures, the adatoms, if they are not free to react with the substrate, may either reevaporate or diffuse over the surface.

(iii) If the concentration of adatoms is high enough, they combine and form clusters.

(iv) Through statistical fluctuations in local adatom concentration, these clusters grow and decay.

(v) Because of free-energy considerations, there will be a critical size above which the probability of growth will be greater than decay.

(vi) These stable clusters are then free to grow either from the continued migration of single adatoms or from the direct impingement of atoms from the vapor phase.

In the cases of bias-enhanced diamond nucleation, the proposed model is only slightly more complicated in that it first involves the formation of an interfacial carbide layer. When the carbon first arrives at the surface, it is more energetically favorable to form silicon carbide than for the atoms to accumulate on the surface and eventually form clusters. Silicon carbide formation, however, is kinetically limited by silicon diffusion through the existing carbide layer to the surface. Thus, although there initially exists an excess concentration of carbon on the surface, it may not be kinetically favorable for critical nuclei to form until after the carbide has reached a critical thickness such that the silicon outdiffusion is too slow to continue. However, in contradiction to this argument, data show that the carbide layer is still growing from 30 to 60 min, yet nucleation has occurred as early as 30 min and is easily visible by 1 h. The reason for this is believed to be that local islands of Si-C have reached a critical thickness such that the carbon on the surface is then allowed to cluster and eventually form a stable, suitable site for diamond nucleation. This also helps explain the rapid increase in nucleation as a function of bias time. As more and more areas reach critical carbide thicknesses, more carbon becomes available to form stable clusters. This variation in thickness of the interfacial SiC layer is supported by the TEM observations.

TEM observations also show that nucleation is occurring closer to the Si/SiC interface than the critical thickness described above. One possible explanation for this may be due to the etching of the SiC. If during the etching process silicon is being preferentially depleted, excess carbon could locally saturate the surface. This local saturation of carbon would allow critical carbon clusters, and eventually diamond nuclei, to form in a region where the carbide is below the critical thickness.

It is important to stress that, although the carbon clusters on the surface may reach a critical size, they may not

be ideally suited for diamond nucleation. Reports have shown that amorphous carbon alone does not act as a strong nucleation promoter.<sup>22,41</sup> The authors suggest that certain clusters may form that, at least locally or in certain regions, have the correct crystal structure and bonding configuration to promote the formation of the diamond structure. This speculation is based on the observations that not all forms of carbon are sufficient for diamond nucleation. Unfortunately, the exact form of this excess carbon necessary for diamond growth is not known, although Angus<sup>47</sup> has recently made some progress in this area, utilizing graphite as the starting point for his model. Judging from the much higher nucleation densities achieved on carbide-versus non-carbide-forming substrates, either the amount or type of excess carbon present is related to the carbide-forming properties of the substrate. There are numerous mechanisms which may account for this influence, including the items discussed in the following sections.

#### B. Role of biasing in enhancing the nucleation

The previous section provided suggestions for nucleation models and the critical steps that may lead up to nucleation. The role that biasing plays in either promoting or accelerating these critical steps is of interest as well. Does the biasing merely accelerate the same process that would otherwise occur at much slower rates, or does it create alternative path(s) that would not occur, under standard CVD conditions? The following are the envisioned possible effects that biasing may have on the CVD process in so far as they relate to diamond nucleation: (i) increased flux of positively charged carbon ions to the surface ( $C_xH_y^+$ ); (ii) reduced flux of electrons and negatively charged ions to the surface; (iii) higher-energy transfer from the ions to the surface, resulting in increased surface mobilities of adsorbed species; (iv) enhancement of reactions and molecular dissociation just above the substrate as a result of an increase in, and higher energy for, ion-neutral collisions within the sheath region; and (v) reduction and suppression of oxide formation on the surface.

It is easy to conceptualize how an increase in the arrival rate of carbon or hydrocarbon ions to the surface may help to expedite the nucleation process as outlined above. The possible role of electrons in preventing or suppressing nucleation is unclear. Since electrons are being repelled during the negative biasing, one may suggest that they may indeed inhibit nucleation. However, positive biasing during hot-filament CVD experiments did not significantly suppress diamond nucleation.<sup>63,64</sup>

The approximate ion-impingement energy may be calculated from the Stefan-Boltzmann law,

$$E = \sigma T^4,$$

by measuring the increase in temperature as a result of the biasing. From this relationship the ion energies were calculated to be approximately 5 eV. Ions of this energy are not expected to create much damage to the surface, although some energy is expected to be transferred upon

collision with substrate atoms. Ion bombardment of the surface could locally increase the surface mobilities of adatoms and may thus help to explain how carbon clusters can form more rapidly on the surface. It may also explain why the interfacial layer is amorphous. The continual ion bombardment may prevent the amorphous-surface carbide from crystallizing.

The increased dissociation due to accelerated ions in the sheath region is easy to envision, yet again the consequences are unclear. The ions that are accelerated through the sheath region have a much higher kinetic energy than in the rest of the plasma; therefore, when they collide with another ion or neutral molecule, there is a higher ionization or dissociation efficiency. This could result in a much higher concentration of dissociated hydrocarbons, and atomic hydrogen, near the sample surface.

Since oxide formation does play a significant role in inhibiting diamond nucleation, it is necessary to discuss the role that the elimination of oxide formation might play during bias-enhanced nucleation. It is agreed by most researchers that the presence of a native oxide on silicon will impede the nucleation process.  $SiO_2$  masks have been used widely as a method of obtaining selected-area nucleation of diamond.<sup>65,66</sup> On a similar *in vacuo* study performed by Williams *et al.*<sup>38</sup> on a silicon substrate prepared by scratching only, Si-O was observed throughout the entire analytical series. The present study was performed using the same *in vacuo* growth and analytical chamber. The current data from the biasing series showed that no Si-O could be detected after 15 min indicating that the biasing is very effective in removing the oxide.

The actual mechanism by which the oxide is removed is unclear; however, initial results in the authors' laboratory showed that biasing in a hydrogen plasma alone were unsuccessful in removing the oxide. This preliminary data suggest that a reaction involving the C-O bond is responsible for the removal of Si-O. Lee, Miller, and Cutler<sup>67</sup> proposed the following mechanism by which  $SiO_2$  may be reduced by carbon:



Once the reaction is initiated, CO will be regenerated as long as there is  $SiO_2$  available. The initial CO gas required to initiate the above reaction may be obtained from the solid-solid reaction between initial carbon species arriving on the surface and the oxide according to the reaction



Reaction (4) has also been suggested by Pickrell *et al.*<sup>68</sup> as an intermediate reaction for the nucleation of diamond on silica. An increase in the flux and kinetic energy of  $C_xH_y^+$  species to the surface may help explain why the oxide becomes less stable under biasing conditions. If the arriving carbon species have higher kinetic energy as a

result of the biasing, then reactions (2)–(4) may proceed more rapidly to the right, thus resulting in an increased removal of oxide from the surface. The authors are not suggesting that the elimination of the oxide alone should explain the substantial increase in nucleation density; however, it should be considered as to have played a major role in allowing nucleation to occur. Once the oxide has been eliminated, the other major nucleation steps, as outlined in the previous section, must then occur for the successful development of the diamond nuclei.

The above are only speculations on how the biasing may be aiding the nucleation process. A more in-depth discussion requires a much greater understanding and more thorough study of the plasma conditions during this biasing process. Plasma diagnostics within the sheath region, under various biasing conditions, would be very beneficial in aiding the understanding of bias-enhanced diamond nucleation.

### C. Schematic summary of the nucleation model

In view of the previous discussions, a schematic representation of the steps for nucleation which are speculated to be important can be developed. This is displayed in Fig. 17.

(i) Before biasing begins there are both adsorbed oxygen and amorphous carbon present on the silicon surface [Fig. 17(a)].

(ii) The adsorbed carbon is then either etched away or converted to Si-C, and the physisorbed oxygen is converted into Si-O [Fig. 17(b)].

(iii) As biasing continues, the oxide is etched as the carbide islands continue to grow. Preferential etching of the silicon from the Si-C and/or continued high flux of carbon to the surface creates an excess concentration of carbon on the surface [Fig. 17(c)].

(iv) As the local carbide islands reach a critical thickness, such that continued carbide growth is unlikely, the excess carbon on the surface becomes free to form small clusters. Surface mobility of the carbon may be enhanced by the bombardment during the biasing.

(v) Some of these clusters become favorable for diamond nucleation [Fig. 17(d)].

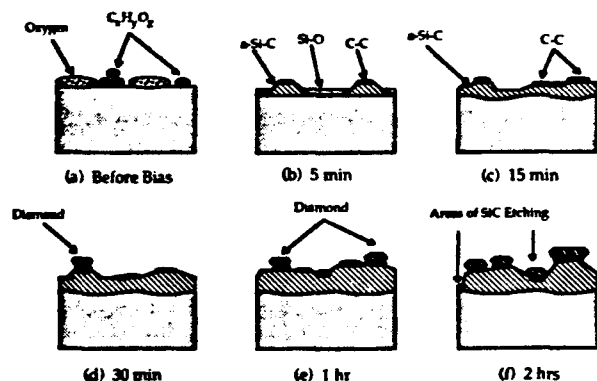


FIG. 17. Model of diamond nucleation, via biasing, on silicon.

(vi) As most of the carbide reaches a critical thickness (90 Å), more free carbon becomes available to form other diamond-nucleation sites, and thus a greater number of diamond nuclei are observed [Fig. 17(e)].

(vii) As biasing continues, there is ongoing etching of the surface (but not the more stable diamond nuclei) and adsorption of the carbon. This local etching creates a rougher silicon carbide surface. If silicon is preferentially etched from the carbide, increasing the carbon concentration in that region, then nucleation clusters may actually form on thinner areas of the carbide.

(viii) The etching, cluster formation, and diamond nucleation continue until the surface is eventually covered with diamond nuclei [Fig. 17(f)].

### V. SUMMARY

It has been shown here that biasing may be used as an effective means of nucleation enhancement. The major purpose of this work was to gain a better understanding of this method of enhancing diamond nucleation on silicon. *In vacuo* surface analysis as well as high-resolution XTEM, SEM, and Raman spectroscopy were used to study the nucleation and growth of diamond using biasing and microwave plasma CVD. Biasing was found to increase the nucleation density for unscratched silicon substrates by over five orders of magnitude. The nucleation density may be controlled over three orders of magnitude by varying the length of the bias pretreatment. Once the bias was turned off, diamond grew on diamond nuclei that were created during the pretreatment and no further significant nucleation occurred. If the bias was left on indefinitely, the resulting diamond film was of much poorer quality than that produced under a 1–2-h bias followed by a growth with no bias. This suggested that conditions which are favorable for diamond nucleation are not ideal for diamond growth.

An amorphous silicon carbide interfacial layer developed before significant diamond nucleation occurred. Preferential etching of the Si-C and/or a decreased reaction with Si were thought to be responsible for the development of an excess carbon concentration on the Si-C. Once the silicon carbide layer had reached a critical or maximum thickness, which under these experimental conditions was approximately 90 Å, it was believed that the carbon on the surface was free to form critical clusters that were eventually favorable for diamond nucleation. Once significant diamond nucleation has occurred, the preferential etching of the carbide appears to have allowed carbon clusters to form on thinner regions, closer to the Si substrate, thus explaining why some diamond nuclei were observed to be closer to the substrate than others. The ability of the biasing pretreatment to remove and suppress the formation of a surface oxide was also thought to play a role in the nucleation enhancement.

### ACKNOWLEDGMENTS

The authors wish to thank X. H. Wang and R. J. Nemanich for performing the Raman spectroscopy and M. Veil for assisting with the diamond growth. Techni-

cal assistance from K. L. More and N. D. Evans in performing HRTEM and EELS analysis at Oak Ridge National Laboratory is also deeply appreciated. Useful advice from D. Belton and J. Angus is also gratefully acknowledged. This research was financially supported in part by SDIO/IST through ONR and by Kobe Steel, Ltd. Transmission EELS analysis was supported in part by the Division of Materials Sciences, U.S. Department of Ener-

gy through the SHaRE Program under Contract No. DE-AC05-76OR00033 with Oak Ridge Associated Universities. High-resolution TEM was sponsored by the U.S. Department of Energy, Office of Transportation Technologies, as part of the High Temperature Materials Laboratory User Program, under Contract No. DE-AC05-84OR21400 with Martin Marietta Energy Systems, Inc.

- <sup>1</sup>S. Matsumoto, Y. Sato, M. Kamo, and N. Setaka, *Jpn. J. Appl. Phys.* **21**, L183 (1982).
- <sup>2</sup>D. V. Fedoseev, B. V. Deryagin, I. G. Varshavskaya, A. V. Lavrent'ev, and V. V. Matveev, *Zh. Eksp. Teor. Fiz.* **80**, 413 (1981) [*Sov. Phys.—JETP* **53**, 210 (1981)].
- <sup>3</sup>R. Mania, L. Stobierski, and R. Pampuch, *Cryst. Res. Technol.* **16**, 785 (1981).
- <sup>4</sup>S. Matsumoto, Y. Sato, M. Tsutsumi, and N. Setaka, *J. Mater. Sci.* **17**, 3106 (1982).
- <sup>5</sup>D. V. Fedoseev, *Kolloidn. Zh.* [*Colloid J. USSR* **46**, 727 (1984)].
- <sup>6</sup>D. V. Fedoseev, I. G. Varshavskaya, and B. V. Derjaguin, *J. Electrochem. Soc.* **81**, 284 (1981).
- <sup>7</sup>D. V. Fedoseev and T. S. A. S. Semenova, *Sov. J. Superhard Mater.* **6**, 1 (1984).
- <sup>8</sup>M. Frenklach, W. Howard, D. Huang, J. Yuan, K. E. Spear, and R. Koda, *Appl. Phys. Lett.* **59**, 546 (1991).
- <sup>9</sup>M. Frenklach, R. Kematic, D. Huang, W. Howard, K. E. Spear, A. W. Phelps, and R. Koba, *J. Appl. Phys.* **66**, 395 (1989).
- <sup>10</sup>J. C. Angus, H. A. Will, and W. S. Stanko, *J. Appl. Phys.* **39**, 2915 (1968).
- <sup>11</sup>W. Howard, D. Huang, J. Yuan, M. Frenklach, K. E. Spear, R. Koba, and A. W. Phelps, *J. Appl. Phys.* **68**, 1247 (1990).
- <sup>12</sup>S. Mitura, *J. Cryst. Growth* **80**, 417 (1987).
- <sup>13</sup>P. K. Bachmann, W. Drawl, D. Knight, R. Weimer, and R. F. Messier, in *Diamond and Diamond-Like Materials Synthesis*, edited by G. H. Johnson, A. R. Badzian, and M. W. Geis (Materials Research Society, Pittsburgh, 1988), p. 99.
- <sup>14</sup>P. K. Bachmann, R. Weimer, W. Drawl, Y. Liou, and R. Messier (unpublished).
- <sup>15</sup>S. Iijima, Y. Aikawa, and K. Baba, *Appl. Phys. Lett.* **57**, 2646 (1990).
- <sup>16</sup>S. Iijima, Y. Aikawa, and K. Baba, *J. Mater. Res.* **6**, 1491 (1991).
- <sup>17</sup>K. Suzuki, A. Sawabe, H. Yasuda, and T. Inuzaka, *Appl. Phys. Lett.* **50**, 728 (1987).
- <sup>18</sup>A. Sawabe and T. Inuzaka, *Thin Solid Films* **137**, 89 (1986).
- <sup>19</sup>C.-P. Chang, D. L. Flamm, D. E. Ibbotson, and J. A. Mucha, *J. Appl. Phys.* **63**, 1744 (1988).
- <sup>20</sup>K. V. Ravi and C. A. Koch, *Appl. Phys. Lett.* **57**, 348 (1990).
- <sup>21</sup>K. V. Ravi, C. A. Koch, H. S. Hu, and A. Joshi, *J. Mater. Res.* **5**, 2356 (1990).
- <sup>22</sup>J. J. Dubray, C. G. Pantano, M. Meloncelli, and E. Bertran, *J. Vac. Sci. Technol. A* **9**, 3012 (1991).
- <sup>23</sup>A. A. Morrish, K. Snail, and W. Carrington (unpublished).
- <sup>24</sup>A. A. Morrish and P. E. Pehrsson, *Appl. Phys. Lett.* **59**, 417 (1991).
- <sup>25</sup>B. R. Stoner, B. E. Williams, S. D. Wolter, K. Nishimura, and J. T. Glass, *J. Mater. Res.* **7**, 257 (1992).
- <sup>26</sup>S. Yugo, T. Kanai, T. Kimura, and T. Muto, *Appl. Phys. Lett.* **58**, 1036 (1991).
- <sup>27</sup>P. A. Dennig and D. A. Stevenson, in *Proceedings of the Second International Conference on the New Diamond Science and Technology*, edited by R. Messier and J. T. Glass (Japan New Diamond Forum, Washington, D.C., 1990).
- <sup>28</sup>P. A. Dennig and D. A. Stevenson, in *Proceedings of the First International Conference on the Applications of Diamond Films and Related Materials*, edited by Y. Tzeng, M. Yoshikawa, M. Murakawa, and A. Feldman (Elsevier, New York, 1991), p. 383.
- <sup>29</sup>A. R. Kirkpatrick, B. W. Ward, and N. P. Economou, *J. Vac. Sci. Technol. B* **7**, 1947 (1989).
- <sup>30</sup>B. E. Williams (unpublished).
- <sup>31</sup>D. E. Meyer, R. O. Dillon, and J. A. Woollam, *J. Vac. Sci. Technol. A* **7**, 2325 (1989).
- <sup>32</sup>S. Yugo, T. Kimura, and T. Muto, *Vacuum* **41**, 1364 (1990).
- <sup>33</sup>S. Yugo, T. Kimura, H. Kanai, and Y. Adachi, in *Noble Refractory Semiconductors*, edited by D. Emin, T. Aselage, and C. Wood, *MRS Symp. Proc. No. 97* (Materials Research Society, Pittsburgh, 1987), p. 327.
- <sup>34</sup>B. E. Williams, D. A. Asbury, and J. T. Glass, in *Surface Analysis of Diamond Nucleation on Silicon and Electron Microscopy of the Diamond/Silicon Interface*, edited by R. Freer (Kluwer Academic, Amsterdam, 1990), p. 169.
- <sup>35</sup>B. E. Williams and J. T. Glass, *J. Mater. Res.* **4**, 373 (1989).
- <sup>36</sup>D. N. Belton, S. J. Harris, S. J. Schmieg, A. M. Wiener, and T. A. Perry, *Appl. Phys. Lett.* **54**, 416 (1989).
- <sup>37</sup>D. N. Belton and S. J. Schmieg, *J. Vac. Sci. Technol. A* **8**, 2353 (1990).
- <sup>38</sup>B. E. Williams, B. R. Stoner, D. A. Asbury, and J. T. Glass, in *Diamond and Diamond-Like Films and Coatings, NATO Advanced Study Institute, Series B: Physics*, edited by J. Angus, R. Clausing, L. Horton, and P. Koidl (Plenum, New York, 1990).
- <sup>39</sup>P. O. Joffreau, R. Haubner, and B. Lux (unpublished).
- <sup>40</sup>P. O. Joffreau, R. Haubner, and B. Lux, *Int. J. Refract. Hard Met.* December, 186 (1988).
- <sup>41</sup>T. Hartnett, R. Miller, D. Montanari, C. Willingham, and R. Tustison, *J. Vac. Sci. Technol. A* **8**, 2129 (1990).
- <sup>42</sup>D. N. Belton and S. J. Schmieg, *J. Appl. Phys.* (to be published).
- <sup>43</sup>S. J. Harris, D. N. Belton, A. M. Wiener, and S. J. Schmieg, *J. Appl. Phys.* **66**, 5353 (1989).
- <sup>44</sup>D. N. Belton and S. J. Schmieg, *J. Appl. Phys.* **66**, 4223 (1989).
- <sup>45</sup>J. C. Angus, Z. Li, M. Sunkara, R. Gat, A. B. Anderson, S. P. Mehandru, and M. W. Geis, in *Proceedings of the International Symposium on Diamond and Diamond Materials, Electrochemical Society Meeting, Washington, D.C.* (Electrochemical Society, New York, in press).
- <sup>46</sup>R. A. Rudder, G. C. Hudson, R. C. Hendry, R. E. Thomas, J. B. Posthill, and R. J. Markunas, in *Proceedings of the First In-*

- International Conference on the Applications of Diamond Films and Related Materials*, edited by Y. Tzeng, M. Yoshikawa, M. Murakawa, and A. Feldman (Elsevier, New York, 1991), p. 395.
- <sup>47</sup>J. C. Angus (unpublished).
- <sup>48</sup>G.-H. M. Ma, Y. H. Lee, and J. T. Glass, *J. Mater. Res.* **5**, 2367 (1990).
- <sup>49</sup>G.-H. M. Ma, B. E. Williams, J. T. Prater, and J. T. Glass, *Diamond Relat. Mater.* **1**, 25 (1991).
- <sup>50</sup>R. E. Shroder, R. J. Nemanich, and J. T. Glass, *Phys. Rev. B* **41**, 3738 (1990).
- <sup>51</sup>R. J. Nemanich, J. T. Glass, G. Lucovsky, and R. E. Shroder, *J. Vac. Sci. Technol. A* **6**, 1783 (1988).
- <sup>52</sup>A. J. Van Bommel, J. E. Crombeen, and A. V. Tooren, *Surf. Sci.* **48**, 463 (1975).
- <sup>53</sup>M. P. Seah and W. A. Danch, *Surf. Interface Anal.* **1**, 2 (1979).
- <sup>54</sup>C. S. Fadley, R. J. Baird, W. Siekhaus, T. Novakov, and S. A. L. Bergstrom, *J. Electron Spectrosc. Relat. Phenom.* **4**, 93 (1974).
- <sup>55</sup>L. C. Feldman and J. W. Mayer, *Fundamentals of Surface and Thin Film Analysis* (Elsevier, New York, 1986).
- <sup>56</sup>Y. Wang, R. W. Hoffman, and J. C. Angus, *J. Vac. Sci. Technol. A* **8**, 2226 (1990).
- <sup>57</sup>Y. Wang, H. Chen, R. W. Hoffman, and J. C. Angus, *J. Mater. Res.* **5**, 1 (1990).
- <sup>58</sup>J. T. Glass, B. E. Williams, and R. F. Davis, *Proc. Soc. Photo-Opt. Instrum. Eng.* **877**, 56 (1988).
- <sup>59</sup>Y. Mitsuda, Y. Kojima, T. Yoshida, and K. Akashi, *J. Mater. Sci.* **22**, 1557 (1987).
- <sup>60</sup>A. R. Badzian and T. Badzian, *Surf. Coat. Technol.* **36**, 283 (1988).
- <sup>61</sup>G.-H. M. Ma, Ph.D. dissertation, North Carolina State University, 1991.
- <sup>62</sup>J. L. Robins, *Appl. Surf. Sci.* **33/34**, 379 (1988).
- <sup>63</sup>Y.-H. Lee, Ph.D. dissertation, North Carolina State University, 1990.
- <sup>64</sup>Y. H. Lee, P. D. Richard, K. J. Bachmann, and J. T. Glass, *Appl. Phys. Lett.* **56**, 620 (1990).
- <sup>65</sup>J. L. Davidson, C. Ellis, and R. Ramesham, *J. Electron. Mater.* **18**, 711 (1989).
- <sup>66</sup>J. Ma, H. Kawarada, T. Yonehara, J.-I. Suzuki, J. Wei, Y. Yokota, and A. Hiraki, *Appl. Phys. Lett.* **55**, 1071 (1989).
- <sup>67</sup>J. G. Lee, P. D. Miller, and I. B. Cutler, in *Proceedings of the Eighth International Symposium on the Reactivity of Solids*, edited by J. Wood, O. Lindqvist, C. Helgesson, and N.-G. Vannerberg (Plenum, New York, 1977), p. 707.
- <sup>68</sup>D. J. Pickrell, W. Zhu, A. R. Badzian, R. E. Newnham, and R. Messier, *J. Mater. Res.* **6**, 1264 (1991).

## V. Textured diamond growth on (100) $\beta$ -SiC via microwave plasma chemical vapor deposition

B. R. Stoner and J. T. Glass

Department of Materials Science and Engineering, North Carolina State University, Raleigh, North Carolina 27695-7907

(Received 21 October 1991; accepted for publication 22 November 1991)

Textured diamond films have been deposited on  $\beta$ -SiC via microwave plasma chemical vapor deposition preceded by an *in situ* bias pretreatment that enhances nucleation.

Approximately 50% of the initial diamond nuclei appear to be aligned with the C(001) planes parallel to the SiC(001), and C[110] directions parallel to the SiC[110] within 3°. The diamond was characterized by Raman spectroscopy and scanning electron microscopy.

The promise that diamond thin films show for electronic applications has been made clear.<sup>1</sup> However, its promising electronic properties are based on the bulk properties of diamond, and for it to be fully utilized as a semiconductor material from which to fabricate electronic devices, it is necessary to produce single-crystal thin films over large areas.<sup>2,3</sup> Homoepitaxial growth of diamond has been reported, however, substrates of sufficient size to make the process economical are not available. The growth of heteroepitaxial, or textured diamond films therefore is an important goal if the economical fabrication of diamond devices is to become a reality.

Heteroepitaxial or textured growth of diamond has been reported on cubic-boron nitride,<sup>4,5</sup> Ni,<sup>6</sup> and Si.<sup>7-9</sup> Cubic-BN shows the most promise as a heteroepitaxial substrate due to its close lattice match and high-surface energy. However, it is presently extremely difficult to grow c-BN in large single-crystal form.<sup>3</sup> The recent results reported<sup>6</sup> of the local epitaxial growth of diamond on Ni are thus very important. Nickel has a close lattice match with diamond although its catalytic properties on the decomposition of hydrocarbons into  $sp^2$ -bonded structures may make it difficult to inhibit the formation of graphite during diamond nucleation and growth.<sup>10,11</sup> Jeng *et al.*<sup>7</sup> reported limited texturing of diamond on silicon substrates that were presumably pretreated in such a manner as to produce a semicrystalline silicon carbide surface conversion layer. However, a complete film was not formed and quantification of the amount of texture was not discussed. Other reported local epitaxy of diamond on silicon<sup>8,9</sup> was most likely a limited epitaxial growth on silicon carbide as well. The lattice mismatch between  $\beta$ -SiC ( $a = 4.36 \text{ \AA}$ ) and diamond ( $a = 3.57 \text{ \AA}$ ) is rather large ( $\sim 20\%$ ), however,  $\beta$ -SiC grows epitaxially on Si<sup>12,13</sup> despite a 24% lattice mismatch, thereby indicating that such a mismatch does not prohibit heteroepitaxy.

In this letter, the authors report the observation of textured diamond growth on (001)  $\beta$ -SiC substrates. The present results were obtained by a bias pretreatment followed by standard microwave plasma chemical vapor deposition (CVD). The biasing pretreatment has been reported elsewhere<sup>14,15</sup> and has been shown to enhance nucleation by several orders of magnitude depending on the biasing time.

Samples were grown in an ASTeX stainless-steel mi-

crowave plasma CVD reactor which has been reported elsewhere.<sup>15</sup> The plasma forms at a stable position in the center of the reactor and the substrate position relative to the plasma may be varied between 0 (immersed) and 8 cm. The heater consists of a tantalum filament encased in a boron-nitride insert that fits inside of a differentially pumped, isolated 0.04-in.-thick tantalum can. The substrate holder fits onto the tantalum can, which is in turn connected to an electrical feedthrough. With this arrangement, the substrate may be biased or isolated from ground.

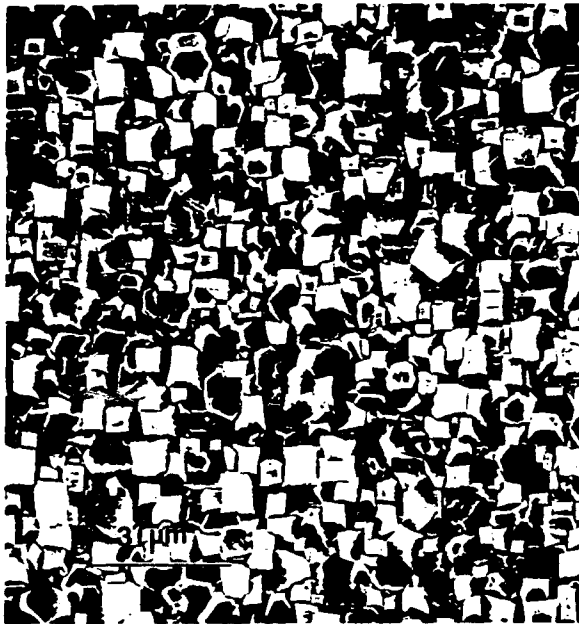
Diamond was deposited on 1-in.-diam (001)  $\beta$ -SiC films that were grown epitaxially in a separate reactor on (001) Si substrates using conventional CVD techniques.<sup>12,13</sup> The  $\beta$ -SiC films (4–5  $\mu\text{m}$  thick) were prepared by polishing the as-grown surface with 0.1  $\mu\text{m}$  diamond paste to minimize the surface roughness. The sample was then oxidized in  $\text{O}_2$  at 1200 °C to a thickness of approximately 0.1  $\mu\text{m}$  in order to remove the majority of the surface damage that occurred during the polishing. This is also expected to eliminate all carbon/hydrocarbon contamination which may have occurred during polishing. Just prior to insertion into the growth chamber, the oxide was stripped using a 10:1 mixture of HF:DI- $\text{H}_2\text{O}$  followed by a DI rinse and drying with nitrogen.

The pretreatment consisted of biasing the substrate for 30 min at  $-250 \text{ V}$  while it was immersed in a 2% methane-in-hydrogen plasma. The pressure was 15 Torr, microwave power 600 W, and total flow rate was 1000 sccm. The substrate temperature was approximately 650 °C and the resulting current was 100–150 mA, collected through the substrate holder with a top surface diameter of 1.5 in. After the 30 min pretreatment, the voltage was turned off, and the substrate was moved to a position approximately 1 cm from the edge of the glow discharge region of the plasma. The methane concentration was reduced to 0.5%, the pressure increased to 25 Torr, and the temperature was maintained at 650–700 °C. These growth conditions are those which in the past have resulted in high-quality diamond films with little secondary nucleation and modest growth rates of approximately 0.05  $\mu\text{m}/\text{h}$ . Diamond was grown on the (001)  $\beta$ -SiC wafer under the above condition for 50 h and then subsequently analyzed via scanning electron microscopy (SEM) and Raman spectroscopy.

Figures 1(a) and 1(b) show SEM micrographs taken near the center and edge of the wafer, respectively. Arrows



(a)



(b)

FIG. 1. SEM micrographs of the textured film near the (a) center and (b) edge of the sample.

pointing in the SiC [110] direction show that over 50% of the diamond particles on the surface are textured with (001) faces parallel to the SiC (001) and with the diamond [110] parallel within  $3^\circ$  to the [110] of SiC. Figure 2 shows a schematic representation of an oriented diamond particle on the SiC wafer. Higher growth in the [110] than in the  $[1\bar{1}0]$  has made the top (001) face rectangular rather than square. In a cubic system one should normally expect uniform growth in all the [110] directions. However, preferential growth in a particular [110] direction may occur along steps which are known to occur along the SiC[110]

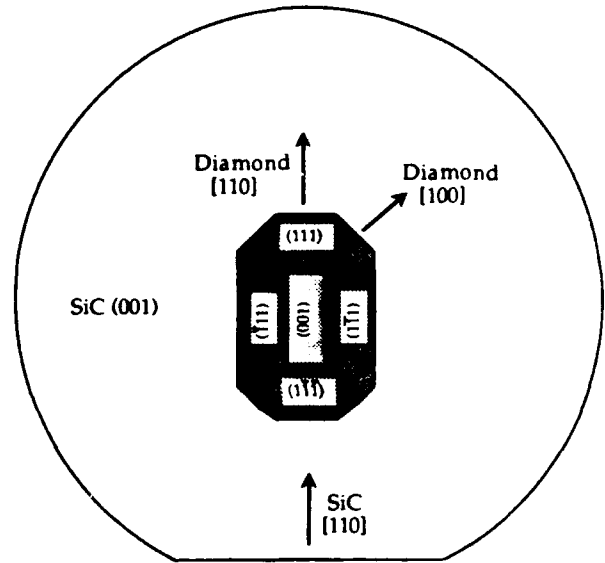


FIG. 2. Schematic representation of the diamond particle orientation relative to the SiC substrate.

on the (001) surface.<sup>1,12</sup> Figure 3 shows an SEM taken at  $45^\circ$ , indicating that the (111) are the most stable, slowest growing planes and are therefore the largest.

Micro-Raman spectroscopy [Figs. 4(a) and 4(b)] was performed on the sample in the regions represented by SEM Figs. 1(a) and 1(b). The sharp  $1332\text{ cm}^{-1}$  diamond peak<sup>16</sup> and the absence of the broad peak at  $1500\text{ cm}^{-1}$  indicate that the diamond is of high quality with an undetectable graphitic component. SiC peaks<sup>17</sup> at  $796$  and  $973\text{ cm}^{-1}$  were also observed from the substrate.

The present authors believed that the biasing pretreatment on SiC has played an important role in enhancing the nucleation of diamond without significantly damaging the surface sc as



FIG. 3. SEM of the center region taken at a  $45^\circ$  tilt to show (111) faceting.

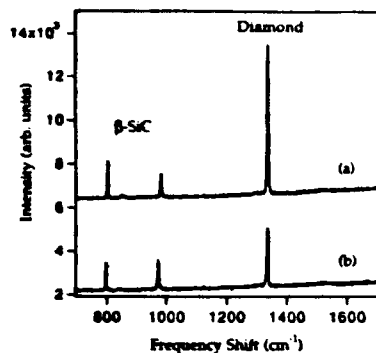


FIG. 4. Micro-Raman spectra taken from the (a) center and (b) edge regions of the sample.

to destroy its crystallinity. In a recent study of the bias-enhanced nucleation process via *in vacuo* surface analysis and transmission electron microscopy (TEM),<sup>14</sup> the authors observed that diamond nucleation on silicon was preceded by the formation of an interfacial carbide layer covered with a very thin (5–10 Å) nondiamond carbon film. It was also found that the biasing process removed oxide and suppressed oxide formation on the surface. Since an amorphous oxide will have obvious deleterious effects on heteroepitaxial nucleation, this oxide removal is believed to be an important factor in the promotion of the present heteroepitaxial nucleation and growth. Attempts to fully remove the oxide from both SiC and Si wafers without biasing proved unsuccessful, thus suggesting that earlier failures to achieve heteroepitaxial nucleation of diamond on SiC<sup>18,19</sup> may have been in part due to the inability to remove the surface oxide. In the present study, the reduction in pretreatment time (from 1.5 h in previous studies<sup>14,15</sup> to 0.5 h here) was believed to have minimized the surface damage while still creating sufficient nucleation via the impingement of carbon ions from the plasma. In conjunction with the oxide suppression, this has allowed the heteroepitaxial nucleation and growth of diamond on SiC in the present study.

It has been shown here that textured and epitaxial diamond particles can be grown on (001)  $\beta$ -SiC. Based on SEM observations, approximately 50% of the diamond nuclei are textured with the (001) parallel to the SiC sub-

strate and [110] directions aligned within 3°. The nucleation was enhanced by first biasing the substrate in a 2% methane/hydrogen plasma for 30 min. This biasing pretreatment is believed to enhance the nucleation without damaging the substrate, thus allowing limited heteroepitaxial growth.

The authors wish to thank X. H. Wang and R. J. Nemanich for performing the Raman spectroscopy, and M. Paisley, Y. C. Wang, and R. F. Davis for providing the SiC substrates and valuable technical assistance. Valuable discussions with G. H. Ma of NCSU, and D. L. Dreifus and W. Hooke of Kobe Steel, EMC, are also greatly appreciated. This research was financially supported in part by SDIO/IST through ONR and the Kobe Steel, Ltd. Professorship at NCSU.

- <sup>1</sup>R. F. Davis and J. T. Glass, in *Advances in Solid-State Chemistry* (JAI, London, 1991), Vol. 2, p. 1.
- <sup>2</sup>W. A. Yarbrough and R. Messier, *Science* **39**, 1 (1989).
- <sup>3</sup>W. A. Yarbrough, *J. Vac. Sci. Technol. A* **9**, 1145 (1991).
- <sup>4</sup>M. Yoshikawa, H. Ishida, A. Ishitani, T. Murakami, S. Koizumi, and T. Inuzuka, *Appl. Phys. Lett.* **57**, 428 (1990).
- <sup>5</sup>S. Koizumi, T. Murakami, T. Inuzuka, and K. Suzuki, *Appl. Phys. Lett.* **57**, 563 (1990).
- <sup>6</sup>Y. Sato, I. Yashima, H. Fujita, T. Ando, and M. Kamo, *Second International Conference on New Diamond Science and Technology*, Washington, D.C., Sept. 23–27, 1990, edited by R. Messier, J. T. Glass, J. E. Butler, and R. Roy (Materials Research Society, Pittsburgh, 1991), p. 371.
- <sup>7</sup>D. G. Jeng, H. S. Tuan, R. F. Salat, and G. J. Fricano, *Appl. Phys. Lett.* **56**, 1968 (1990).
- <sup>8</sup>J. Narayan, A. R. Srivatsa, M. Peters, S. Yokota, and K. V. Ravi, *Appl. Phys. Lett.* **53**, 1823 (1988).
- <sup>9</sup>B. E. Williams and J. T. Glass, *J. Mater. Res.* **4**, 373 (1989).
- <sup>10</sup>T. P. Hilditch, *Catalytic Processes in Applied Chemistry* (Chapman & Hall, London, 1929).
- <sup>11</sup>D. N. Belton and S. J. Schmieg, *J. Appl. Phys.* **66**, 4223 (1989).
- <sup>12</sup>C. H. Carter, R. F. Davis, and S. R. Nutt, *J. Mater. Res.* **1**, 811 (1986).
- <sup>13</sup>H. S. Kong, Y. C. Wang, J. T. Glass, and R. F. Davis, *J. Mater. Res.* **3**, 521 (1988).
- <sup>14</sup>B. R. Stoner, G.-H. M. Ma, S. D. Wolter, and J. T. Glass, *Phys. Rev. B* (to be published).
- <sup>15</sup>B. R. Stoner, B. E. Williams, S. D. Wolter, K. Nishimura, and J. T. Glass, *J. Mater. Res.* (to be published).
- <sup>16</sup>R. E. Shroder, R. J. Nemanich, and J. T. Glass, *Phys. Rev. B* **41**, 3738 (1990).
- <sup>17</sup>D. Olego, M. Cardona, and P. Vogl, *Phys. Rev. B* **25**, 3878 (1982).
- <sup>18</sup>T. Hartnett, R. Miller, D. Montanari, C. Willingham, and R. Tustison, *J. Vac. Sci. Technol. A* **8**, 2129 (1990).
- <sup>19</sup>J. T. Glass, P. Richard, Y. H. Lee, H. S. Kong, and K. J. Bachmann, SDIO/IST-ONR Diamond Technology Initiative Symp., Crystal City, VA, Paper T23 (1988).

## VI. Analysis of the Diamond/SiC Interface via Cross Sectional Transmission Electron Microscopy

### A. Introduction

It has been shown in a previous publication that textured diamond may be nucleated on beta-SiC [1]. This locally epitaxial relationship between the diamond and SiC was confirmed by high resolution cross-sectional TEM. Figure 1 shows an XTEM micrograph of the diamond on SiC interface. In this  $\langle 110 \rangle$  projection, the diamond  $(\bar{1}\bar{1}1)$  planes are shown to be continuous across the interface. A  $4\text{--}6^\circ$  tilting of the diamond  $(\bar{1}\bar{1}1)$  planes towards the  $\langle \bar{1}10 \rangle$  direction is also evident. The large fringes near the interface are Moiré fringes, indicating that there is overlap between the diamond and SiC in this region. Since the Moiré fringes are very sensitive to the misorientation between two overlapping lattices, they provide an excellent measure of the tilt boundary at the interface.

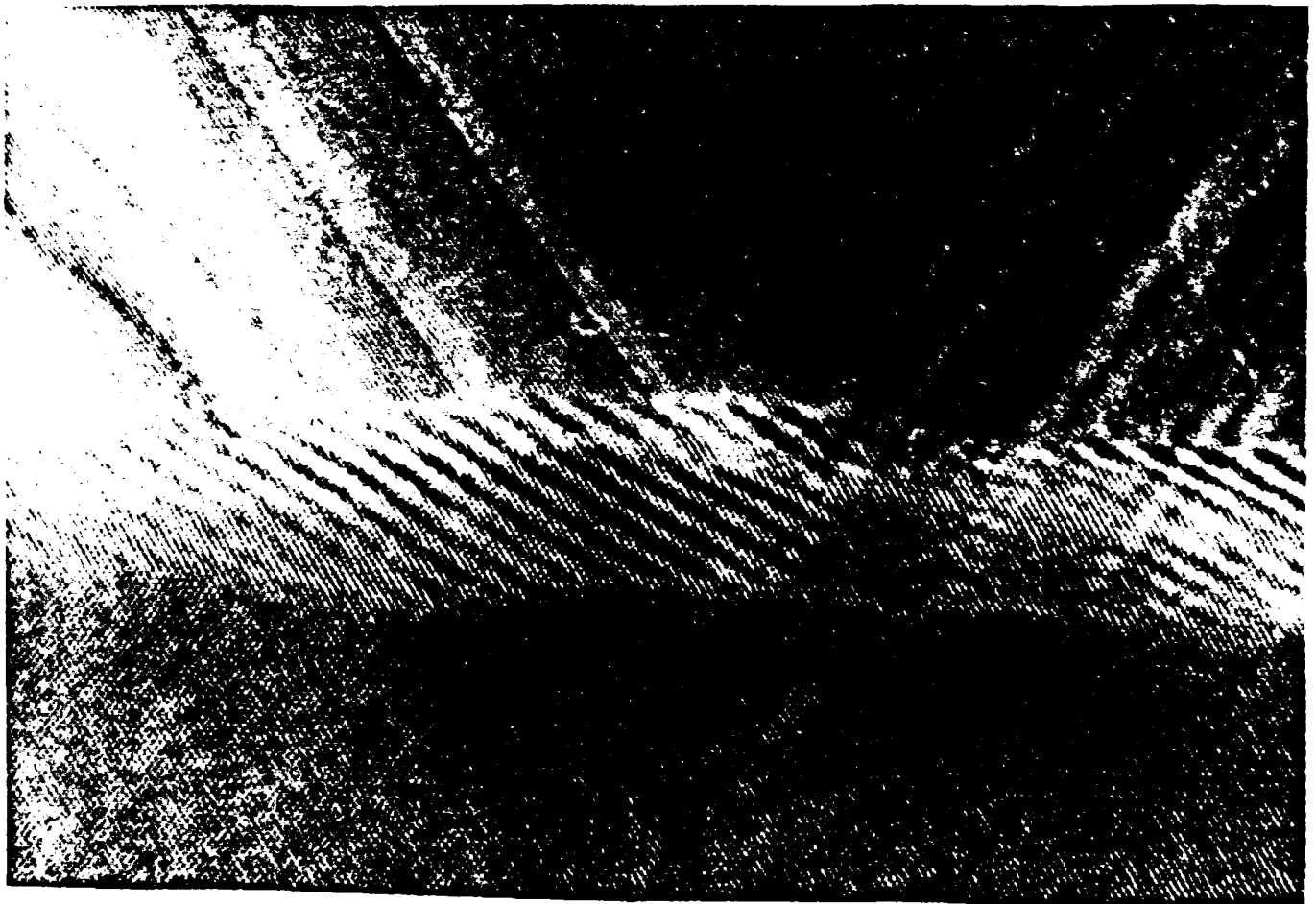


Figure 1. High resolution transmission electron micrograph of the diamond/SiC interface. The largely spaced lines at the interface are Moiré fringes, representing a slight overlap between diamond and SiC.

It is also important to note that there does not appear to be an interfacial layer between the diamond and SiC. In a previous study of bias-enhanced diamond nucleation on silicon [2], an amorphous interfacial layer was observed. In that particular study the bias-pretreatment was performed for 1 hr; in the present study, the duration was 30 min. By reducing the pretreatment time to 30 min, it is believed that nucleation was enhanced significantly, over that for an untreated surface, but, without damaging this surface or depositing on it an amorphous layer.

## B. Results

It was mentioned above that a tilt boundary developed between the diamond and SiC substrate. A misorientation of this nature is not desirable, since it results in low-angle grain boundaries between the various diamond grains once they grow into a complete film. A high density of low angle grain boundaries will degrade the electrical properties of the resulting diamond film, thus the mechanism for the formation of this tilt boundary is of great interest. The possible mechanisms considered are; (i) tilting of the diamond lattice to expose a high index plane, thus reducing the lattice mismatch and the resulting interfacial strain energy, and (ii) a tilt boundary resulting from a high density of inefficient misfit dislocations at the interface.

The first mechanism is shown schematically in Figure 2. The amount of misfit between two dissimilar lattices may be reduced by tilting the smaller lattice to expose a higher index plane to the interface. As illustrated in this figure, the SiC and diamond have lattice parameters of  $a_0$  and  $a_1$  respectively. By tilting through an angle,  $\alpha$ , the smaller lattice may be made to match that of the larger one in this simple two-dimensional model. When all of the mismatch is accounted for by this rotation, resulting in no interfacial strain, the tilt angle may be calculated from simple geometry as follows;

$$\cos(\alpha) = a_1/a_0 \quad (1)$$

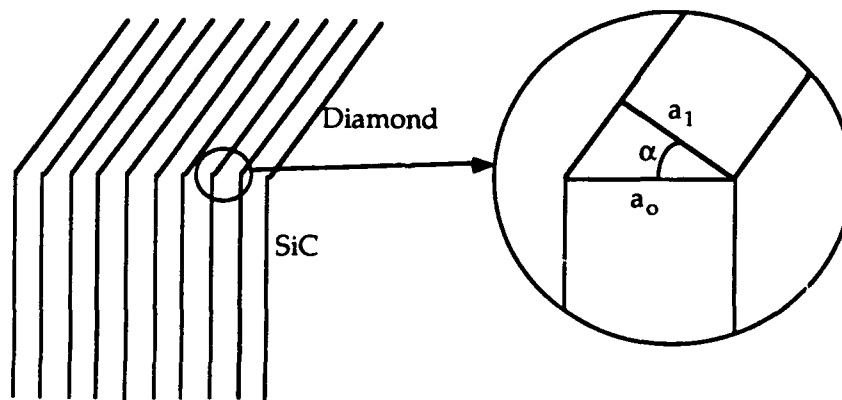


Figure 2. Schematic representation of a tilt boundary, exposing a high index diamond plane on (100) SiC.

For diamond on  $\beta$ -SiC, the one-dimensional rotation angle ( $\alpha$ ) resulting in a minimum strain energy would be;

$$\alpha = \cos^{-1}(3.57/4.36) = 35^\circ.$$

The rotation observed in the TEM micrographs was approximately  $5^\circ$ , which will only offset a lattice mismatch of 0.4%. For diamond on SiC the lattice mismatch is roughly 20%, which implies that a  $5^\circ$  rotation will only reduce the total interfacial elastic strain energy by approximately 2%. It is therefore unlikely that the observed misorientation is a result of this type of interfacial lattice rotation mechanism.

The second possibility is that the tilt may be caused by the high number of misfit dislocations at the interface. It has been shown in previous work that the misfit dislocations in diamond and zincblende lattices consist mostly of the  $60^\circ$  mixed type [3, 4, 5]. These  $60^\circ$ -type dislocations may be resolved into both a tilt ( $b_1$ ) and misfit ( $b_2$ ) component, as discussed by Olsen and Ettenberg [6], and shown schematically in Figure 3. Figure 4 shows also how a tilt boundary may result from an array of dislocations running parallel to the interface. A partial component of the  $60^\circ$  dislocation will be parallel to the interface and thus result in a low angle grain boundary. The magnitude of the tilt resulting from an array of pure horizontal dislocations may be calculated from the relationship [7];

$$\sin(\alpha) = |b|/D. \quad (2)$$

Where  $b$  is the Burgers vector and  $D$  is the dislocation spacing.

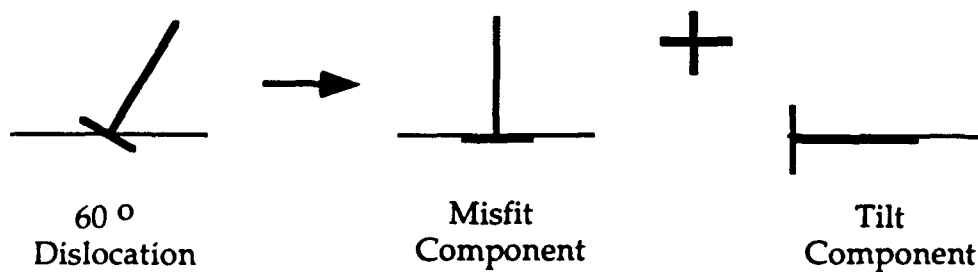


Figure 3. Schematic representation of how a  $60^\circ$  mixed-type dislocation may be resolved into both a misfit and a tilt component.

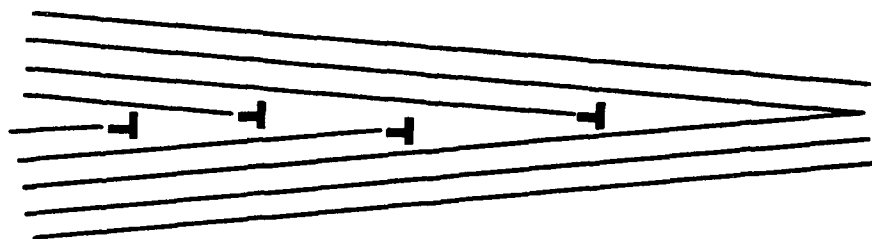


Figure 4. Schematic representation of a low-angle grain boundary, caused by an array of edge-type dislocations with Burgers vectors running normal to the interface.

On a (001) oriented substrate, a mixed interfacial dislocation along an  $\langle 011 \rangle$  direction will have a Burgers vector,  $b = \langle 101 \rangle$ , inclined  $45^\circ$  to the interface [6]. The tilt component ( $b_1$ ) of this Burgers vector will be in the  $\langle 001 \rangle$  direction, with  $b_1 = 0.707b$ . If one then measures the dislocation spacing from the high resolution XTEM in Figure 1, the misorientation( $\alpha$ ) may be calculated from equation (2) as;

$$\sin(\alpha) = 0.707 |b|/D.$$

However, the quantity  $|b|/D$  is simply the dislocation density ( $\rho$ ). From Figure 1, there is on average 1 misfit dislocation every 7 lattice planes, which translates to a dislocation density of 0.14. With this dislocation density the misorientation angle ( $\alpha$ ) is calculated to be;

$$\alpha = \sin^{-1}(0.707\rho) = 5.8^\circ, \quad (3)$$

which is in very good agreement with the measured misorientation of  $5^\circ$ . This suggests that the high density of  $60^\circ$  misfit dislocations is largely responsible for the observed rotation of the diamond grains.

### C. Discussion

It is of interest to point out that the measured misfit dislocation density is slightly lower than that expected for a 20% lattice mismatch. If all of the interfacial strain energy was absorbed via perfect edge-type misfit dislocations, then one would expect on average, 1 dislocation for every 5 lattice planes. For the  $60^\circ$ -type dislocations the misfit component ( $b_2$ ) will be along the interface in the  $\langle 1\bar{1}0 \rangle$  direction with  $|b_2| = |b|/2$ . Therefore the mixed dislocations are only half as efficient in relieving the misfit strain as the perfect edge-type, and thus the predicted dislocation density increases to  $\rho = 0.4$ , or an average of 1 every 2.5 lattice planes. This implies that the diamond nuclei observed in this study are still highly strained near the interface. If the interfacial strain were minimized by a dislocation density of 0.4, the predicted rotation, calculated via equation (3) would be approximately  $16^\circ$  instead of the observed  $5^\circ$ .

A random rotation of this magnitude between the various diamond grains no longer constitutes a low angle grain boundary and should effectively result in a polycrystalline diamond film. It appears to be fortunate therefore that the interfacial strain is not minimized via the incorporation of misfit dislocations that would hence result in large distribution of crystal-misorientations. Of interest is a recent proposal by Zhu *et. al* [8], for the epitaxial growth of diamond(114) on SiC(221). This epitaxial configuration should theoretically result in an elastic interfacial strain energy that is half that of the D(100) on SiC(100) system which has been reported here. Based on the logic presented above, if the misfit strain energy were to be minimized via the incorporation of misfit dislocations for this system, the maximum misorientation would be only approximately  $8^\circ$  versus  $16^\circ$  for the diamond(100) on SiC(100) case. If the interface were to remain partially strained, as in the that observed via XTEM, then it

is plausible that epitaxial films with low-angle grain boundaries misoriented by less than  $5^\circ$  could be achieved.

#### D. Summary

Initial bias-enhanced heteroepitaxial nucleation on single crystal SiC has proven to be successful. Transmission electron microscopy (TEM) showed that approximately half of the diamond nuclei were in epitaxial alignment with the SiC substrate. Further TEM both confirmed this epitaxy and also clearly indicated that the nuclei were tilted by several degrees. This tilting was determined to be a result of the high density of inefficient misfit dislocations at the interface. It was found that the tilt component of the misfit dislocations could account for the misorientation in the crystals. It was also suggested that by attempting to grow diamond(114) on SiC(221) the interfacial strain energy and resulting misorientation could be significantly reduced.

#### E. References

1. B. R. Stoner and J. T. Glass, *Appl. Phys. Lett.* **60**, 698 (1992).
2. B. R. Stoner, G.-H. M. Ma, S. D. Wolter, and J. T. Glass, *Phys. Rev. B* in press (1992).
3. P. M. J. Maree, J. C. Barbour, J. F.v.d. Veen, K. L. Kavanagh, C. W. T. Bulle-Lieuwma, and M. P. A. Vieggers, *J. Appl. Phys.* **62**, 4413 (1987).
4. R. J. Matyi, J. W. Lee, and H. F. Schaake, *J. Electronic Mater.* **17**, 87 (1988).
5. R. J. Matyi, H. F. Schaake, D. G. Deppe, and J. N. Holonyak, **1**, 195 (The Electrochemical Society, Chicago, Il, 1988).
6. G. H. Olsen, and M. Ettenberg, in *Crystal Growth: Theory and Techniques*, C. H. L. Goodman, ed. (Plenum Press, New York, 1978).
7. D. A. Porter, and K. E. Easterling, *Phase Transformations in Metals and Alloys* (Van Nostrand Reinhold Co. Ltd., Berkshire, 1988).
8. W. Zhu, X. H. Wang, B. R. Stoner, H. S. Kong, M. Braun, G.-H. M. Ma, and J. T. Glass, to be submitted to *Phys. Rev. B.* (1992).

## VII. *In-Situ* Growth Rate Measurement and Nucleation Enhancement for Microwave Plasma CVD of Diamond

Laser reflection interferometry (LRI) has been shown to be a useful *in-situ* technique for measuring growth rate of diamond during microwave plasma chemical vapor deposition (MPCVD). Current alternatives to LRI usually involve *ex-situ* analysis such as cross-sectional SEM or profilometry. The ability to measure the growth rate in 'real-time' has allowed the variation of processing parameters during a single deposition and thus the extraction of much more information in a fraction of the time. *In-situ* monitoring of growth processes also makes it possible to perform closed loop process control with better reproducibility and quality control. Unfortunately LRI requires a relatively smooth surface to avoid surface scattering and the commensurate drop in reflected intensity. This problem was remedied by greatly enhancing the diamond particle nucleation via the deposition of an intermediate carbon layer using substrate biasing. When an unscratched silicon wafer is pretreated by biasing negatively relative to ground while in a methane-hydrogen plasma nucleation densities much higher than those achieved on scratched silicon wafers are obtained. The enhanced nucleation allows a complete film composed of small grains to form in a relatively short time, resulting in a much smoother surface than is obtained from a film grown at lower nucleation densities.

It is commonly agreed upon that the unique combination of properties which diamond films possess will lead to both the improvement of existing technologies as well as the establishment of new technologies which can not yet be envisioned.<sup>1-4</sup> In this sense, diamond is an "enabling" technology. Thus, any improvements in the current status of film processing are potentially quite valuable. In the present research such progress has been achieved by employing Laser Reflection Interferometry (LRI), which has been used previously to monitor the processing of thin films other than diamond.<sup>5-7</sup> The purpose of this letter is to show how this technique may aid the study of diamond growth, making it simpler and more efficient to perform parametric studies of growth rate responses, and eventually be used as an *in-situ* process control tool. The primary advantage of LRI, is that it makes possible the continuous monitoring of growth rates while a deposition is in progress. Thus changes in these rates during a single deposition (either due to purposeful changes in growth parameters or accidental changes due to unforeseen problems) can be determined. It also allows one to account

---

Submitted to Applied Physics Letters on April 20, 1991: B. R. Stoner, B. E. Williams, S. D. Wolter, J. T. Glass, Department of Materials Science and Engineering, North Carolina State University, Raleigh, NC 27695-7919 and K. Nishimura, Visiting from the Electronics Research Laboratory, Kobe Steel, Ltd., Kobe, Japan

for the initial "incubation" period during diamond deposition prior to the actual onset of growth.

Laser interferometry works by the simple superposition of two light waves. There is a reflection of the waves from both the top surface of the growing diamond film as well as the interface between the film and the substrate. The light waves add, and as the film continues to grow there is a cycling of the intensity due to periods of both constructive and destructive interference. Typical data of the reflected intensity as a function of time are shown in Figure 5. For monochromatic light the growth rate (GR) may be calculated as;

$$GR = (\lambda/2\eta)/T,$$

where  $\lambda$  = wavelength of the laser light

$\eta$  = index of refraction of the film

and  $T$  = period between interference cycles.

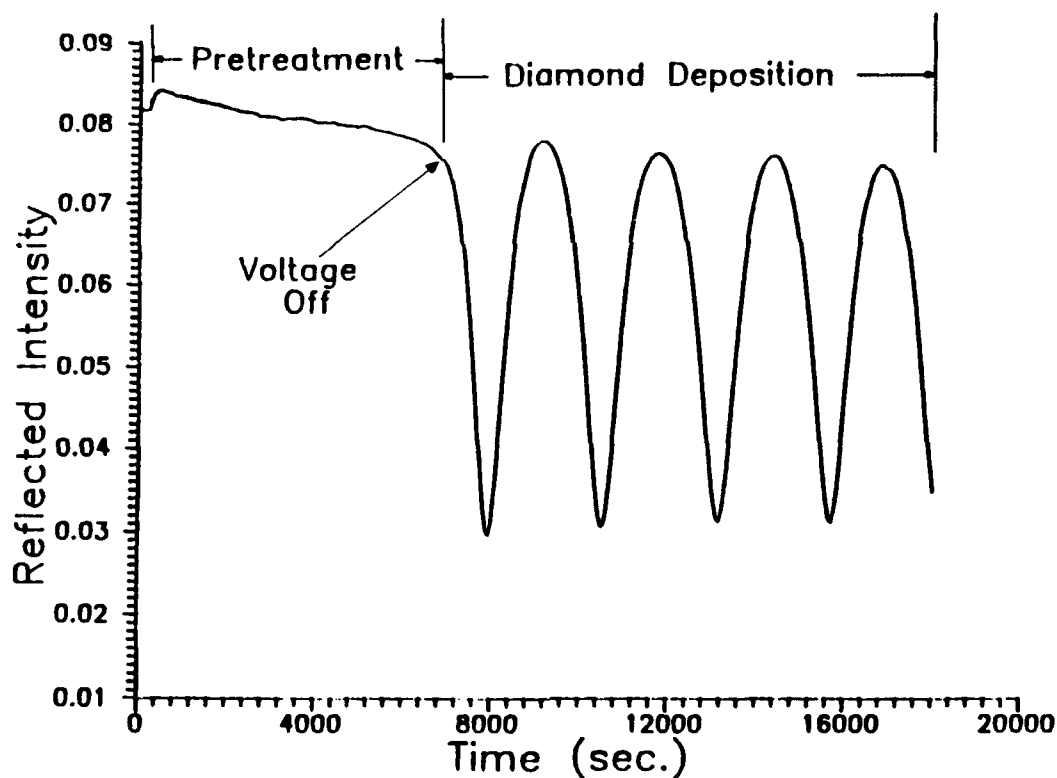


Figure 5. Typical data showing the interference cycles in the reflected intensity during diamond film growth, and the incubation period at the beginning of the deposition run.

Since the index of refraction may vary with the quality of diamond<sup>8</sup>, it is necessary to adjust the value of  $\eta$  utilizing a series of calibration experiments. This may be done by performing depositions to cover the desired extremes in relative quality (as

determined by some independent technique such as Raman Spectroscopy). Next the thicknesses of the films are independently measured and compared to those calculated from LRI. One then solves for  $\eta$  in the above equation to determine the index of refraction at those extremes.

The diamond films for this study were grown in an ASTeX, cylindrically coupled, stainless steel microwave chamber. Figure 6 shows how LRI was used to monitor the

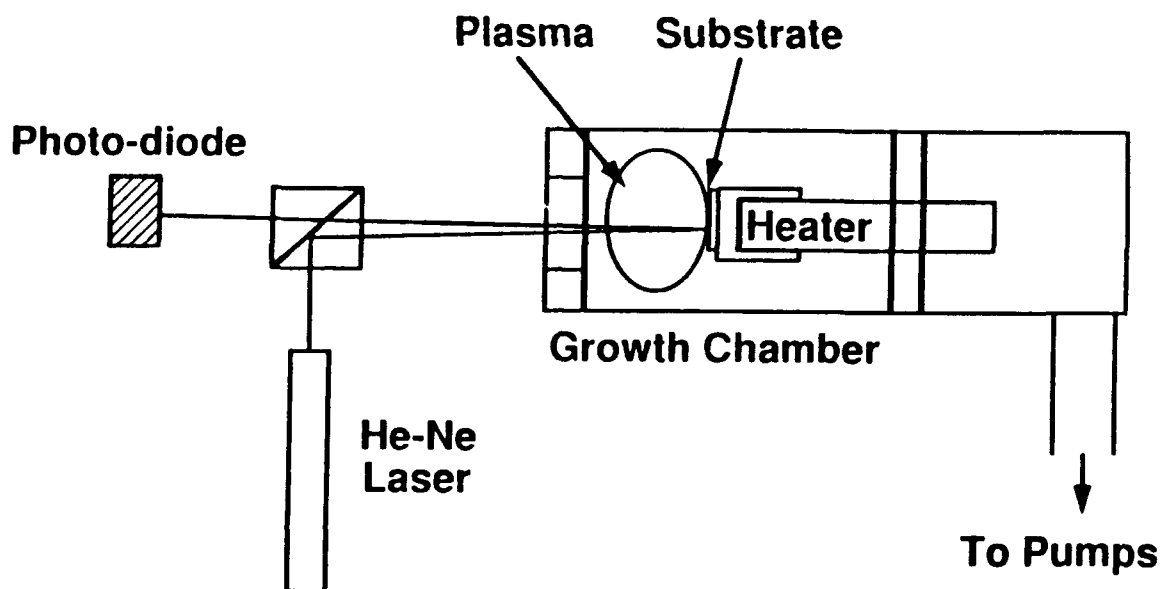


Figure 6. Diagram of the microwave plasma CVD system and the LRI apparatus.

growth rate in this system. The laser was reflected nearly perpendicular to the substrate and the reflected intensity, monitored via a silicon photo-diode, was recorded by a computer. A helium-neon laser was used ( $\lambda = 630 \text{ nm}$ ) in this study, which corresponds to  $0.13 \text{ }\mu\text{m}$  of film growth per intensity cycle (see Figure 5) in the case of a high quality diamond film with  $\eta = 2.4$ . Several initial calibration runs were performed with methane concentrations ranging from 0.5% to 5%. Even in the case of the poorest quality film, the actual thicknesses varied less than 10% for films  $1\text{-}4 \text{ }\mu\text{m}$  thick, from that measured by LRI assuming this index of refraction.

It was mentioned earlier that LRI has been previously used to measure the growth rate during thin-film epitaxial growth. The strict theory for this technique is based on a layer-by-layer increase in film thickness, and is understandably not ideally suited for measuring discrete island or polycrystalline film growth due to scattering of the laser light. This is the reason that initial attempts by the authors to measure the MPCVD growth rate of diamond on silicon using LRI had failed. Due to the relatively low nucleation density the surface was simply not smooth enough, even when optimum

diamond "scratching" was employed as a pretreatment. This lead to the biasing enhancement of nucleation density discussed below. This biasing increases the initial density of nuclei allowing a complete film to be formed more quickly, resulting in more uniform thickness than in the case where there are few initial nucleation sites. In the limiting case, where there is nucleation at every surface lattice site, the result would be the ideal layer-by-layer film growth mentioned above. This biasing allows LRI to be utilized for depositions lasting as long as 70 hours and film thicknesses greater than 7 $\mu$ m.

Previous techniques for increasing the nucleation density of diamond have been reported.<sup>9-13</sup> These techniques range from the pre-deposition of an amorphous or 'diamond-like' carbon film<sup>9-11</sup> to more efficient methods of surface abrasion.<sup>12,13</sup> Although each of these techniques was successful in enhancing nucleation density, there are several advantages to the biasing pretreatment described herein. It may be performed '*in-situ*' and thus is very convenient due to the elimination of any abrasion step. Furthermore, it is very reproducible, easy to control and the instrumentation is minimal.

The nucleation density of diamond on unscratched silicon was enhanced by biasing the substrate negatively prior to deposition, while it was immersed in the plasma. In so doing, the nucleation densities were several orders of magnitude higher than on unscratched silicon, and approximately an order of magnitude higher than on conventionally scratched silicon wafers. In the present study, bias voltage and current were approximately -250 volts and 100 mA respectively (for a 1% methane in hydrogen mixture at 15 torr), and the optimum biasing period appears to be 1 to 2 hours. The nucleation density may be controlled by either changing the time of pretreatment or varying the bias voltage.

Aside from utilizing LRI as an *in-situ* probe, this technique had several other benefits. First, it became no longer necessary to damage the as-received polished surface of the silicon wafer by abrading it with diamond paste. If heteroepitaxial growth is ever expected to be obtained, this is essential. Second, all the pretreatment may be preformed in a much more controlled, cleaner environment, where it may be directly followed by the the diamond deposition. Thus, it is possible to create a smooth transition from the pretreatment layer to the diamond film by slowly decreasing the bias voltage. A clean and graded interface of this type may help improve the adhesion of diamond films to substrates where there is a significant mismatch in the coefficient of thermal expansion. Finally, under optimum conditions the nucleation density is much higher than any other technique examined by the authors, yielding the smoothest, most uniform as-grown surface.

Almost always during low pressure CVD of diamond there is period of time in the beginning of a deposition where no film growth is observed, as discussed in Figure 5. LRI allows one to directly observe and account for this "incubation" or "nucleation" period. During the incubation period, the reflected intensity is relatively constant, but as soon as a film begins to grow, there is a noticeable decrease in the reflected intensity. This initial drop in intensity is thought to be due to the absorption of light by the surface layer of carbon which is deposited during the bias pretreatment. When this drop in intensity is observed, the pretreatment (or voltage) may be turned off, and standard diamond growth allowed to begin. If the voltage is maintained the carbon layer will continue to grow, followed by a poorer quality diamond than in the case where the bias is removed. This result is similar to that observed by Yugo et al.<sup>14</sup>, where poorer quality diamond growth was observed under negative substrate bias than under positive or no bias. It should be noted that most current methods for measuring growth rate involve dividing the resulting film thickness by the total growth time. If the nucleation period is not accounted for, then considerable error may be introduced in this growth rate determination. LRI makes it possible to measure this nucleation period as well as growth rate, either of which may vary with changes in processing parameters.

The chemical and physical nature of the pretreatment layer created by biasing is not yet fully understood; however initial in-vacuo surface analytical studies using both X-ray photoelectron spectroscopy (XPS) and Auger electron spectroscopy (AES), show it to be a mixture of both carbon and silicon carbide. Micro-Raman spectroscopy suggests that the film is amorphous carbon, as opposed to micro-crystalline graphite, however more work is necessary in this area due to the thinness of the layer. Furthermore, at these thicknesses (20 - 50 nm), the relative cross section for silicon carbide is too small for detection by Raman spectroscopy. No faceted structures could be observed by SEM; although future research will involve the study of diamond growth on this amorphous carbon layer with scanning tunneling microscopy and transmission electron microscopy in hopes of better understanding the diamond nucleation process.

Both SEM and Raman spectroscopy were used to determine the quality of the diamond grown on this pretreatment layer (Figures 7a, 7b and 7c). The diamond films shown here were grown on unscratched silicon wafers at 25 Torr in a 1% methane in hydrogen mixture. The total flow rate was 1000 sccm, the substrate temperature was 800 °C and the microwave power was about 750 watts. The pretreatment consisted of biasing the substrate at -250 V relative to ground for 1.5 hours, in a 1% methane mixture at 1000 sccm total flow and 15 Torr. The ion current was measured to be

between 75 and 125 mA during this process. The pretreatment was performed at lower pressures in order to obtain higher ion currents. There appears to be a relationship between the ion current and the time required to grow an appropriate nucleation layer. Future experiments will involve differentiating between the importance of ion flux to the substrate and the energy at which they arrive.

Laser reflection interferometry has proven to be a useful technique in the study of diamond growth processes. The ability to monitor the nucleation and growth rates in real-time makes it possible to perform systematic kinetic studies more accurately, in a fraction of the time. The problem of surface roughness of polycrystalline films has been overcome by growing diamond on a thin amorphous carbon or diamond-like film created by biasing the substrate negatively while it is in the plasma. By preparing the surface in this manner, it is also conceivable that diamond may be grown on irregularly shaped objects, where uniform substrate preparation by conventional methods may be difficult.

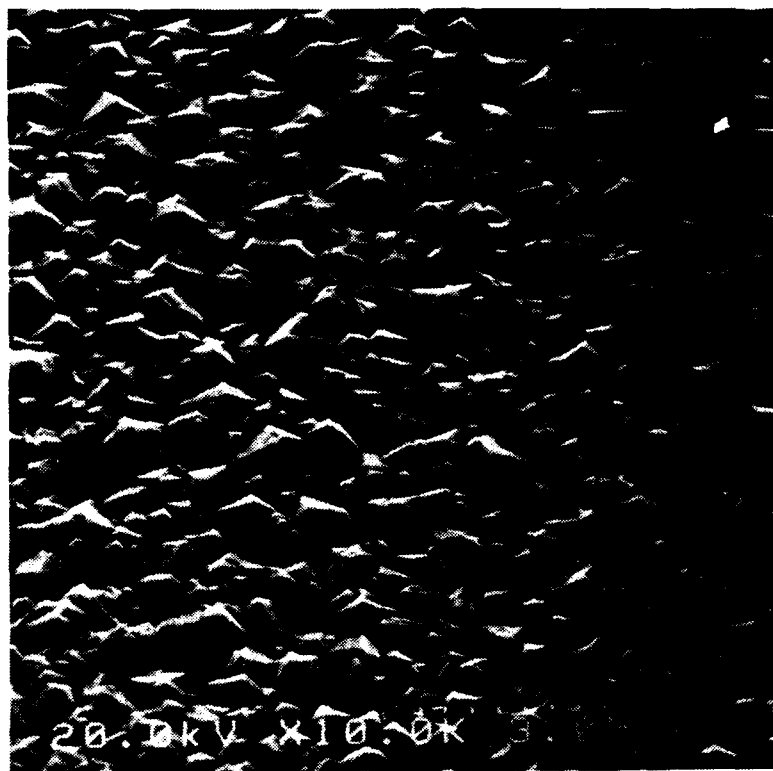


Figure 7a. Surface SEM.

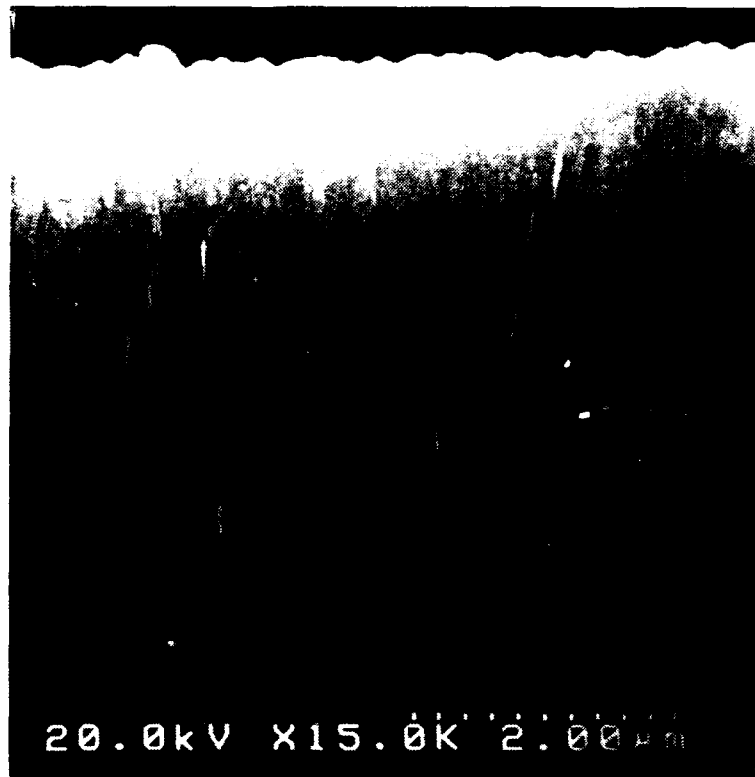


Figure 7b. Cross sectional SEM.

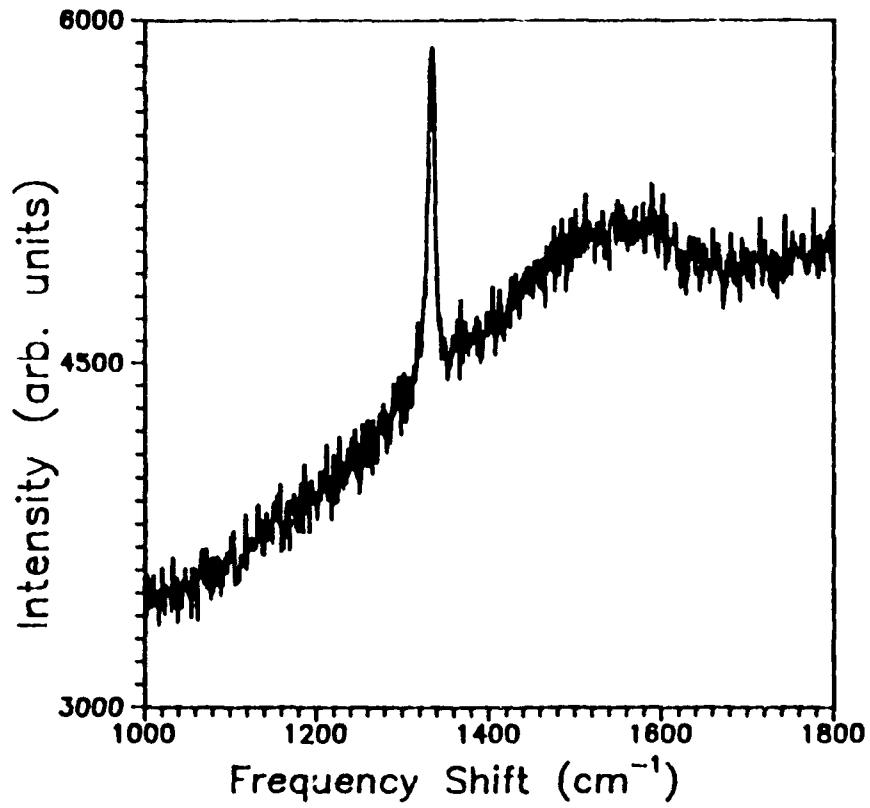


Figure 7(c). Raman spectra of the diamond film grown on the pretreated surface.

The authors wish to acknowledge the partial financial support of SDIO/IST through ONR and Kobe Steel, Ltd. through their Professorship at NCSU. The authors also wish to thank Dr. William Hooke of the University of North Carolina, and Xiao-Hong Wang, of NCSU, for their technical support.

#### References

1. Advance Materials & Processes , 13, (8/89).
2. P. K. Bachman and D.U. Wiechert; Proc. Nato Advanced Study Institute, Castelvechio, Italy, July 23- Aug. 3, (1990).
3. A. H. Deutchman and R. J. Partyka, Advanced Materials & Processing , 29, (6/89).
4. D. S. Hoover, S-Y Lynn and D. Garg, Solid State Technology, 89, Feb. (1991).
5. A.J. SpringThorpe and A. Majeed, J. Vac. Sci. Technol. B 8 (2)., 266, Mar/Apr, (1990).
6. C. Licoppe, Y. I. Nissim, and C. Meriadec, J. Appl. Phys. 58 (8), 15 , 3094, October (1985).
7. G. L. Olson, S.A. Koborowski, J.A. Roth, R.S. Turley, L.D. Hess, SPIE vol. 276, Optical Characterization Techniques for Semiconductor Technology, 128, 1981)
8. N. Savvides, J. Appl. Phys. 58 (1), 1 July (1985).
9. K. V. Ravi, C. A. Koch, H. S. Hu and A. Joshi, J. Mater. Res., Vol. 5, No. 11, 2356, Nov. (1990).
10. T. Hartnett, R. Miller, D. Montanari, C. Willingham, and R. Tustison, J. Vac. Sci. Tech. A 8 (3), May/Jun (1990), 2129.
11. J.J. Dubray, M. Meloncelli, E. Bertran, C.G. Pantano, "Diamond Nucleation on Silicon, SiAlON and Graphite Substrates Coated with an a-C:H layer", To be published.
12. Richard Post, Astex Co., Personal Communication.
13. S. Yugo, T. Kimura and H. Kanai, 1st. Int. Conf. on the New Diamond Sci. Tech., Tokyo, (1988).
14. S. Yugo, T. Kimura and T. Muto, Vacuum, vol. 41, no. 4-6, 1364, (1990).

## VIII. Analysis of the composite structures in diamond thin films by Raman spectroscopy

R. E. Shroder\* and R. J. Nemanich

*Department of Physics and Department of Materials Science and Engineering, North Carolina State University, Raleigh, North Carolina 27695-8202*

J. T. Glass

*Department of Materials Science and Engineering, North Carolina State University, Raleigh, North Carolina 27695-7907*

(Received 15 August 1989)

Diamond and diamondlike thin films produced by various chemical-vapor-deposition processes have been examined using Raman spectroscopy. These films exhibit features in the Raman spectra, suggesting that they are composites of crystalline and amorphous diamond and graphitic structures. The components of this composite structure that contribute to the Raman scattering are discussed in terms of  $sp^2$ - and  $sp^3$ -bonded structures. The use of Raman spectroscopy as a technique for estimating the  $sp^2$ -to- $sp^3$  bonding ratio is considered. Powder composites of BN-diamond and graphite-diamond have been studied as a means of modeling the films, and a simple theoretical model of the Raman scattering from these samples is proposed. From these results it is shown that it is necessary to make assumptions about the domain size of the graphitic  $sp^2$  regions. It is found that the Raman scattering associated with  $sp^2$  bonding in the films is much stronger than that from single-crystalline or microcrystalline graphite structures. Shifts of the vibrational modes are also observed. The optical and vibrational properties of the  $sp^2$  component in the films implies a different atomic microstructure. A model of the  $sp^2$ -bonding configurations in the films is proposed which may account for the observed features in the Raman spectra.

### I. INTRODUCTION

Considerable attention has been focused recently on the growth of carbon films by plasma-enhanced chemical-vapor deposition (CVD) or similar methods.<sup>1-8</sup> The carbon films produced have generally been described as diamond<sup>2,4,9</sup> or diamondlike.<sup>3,10,11</sup> Some of these films have exhibited properties such as hardness, thermal conductivity, and optical band gaps which approach that of natural diamond. The films can be used as heat- and chemical-resistant optical coatings, and wear resistant mechanical coatings. Another application is for novel electronic devices. The mobilities of diamond are larger than those of Si, and the large band gap offers the possibility of high-temperature and/or high-power devices.

The CVD techniques use plasma or hot filaments or other methods to excite mixtures of methane or other hydrocarbon gases diluted in hydrogen. Typical gas ratios are 1% methane with a pressure of 30 torr. Substrate temperatures of 700–900°C are often used. Variation in the process parameters leads to the formation of films with graphitic structures. Graphite is the stable crystalline form of carbon at ambient conditions, while diamond is metastable. The two crystalline forms exhibit different bonding often characterized as  $sp^3$  for diamond and  $sp^2$  for graphite. These two bonding configurations result in significantly different vibrational spectra, and Raman spectroscopy has proved particularly sensitive to the different structures.<sup>12,13</sup>

The question arises as to whether these various structures may coexist in CVD diamond and diamondlike

films (i.e., the films are actually composites of the diamond and graphite structures discussed above). In a recent paper,<sup>12</sup> we explored these possibilities by examining the Raman spectra of diamond and diamondlike thin films. In this paper, we demonstrate the compositional nature of the films using Raman spectroscopy. The features of the different carbon structures are first identified. The features appearing in the Raman spectra of the films are compared to those of different carbon bonding structures, and the results are discussed in light of the composite structures present. We will also describe how the components of the composite can affect the corresponding Raman spectrum.

Several authors<sup>14-16</sup> have proposed methods to determine the  $sp^2$ -to- $sp^3$  bonding ratio in the films. The Raman technique may also be appropriate for making this determination. With this in mind, we have attempted to model the Raman scattering in the films by preparing composites of powders of boron nitride-diamond and graphite-diamond. The Raman results of the composites prepared from powders of BN and diamond and from graphite and diamond are presented, and a simple theoretical model of the Raman scattering is discussed. The Raman spectra from the diamond thin films also indicate that the optical absorption and Raman peak position of the  $sp^2$ -bonded structures is significantly different from that of natural graphite. We consider a model of these structures, similar to models proposed for *a*-C, in which the  $sp^2$  bonding in the local microstructure is terminated in  $sp^3$ -bonded sites. This model may account for the observed features in the Raman spectra.

## II. EXPERIMENT

The Raman-scattered light spectra were taken using the 5145-Å line of an Ar<sup>+</sup> laser. The diamond and diamondlike thin films were mounted in the backscattering configuration, and the scattered light was focused into a Spex model 1403 spectrometer equipped with a third monochromator and holographic gratings. A photomultiplier tube with photon-counting electronics was employed, and the entire system was controlled using an IBM PC/AT computer. The software used is unique in that it allowed for a single scan to be separated into several scanning regions.

In order to model the ratio of  $sp^2$ -to- $sp^3$  bonding in diamond thin films, composites of boron nitride-diamond and graphite-diamond powders were examined. These powders were obtained from commercially available sources.<sup>17,18</sup> Boron nitride was chosen because of its similar crystal structure to graphite, although, unlike graphite, it is optically transparent in the visible region so that effects on the Raman spectra due to absorption could be neglected. The diamond powder was slightly gray in appearance and of  $\sim 1 \mu\text{m}$  crystallite size. The graphite powder was black and very cohesive, and the boron nitride was white and also cohesive. Both materials contained crystallites of 30–40  $\mu\text{m}$  size. Admittedly, this is large for our purposes, but we were primarily interested in the effects on the Raman spectra of the relative concentration of diamond in the composites. The examination of effects due to crystallite size was left for later.

The composites were created as follows; appropriate amounts of boron nitride and diamond powder were weighed, and the relative concentrations determined. We used wt. % (corrected for the atomic mass difference between BN and 2C) to describe the composites. In this way a 50% mixture would have the same number of B—N and C—C "molecules." The powders were then mixed using a mortar and pestle, and the resulting composites lightly pressed into aluminum sample holders. This process was then repeated for the graphite and diamond powders. These samples were also mounted in the backscattering configuration, and the Raman spectra were taken.

## III. RESULTS AND DISCUSSION

### A. Carbon film structures

The two common phases of carbon are graphite and diamond and both of these may be produced in the CVD process. Diamond is characterized by fourfold-coordinated  $sp^3$  bonding of  $O_h$  symmetry.<sup>19</sup> Figure 1(a) shows the first-order Raman mode of natural diamond at  $1332 \text{ cm}^{-1}$ . This mode corresponds to a single triply-degenerate zone-center optical phonon, and is within  $2 \text{ cm}^{-1}$  of the highest-energy mode in the phonon dispersion curves of diamond. The threefold-coordinated  $sp^2$ -bonded structure of graphite may also be formed. The first-order Raman mode of graphite<sup>20</sup> at  $1580 \text{ cm}^{-1}$  is shown in Fig. 1(b). It is important to note that either crystalline or amorphous structures may be formed during deposition. By amorphous, we mean a network in

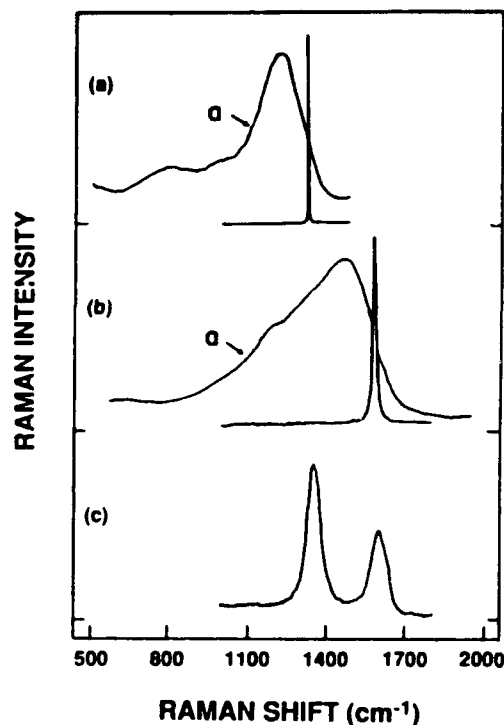


FIG. 1. Raman spectra of (a) diamond, (b) graphite, and (c) microcrystalline graphite. The solid lines in (a) and (b) represent the first-order spectra of crystalline diamond and graphite, respectively. The line in (a) labeled *a* is the spectrum of *a*-Si scaled to the diamond frequency to represent the spectrum of amorphous diamond, while the line in (b) labeled *a* is that due to amorphous graphite (from Ref. 21).

which the local atomic bonding in the structure would be approximately tetrahedral for amorphous diamond, and planar threefold coordinated for amorphous graphitic structures. To our knowledge, the Raman spectra of amorphous diamond has not been reported, but assumptions can be made for its appearance by comparison to the spectrum of *a*-Si. In Fig. 1(a), we have scaled the Raman spectrum of *a*-Si to that of diamond using the ratio of the first-order Raman modes of the crystalline form of these two materials ( $520 \text{ cm}^{-1}/1332 \text{ cm}^{-1}$ ). The Raman spectrum of amorphous graphite has been reported,<sup>21</sup> and the spectrum is overlaid on that of natural graphite in Fig. 1(b). Figure 1(c) shows the Raman spectrum of microcrystalline graphite. In this case the scattering at  $1355 \text{ cm}^{-1}$  is due to disorder-induced scattering from a strong peak in the vibrational density of states.<sup>20</sup> An important point of the comparison of these spectra is that  $sp^3$  bonding yields Raman peaks at  $1332 \text{ cm}^{-1}$  or lower, while  $sp^2$  bonding yields strong scattering with peaks ranging from  $1355$  to  $\sim 1600 \text{ cm}^{-1}$ .

### B. Diamond and diamondlike thin films

The Raman spectra of three carbon films produced under differing deposition conditions are shown in Fig. 2. Spectrum (a) shows features at  $1355$  and  $1580 \text{ cm}^{-1}$  which are similar to those associated with microcrystal-

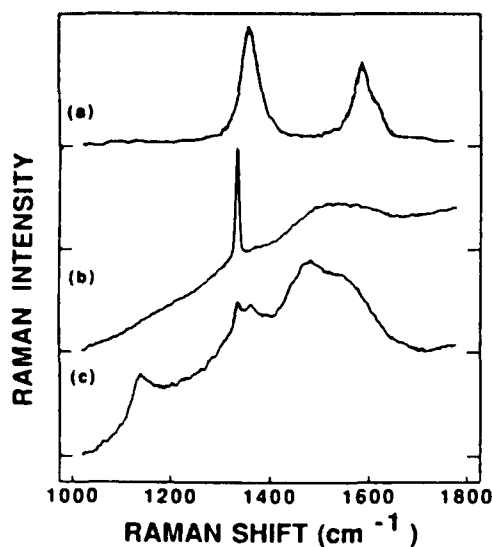


FIG. 2. First-order Raman spectra of diamond thin films. (a) Diamondlike film with features similar to microcrystalline graphite. (b) and (c) The sharp feature at  $1322\text{ cm}^{-1}$  is indicative of crystalline diamond, while features between  $1350$  and  $1600\text{ cm}^{-1}$  are attributed to  $sp^2$ -bonded carbon.

line graphite.<sup>20</sup> This type of film is generally described as "diamondlike" because of its physical properties such as semitransparency and hardness which are similar to diamond.<sup>22</sup> We have reported<sup>12</sup> the appearance of a peak in the second-order Raman spectrum of this material at  $\sim 2940\text{ cm}^{-1}$  which is a combination of the two first-order modes given above. This peak indicates that both first-order modes are generated from the same region of the sample. Therefore, this type of film is predominated by  $sp^2$ -bonded microcrystalline graphitic structures, and is not considered a composite film. Regions of  $sp^3$  bonding may exist in the film, but are not detected in the Raman scattering.

Spectrum (b) is dominated by the diamond peak at  $1332\text{ cm}^{-1}$ , but also contains a broad feature at  $\sim 1500\text{ cm}^{-1}$  which has been ascribed to regions of highly disordered graphite<sup>2</sup> or amorphous carbon.<sup>22</sup> As stated previously, the  $1332\text{-cm}^{-1}$  mode of diamond is essentially the highest-energy vibrational mode of that structure; thus, none of the features in the Raman spectrum with energy higher than  $1332\text{ cm}^{-1}$  can be attributed to diamond structures of long-range order. In comparison, spectrum (c) appears to be a linear combination of the features in (a) and (b). A peak at  $1490\text{ cm}^{-1}$  is now the strongest feature in the spectrum, but the features of diamond and graphite structures are clearly seen. An additional feature is observed at  $1140\text{ cm}^{-1}$  which is not observed in the other spectra. It has been proposed that this feature is due to disordered  $sp^3$ -bonded carbon which forms as a precursor to diamond formation.<sup>12</sup> Note that the peak at  $\sim 1550\text{ cm}^{-1}$  is down-shifted from the position of the first-order mode of graphite ( $1580\text{ cm}^{-1}$ ). This effect will be examined in more detail in Sec. III E. The two films described in (b) and (c) are often termed diamond films because of the presence of crystalline diamond. In this study, it is found that the size and absorption properties

of these  $sp^2$ - and  $sp^3$ -bonded domains strongly affect the relative strengths of the Raman features described above. This will be discussed later in conjunction with the powder composition results. The details of Raman scattering from different carbon structures has been discussed elsewhere,<sup>12</sup> so a brief overview of Raman scattering from composites is presented.

### C. Composite properties

In order to examine the Raman scattering from composites, three length scales are considered: micrometer scale, microcrystalline, and atomically disordered. (The term microcrystalline is used to represent submicrometer sizes typically less than  $100\text{ nm}$ .) For micrometer-scale constituent materials, the Raman spectrum should appear as a linear combination of the features of the bulk materials. The absolute and relative intensities of the features will be strongly affected by the optical absorption of the two materials. These effects are clearly seen in the graphite-diamond composites where graphite is highly absorbing and diamond is effectively transparent in the visible range. Relative concentration and crystallite size are also very important to the resulting Raman spectrum. The details of these effects will be discussed later. As the domains decrease to microcrystalline scales, features should begin to appear in the Raman spectrum due to size effects associated with the breakdown of the conservation of wave vector.<sup>20</sup> Vibrational modes of the small crystallites are described as phonons with an uncertainty in the wave vector ( $\Delta k \sim 2\pi/d$ , where  $d$  is the domain size), and the momentum selection rules for the Raman process are, therefore, relaxed. The absorption depths and the phonon decay lengths for the constituent materials will generally be larger than the domain size. If the phonons are confined to the different regions, then the spectra will again be a superposition, but of microcrystalline components. Diffraction of the incident light will more uniformly illuminate the composite than would be the case for a micrometer-scale sample, and for very small domains optical absorption will not affect the relative intensities. If an atomically disordered composite were possible, the Raman spectrum would become the average of the vibrational and electronic properties of the disordered network. This spectrum would be quite different from the features of the bulk materials.

### D. BN and diamond composites

Several of the Raman spectra taken from the BN and diamond composites are shown in Fig. 3. The two peaks exhibited are the first-order Raman mode of diamond at  $1332\text{ cm}^{-1}$  and the first-order mode of BN which has been shown previously to occur at  $1366\text{ cm}^{-1}$ .<sup>23</sup> The relative concentration of diamond in the samples ranges from  $\sim 10\%$  up to  $66\%$ . As is to be expected, the relative intensities of the two peaks change in proportion to the concentration of diamond present in the composite. If the ratio of the peak intensities of BN and diamond versus concentration of diamond in the samples is plotted, Fig. 4 is obtained. The data follow a smooth curve

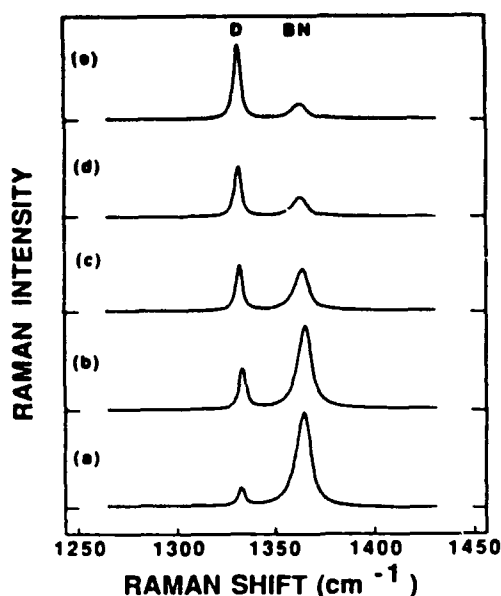


FIG. 3. First-order Raman spectra of the composites of diamond and BN powders. The relative concentrations of diamond in the samples are (a) 15%, (b) 20%, (c) 35%, (d) 55%, and (e) 67%. The features due to diamond (*D*) and BN are identified. The spectra have been multiplied by the indicated value.

which might be fitted very well using an appropriate model of the Raman scattering from composites.

In order to model the BN and diamond composites, we must understand the various parameters which effect the intensity of the Raman signal from these materials. Loudon<sup>24</sup> demonstrated that for a sample mounted in a

$$\frac{I_D}{I} = \frac{I_{0D}}{I_0} \left[ \frac{A_D}{A} \right] \left[ \frac{L_D(\alpha_1 + \alpha_2)}{1} \right] \left[ \frac{\Delta\Omega_D}{\Delta\Omega} \right] \left[ \frac{1 - R_D}{1 - R} \right]^2 \left[ \frac{\left[ \sum_j (\hat{e}_2 \cdot \mathbf{R}_j \cdot \hat{e}_1)^2 \right]_D}{\left[ \sum_j (\hat{e}_2 \cdot \mathbf{R}_j \cdot \hat{e}_1)^2 \right]} \right], \quad (2)$$

where *S* has been redefined in terms of a scattering efficiency, *A*, and a summation over the inner product of the Raman tensor,  $\mathbf{R}_j$ , of the degenerate first-order mode and the polarization units vectors of the incident and scattered light,  $\hat{e}_1$  and  $\hat{e}_2$ . *I* is the scattering intensity of the material being compared, and *I<sub>D</sub>* represents the scattered intensity from the diamond power. *I<sub>0</sub>* is the incident intensity.  $\Delta\Omega$  is the solid angle into which light is scattered, and the term in *R* corrects for reflection of the scattered light at the sample surface and multiple reflections in the sample as in diamond. Here,  $\alpha_1$  and  $\alpha_2$  are the previously defined absorption coefficients of the material to be compared to diamond since it has been assumed that diamond is transparent to the visible laser radiation. The formulation assumes that  $1/\alpha < L$  for the material to be compared to diamond.

If we now apply Eq. (2) to the composite samples, several approximations can be made. Since the Raman

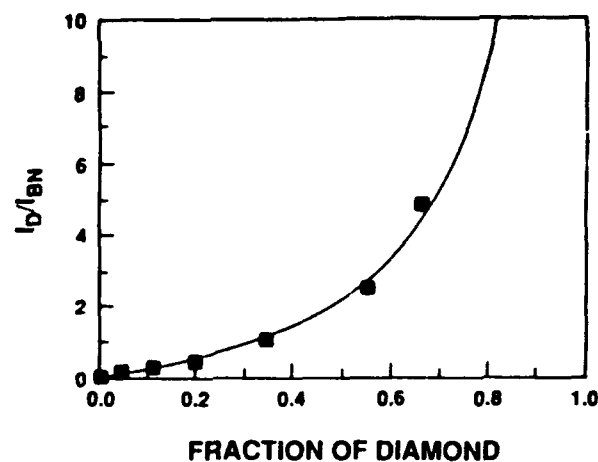


FIG. 4. Ratio of peak intensities ( $I_D/I_{BN}$ ) vs relative concentration of diamond in the composite samples. Theoretical best fit assumes  $a_{BN}/a_D \sim 2.9$ .

backscattering geometry, the scattering intensity is given by

$$I = I_0 S / S + \alpha_1 + \alpha_2 \{ 1 - \exp[-(S + \alpha_1 + \alpha_2)L] \}, \quad (1)$$

where *S* is the scattering efficiency, *I<sub>0</sub>* is the incident intensity, *L* is the sample thickness in the direction of the incident laser light, and  $\alpha_1$  and  $\alpha_2$  are the absorption coefficients at the respective frequencies of the incident and scattered light. Wada and Solin<sup>25</sup> showed that this equation could be modified to give the ratio of the scattering intensities of two different materials:

signal is being collected from a region of discrete particles, the values for *L<sub>D</sub>* and  $\Delta\Omega$  are the same for both materials. Also, our model will neglect the reflection losses due to light scattering between the BN and diamond particles. Finally, note that the last term in Eq. (2) provides unique values for the summations if the polarization directions of the incident and scattered light are known *a priori*. Since the BN and diamond composites contain particles of completely random orientation, an angle-averaged value of the summations over all possible polarization directions must be taken.

Using the above model, the ratio of the Raman-scattering intensities of diamond to BN may be written

$$\frac{I_D}{I_{BN}} \sim \frac{4 A'_D N_D V_D}{3 A'_{BN} N_{BN} V_{BN}}, \quad (3)$$

where *A'* is the angle- and polarization-averaged scatter-

ing efficiency per nearest-neighbor bond,  $N$  is the atomic density of BN or diamond, and  $V$  is the volume of material which is actually sampled by the Raman scattering. The factor of  $\frac{1}{4}$  accounts for the fact that diamond contains four nearest neighbors and BN has three nearest neighbors at each site. In terms of  $P_D$ , the atomic percentage of diamond,  $N_D V_D / N_{BN} V_{BN} = P_D / (1 - P_D)$ , so that Eq. (3) becomes

$$\frac{I_D}{I_{BN}} = \frac{4A'_D}{3A'_{BN}} \left[ \frac{P_D}{1 - P_D} \right] \quad (4)$$

The first-order Raman mode in both diamond and BN is a bond-stretching mode. Using Eq. (4), we find excellent agreement with the data shown in Fig. 4 if the value for the ratio of the scattering efficiencies,  $A'_D/A'_{BN}$ , approximately equals 1.6. Using the fact that the ratio of the bond densities of diamond and BN is  $\sim 2$ , then  $A_D/A_{BN} \sim 3.2$  (where  $A_D$  and  $A_{BN}$  are the scattering efficiencies per unit volume). This value is applicable to the BN and diamond powders, but not necessarily to the bulk materials.

#### E. Graphite and diamond composites

Since our model provides such good agreement with the data obtained from the BN and diamond particle composites, it might be modified to accurately predict the relative concentration of diamond in other types of composite samples. We have therefore extended this analysis to composites of graphite and diamond to determine if the same close agreement between theory and experiment might be found. Composite samples were prepared, and several of the Raman spectra obtained from these samples are shown in Fig. 5. The diamond peak at  $1332 \text{ cm}^{-1}$  is now accompanied by the first-order Raman mode of graphite<sup>26</sup> at  $1580 \text{ cm}^{-1}$ . The relative concentration of diamond in these samples ranges from  $\sim 1\%$  up to  $60\%$ . It has been previously reported that the Raman efficiency of graphite is  $\sim 50$  times larger than that of diamond.<sup>25</sup> An interesting aspect of these spectra is that the  $\sim 1\%$  diamond composite displays a 1:1 ratio between the peak intensities of the first-order modes of diamond and graphite. At  $50\%$  diamond, it is seen that the peak due to graphite has practically disappeared. Thus the absorption of graphite has a significant effect on the Raman spectra of the composites, and is shown in the large disparity of the absolute intensity scales of the samples. This may be compared to the Raman spectra of the BN and diamond composites in Fig. 3 in which the absolute intensity scale is the same for all samples.

Again, the model described for the BN and diamond samples may be extended to the graphite and diamond composites if the effect of optical absorption due to graphite is included. Therefore, Eq. (3) can be written

$$\frac{I_D}{I_G} = \frac{4A'_D N_D V_D}{3A'_G N_G V'_G} = \frac{4A'_D N_D V_D}{3A'_G N_G V_G} \left[ \frac{V_G}{V'_G} \right] \quad (5)$$

where  $V'_G/V_G$  represents the fraction of each graphite particle sampled in the Raman process. Since the particle size is larger than the absorption depth of the graph-

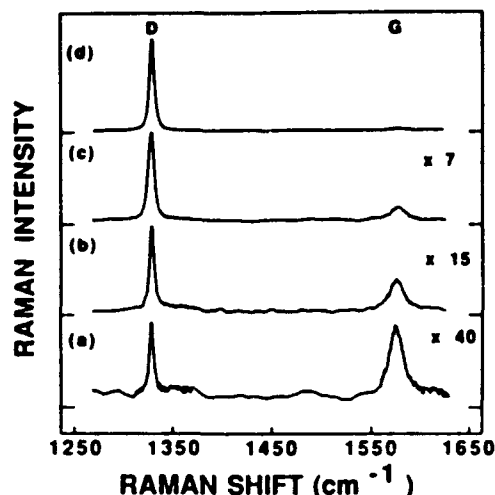


FIG. 5. First-order Raman spectra of the composites of diamond and graphite powders. The relative concentrations of diamond in the samples are (a) 1.3%, (b) 6.6%, (c) 21.5%, and (d) 50.0%. The features due to diamond (D) and graphite (G) are identified. The spectra have been multiplied by the indicated value.

ite, this term accounts for only that portion of each graphite particle contributing to Eq. (5). Again, light incident on a diamond particle will sample the entire particle in the Raman process. Equation (5) can now be written in terms of  $P_D$ , the percentage of diamond in the composites:

$$\frac{I_D}{I_G} \sim \frac{4A'_D}{3A'_G} \left[ \frac{P_D}{1 - P_D} \right] \left[ \frac{V_G}{V'_G} \right] \quad (6)$$

From this analysis, it becomes apparent that the size and shape of the crystallites will affect the observed ratio of the Raman peaks. The geometric and absorption factors are accounted for in the  $V'_G/V_G$  term. At the  $5145\text{-}\text{\AA}$  exciting wavelength, graphite has an absorption depth<sup>25</sup> of  $\sim 300 \text{ \AA}$ . For simplicity, we have assumed that the graphite particles are cubic, and oriented with a flat surface toward the beam. Because the scattered light must also exit the absorbing region, the volume of graphite sampled will be a thin layer,  $\sim 150 \text{ \AA}$  thick, across the top of each graphite "cube."

It is important to note that the value for  $V'_G/V_G$  would increase for decreasing crystallite sizes, suggesting the graphite features would then appear more strongly in the Raman spectrum of very-fine-grain particles. The results of this model are demonstrated in Fig. 6, where the ratio of the two peaks versus concentration of diamond is again plotted along with several fitting curves based on Eq. (6). For these calculations we have determined  $A'_D/A'_G$  as follows. The ratio of the scattering efficiencies per unit volume was reported by Wada and Solin to be  $\sim 1/50$ .<sup>26</sup> They noted a significant uncertainty depending on which values of the optical constants were used.<sup>25</sup> In our model we have considered the scattering in terms of the number of nearest-neighbor C—C bonds. The ratio of the bond density of graphite to

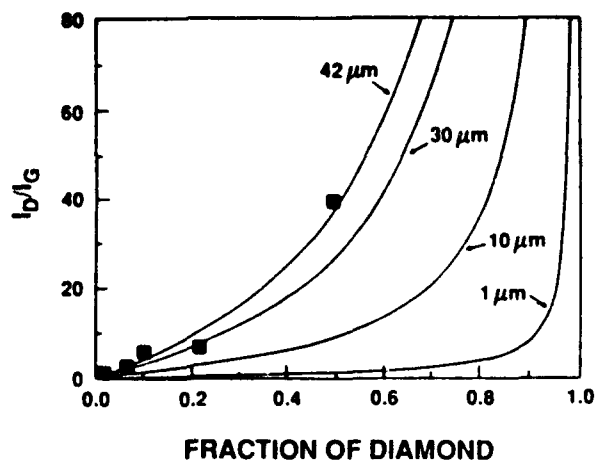


FIG. 6. Ratio of peak intensities ( $I_D/I_G$ ) vs relative concentration of diamond in the composite samples. The solid lines are derived from Eq. (6) assuming an average graphite particle size of 30, 10, and  $1 \mu\text{m}$ , respectively.

diamond is 0.48. Thus the value of  $A'_D/A'_G$  will be  $\sim 1/100$  in terms of scattering per nearest-neighbor bond. Theoretical curves are shown assuming "cubic" graphite particles of 42, 30, 10, and  $1 \mu\text{m}$  size. The model, using  $42\text{-}\mu\text{m}$  "cubes," follows the data very well. The curves for 10 and  $1 \mu\text{m}$  particle size indicate that the diamond peak would begin to dominate the spectrum only at high concentrations of diamond. Clearly the observed ratio is strongly dependent on the crystallite size.

The model reaches a limit where the crystalline domains are smaller than the absorption length of the absorption regions. In this limit, the value of  $V'_G/V_G$  becomes 1 and the effects of absorption can be ignored. The relation is then the same as that for two transparent materials as in Eq. (4).

#### F. Graphitic bonding in diamond films

While the Raman spectra of the CVD carbon films show diamond crystal structures, they also display features indicating  $sp^2$  bonding in the films. The Raman spectra of one of the films are compared to highly oriented pyrolytic graphite (HOPG) and microcrystalline or "glassy" carbon in Fig. 7. The features in the film are broader than those of the graphitic compound, but they clearly represent the presence of  $sp^2$  bonding. Spectrum (a) of HOPG and (b) of glassy carbon display the  $1580\text{-cm}^{-1}$  peak characteristic of crystalline or microcrystalline graphite. We also note again that the highest-frequency peak in the film is down-shifted from that of the graphitic materials. The absolute intensity scales of the graphitic materials are approximately equal. By comparison, the Raman spectrum of the composite diamond thin film in Fig. 7(c) shows an absolute intensity scale  $\sim 15$  times greater than that of HOPG or glassy carbon. This implies that the features in spectrum (c) at  $1355$  and  $1580\text{ cm}^{-1}$  must be associated with structures having optical properties quite different from those of graphite.

The two parameters related to the bonding structure

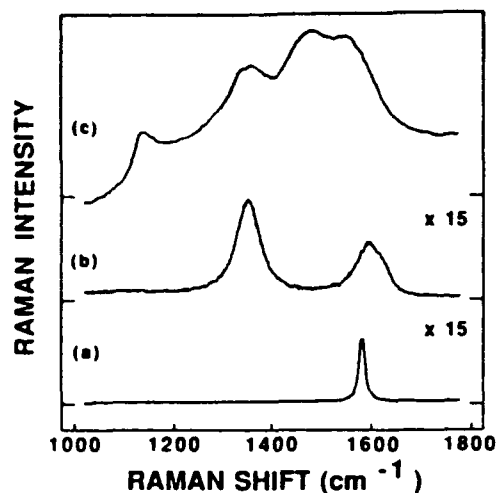


FIG. 7. First-order Raman spectra of (a) highly oriented pyrolytic graphite, (b) glassy carbon, and (c) diamond thin film produced by microwave-plasma-excited CVD. The spectra have been multiplied by the indicated value.

which can affect the absolute Raman intensity are the scattering cross section,  $A$ , and the absorption coefficients,  $\alpha_1$  and  $\alpha_2$ . Since the Raman cross section for diamond is less than that for graphite, we would suggest that microstructural changes would not tend to increase the Raman cross section of the  $sp^2$  regions. Let us, therefore, consider the optical absorption. At an  $sp^2$  site, three of the four valence electrons form in-plane  $\sigma$  bonds, while the fourth enters a  $\pi$  orbital lying perpendicular to this plane. Note that in graphite the  $\pi$  orbitals are not localized at their respective  $sp^2$  sites, but can move relatively freely among the C atoms. This does not lead to true  $\text{C}=\text{C}$  "double" bonds, but nevertheless the  $\pi$  bonds contribute to the bond strength of the in-plane bonds. Since they are weakly bonding, the  $\pi$  states lie closest to the Fermi level,  $E_F$ . Therefore,  $\pi-\pi^*$  transitions occur at lower energies than  $\sigma-\sigma^*$  transitions and account for the strong optical absorption in graphite. Savvides<sup>14</sup> has considered the optical properties associated with  $a\text{-C}$  containing no hydrogen. He demonstrated that in a matrix of  $sp^2$  and  $sp^3$  sites the density of states at the top of the valence band decreases as the relative concentration of  $sp^3$  sites increases. Therefore, incorporation of  $sp^3$  sites into the network leads to an increasing optical gap and, consequently, lower optical absorption. More recently, Robertson and O'Reilly<sup>27</sup> have followed the model of  $a\text{-C}$  suggested by Wada *et al.*,<sup>22</sup> and proposed that an  $a\text{-C}$  network should consist of  $\sim 15\text{-}\text{\AA}$  graphitic "islands" of fused sixfold rings surrounded by  $sp^3$  sites. The  $\pi$  bonds would be broken at the island boundary as a mechanism for relieving strain in the network. This model also suggests a higher optical gap with decreasing absorption.

The incorporation of very small graphitic regions in the diamond films could then lead to a lowering of the optical absorption of the regions and an enhanced Raman intensity. In this limit, the nearby diamond and graphitic regions would be uniformly illuminated, and our analysis would suggest that the Raman scattering from  $sp^2$ -bonded materials should be  $\sim 100$  times stronger than

that from diamond regions.

We have analyzed the integrated Raman intensities of the spectra shown in Figs. 2(b) and 2(c). If the integrated Raman intensities of the  $sp^2$  and diamond peaks are used, and the 100-fold difference in scattering efficiencies, we obtain 87% and 28% diamond, respectively. Transmission-electron-microscopy (TEM) measurements of films similar to that used to obtain the spectrum shown in Fig. 2(c) show predominantly diamond structures.<sup>8</sup> Therefore, the number of  $sp^2$  regions is still higher than would be anticipated from TEM. One possibility of accounting for this enhancement is that the microcrystalline regions lead to disorder-induced scattering from the breakdown in the wave-vector selection rules for the Raman scattering,<sup>23</sup> and this adds an additional correction.

In addition to the apparent optical properties of the  $sp^2$  component in the diamond films, we also observed that the highest-energy feature in the Raman spectra of the films occurs at  $\sim 1550\text{ cm}^{-1}$ , and this is down-shifted from the expected position of graphite at  $\sim 1580\text{ cm}^{-1}$ . We considered whether this might be due to the convolution of the  $1580\text{-cm}^{-1}$  peak with the feature due to amorphous  $sp^2$  structures at  $\sim 1480\text{ cm}^{-1}$ . In order to examine this, we formed a computer-generated linear combination of the Raman spectra of a diamond thin film and a sample of microcrystalline graphite, similar to Figs. 2(a) and 2(c). The various peaks were scaled to approximately the same absolute intensity as the features in Fig. 2(b). This "combined" spectrum is shown in Fig. 8(a), and is compared to other similar spectra from various diamond thin films. Figures 8(b) and 8(c) were taken from films

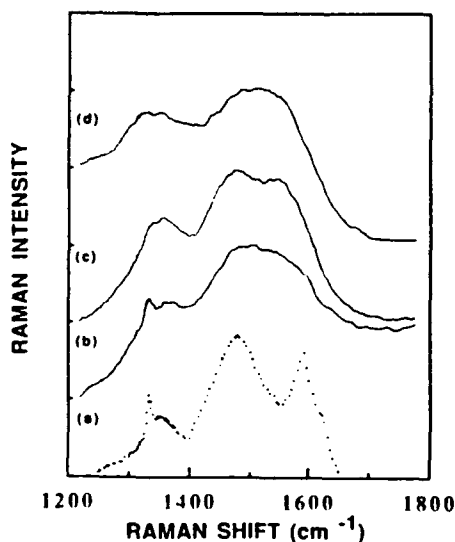


FIG. 8. Comparison of Raman spectra from CVD diamond films and computer model to examine down shift of highest-energy peak. (a) Computer-generated Raman spectra assuming linear combination of spectra of diamond thin film and microcrystalline graphite (b) deposited at 1.5%  $\text{CH}_4/\text{H}_2$  concentration, (c) deposited at 3.0%  $\text{CH}_4/\text{H}_2$  concentration, and (d) "just-nucleated" diamond film with substrate coverage  $\sim 50\%$ .

created by a microwave-plasma-excited CVC process in which the  $\text{CH}_4/\text{H}_2$  dilution was 1.5% and 3.0%, respectively. The spectrum in Fig. 8(d) was obtained from a "just-nucleated" diamond sample in which the surface coverage was  $\sim 50\%$ . All three samples show approximately the same Raman features. The spectra clearly demonstrate, when compared to Fig. 8(a), that the peak at  $\sim 1550\text{ cm}^{-1}$  must be down-shifted from  $\sim 1580\text{ cm}^{-1}$ , and is not due to a convolution of peaks.

Several authors<sup>22,28,29</sup> have noted similar down shifts in the Raman spectra of  $a\text{-C:H}$ . All of these films contained  $> 30\text{ at. \% H}$  though, whereas the films examined in this paper were deposited at temperatures  $> 800^\circ\text{C}$  such that they contained  $< 1\text{ at. \% H}$ . Ramsteiner and Wagner<sup>28</sup> also showed that upon annealing their  $a\text{-C:H}$  films to  $600^\circ\text{C}$  almost all H was removed from the samples, leaving  $sp^2$ -bonded microcrystalline graphite, and the first-order mode was observed at the unshifted  $\sim 1580\text{-cm}^{-1}$  frequency. Dillon *et al.*<sup>30</sup> have used Raman spectroscopy to examine  $a\text{-C}$  films produced by ion-beam sputtering and by rf-plasma deposition. The ion-beam-sputtered samples, containing little H, also showed a down shift in the first-order mode, but the disorder mode at  $1355\text{ cm}^{-1}$  was not distinct from the background. Upon annealing to  $400^\circ\text{C}$ , the disorder mode became apparent at  $\sim 1355\text{ cm}^{-1}$ , and the first-order mode was slightly down-shifted. Higher-temperature annealing restored this feature to its original value. Their analysis focused on the continuous-random-network models of Beeman<sup>31</sup> which assumed bond-angle distortion and the existence of fourfold coordination in the films to explain the Raman features.

We can now consider both the optical and vibrational properties of the  $sp^2$  component in diamond thin films, in order to provide a clearer picture of the nature of the bonding. The vibrational properties show two  $sp^2$  components, one similar to amorphous carbon and one that is graphitic. The peak intensity at  $1355\text{ cm}^{-1}$  indicates that the microcrystalline domain sizes are less than  $30\text{ \AA}$ .<sup>26</sup> In the light of the disparity in the Raman intensity, the model proposed by Robertson and O'Reilly<sup>27</sup> seems to be valid for diamond thin films; namely the  $sp^2$  graphitic regions are small and are terminated at  $sp^3$  sites, resulting in lower optical absorption. This possibility is also consistent with TEM measurements which show that the graphitic regions apparently lie between regions of crystalline or microcrystalline diamond. The decreased density of  $\pi$  states at the top of the valence band would lower the absorption, and their localization at an  $sp^3$  site would decrease the corresponding bond strength. The weaker bonding can then account for the down shift in the first-order Raman mode of the graphitic regions. The graphitic regions do not have to be limited to 15–20- $\text{\AA}$  island structures, but it seems unlikely that much larger structures would produce the same results. This is because larger structures would have a smaller percentage of sites terminated in  $sp^3$  bonding; thus, the optical properties would be more heavily influenced by the bulk structure. Disordered regions must also be assumed to explain the appearance of the feature at  $\sim 1480\text{ cm}^{-1}$ , but how this disorder is incorporated into the polycrystalline film is uncertain.

## IV. CONCLUDING REMARKS

The Raman spectra of various diamond and diamond-like thin films have been examined. The features displayed by the diamond films suggest that they are composites of  $sp^2$  and  $sp^3$  bonding. We have attempted to understand the nature of these films using composites of BN-diamond and graphite—diamond powder samples. A simple model of the Raman scattering from these composites has been proposed, and reasonable agreement with the experimental data has been obtained. This investigation of graphite and diamond composites demonstrates that both concentration and crystallite size have significant effects on the resulting Raman spectra. In diamond films containing regions of diamond and graphite, it is predicted that the Raman spectra could be used to estimate the relative concentrations of these regions, but we emphasize that the sizes of the various domains in the films must first be known. We have found that the characteristics of the  $sp^2$  bonding in the films do not correlate well to regions of microcrystalline graphite. The Raman spectra suggest that the optical absorption of these regions in the visible is less than in natural graphite

for the wavelength used. Also, a peak exhibited in the Raman spectra at  $1550\text{ cm}^{-1}$  is down-shifted from the position of the first-order Raman mode of graphite, but a peak at  $1355\text{ cm}^{-1}$ , corresponding to a disorder mode in small graphite crystallites, is still observed. We have proposed a model in which the  $\pi$  bonds in the graphitic regions are localized or attached to  $sp^3$  sites. This model can account for the features observed in the Raman spectra of the diamond thin films.

## ACKNOWLEDGMENTS

We gratefully acknowledge K. Kobashi and Y. Kawate of Kobe Steel, Ltd., for supplying the diamond samples used in this study. We also appreciate the helpful discussions of R. Rudder of the Research Triangle Institute and B. Williams of North Carolina State University (NCSU), as well as the help of R. Russell of NCSU in the preparation of the composite powder samples, and Shannon Wells of NCSU for data analysis. This work was supported in part by SDIO/IST through the U.S. Office of Naval Research under Contract No. N00014-86-K-0666.

\*Present address: Rocketdyne Div., Rockwell Int., Canoga Park, CA 91303.

<sup>1</sup>B. V. Derjaguin, B. V. Spitsyn, A. E. Gorodetsky, A. P. Zacharov, L. I. Bouilov, and A. E. Aleksenko, *J. Cryst. Growth* **31**, 44 (1975).

<sup>2</sup>S. Matsumoto, Y. Sato, M. Tsutsumi, and N. Setaka, *J. Mater. Sci.* **17**, 3106 (1982).

<sup>3</sup>T. Mori and Y. Namba, *J. Appl. Phys.* **55**, 3276 (1984).

<sup>4</sup>A. Sawabe and T. Inuzuka, *Thin Solid Films* **137**, 89 (1986).

<sup>5</sup>C. P. Chang, D. L. Flamm, D. E. Ibbotson, and J. A. Mucha, *J. Appl. Phys.* **63**, 1744 (1988).

<sup>6</sup>B. Singh, O. R. Mesker, A. W. Levine, and Y. Arie, *Appl. Phys. Lett.* **52**, 1658 (1988).

<sup>7</sup>K. Ito, T. Ito, and I. Hosoya, *Chem. Lett.* **1988**, 589.

<sup>8</sup>B. E. Williams and J. T. Glass, *J. Mater. Res.* **4**, 373 (1989).

<sup>9</sup>Y. Hirose and Y. Terawasa, *Jpn. J. Appl. Phys.* **25**, L519 (1986).

<sup>10</sup>C. B. Zarowin, N. Venkataramanan, and R. R. Poole, *Appl. Phys. Lett.* **48**, 759 (1986).

<sup>11</sup>V. Natarajan, J. D. Lamb, J. A. Woollam, D. C. Liu, and D. A. Gulino, *J. Vac. Sci. Technol. A* **3**, 681 (1985).

<sup>12</sup>R. J. Nemanich, J. T. Glass, G. Lucovsky, and R. E. Shroder, *J. Vac. Sci. Technol. A* **6**, 1783 (1988).

<sup>13</sup>D. S. Knight and W. B. White, *J. Mater. Res.* **4**, 385 (1989).

<sup>14</sup>N. Savvides, *J. Appl. Phys.* **58**, 518 (1985).

<sup>15</sup>S. Kaplan, F. Jansen, and M. Machonkin, *Appl. Phys. Lett.* **47**, 750 (1985).

<sup>16</sup>S. D. Berger, D. R. McKenzie, and P. J. Martin, *Philos. Mag. Lett.* **57**, 285 (1988).

<sup>17</sup>The BN and diamond powders were obtained from AESAR Chemical, Seabrook, NH 03874.

<sup>18</sup>The graphite powder was obtained from ALFA Chemical, Danvers, MD, 01923.

<sup>19</sup>S. A. Solin and A. K. Ramdas, *Phys. Rev. B* **1**, 1687 (1970).

<sup>20</sup>R. J. Nemanich and S. A. Solin, *Phys. Rev. B* **20**, 392 (1979).

<sup>21</sup>S. A. Solin and R. J. Kobliska, in *Amorphous and Liquid Semiconductors*, edited by J. Stuke (Taylor and Francis, London, 1974), p. 1251.

<sup>22</sup>N. Wada, P. J. Gaczi, and S. A. Solin, *J. Non-Cryst. Solids* **35&36**, 543 (1980).

<sup>23</sup>R. J. Nemanich, S. A. Solin, and R. M. Martin, *Phys. Rev. B* **23**, 6348 (1981).

<sup>24</sup>R. Loudon, *J. Phys.* **26**, 677 (1964).

<sup>25</sup>N. Wada and S. A. Solin, *Physica B+C* **105B**, 353 (1981).

<sup>26</sup>F. Tuinsta and J. L. Koenig, *J. Chem. Phys.* **53**, 1126 (1970).

<sup>27</sup>J. Robertson and E. P. O'Reilly, *Phys. Rev. B* **35**, 2946 (1987).

<sup>28</sup>M. Ramsteiner and J. Wagner, *Appl. Phys. Lett.* **51**, 1355 (1987).

<sup>29</sup>M. Yoshikawa, G. Katagiri, H. Ishida, A. Ishitani, and T. Akamatsu, *Appl. Phys. Lett.* **52**, 1639 (1988).

<sup>30</sup>R. O. Dillon, J. A. Woollam, and V. Katkanant, *Phys. Rev. B* **29**, 3482 (1984).

<sup>31</sup>D. Beeman, J. Silverman, R. Lynds, and M. R. Anderson, *Phys. Rev. B* **30**, 870 (1984).

# IX. Microphotoluminescence and Raman scattering study of defect formation in diamond films

L. Bergman, B. R. Stoner, K. F. Turner, J. T. Glass, and R. J. Nemanich  
*Department of Physics and Department of Materials Science and Engineering,  
North Carolina State University, Raleigh, North Carolina 27695-8202*

(Received 30 September 1992; accepted for publication 17 December 1992)

Photoluminescence and Raman spectroscopy are employed to explore the time evolution of defect formation in chemical vapor deposition diamond films for stages of growth spanning nucleation to continuous film formation. Our research is concentrated on three types of defects which give rise to the 1.68 eV optical band, the  $sp^2$  phase which centers at  $1500\text{ cm}^{-1}$ , and the broadband luminescence at 565–800 nm. The investigation of these types of defects suggests the following conclusions. Si atoms are most likely responsible for the creation of the 1.68 eV optical centers which takes place at the initial stages of growth. Plasma interactions with the Si substrate contribute to the 1.68 eV defect formation. The broad luminescence and  $sp^2$  bonding defects were not present in the isolated nuclei but were significantly present when a continuous film was formed. Two rates of diamond growth were obtained and the changes of the rates were attributed to the lowering degree of freedom available for the growth of the nuclei as well as to the formation of the  $sp^2$  phase.

## I. INTRODUCTION

Investigation of defect formation in chemical vapor deposition (CVD) diamond films is critical in understanding the basic mechanisms of electronic transport and optical interactions which underlie applications in developing electronic and optical devices. In this study Raman and photoluminescence (PL) microscopy was employed to investigate the formation over time of defects in CVD diamond, from the very early stages of diamond nucleation through formation of groups of particles and finally to the growth of continuous thick films. At each stage of the growth, the morphology of the sample was obtained from scanning electron microscope (SEM) images and this information was correlated to the PL and to the Raman line intensities of the defects. This article presents an analysis of the creation of three types of defects associated with optical bands referred to as the 1.68 eV, the  $sp^2$ -type bonding, and the broadband luminescence at 565–800 nm, for stages of growth spanning nucleation to continuous film formation.

One part of our experiment examined the 1.68 eV defect center, for which conflicting models have been proposed. Previous work has suggested a relation of the 1.68 eV center to the GR1 optical active center which exists in natural and synthetic diamond. Upon interaction with light the GR1 gives rise to the photoluminescence band at 1.673 eV. The GR1 defect center can be produced in any type of natural or synthetic diamond by the introduction of radiation damage into the diamond,<sup>1-4</sup> which creates vacancies and interstitials of carbon atoms. It is commonly accepted that the GR1 band is associated with the natural vacancy center which possesses tetrahedral symmetry<sup>5</sup> and has an unpolarized zero-phonon line emission of 1.673 eV arising from a transition between the  $T_2$  and the  $E$  state.<sup>6</sup>

In many thin diamond films grown from the vapor phase, the PL emission line can be observed at 1.68 eV which is a shift of 7 meV from the GR1 peak of the natural

diamond. This shift may indicate that the 1.68 eV center originates from a different defect center than the natural vacancy. Various works show evidence that the introduction of Si during growth increases the 1.68 eV peak significantly.<sup>7,8</sup> One explanation was that the Si atoms were incorporated into the diamond octahedral lattice sites and formed a radiative center there.<sup>7</sup> Another study on Si-implanted natural diamond showed that the 1.68 eV center was due to defects containing two interstitial silicon atoms.<sup>9</sup> Yet another possible explanation for the 7 meV shift is that it arises from the presence of the internal stress which exists in the individual crystallites of the CVD diamond films. This residual stress can induce the 6–7 meV shift of the GR1 center.

Another part of our experiment examined the broadband luminescence. The broad luminescence band, extending from approximately 565 to 800 nm and centered at around 608 nm, has been observed in various luminescence studies. The broadband is exhibited in both cathodoluminescence (CL) spectra of natural and polycrystalline diamond,<sup>10-16</sup> and has also been observed in the PL spectra of other studies.<sup>15-17</sup> In most of the PL and CL spectra, the 2.15 eV center was detected as well. This center has been attributed to the zero-phonon line (ZPL) of the interstitial nitrogen-vacancy complex. It has been suggested that the broad luminescence band is the result of vibronic interaction corresponding to the 2.15 eV ZPL.<sup>13</sup> Inspection of the PL spectra of hydrogenated amorphous carbon<sup>18,19</sup> reveals that a broadband luminescence exists with similar characteristics as the diamond broadband PL/CL. However, since the CVD diamond film was found to possess  $sp^2$  amorphous-like carbon bonding, it is surmised that the broadband luminescence may be due to that type of defect.

In this article the experimental results and analysis of the formation of 1.68 eV,  $sp^2$ -type and broadband luminescence defects is presented. Section III A of this article describes measurements of the Raman linewidth, the ratio of

the  $sp^2$ -type bonding to the  $sp^3$  diamond-type bonding ( $sp^2/sp^3$ ), and the absolute integrated diamond Raman line intensities as a function of the growth time. At the very early stages of the deposition when the morphology of the substrate consisted of isolated diamond particles, no  $sp^2$  phase was found and the Raman linewidth exhibited a decrease with time. Furthermore the integrated diamond line followed a power-law increase with time. At later stages when coalescing of particles took place,  $sp^2$ -type bonding was found to form linearly with deposition time and the diamond linewidth increased monotonically with time. Also, the integrated diamond line still exhibited a power-law increase but with a smaller exponent than at earlier stages of growth. From the analysis of Raman linewidth and diamond intensity, a common critical threshold time was obtained which separated the early growth time phenomena from the longer time events, corresponding to the time when the diamond particles just started to coalesce as observed in the SEM images.

Section III B reports a study of the 1.68 eV defect center. The PL measurements indicated that the formation of the 1.68 eV centers takes place at very early stages of nucleation and growth of the diamond particles. The rate of incorporation of the defects into the growing film diminishes as the sample becomes continuous. It is hypothesized that plasma etching of the Si substrate is a possible mechanism to provide Si atoms which enhance the formation of the 1.68 eV optical centers. This hypothesis about the interaction of plasma and Si substrate was checked via an experiment in which five diamond films were grown at different distances from the plasma. The 1.68 eV relative intensities of these samples were significantly higher for the samples which were placed next to the plasma core than for the samples which were located farther away.

In Sec. III C preliminary results of the study on the broadband luminescence are presented. The initial analysis indicates that the type of defects responsible for the broad PL does not exist in the isolated diamond nuclei, but rather tend to be created in later stages of growth. The broad PL follows similar growth versus time behavior as the  $sp^2$  phase, and therefore it is suggested that the amorphous  $sp^2$ -bonded carbon contributes to the broad PL in the CVD diamond film.

## II. EXPERIMENT

Diamond samples for this study were grown in an AS-TeX stainless steel microwave plasma CVD chamber described in detail in previous publications.<sup>20,21</sup> Briefly, the chamber consists of a cylindrical stainless steel cavity with an inner diameter of 6 in. The plasma forms in a stable position at the center of the cavity and the substrate may be positioned relative to the plasma up to 8 cm downstream. The Si (100) substrates in this study were prepared by first abrading them with 1  $\mu\text{m}$  diamond paste in order to increase the nucleation density of the diamond particles. The abrasion was followed by an ultrasonic cleaning in TCE, acetone, and methanol, a rinse with de-ionized (DI) water, and then dried with nitrogen.

For the study of defect formation as a function of time, a series of stop-growths was performed. The growth sequence was interrupted after deposition times of 1.5, 3, 5, 7, 10, 17, and 40 h. Each step of the growth was followed by SEM, Raman microscopy, and photoluminescence analysis. Following the analysis, the sample was solvent-cleaned as discussed above and then reinserted into the growth chamber. The sample was grown in an immersed mode and was located 0.5 cm into the plasma. The plasma consisted of 1%  $\text{CH}_4$  in  $\text{H}_2$  at 1000 sccm total flow. The plasma power, chamber pressure, and substrate temperature were maintained at 800 W, 25 Torr, and 750  $^\circ\text{C}$ , respectively. For the study of the role of plasma in defect creation, five diamond samples were grown on Si substrates at positions 0, 1, 2, 3, and 4 cm below the plasma edge.

The photoluminescence and microwave Raman spectroscopy were carried out at room temperature using the ISA U-1000 scanning monochromator. The samples were excited with the 514.5 nm line of an Argon-ion laser, which was focused on the sample to a spot of about 5  $\mu\text{m}$  diameter. Focusing was facilitated by using the Olympus BH-2 microscope. The laser power at the sample was measured to be about 20 mW. The Raman spectra were taken at the region 1000–1800  $\text{cm}^{-1}$  and the PL spectra were taken at the region 400–7000  $\text{cm}^{-1}$  (2.36–1.54 eV). In order to check the spatial variation and to improve statistical significance the Raman and the PL data were taken at 12 different locations on the sample for each stage of the experiment. The data reported in this article represent an average of these 12 points.

## III. RESULTS AND DISCUSSION

### A. Analysis of the diamond and the graphitic Raman spectra

The first part of our experiment focused on an analysis of the Raman spectra as a function of growth time. In the Raman spectra of our cyclic growth sample, two main Raman features centered at 1332 and at 1500  $\text{cm}^{-1}$  were observed. The Raman scattering at 1332  $\text{cm}^{-1}$  has proved to be an indication of  $sp^3$  diamond bonding while the broad feature at 1500  $\text{cm}^{-1}$  has been attributed to  $sp^2$  amorphous-type graphitic bonding.<sup>22–26</sup>

The diamond Raman linewidth, full width at half maximum (FWHM), was first analyzed as a function of deposition time. Figure 1 shows the FWHM plotted as a function of growth time. The linewidth exhibits a minimum at about 8 h and a monotonic increase thereafter. The relatively large linewidth at 1.5 h and 3 h of growth time may be attributed to the grain-size broadening mechanism of the small nuclei<sup>27</sup> as well as to the incorporation of the relatively large Si atoms into the diamond matrix which takes place at early stages as will be discussed in Sec. III B of this article. The minimum Raman linewidth occurs at around 8 h when the diamond particles are large (about 1.5  $\mu\text{m}$ ), and for the most part are isolated and just beginning to cluster as indicated by the SEM images shown in Fig. 2. The broadening of the linewidth at the later stages of deposition when the particles coalesce and a continuous

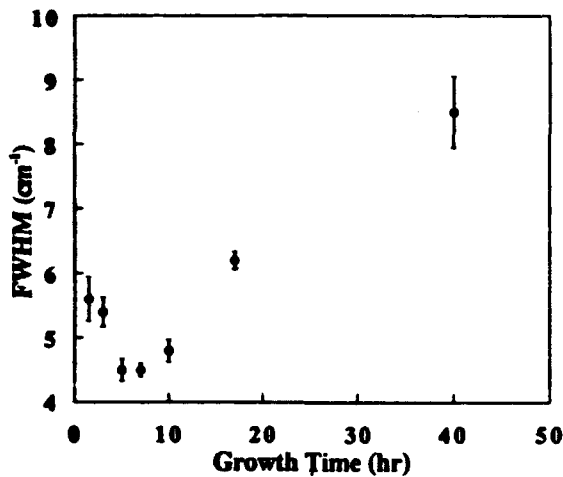


FIG. 1. The diamond Raman linewidth (FWHM) as a function of deposition time. The optimum of the linewidth occurs at  $\sim 5$  h.

film forms can be attributed to three possible broadening mechanisms: the inhomogeneous strain induced by the increasing concentration of the grain boundaries in the film, the increasing presence of the  $sp^2$ -type defects, and the size effect of the secondary nucleation.

Next the diamond Raman integrated intensity as well as the  $sp^2/sp^3$  ratio was analyzed as a function of deposition time. Figure 3 shows the Raman spectra at the seven stages of growth time. The  $sp^2$  feature at  $1500\text{ cm}^{-1}$  starts to be noticeable at around 7 to 10 h of growth time and becomes relatively large thereafter. For growth times under 7 h the  $sp^2$  feature was hard to detect in the spectra. Figure 4 shows for the same Raman spectra the plot of  $sp^2/sp^3$  ratio

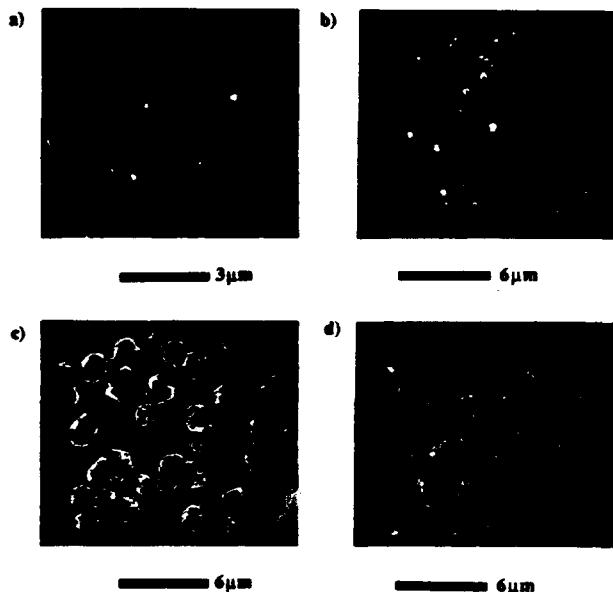


FIG. 2. The SEM micrographs of the diamond sample at (a) 1.5, (b) 3, (c) 10, and (d) 40 h of deposition time.

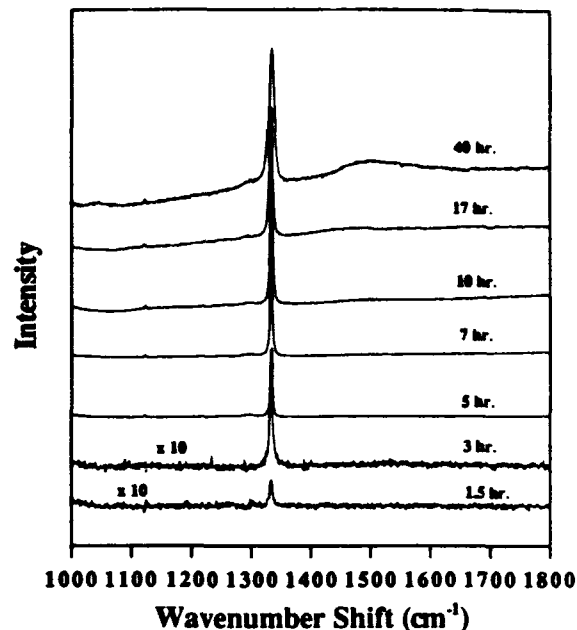


FIG. 3. The Raman spectra at the seven stages of deposition time: 1.5, 3, 5, 7, 10, 17, and 40 h.

versus growth time. The plot indicates the absence of  $sp^2$  defects until around 7 h and a linear increase for longer growth times.

The growth rate of CVD diamond is controlled by a complex dynamic balancing of the competitive growth of  $sp^2$  and  $sp^3$  phases and the preferential etching of  $sp^2$  by atomic hydrogen.<sup>28,29</sup> Determination of the growth mechanism and the kinetics of the CVD diamond is beyond the scope of this research, but the following data suggests several tentative conclusions.

The absence of  $sp^2$ -type defects at 1.5, 3, 5, and 7 h of growth time, at which stages the morphology was observed to be one of unconnected nuclei of random orientation, may be the result of the preferential etching of the defects by the atomic hydrogen. Kobashi *et al.*<sup>29</sup> have found that

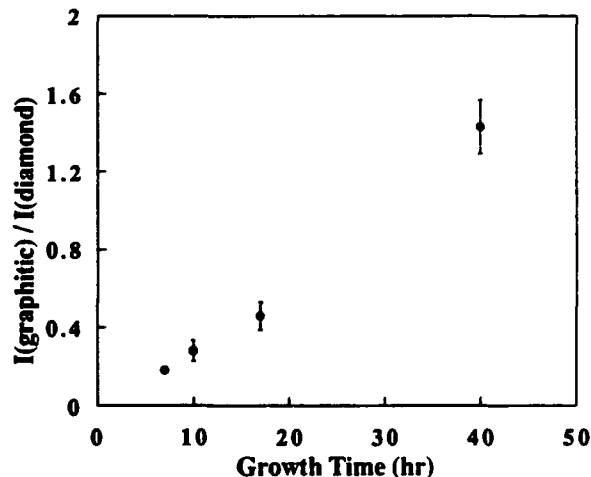


FIG. 4. The relative Raman intensity of the  $sp^2$ -type bonding vs growth time. The graphitic component is not present in the spectra at the early stages of growth (1.5–7 h).

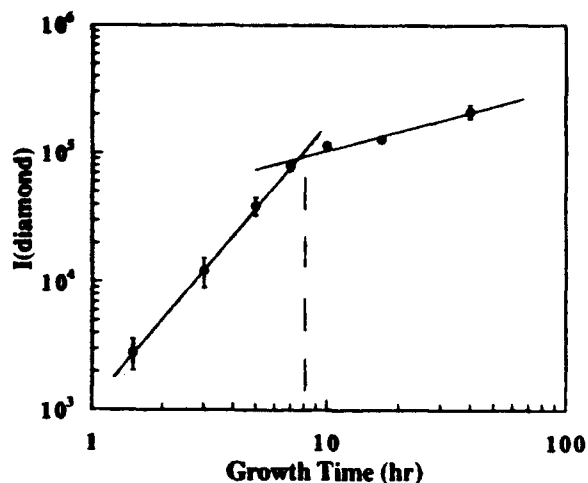


FIG. 5. The integrated intensity of the diamond Raman peak as a function of growth time. The transition from higher to lower growth rate occurs at  $\sim 8$  h.

the chemical reaction rate of graphite with hydrogen is about 30 times faster than that of diamond. Therefore,  $sp^2$ -type clusters are removed rapidly from the substrate surface and only diamond grains remain and grow. If this is the main mechanism preventing the presence of  $sp^2$ -type defects at early stages, then the rate of growth of  $sp^2$ -type defects should be approximately equal to the rate of its removal.

At later stages when coalescing and clustering of the nuclei occur resulting in the formation of grain boundaries, the  $sp^2$  phase follows a linear increase with deposition time. This implies that the rate of growth of  $sp^2$ -type defects is higher than the rate of its etching by the atomic hydrogen. One possible mechanism for the change in rate which takes place at around 8 h is incipient formation at that time of grain boundaries where particles join. The grain boundaries may provide favorable sites for the  $sp^2$  phase to nucleate and grow. The hypothesis that  $sp^2$ -type bonding is present predominantly at grain boundaries was also stated in the work of other groups.<sup>30,31</sup>

In order to determine how the diamond growth rate is impacted by the initial incorporation of the  $sp^2$ -type defect and the morphology transition from isolated nuclei to clusters, the integrated intensity of the diamond Raman peak versus time was calculated. Figure 5 shows the plot of the diamond integrated intensity as a function of growth time. The plot indicates two different power-law growth rates of the diamond, and a transition time at around 8 h. This transition time is consistent with the time of the initial appearance of the  $sp^2$  defect and the time when a change in the morphology takes place.

The growth rate is higher at early stages when nuclei are isolated from one another and space is available for the grains to grow in both lateral and vertical directions. Above the transition time the growth rate is lowered due to the coalescing which reduces the lateral degree of freedom available for the growth of the nuclei, as well as due to the

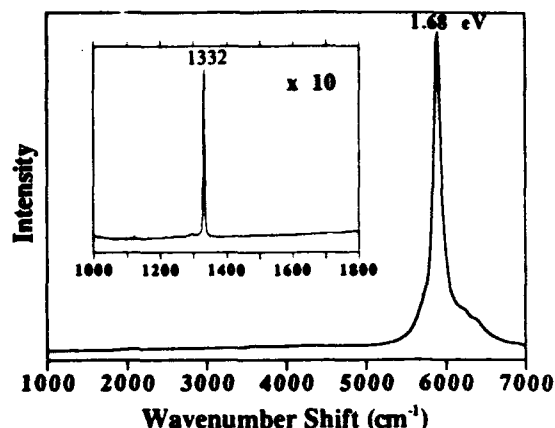


FIG. 6. The PL and Raman spectra of the diamond particles at 7 h of growth time.

competitive formation of the  $sp^2$  phase in the growing film as discussed in the previous paragraphs.

### B. The 1.68 eV optical center

In the second part of this study the formation of the 1.68 eV centers as a function of growth time was examined. Figure 6 shows the spectra of the 1.68 eV band at 7 h of growth time. For the cyclic growth sample, the PL integrated intensity of the 1.68 eV line was calculated and normalized to the diamond integrated Raman line for various growth times. The results shown in Fig. 7 indicate an initial increase of the 1.68 eV relative intensity until a maximum is reached at about 8 h; thereafter the PL relative line is seen to decrease with increasing growth time. The SEM images of this sample shown in Fig. 2 reveal that initially the film consists of isolated diamond particles; after  $\sim 8$  h the diamond particles start to coalesce, forming grain boundaries until most of the Si substrate is covered by the growth.

A possible mechanism for the effect shown in Fig. 7 is that etching of the Si substrate by the plasma releases Si atoms in the gas phase and allows them to become incorporated into the growing diamond film. In the early stages when the nucleation and growth of the isolated particles

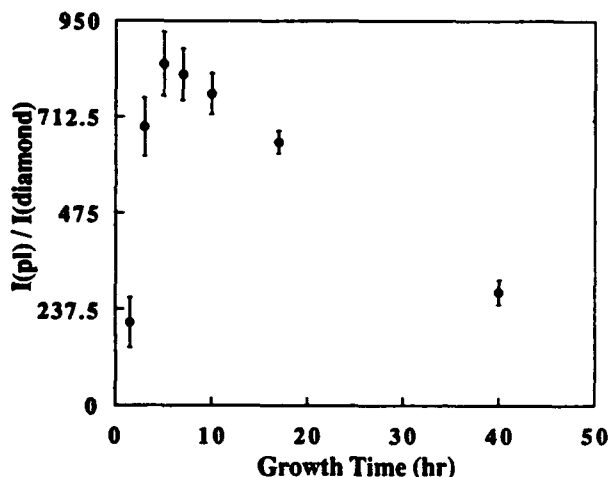


FIG. 7. The relative integrated PL intensity of the 1.68 eV band as a function of deposition time. The highest intensity occurs at  $\sim 7$  h.

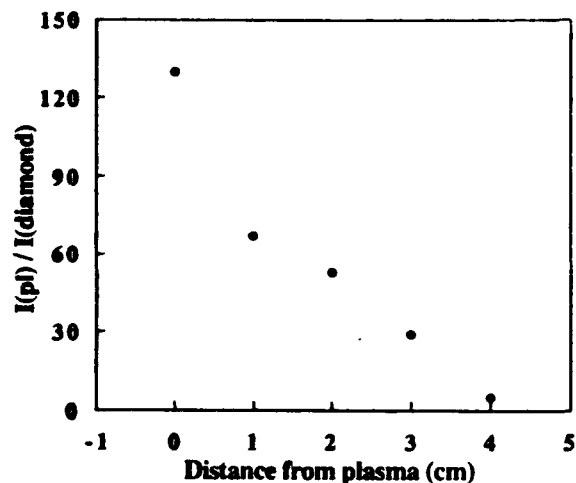


FIG. 8. The relative integrated PL intensity of the 1.68 eV band vs distance from the plasma during growth.

take place, the probability of creating the 1.68 eV centers is high since the Si substrate is almost entirely exposed to the plasma. As the diamond nuclei continue to grow in an isolated fashion, the concentration of the defect centers increases. At deposition times longer than 8 to 10 h, less of the Si substrate is exposed to the plasma, resulting in a reduced concentration of the 1.68 eV defect centers.

The absolute integrated intensity of the 1.68 eV line was also measured at ten different positions on the 10 h growth sample. No significant variation in intensity was found which implies that the final spatial distribution of these defects was nearly uniform across the sample. For the sample of 40 h growth time, large fluctuations in the 1.68 eV absolute intensities were observed across the sample. Furthermore, on average, the PL intensity was 35% lower than the absolute integrated intensity exhibited by the 10 h sample which possessed the maximum concentration of defects. The diamond Raman signal also exhibited up to 30% variation in intensity across the sample. The above observations suggest that the film thickness and the presence of grain boundaries caused the luminescence of the 40 h sample to scatter, thereby making the PL signal hard to collect. This scattering of the luminescence implies that the 1.68 eV defect centers reside mainly next to the interface of the diamond and the Si substrate.

To support the assumption that plasma interaction with Si substrate initiates formation of the optical defect centers, five incomplete diamond films were grown at different distances from the hydrogen plasma. Figure 8 shows the resulting 1.68 eV integrated relative intensity as a function of distance from the plasma, and indicates that the film which was grown nearest the plasma (i.e., immersed in it) exhibited the highest concentration of the 1.68 eV centers. The film which was grown 4 cm from the plasma exhibited very small concentrations of these centers. Saito *et al.*<sup>32</sup> have found other evidence of hydrogen plasma interaction with the Si substrate: their experiments revealed that when placing the Si substrate in the plasma center,

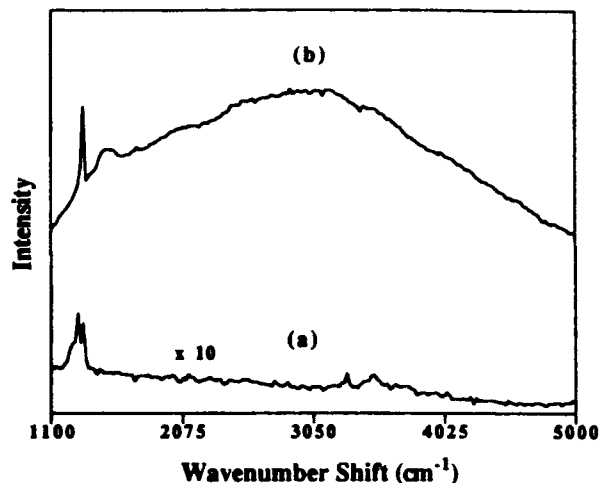


FIG. 9. The broad PL spectra of (a) the isolated nuclei at 3 h and (b) of the continuous film at 40 h of growth time.

etching and redeposition of Si atoms was the predominant reaction due to the high concentration of electrons and hydrogen radicals.

### C. The broadband PL at 565–800 nm

An analysis of the broadband photoluminescence as a function of growth time is now presented. Figure 9 shows the broadband PL spectra for the isolated diamond nuclei at 3 h of growth time and for the continuous film at 40 h. The spectra of the continuous film exhibits a strong PL band ranging from approximately 1000 to 6000  $\text{cm}^{-1}$  (565–800 nm), and centered at around 2 eV ( $\sim 3000 \text{ cm}^{-1}$ ). The broadband PL is not present in the spectra of the isolated diamond nuclei.

The graph of the relative integrated intensity of the PL band versus growth time is shown in Fig. 10. The PL band was not observed in the spectra of the initial stages of growth, and was noticeable only from 7 to 40 h during

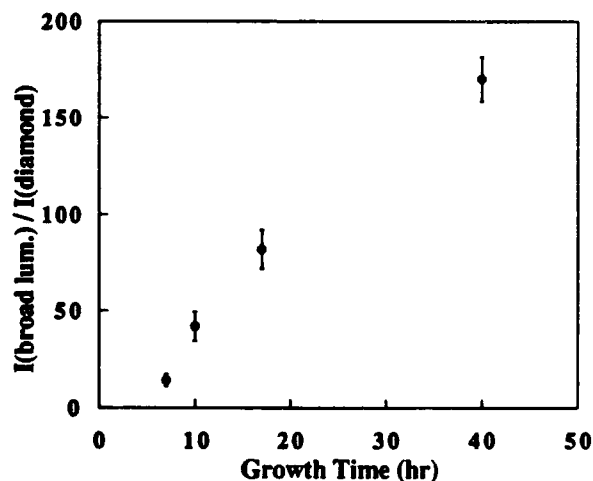


FIG. 10. The relative integrated intensity of the broadband PL vs deposition time. The broadband is not present in the spectra at the early stages of growth.

which interval it behaved linearly with growth time. The time evolution of the broadband PL is similar to that of the  $sp^2$ -type bonding (see Fig. 4). The similarity in the formation of the two types of defects may be an indication that the presence of defects which caused the broad PL is due to the  $sp^2$  carbon bonding which exists in disordered configuration in the diamond film.

Broadband PL spectra very similar to those found in our work have been observed in many studies of amorphous hydrogenated carbon material (*a*-C:H) which possess a random network of  $sp^2$  and  $sp^3$  bonding configuration.<sup>18,19</sup> The lineshape and the peak position of the PL was found in these studies to vary from sample to sample depending on the growth condition. The broad PL in *a*-C:H has been assumed to originate from transitions in the exponential distribution of tail states which extend into the forbidden gap. The presence of tail states is a consequence of the lost long-range order in the material.

Other studies using cathodoluminescence (CL) spectroscopy suggest that the broad luminescence in diamond is due to interaction of the 2.16 eV ZPL center with the lattice vibration (vibronic interaction).<sup>10,12-14</sup> The 2.16 eV band which arises from the interstitial nitrogen-vacancy complex was observed in our spectra and had a very weak intensity. The nitrogen in the diamond film was probably deposited from the residual amount of this element which existed in the environment of the growth chamber.

The fact that both PL and CL extend over the same range of luminescence and have similar lineshape does not exclude the possibility that CL is due to a different type of defect center than that of PL, since the two spectroscopies differ in their energy range and in their cross section. The determination of the origin of the broad luminescence will be addressed in a future study.

From the present data it can be concluded that the type of defect responsible for the broadband PL in the CVD diamond does not form at early stages when isolated nuclei constitute the morphology. The defects instead start to form at approximately 7 h of growth time and have increasing concentration thereafter. A possible type of defect which may cause this broad PL is the amorphous  $sp^2$ -type bonding which has time evolution consistent with the PL luminescence intensity.

#### IV. CONCLUSIONS

The following conclusions about the formation of defects in CVD diamond films are suggested by the study:

(1) The diamond linewidth exhibits an optimum when the particles are large and disconnected. As the film became continuous, a broadening of the line was observed, and was attributed to the strain induced by the grain boundary and to the  $sp^2$  phase, both of which appear at later stages of the growth.

(2) The Raman spectra revealed that the isolated nuclei did not contain  $sp^2$ -type defects. At later stages when clustering occurred and grain boundaries formed, the  $sp^2$  phase was found to increase with growth time. The increase of the  $sp^2$  defect concentration may be attributed to

the presence of the grain boundaries which provide sites for the  $sp^2$ -type bonding.

(3) From any analysis of the integrated diamond Raman lines as a function of time, a characteristic time was obtained for which a morphological transition of isolated nuclei to clusters took place. The characteristic time marked also the time when the  $sp^2$  phase started to appear. It is surmised that these two events were responsible for the decreased growth rate of the diamond.

(4) The 1.68 eV defects are found to be created mostly at early stages of diamond nucleation and growth when most of the substrate is exposed to the plasma. Hence higher concentrations of this type of defect reside in the vicinity of the Si substrate and less in the bulk of the diamond film. In our experiment, no variation in concentration of the 1.68 eV defect was found across the sample.

(5) The plasma interaction with the Si substrate is essential to the formation of the 1.68 eV defect in the CVD diamond. Since the creation of the optical center is greatly enhanced by the availability of Si, most likely the center contains Si atoms. This conclusion is supported by our observations that the relative integrated intensity of the 1.68 eV band of the samples, which were grown in various distances from the plasma, exhibited a decrease with distance from the plasma, combined with the finding that the creation of the defects took place at early stages when most of the Si substrate was exposed to the plasma.

(6) The broad PL band which centers at  $\sim 2$  eV was not observed in the spectra of the early stages of nucleation and growth, but was present in the spectra of the later stages. The broad PL and the  $sp^2$  intensities both follow similar time evolution. Amorphous carbon hydrogenated material, which contains the same bond configuration as the  $sp^2$  phase in the diamond film,<sup>18,19</sup> exhibits broad photoluminescence spectra similar to that observed in our spectra. These two observations lead us to suggest that the  $sp^2$  bonding configuration may give rise to the broadband luminescence. This topic will be investigated in a future study.

In summary, the isolated diamond nuclei contain only the 1.68 eV optical defect. The diamond bulk film contains the  $sp^2$ -type defects and the defects which give rise to the broad PL.

#### ACKNOWLEDGMENTS

We gratefully acknowledge the support of the Office of naval Research through grants N00014-90-J-1604 and N00014-92-J-1477.

<sup>1</sup>C. D. Clark and J. Walker, Proc. Roy. Soc. London A 234 (1973).

<sup>2</sup>C. D. Clark and E. W. J. Mitchell, in *Proceedings of the 1970 Conference on Radiation Damage in Semiconductors*, edited by J. W. Corbett and G. D. Watkins (Gordon and Breach, London, 1971), p. 257.

<sup>3</sup>A. M. Stoneham, *Theory of Defects in Solids* (Clarendon, Oxford, 1975).

<sup>4</sup>J. Walker, Rep. Prog. Phys. 42, 1605 (1979).

<sup>5</sup>G. Davis, in *Chemistry and Physics of Carbon* 13, 2 (1977).

<sup>6</sup>C. D. Clark and C. A. Norris, J. Physics C: Solid State Phys. 4, 2223 (1971).

<sup>7</sup>A. R. Badzian, T. Badzian, R. Roy, R. Messier, and K. E. Spear, Mater. Res. Bull. 23, 531 (1988).

- <sup>8</sup>J. Ruan, W. J. Choyke, and W. D. Partlow, *Appl. Phys. Lett.* **58**, 295 (1991).
- <sup>9</sup>V. S. Vavilov, A. A. Gippius, A. M. Zaitsev, B. V. Deryagin, B. V. Spitsya, and A. E. Aleksenko, *Sov. Phys. Semicond.* **14**, 1078 (1980).
- <sup>10</sup>G. Davies, *J. Phys. C: Solid State Phys.* **12**, 2551 (1979).
- <sup>11</sup>R. J. Graham and K. V. Ravi, *Appl. Phys. Lett.* **60**, 1310 (1992).
- <sup>12</sup>A. T. Collins and S. H. Robertson, *J. Mater. Sci. Lett.* **4**, 681 (1985).
- <sup>13</sup>L. H. Robins, L. P. Cook, E. N. Farabaugh, and A. Feldman, *Phys. Rev. B* **39**, 39 (1989).
- <sup>14</sup>A. M. Zitev, A. A. Gippius, and V. S. Vavilov, *Sov. Phys. Semicond.* **16**, 252 (1982).
- <sup>15</sup>E. S. Eitz, E. N. Farabaugh, A. Feldman, and L. H. Robins, *SPIE* **969**, 86 (1988).
- <sup>16</sup>J. A. Freitas, Jr., J. E. Butler, and U. Strom, *J. Mater. Res.* **5**, 2502 (1990).
- <sup>17</sup>D. S. Knight and W. B. White, *SPIE* **1055**, 144 (1989).
- <sup>18</sup>S. Lin and B. J. Feldman, *Phys. Rev. Lett.* **48**, 829 (1982).
- <sup>19</sup>J. Wagner and P. Lautenschlager, *J. Appl. Phys.* **59**, 2044 (1986).
- <sup>20</sup>B. R. Stoner, J. T. Glass, L. Bergman, R. J. Nemanich, L. D. Zoltan, and J. W. Vandersande, *J. Electron. Mater.* **21**, 629 (1992).
- <sup>21</sup>B. R. Stoner, G.-H. M. Ma, S. D. Wolter, and J. T. Glass, *Phys. Rev. B* **45**, 11067 (1992).
- <sup>22</sup>R. J. Nemanich, J. T. Glass, G. Lucovsky, and R. E. Shroder, *J. Vac. Sci. Technol. A* **6**, 1783 (1988).
- <sup>23</sup>R. J. Nemanich and S. J. Solin, *Phys. Rev. B* **20**, 392 (1979).
- <sup>24</sup>L. H. Robins, E. N. Farabaugh, and A. Feldman, *J. Mater. Res.* **5**, 2456 (1990).
- <sup>25</sup>L. H. Robins, E. N. Farabaugh, and A. Feldman, *SPIE* **1325**, 131 (1990).
- <sup>26</sup>D. S. Knight and W. B. White, *J. Mater. Res.* **4**, 385 (1989).
- <sup>27</sup>Y. M. LeGrice, R. J. Nemanich, J. T. Glass, Y. H. Lee, R. A. Rudder, and R. J. Markunas, *Mater. Res. Soc. Symp. Proc.* **162**, 219 (1990).
- <sup>28</sup>A. R. Badzian and R. C. DeVries, *Mater. Res. Bull.* **23**, 385 (1988).
- <sup>29</sup>K. Kobashi, K. Nishimura, Y. Kawate, and T. Horiuchi, *Phys. Rev. B* **38**, 4067 (1988).
- <sup>30</sup>Y. Sato and M. Kamo, *Surf. Coatings Technol.* **39/40**, 183 (1989).
- <sup>31</sup>A. V. Hetherington, C. J. H. Wort, and P. Southworth, *J. Mater. Res.* **5**, 1591 (1990).
- <sup>32</sup>Y. Saito, S. Matsuda, and S. Nogita, *J. Mater. Sci. Lett.* **5**, 565 (1986).

## X. Effects of Hydrogen and Argon Plasma Exposure on the Diamond (111) Surface

### A. Introduction

Diamond has excellent properties to be used as a high speed, high temperature semiconductor. With the advent of low temperature low pressure growth of diamond it has the possibility to become an economically viable semiconductor. In the current semiconductor technologies surface preparation is an important aspect of device fabrication and it will certainly become an issue in the fabrication of diamond devices. Currently there are many different *ex situ* cleaning methods in use. These are generally a combination of polishing the diamond, followed by a solvent rinse or an acid etch. Diamond (111) surfaces that have been polished and chemically cleaned are typically hydrogen terminated [1-3] and have been shown to exhibit a negative electron affinity [1,2]. The hydrogen can be desorbed from the surface by heating the diamond *in situ* to a temperature above 950°C. After the hydrogen has been removed the negative electron affinity effect is removed. It has been shown that the negative electron affinity effect only reappears upon exposure to mono-atomic hydrogen, whereas exposure to molecular hydrogen has no effect on the negative electron affinity [1]. This confirms the relation between chemisorbed hydrogen and the negative electron affinity on the diamond (111) surface. In this paper we confirm the above described experimental result, and use it to show that a low temperature method, based on a RF induced argon plasma, can also be used to remove hydrogen from the diamond (111) surface.

Angle resolved ultra-violet photoemission spectroscopy was used to analyze the surface. The presence of a negative electron affinity can be easily verified by the presence of a sharp peak at the low energy end of the spectrum. This peak is due to emission of secondary electrons that are quasi-thermalized to the edge of the conduction band [4].

### B. Experimental Procedure

The diamond substrates used in this study were a  $3 \times 3 \times 0.5 \text{ mm}^3$  IIB (p-type) natural diamond with a (111) surface orientation and a  $1.6 \Omega \text{ cm}$  resistivity. The substrates were polished with  $0.1 \mu\text{m}$  diamond grit and cleaned in a chromic acid solution before loading. The diamond was sutured on to a 2.5mm thick molybdenum disk with tantalum wire. In the first set of experiments the diamond was heated radiatively from the back of the molybdenum disk. Using a thermocouple the temperature was measured at the back of the disk. In order to completely desorb hydrogen the disk had to be heated twice to 1100°C for about 10 minutes. Using an optical pyrometer it was found that this corresponds to temperature of about 950°C on the front side of the disk. The diamond was then exposed to  $10^{-6}$  Torr molecular hydrogen for 5 minutes. Which was followed by 3 min in  $10^{-6}$  Torr molecular hydrogen with a hot (1600°C) filament present. This was done to create mono-atomic hydrogen. The amount of dissociated

hydrogen actually present, however, was not determined. In the final step the hydrogen was desorbed again by a 950°C anneal. After every step in the process the sample was examined with ultra-violet photoemission spectroscopy.

In a second set of experiments the diamond was exposed to a remote, RF induced, hydrogen plasma, followed by an argon plasma and a hydrogen plasma. While exposed to either plasma the sample was heated in a similar fashion as described above to about 350°C. The gas flow was kept at 10 sccm while the pressure was held at 14 mTorr. The power to the plasma was 20W. The samples were exposed for a duration of 10 minutes. A more extensive description of the plasma chamber can be found in the literature [5]. After exposure to the plasma the sample was transferred under UHV conditions to the angle resolved photoemission chamber for analysis.

The photoemission was excited with 21.21 eV He(I) radiation, and the data presented here was obtained with a 50 mm hemispherical analyzer with an angular resolution of 2° and an energy resolution of 0.2 eV. When necessary a small bias voltage, less than 1V, was applied to the sample during the measurements to overcome the work function of the analyzer. This was done to include the low energy electrons, which show the negative electron affinity effect, in the spectrum. The presence of a negative electron affinity can be clearly seen by a sharp peak in the low energy end of the spectrum

### C. Results and Discussion

In our experiment we started by verifying the experiment of Pate [1] in which the relation between the negative electron affinity effect and the presence of hydrogen on the surface is established. Photoemission spectra from the diamond before and after thermal desorption of the hydrogen are shown in Figure 1. The negative electron affinity of the surface, which results in the sharp peak at the low energy end of the spectrum, has clearly been removed from the surface. Since the annealing temperature used to obtain the effect is the same as the reported temperature for the desorption of hydrogen, this suggest that hydrogen on the surface plays a role in the negative electron affinity effect. The spectra of the diamond before and after annealing, are followed by spectra from the diamond after exposure to molecular and mono-atomic hydrogen. As is shown in Figure 1, the molecular hydrogen has no effect on the electron affinity of the surface. The mono-atomic hydrogen, however, returned the surface to a negative electron affinity state. The fact that exposure to mono-atomic hydrogen causes the surface to exhibit a negative electron affinity confirms that the hydrogen is associated with the negative electron affinity. The difference between the results after exposure to molecular and mono-atomic hydrogen suggest that the hydrogen has to be chemically bonded to the surface. The series is concluded by a spectrum of the diamond after another high temperature anneal, which shows that the cycle is repeatable.

## The Effect of Hydrogen on Diamond (111)

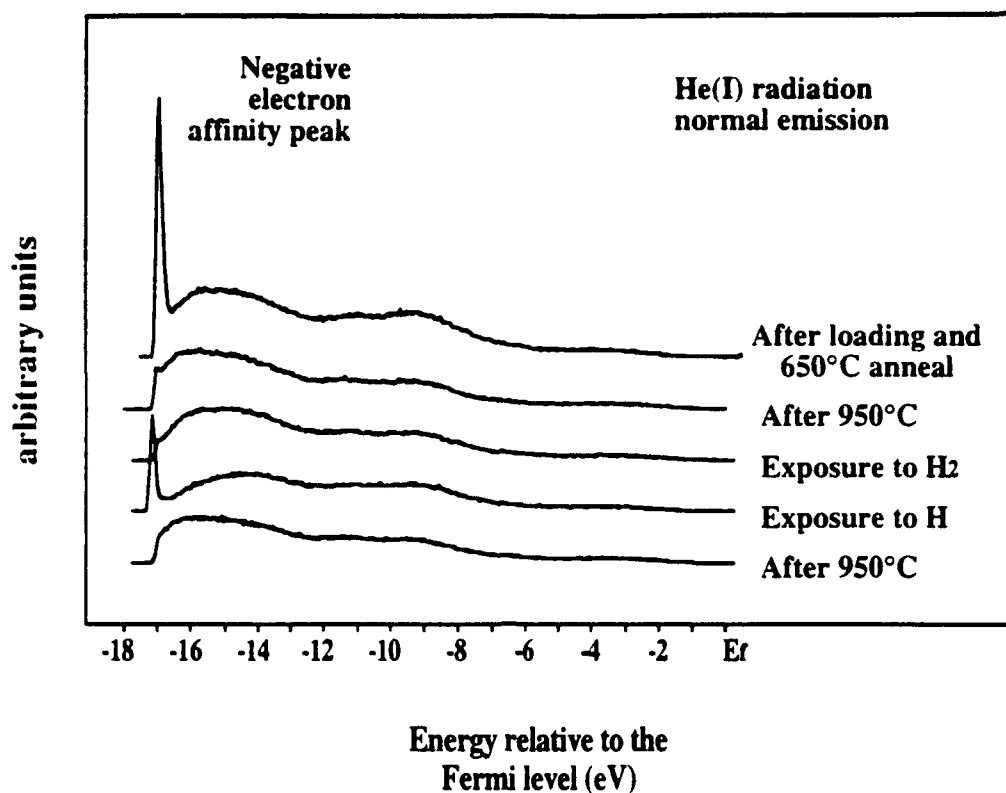


Figure 1. Photoemission spectra of diamond (111). The as loaded spectrum (top) shows the presence of a negative electron affinity, causing the sharp peak (A). After a 950°C anneal the peak is gone, indicating the absence of a negative electron affinity. No significant changes occur after exposure to 5 Langmuir molecular hydrogen. After exposure to mono-atomic hydrogen however the negative electron affinity returns. The bottom spectrum, after another 950°C anneal, shows that the cycle can be repeated.

In a second series of experiments the diamond (111) was exposed to a hydrogen plasma after loading. The resulting spectrum in Figure 2 reveals the presence of a negative electron affinity. After a subsequent exposure to an argon plasma, however, the sharp peak that is associated with a negative electron affinity, was absent. Since the negative electron affinity is associated with the presence of hydrogen on the surface we conclude that the argon plasma removed the hydrogen from the surface. Exposure to another hydrogen plasma causes the negative electron affinity effect to reappear. This is to be expected in light of the first experiment where exposure to mono-atomic hydrogen also caused the negative electron affinity to reappear.

### D. Conclusions

We have repeated and confirmed the experiment done by Pate et al. that showed that the observed negative electron affinity of the diamond (111) surface is related to hydrogen chemisorbed to the surface. It has been established that hydrogen plasma exposure is efficient

## Diamond (111) after Argon and Hydrogen plasma

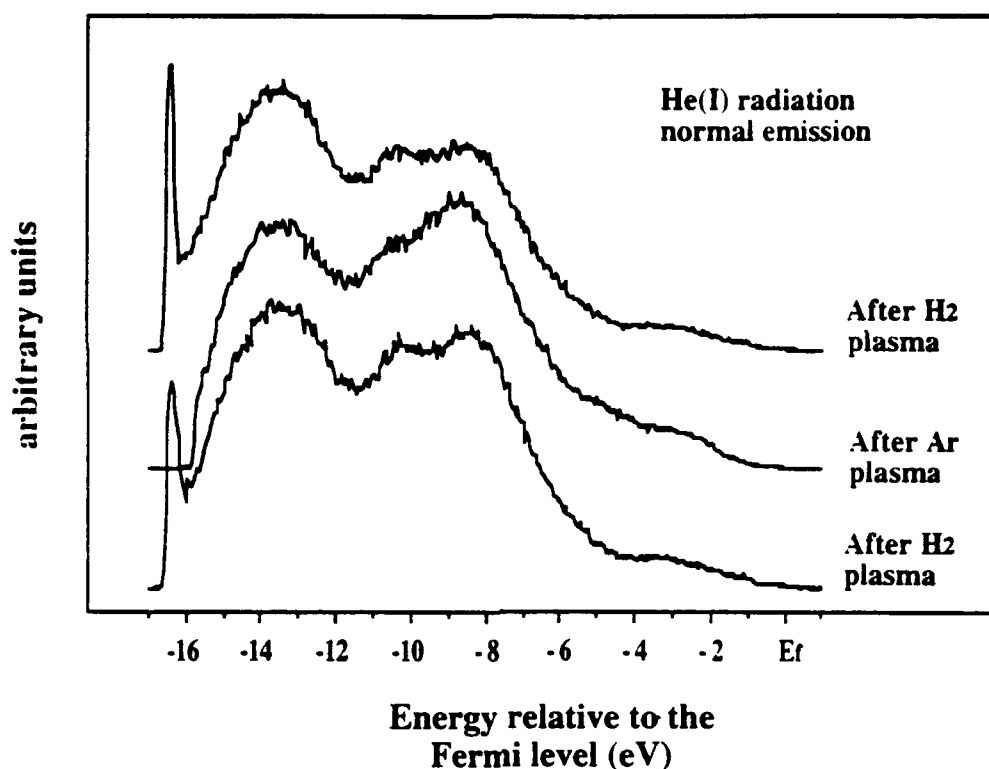


Figure 2. Photoemission spectra of diamond (111) after exposure to: from bottom to top, an hydrogen plasma, an argon plasma and a hydrogen plasma. The diamond was heated to approximately 350°C during each exposure. The spectrum after the first hydrogen plasma shows a sharp peak, due to the negative electron affinity of the surface. In the second spectrum, after argon plasma exposure, the peak is absent, indicating a positive or zero electron affinity. Since the negative electron affinity is linked to the presence of hydrogen, this suggests that hydrogen can be removed from the diamond (111) surface by an argon plasma. In the third spectrum the negative electron affinity is seen to reappear, after exposure to another hydrogen plasma.

at producing an H-termination of the (111) surface resulting in a negative electron affinity. The temperature needed to desorb the hydrogen, is of the order of 950°C. We have used the relation between the negative electron affinity and the presence of hydrogen on the surface to show that an RF induced argon plasma can be used to induce a surface which does not exhibit a negative electron affinity, and it is proposed that the process results in the removal of the hydrogen from the diamond surface. In this process the diamond was heated to ~350°C, which is considerably lower than the temperature needed for thermal desorption.

### E. Future Research Plans and Goals

The main focus of our research is to explore Schottky barrier formation for metals on diamond. We have completed the initial stages of work on the titanium-diamond (111) interface [6,7], and are about to finish the titanium-diamond (100) interface. One of the interesting

results from the experiments on the titanium-diamond(111) interface was the fact that a thin layer of titanium can lower the work function of the diamond (111) surface sufficiently to create a negative electron affinity surface. A model, linking the work function of titanium and the Schottky barrier height of the titanium-diamond(111) interface, was proposed to explain this result [7]. A similar effect was observed on the diamond (100) surface, which is something that we plan to investigate further.

In the beginning of this year we brought a new transfer system on-line, which allows us to transfer under UHV conditions to a number of chambers, notably our MBE system. The MBE is currently loaded with nickel and hafnium which are the next metals that will be investigated. We intend to determine the Schottky barrier height of these metals with the diamond (111) and (100) surfaces. We will also be looking at negative electron affinity effects of these metals on the diamond surfaces in order to expand our model to other metals.

On the subject of cleaning and surface preparation of diamond, we intent to finalize for publication the results described above. We are currently initiating a collaboration with a theory group in the physics department. Our aim is to do cluster calculations on the charge distribution of a hydrogen terminated diamond (111) surface to determine the sign and magnitude of the surface dipole layer. This would indicate how the presence of chemisorbed hydrogen can lower the work function of the surface.

*Acknowledgments.* We thank K. Das of Kobe Research for his help in establishing the diamond cleaning procedure, T. P. Schneider for the plasma cleaning work and T. P. Humphreys for helpful discussions. This work is supported in part by the ONR through grant N00014-90-J-1707 and the NSF through grant DMR 8717816.

#### F. References

1. B. B. Pate, M. H. Hecht, C. Binns, I. Lindau, W. E. Spicer, *J. Vac. Sci. Technol.*, **21**:364, (1982).
2. F. J. Himpsel, J. A. Knapp, J. A. VanVechten, D. E. Eastman, *Phys. Rev.* **B20**, 624 (1979).
3. A. V. Hamza, G. D. Kubiak, R. H. Stulen, *Surf. Sci. Lett.* **206**, L833 (1988).
4. C. Piaget, J. Vannimenus, P. Saget, *J. Appl. Phys.* **48**, 3901 (1977).
5. Jeawon Cho, T. P. Schneider, J. van der Weide, Hyeontag Jeon, R. J. Nemanich, *Appl. Phys Lett*, **59**, 1995 (1991).
6. J. van der Weide, R. J. Nemanich, *Proceedings of the First International Conference on the Applications of Diamond Films and Related Materials*, edited by Y. Tzeng, M. Yoshikawa, M. Murakawa, A. Feldman, (Elsevier, New York, 1991), p. 359.
7. J. van der Weide, R. J. Nemanich, *J. Vac. Sci. Technol.* **B10**(4), (in press) 1992.

## XI. Properties of interfaces of diamond

R.J. Nemanich, L. Bergman, K.F. Turner, J. van der Weide and T.P. Humphreys

*Department of Physics and Department of Materials Science and Engineering, North Carolina State University, Raleigh, NC, USA*

Results related to two different interface aspects involving diamond are described: (1) the initial states of CVD diamond film growth, and (2) the negative electron affinity and formation of metal-diamond interfaces. The surface and interface properties are probed with STM, Raman scattering/photoluminescence and angle-resolved UV photoemission spectroscopy (ARUPS). STM measurements of diamond nuclei on Si after various plasma growth processes show both flat and hillocked structures characteristic of 2-dimensional and 3-dimensional growth modes, respectively. STS measurements show distinct  $I-V$  characteristics of the nuclei and the substrate. The presence of optical defects and the diamond quality are studied with micro-Raman/photoluminescence measurements. The results indicate an increased density of impurity-related defects during the initial stages of growth. The interface properties of Ti on natural crystal (111) and (100) surfaces are studied with ARUPS using 21.2 eV HeI emission. Prior to deposition the diamond (111) is chemically cleaned, and a sharp (0.5 eV FWHM) peak is observed at the position of the conduction band minimum, indicating a negative electron affinity surface. After a subsequent argon plasma clean this peak disappears, while the spectrum shows a shift of 0.5 eV towards higher energies. Upon sub-monolayer titanium deposition on (111) diamond, the negative electron affinity peak reappears. Further titanium depositions causes this titanium-induced negative electron affinity peak to be attenuated, indicating that the emission originates from the interface. A similar experiment, done on the diamond (100) surface, however, does not result in a negative electron affinity. By determining the relative positions of the diamond valence band edge and the titanium Fermi level, the Schottky barrier height of titanium on diamond is measured. A model, based on the Schottky barrier height of titanium on diamond, and the work function of titanium, is proposed for the observed titanium-induced negative electron affinity.

### 1. Introduction

Continuing advances in the CVD growth of doped diamond thin films offer the possibility of diamond semiconductor devices [1]. Because large diamond substrates are, at this time, prohibitively expensive, most potential electronic applications have focused on heteroepitaxial structures. The nucleation of diamond on non-diamond substrates has, however, proved difficult. Because of the potential for electronic applications, much effort has been focused on the nucleation and growth of diamond on Si. While small regions of heteroepitaxial growth have recently been reported on SiC and BN substrates

[2,3] only polycrystalline growth has been achieved on Si and other commonly used substrates. In fact, without special processing of the substrate, the initial nucleation rate is so low, that no diamond growth is achieved within an exposure to the growth conditions for over 60 min. In this study, the initial growth nucleation and growth modes of diamond on Si are studied by STM and Raman photoluminescence measurements.

To achieve diamond devices, metal contacts and Schottky barriers will be critical. One of the most important advances with regards to device applications is the growth of p-type diamond with boron incorporation. This is achieved either by implantation or by incorporation during the growth. Device structures have been demonstrated with the p-type material, and it is apparent that understanding contacts and Schottky

*Correspondence to:* R.J. Nemanich, Department of Physics and Department of Materials Science and Engineering, North Carolina State University, Raleigh, NC 27695-8202, USA.

barrier properties will be critical. Because of the large band gap, diamond has the potential of high temperature operation, thus it is critical to obtain contacts and Schottky barrier structures that are both chemically and electrically stable at high-temperature operation.

A particularly interesting property of diamond is that under some surface preparation conditions, a negative electron affinity can be achieved. The term negative electron affinity means that the conduction band of the semiconductor at or near the surface is above the vacuum level (i.e. the zero kinetic energy of an electron in free space). In this condition electrons in the conduction band will not be bound in the sample and electron emission can occur. In this study we demonstrate that the electron affinity is dependent on the sample surface preparation. Both surface termination and overlayer coverage can substantially affect the electron affinity.

## 2. Experimental

The diamond films were prepared by microwave plasma CVD on 1 inch diameter n-type Si(111) or Si(100) substrates. The substrates were polished with 0.25  $\mu\text{m}$  diamond powder, followed by an ultrasonic clean in TCE, acetone, methanol, a rinse with de-ionized water and then a drying with nitrogen. A 30 minute hydrogen plasma etch was performed before growth. The growth occurred at a pressure of 25 Torr, a methane to hydrogen ration of 1% with a total flow rate of 1000 sccm and a substrate temperature of  $\sim 750^\circ\text{C}$ . No intentional dopant was used in the growth process. SEM micrographs were obtained of the surfaces to show the surface topography on a large scale and to provide an estimate of the nucleation density and the evolution of growth on the surface. Raman spectroscopy and photoluminescence analysis were also performed. The subsequent growth was observed by stopping the growth process after 1.5, 3, 5, 7, 10, 17 and 40 hours of deposition.

The STM analysis of the diamond was done over a wide range of parameters. All of the

analysis was performed using an Park Scientific Instruments SU-200 scanning tunneling microscope operated in the ambient atmosphere. The surfaces were scanned over several scan ranges (20  $\text{\AA}$ –5  $\mu\text{m}$ ), tunneling currents (0.5 nA–4.0 nA) and at both positive- and negative-bias voltages. With the STM used, a positive-bias voltage corresponds to a voltage applied to the tip that is positive relative to the sample.

Current-voltage measurements were also performed using the STM, in a process that is called tunneling spectroscopy. In these measurements, the bias voltage is ramped from positive to negative voltages, and the current monitored. All current-voltage measurements presented are averaged over many voltage cycles and were representative of the  $I$ - $V$  characteristics of the entire surface. Measurements also allowed for measurement of the surface density of states, which is proportional to the ratio of the differential conductance to the conductance.

The photoemission data presented in this paper, were obtained from natural single crystal diamond. The diamond substrates used in this study were  $3 \times 3 \times 0.5 \text{ mm}^3$ , type IIb wafers, with a (111) or a (100) surface orientation. These wafers are p-type semiconducting, with typical resistivities ranging from 1.3  $\text{k}\Omega \text{ cm}$  to 16  $\text{k}\Omega \text{ cm}$ . The substrates were polished with 0.25  $\mu\text{m}$  diamond grit and cleaned in a boiling chromic acid solution before loading. Once in a vacuum the diamond (111) was further cleaned in a plasma cleaning chamber by exposing it to a remote, RF induced, argon plasma. During the exposure the diamond was heated to  $350^\circ\text{C}$ . The diamond (100) was cleaned by heating it in UHV to about  $600^\circ\text{C}$  for 10 min. Titanium was evaporated by resistively heating a titanium filament, and spectra were taken at increasing thicknesses. The thickness of the deposited films was monitored with a crystal rate monitor. The plasma cleaning chamber is connected to the ARUPS chamber through an UHV transfer system. The photoemission was excited with 21.21 eV HeI radiation, and the data presented here was obtained with an angle-resolved ultraviolet photoemission spectroscopy (ARUPS) system, which included a 50 mm radius hemi-

spherical analyzer with an angular resolution of  $2^\circ$ . A bias voltage of  $\sim 1$  V or less, was applied to the sample during the measurements to overcome the work function of the analyzer. The bias voltage allowed the collection of the low energy electrons, which show the negative-electron-affinity effect.

### 3. Results and discussion

#### 3.1. Nucleation and initial growth

The results of the investigation of the initial stages of diamond growth can be broken down into different properties: changes in the surface which occur during growth, observation and analysis of the nuclei formed during growth, and the electronic properties of the nuclei and the substrate surface. STM analysis of diamond and diamond-like materials has been described in several recent studies. Previous works using STM by the authors have examined topography of CVD-doped diamond films and undoped nuclei, changes in the growth surface and nuclei during growth, and examination of Ni contacts to

single-crystal diamond [4-6]. Tsuno et al. have examined homoepitaxial CVD diamond films grown on the diamond (001) surface and observed surface reconstructions [7]. Everson and Tamor have investigated the structure of doped nuclei grown on silicon [8]. The only group to report successful STM examination of thick undoped diamond films has come from Busmann et al. [9]. Several other groups have examined amorphous diamond and diamond-like carbon [10-14]. Discussions of the theory and practice of imaging diamond can be found in these references.

The changes in the surface which occur during growth can be examined before the first observation of nucleation. Figure 1 shows the surface structure of one of the samples as viewed by STM. Comparisons of the 30 minute and the 60 minute growth samples showed that the surface of the 60 minute sample appeared to be rougher than the 30 minute sample. Neither sample showed diamond nucleation. The surface, however, showed an increased roughness for the longer growth. This indicates the formation of a surface layer, presumably SiC or disordered carbon.

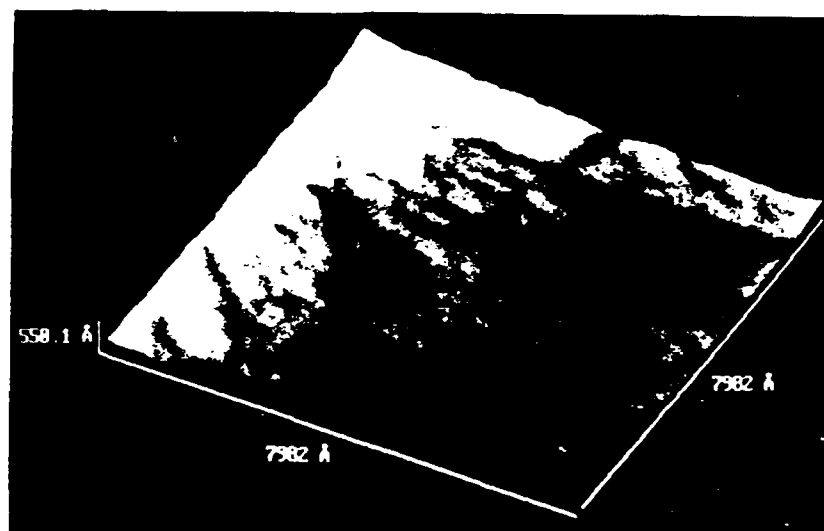


Fig. 1. STM micrograph of the scratched Si surface after a 60 minute exposure to plasma growth conditions. Scratches can be seen on the substrate which have been used to increase the nucleation density. The roughness of this sample provides evidence of plasma-induced surface modification preceding diamond nucleation.

During the initial phase of the growth process examined here, a majority of nuclei exhibit a 3-dimensional structure. A minority of the nuclei do exhibit a more 2-dimensional structure, which indicates a 2-dimensional growth mode. Figure 2

shows both flat and hillock structures characteristic of 2-dimensional and 3-dimensional growth modes, respectively. The top of the flat nucleus shown is smooth to within  $\sim 20 \text{ \AA}$  and has a 'height' to 'width' ratio of 1:4. The surface

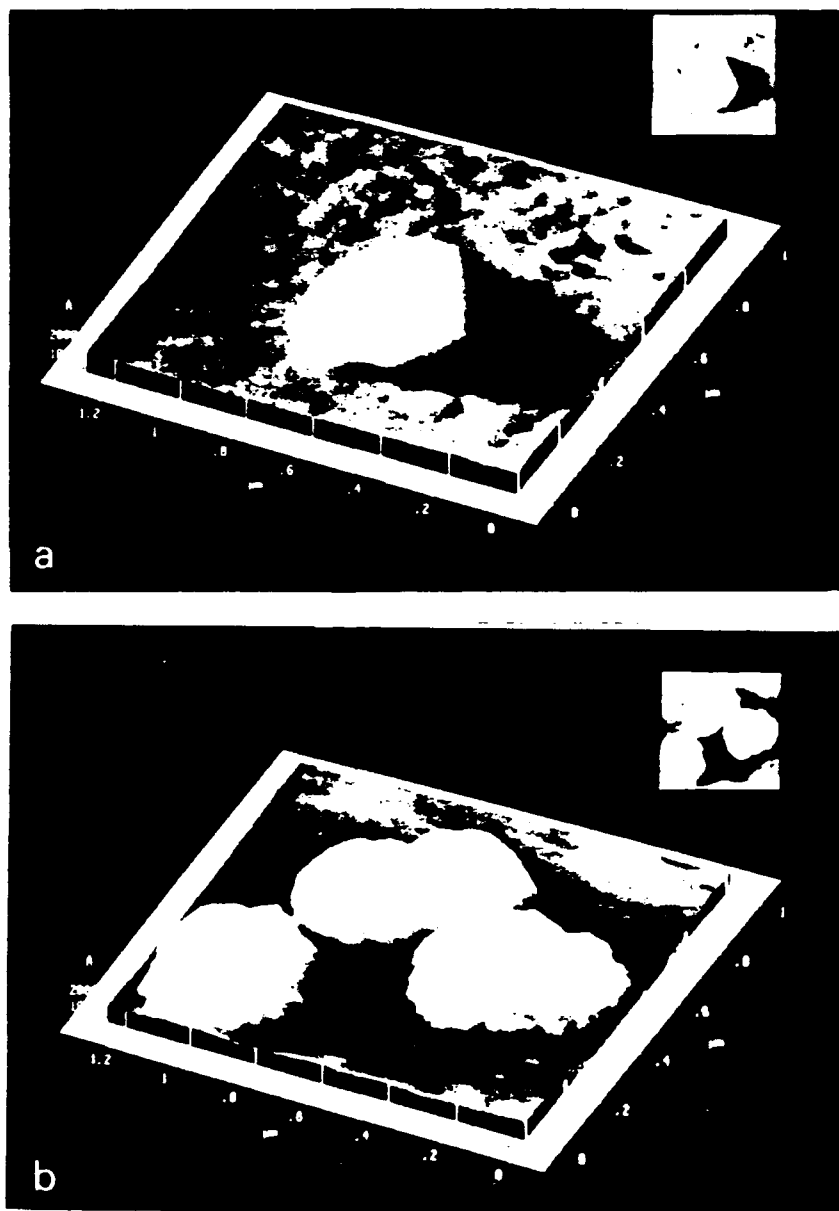


Fig. 2. STM images of diamond nuclei on Si. The upper STM micrograph shows a nucleus of diamond grown on silicon that is exhibiting a flat surface nearly parallel to the substrate. The lower micrograph shows several nuclei that are growing 3-dimensionally. Both types of nuclei were found on the same silicon substrate after 1 hour of deposition.

of the nucleus is parallel to the substrate and indicates that the interactions with the substrate contribute to the growth and morphology. This is an important aspect because it is likely that the initial diamond has formed in the scratched regions. We would suggest that it is possible that the initial diamond formation in the scratches is highly disordered, thus allowing the substrate interactions to contribute to determination of the growth morphology. The second image shows several nuclei, one of which appears to be twinned, which have 'height' to 'width' ratios of  $\sim 1:2$ . The fact that both types of nuclei were observed after the same exposure to growth, supports the fact that two distinct modes exist and that the 2-D mode is not merely an early manifestation of a 3-D growth mode. Evidence of this 2-dimensional mode is interesting because it may be an indication that conformal growth is possible and if it could be enhanced, creating planer diamond films with fewer polycrystalline domains might be possible.

Tunneling spectroscopy measurements show distinct  $I$ - $V$  characteristics of the nuclei and the substrate. Examples of  $I$ - $V$  curves obtained from different points are shown in fig. 3. The ability to distinguish between the types of materials on the surface is an important one. The curve obtained by tunneling to the diamond nucleus is smoothly varying and shows little response at positive bias

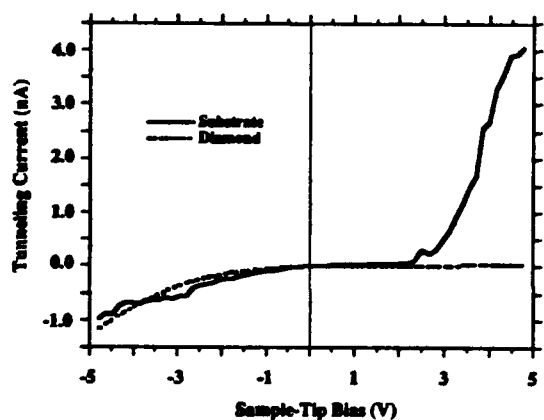


Fig. 3. A comparison of the scanning tunneling spectroscopy current-voltage characteristics of a diamond nucleus and areas of the substrate near the nucleus.

voltages. The substrate  $I$ - $V$  curve shows much more structure including a large change in the current starting at +2.5 V. The 'peaks' in the  $I$ - $V$  curve taken over the substrate are indicative of the electronic structure of the carbonic layer that has formed on the substrate during growth. These 'peaks' may be a result of absorbates, bonded to the silicon, which are weakly connected to bulk states.

The ability to carry out tunneling experiments from undoped diamond regions is in itself unique since diamond has such a high electrical resistivity. To probe the defect and impurity properties of the initial stages of growth, micro-photoluminescence measurements were carried out as a function of growth time. In this experiment, the same sample was measured after various growth times. A relatively strong feature was observed in the micro-photoluminescence at an emission energy of 1.68 eV, which is shown in fig. 4. There has been considerable discussion about the origin of this feature. It occurs at an energy near to that of the GR1 peak in single-crystal diamond. This feature has been assigned to a neutral vacancy. Since vacancies are mobile in

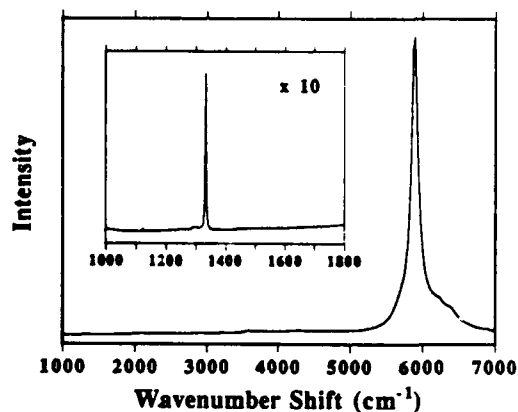


Fig. 4. The Raman/photoluminescence spectrum of CVD diamond after 7 hours of growth. The spectrum was excited with 514.5 nm Ar ion laser light. The spectrum is dominated by the 1.68 eV photoluminescence center for a CVD diamond, and the inset shows an expanded higher-resolution scan over the region of the diamond- $sp^2$  Raman peaks. At this growth time, the emission from the 1.68 eV PL center showed a maximum relative to the intensity of the diamond Raman.

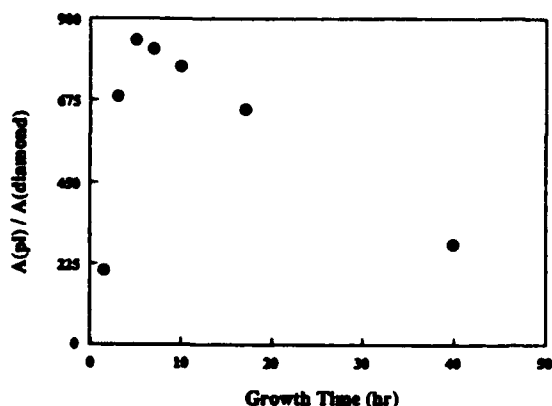


Fig. 5. The integrated intensity of the 1.68 eV PL center relative to the diamond Raman peak as a function of deposition time. A maximum is observed after  $\sim 7$  hours of growth.

diamond at temperatures  $\sim 800^\circ\text{C}$ , it is unlikely that the 1.68 eV feature in the CVD films (growth temperature  $\sim 800^\circ\text{C}$ ) is due to a vacancy. It has also been suggested that the feature is due to a complex involving Si and/or N [15,16].

The results of the experiment are shown in fig. 5. The relative intensity of the 1.68 eV feature to the Raman diamond feature reaches a maximum after  $\sim 7$  h and then is reduced with increased growth time. The absolute intensity of the 1.68 eV feature actually increases at least up to a growth time of 15 h (at this time the substrate is nearly completely covered). Thus we can conclude that there is initially a higher rate of impurity incorporation in the film. From the data, it can also be concluded that a higher concentration of defect centers exists near the interface between the diamond and the silicon, with a lower concentration found in the bulk. It is now well established that Si is etched in the presence of atomic H, with  $\text{SiH}_4$  being released. We suggest that the observed photoluminescence trend is due to the incorporation of Si which has been etched from the substrate. The rate of incorporation decreases when the Si substrate is covered by diamond after subsequent growth.

### 3.2. Schottky barrier height measurement

Diamond-metal interfaces and their prop-

erties as electrical contacts have received recent attention, and both ohmic and rectifying contacts to both natural diamond and CVD-grown diamond have been reported [6,17–21]. To fully understand the rectifying contact it is necessary to determine the Schottky barrier characteristics. Current-voltage measurements of the rectifying contacts typically show a high ideality factor and cannot be used for an accurate Schottky barrier determination [22]. Photoemission, however, has been successfully used to measure the Schottky barrier height of Al and Au on diamond [23].

Previous current-voltage measurements have demonstrated that titanium, deposited at room temperatures, forms a rectifying contact to p-type diamond. Upon annealing to  $>400^\circ\text{C}$  the current-voltage characteristics become ohmic [21]. It has been suggested that this transformation is due to the formation of a titanium carbide [17]. In a previous study we have shown that titanium carbide formation does indeed occur in the same temperature range in which titanium contacts are found to change from rectifying to ohmic [24]. In this paper we report a UV photoemission study of thin titanium layers deposited on a diamond (111) surface. From the measurements, the Schottky barrier height of titanium on p-type diamond (111) is determined.

The Schottky barrier height of a metal on a p-type semiconductor is defined as the difference between the valence band edge of the semiconductor and the Fermi level of the metal at the interface. The determination of the Schottky barrier height from UV photoemission, relies on the fact that features of both the metal and the underlying semiconductor are visible in one spectrum. Experiments are therefore limited to thin metal films with a thickness on the order of the mean free path of the electrons ( $\sim 5 \text{ \AA}$ ). Even at metal coverages less than the mean free path, it is not always possible to determine the position of the valence band edge accurately from the spectra, since emission from the metal d-band obscures the relatively weak semiconductor valence band emission. In those cases, a more accurate determination can be made, by relating the valence band edge to a feature in the diamond spectra that does remain visible at high-

er metal coverages. In this analysis it is assumed that shifts in the diamond features are uniform so that relative positions are maintained. In the experiments on the (111) surface, the valence band edge was determined from the spectrum of the argon-plasma-cleaned diamond and related to a stronger emission feature at lower energies, labeled B, in fig. 6. Although this diamond feature was attenuated upon metal coverage, it remained much more visible than the valence band edge. In order to determine the valence band edge from the position of peak B, their relative positions should not change upon titanium deposition. Since the relative positions of feature B and the valence band edge did not change after the first metal depositions in which both were visible, we do not expect this to occur at the higher metal thicknesses.

The location of the valence band edge was determined by extrapolating the spectrum to zero, as illustrated in fig. 7. The valence band edge was found to be 8.2 eV above feature B. After the first titanium deposition the diamond spectrum shifted 0.5 eV towards lower energies, indicating a change in the pinning position of the Fermi level in the gap. No Fermi level emission due to the titanium could be discerned, however,

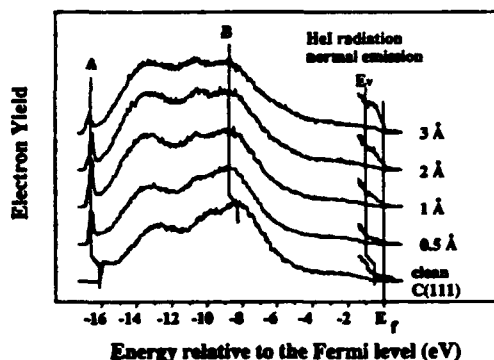


Fig. 6. ARUPS spectra of titanium on diamond (111) for increasing titanium thicknesses. After the first deposition the spectrum shifts 0.5 eV toward lower energies and a sharp peak (A), indicative of a negative electron affinity, develops at the low-energy cutoff. For increasing titanium thicknesses a Fermi level edge ( $E_f$ ) develops, while at the same time the position of the valence band edge ( $E_v$ ) becomes harder to locate. The Schottky barrier height is the energy difference between  $E_v$  and  $E_f$ .

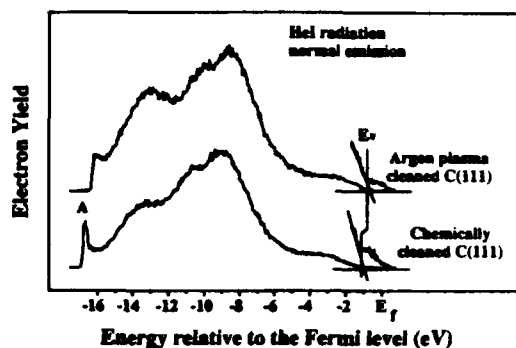


Fig. 7. ARUPS spectra of diamond (111) before and after argon plasma cleaning. The spectrum shifts by 0.5 eV towards higher energies while the negative electron affinity peak (A) is significantly reduced after the argon plasma cleaning. The latter effect is attributed to the removal of hydrogen from the surface. The valence band edge is determined by linearly extrapolating the onset of emission down to zero.

at this coverage. Upon further titanium deposition, emission from the d-bands of titanium became pronounced, and the Fermi level could be clearly discerned. The position of the valence band edge, however, became more difficult to locate. Based on the position of feature B, no further shifts in the diamond spectrum were observed. This indicates that the Fermi level was pinned, and the Schottky barrier height established, after the first titanium deposition. The Fermi level was found to be 9.2 eV above feature B. Since the valence band edge was 8.2 eV above B this results in a Schottky barrier height for titanium on p-type diamond (111) of  $1.0 \pm 0.2$  eV.

Similar measurements were performed for titanium on the diamond (100) surface, as shown in fig. 8. The position of the valence band edge, relative to peak B, was determined again from the clean diamond (100) surface, and was found to be 8.0 eV, in agreement with the value found from the (111) surface. No shifts were observed before cleaning, and no significant shifts occurred upon titanium deposition. The position of the Fermi level was determined, and found to be 9.4 eV above feature B. The Schottky barrier height of titanium on the diamond (100) surface was therefore found to be  $1.5 \pm 0.2$  eV. Reported values for the Schottky barrier

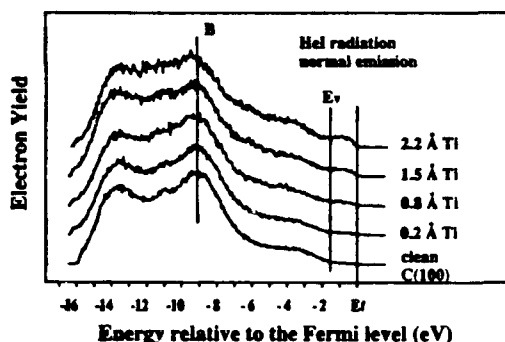


Fig. 8. ARUPS spectra of titanium on diamond (100) for increasing titanium thicknesses. The position of  $E_F$  relative to peak B is determined from the clean surface and is found to be 8.0 eV. The Fermi level is found from the metal-covered diamond (100) and lies 9.4 eV above peak B, resulting in a Schottky barrier height of  $1.5 \pm 0.2$  eV.

height of titanium on CVD-grown diamond films range from  $0.9(+0.5/-0.2)$  eV [24] to 1.3 eV [25].

### 3.3. Negative electron affinity

The relation between the bands of a semiconductor and the vacuum level can be described by the electron affinity. This quantity which is the energy difference between the conduction band minimum and the vacuum level, is an important parameter in the Schottky-Mott model for Schottky barrier heights. The electron affinity is however dependent on the surface structure of the crystal. A dipole layer on the surface will shift the potential of the material with respect to the vacuum, thus changing the electron affinity. The dipole layer can result from surface structures such as reconstruction or molecular adsorption or interface structures such as Schottky barriers or heterojunctions.

Photoemission spectra of negative-electron-affinity surfaces generally show a sharp peak at the low-kinetic-energy end of the spectrum. This peak is attributed to emission of electrons that are quasi-thermalized to the bottom of the conduction band of the semiconductor. For materials with a positive electron affinity, the conduction band minimum is below the vacuum level, and the quasi-thermalized electrons are trapped

in the sample. In the experiments described here, the presence of a sharp peak at the onset of the photoemission will be considered as an indication of a negative-electron-affinity surface.

#### 3.3.1. Hydrogen-terminated surfaces

We initiated the study of the negative electron affinity of diamond by verifying the experiment of Pate et al. [26] in which the relation between the negative electron affinity effect and the presence of hydrogen on the surface is established. The H-terminated surfaces were obtained by polishing and etching a diamond (111) wafer. Followed by a low-temperature anneal (350°C) to desorb contaminants. Photoemission spectra from the diamond before and after thermal desorption of the hydrogen are shown in fig. 9. The negative electron affinity of the surface, which results in the sharp peak at the low-energy end of the spectrum, has clearly been removed from the surface. Since the annealing temperature used to obtain the effect is the same as the reported temperature for the desorption of hydrogen, this suggests that hydrogen on the surface plays a role in the negative electron affinity effect. The spectra of the diamond before and after annealing are followed by spectra from the diamond after exposure to molecular and mono-atomic hydrogen. As is shown in fig. 9, the molecular hydrogen has no effect on the electron affinity of the surface. The mono-atomic hydrogen, however, returned the surface to a negative-electron-affinity state. The fact that exposure to mono-atomic hydrogen causes the surface to exhibit a negative electron affinity confirms that the hydrogen is associated with the negative electron affinity. The difference between the results after exposure to molecular and mono-atomic hydrogen suggest that the hydrogen has to be chemically bonded to the surface. The series is concluded by a spectrum of the diamond after another high temperature anneal, which shows that the cycle is repeatable.

In a second series of experiments, described in fig. 10, the diamond (111) was exposed to a hydrogen plasma after loading, and the spectrum shows the presence of a negative electron affinity. After a subsequent exposure to an argon

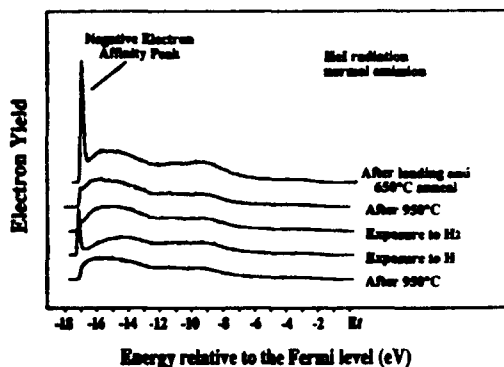


Fig. 9. ARUPS spectra of diamond (111). The as-loaded spectrum (top) shows the presence of a sharp peak at the lowest energy indicating a negative electron affinity. After a 950°C anneal the peak is gone, indicating the absence of a negative electron affinity. No significant changes occur after exposure to molecular hydrogen for 5 minutes at  $10^{-6}$  Torr. After exposure to mono-atomic hydrogen however the negative electron affinity returns. The bottom spectrum, after another 950°C anneal, shows that the cycle can be repeated.

plasma, however, the sharp peak that is associated with a negative electron affinity, was absent. Since the negative electron affinity is associated with the presence of hydrogen on the surface we conclude that the argon plasma re-

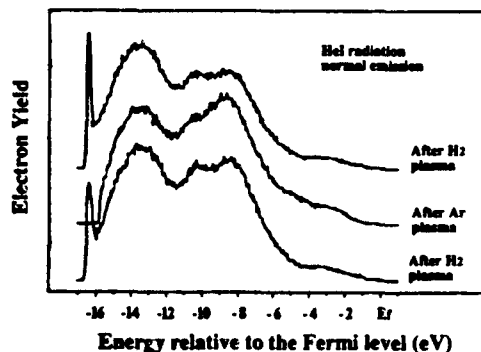


Fig. 10. ARUPS spectra of diamond (111) after exposure to (from bottom to top) a hydrogen plasma, an argon plasma and a hydrogen plasma. The diamond was heated to approximately 350°C during each exposure. The spectrum after the first hydrogen plasma shows a sharp peak, due to the negative electron affinity of the surface. In the second spectrum, after argon plasma exposure, the peak is absent, indicating a positive or zero electron affinity. In the third spectrum the negative electron affinity is seen to reappear, after exposure to another hydrogen plasma.

moved the hydrogen from the surface. Exposure to another hydrogen plasma causes the negative electron affinity effect to reappear. This is to be expected in light of the first experiment where exposure to mono-atomic hydrogen also caused the negative electron affinity to reappear.

### 3.3.2. Metal-induced negative electron affinity

The potential of metals inducing a negative electron affinity were explored. In this case the initial starting surface was a diamond (111) surface treated with a remotely excited Ar plasma to induce a surface with a slightly positive electron affinity. After the first titanium dose, a sharp peak, similar to the one found on the hydrogen-passivated diamond (111) surface, develops at the low-energy end of the spectrum. In the same spectrum a 0.5 eV shift towards lower energies is observed. For increasing titanium coverages the peak is attenuated, and no further shifts in the diamond features are observed. We attribute this peak to a titanium-induced negative electron affinity. This would be due to a lowering of the work function by the titanium, as illustrated in fig. 11. Before the titanium deposi-

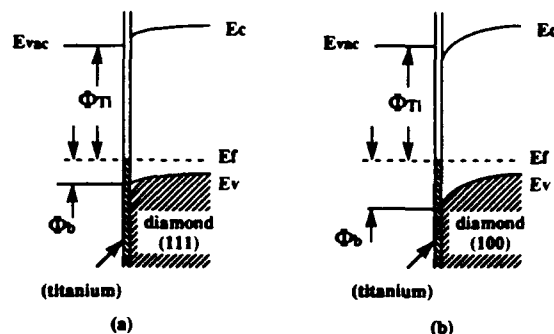


Fig. 11. Model for the titanium-induced negative electron affinity on diamond (111). In (a) the sum of the work function of the titanium ( $\Phi_{Ti}$ ) and the Schottky barrier height of titanium on the diamond (111) surface ( $\Phi_b$ ) is less than the bandgap of the diamond. This lowers the effective work function of the surface such that the conduction band minimum is above the vacuum level, thus resulting in a negative electron affinity. For the diamond (100) surface (b) however the Schottky barrier height with the titanium is larger than the Schottky barrier height on the diamond (111) surface, and the sum of the Schottky barrier height and the work function of titanium is more than the bandgap of the diamond, resulting in a positive electron affinity.

tion the Fermi level at the surface is 0.5 eV above the valence band edge. The vacuum level was determined from the low-energy cutoff point of the emission, and is found to be about 5.5 eV above the valence band edge. Using a value of 5.45 eV for the bandgap of diamond we find therefore the vacuum level to be  $\sim 0.05$  eV above the conduction band edge; electrons that are quasi-thermalized to the bottom of the conduction band are therefore unable to escape the surface. After the first sub-monolayer of titanium is deposited, the Fermi level is pinned at 1.0 eV above the valence band edge, which is the Schottky barrier height described in the previous section. The effective work function of the surface is now determined by the work function of the titanium. Using the value of 4.33 eV for the work function of bulk titanium [27] we find that the vacuum level of the surface is now located 0.2 eV below the conduction band edge and quasi-thermalized electrons can escape, causing the sharp peak in the spectrum. The fact that this peak is due to the interface of the diamond and the titanium, can be deduced from the attenuation of the peak as a function of coverage. Note that in this model the Schottky barrier height plays an important role in determining the position of the vacuum energy level. In fig. 10(b) the titanium-diamond(100) interface is described. Here the Schottky barrier height is 1.5 eV and the vacuum level lies now above the conduction band edge. Based on this model we do not expect a negative-electron-affinity surface. This is supported by the data, as can be seen in fig. 8. No low-energy peak appears upon titanium coverage. It should be noted, that the model presented here, is the reverse from the Schottky-Mott model. There the Schottky barrier height is determined by aligning the vacuum levels of the metal and the semiconductor.

#### 4. Conclusions

The initial stages of diamond growth show both substrate interactions which lead to non-diamond structures and diamond nuclei which

form at scratches on the surface. Even though the initial diamond formation occurs in the scratches, the nuclei growth morphology is related to the substrate. We propose that the initial diamond formation is highly disordered and that as the growth proceeds beyond the scratches, the substrate interactions contribute to the growth morphology. Because of the high resistivity of undoped diamond, tunneling to these structures was not anticipated. Defect structures were observed in the microphotoluminescence measurements. These defects were apparently associated with Si impurities which were due to etching of the exposed substrate.

From the UV photoemission spectroscopy measurements presented here, a Schottky barrier height of  $1.0 \pm 0.2$  eV was found for the titanium-diamond(111) interface, and  $1.5 \pm 0.2$  eV for the titanium-diamond(100) interface. It was found that the Schottky barrier heights were established for sub-monolayer titanium coverages. Upon titanium deposition on the diamond (111) surface, a sharp (0.5 eV FWHM) peak developed at the position of the conduction band edge. This is indicative of a negative-electron-affinity surface. Negative-electron-affinity surfaces are commonly obtained on III-V semiconductors by depositing a thin layer of a low work function material such as cesium or cesium-oxide. This study shows that it is possible to obtain a negative electron affinity on diamond (111) by depositing a sub-monolayer of a titanium, and suggests the possibility of inducing a negative electron affinity on diamond using other transition metals. A model for the observed negative electron affinity was presented, based on the Schottky barrier height of the diamond-metal interface, and the work function of the metal.

#### Acknowledgements

We thank B. Stoner and J.T. Glass for providing the initial diamond growth films, K. Das of Kobe Research for his help in establishing the diamond cleaning procedure, T.P. Schneider for the plasma cleaning work, and R. Rudder and

R. Markunas of RTI for helpful discussions. This work is supported in part by the ONR through grants N00014-92-J-1477, N00014-90-J-1604 and N00014-90-J-1707, the NSF through grant DMR 9204285 and the MITI of Japan through the NEDO program.

## References

- [1] R.J. Nemanich, *Ann. Rev. Mater. Sci.* 21 (1991) 535.
- [2] B.R. Stoner and J.T. Glass, *Appl. Phys. Lett.* 60 (1992) 698.
- [3] S. Koizumi, T. Murakami, T. Inuzuka and K. Suzuki, *Appl. Phys. Lett.* 57 (1990) 563.
- [4] K.F. Turner, B.R. Stoner, L. Bergman, J.T. Glass and R.J. Nemanich, *J. Appl. Phys.* 69 (1991) 6400.
- [5] K.F. Turner, Y.M. LeGrice, B.R. Stoner, J.T. Glass and R.J. Nemanich, *J. Vac. Sci. Technol. B* 9 (1991) 914.
- [6] T.P. Humphreys, J.V. LaBrasca, R.J. Nemanich, K. Das and J.B. Posthill, *Jpn. J. Appl. Phys. II* 30 (1991) 1409.
- [7] T. Tsuno, T. Imai, Y. Nishibayashi, N. Fujimori and K. Hamada, *Jpn. J. Appl. Phys. I* 30 (1991) 1063.
- [8] M.P. Everson and M.A. Tamor, *J. Vac. Sci. Technol. B* 9 (1991) 1570.
- [9] H.G. Busmann, H. Sprang, I.V. Hetel, W. Zimmermann-Edling and H.J. Guentherodt, *Appl. Phys. Lett.* 59 (1991) 295.
- [10] J.A. Martin, L. Vazquez, P. Bernard, F. Comin and S. Ferrer, *Appl. Phys. Lett.* 57 (1990) 1742.
- [11] C.B. Collins, F. Devanloo, D.R. Jander, T.J. Lee, H. Park and J.H. You, *J. Appl. Phys.* 69 (1991) 7862.
- [12] S. Ferrer, F. Comin, J.A. Martin, L. Vazquez and P. Bernard, *Surf. Sci.* 251/252 (1991) 960.
- [13] C.B. Collins, F. Devanloo, E.M. Juengerman, D.R. Jander and T.J. Lee, *Surf. Coat. Technol.* 47 (1991) 754.
- [14] N.H. Cho, D.K. Veirs, J.W. Ager III, M.D. Rubin, C.B. Hopper and D.B. Bogy, *J. Appl. Phys.* 71 (1992) 2243.
- [15] A.T. Collins, M. Kamo and Y. Sato, *J. Mater. Res.* 5 (1990) 2507.
- [16] J.A. Freitas Jr., J.E. Butler and U. Strom, *J. Mater. Res.* 5 (1990) 2503.
- [17] G.S. Gildenblat, S.A. Grot, C.W. Hatfield, A.R. Badzian and T. Badzian, *IEEE Electron Devices Lett.* 11 (1990) 371.
- [18] K.L. Moazed, R. Nguyen and J.R. Zeidler, *IEEE Electron Device Lett.* 9 (1988) 350.
- [19] H. Shiomi, H. Nakahata, T. Imai, Y. Nishibayashi and N. Fujimori, *Appl. Phys. I* 28 (1989) 758.
- [20] J.W. Glesener and A.A. Morrish, K.A. Snail, *J. Appl. Phys.* 70 (1991) 5144.
- [21] K.L. Moazed, J.R. Zeidler and M.J. Taylor, *J. Appl. Phys.* 68 (1990) 2246.
- [22] M.C. Hicks, C.R. Wronski, G.S. Gildenblat, A.R. Badzian, T. Badzian and R. Messier, *J. Appl. Phys.* 65 (1989) 2139.
- [23] F.J. Himpel, P. Heimann and D.E. Eastman, *Solid State Commun.* 36 (1980) 631.
- [24] J. van der Weide and R.J. Nemanich, in: *Proceedings of the First International Conference on the Applications of Diamond Films and Related Materials*, eds. Y. Tzeng, M. Yoshikawa, M. Murakawa and A. Feldman (Elsevier, New York, 1991) p. 359.
- [25] T. Tachibana, B.E. Williams and J.T. Glass, *Phys. Rev. B* 45 (1992) 11975.
- [26] B.B. Pate, M.H. Hecht, C. Binns, I. Lindau and W.E. Spicer, *J. Vac. Sci. Technol.* 21 (1982) 364.
- [27] E.H. Rhoderick and R.H. Williams, *Metal-Semiconductor Contacts* (Clarendon Press, Oxford, 1988).

## XII. Growth and Characterization of SiGe Contacts on Semiconducting Diamond Substrates

T. P. Humphreys, P. K. Baumann, K. F. Turner and R. J. Nemanich  
Department of Physics, North Carolina State University, Raleigh, North Carolina 27695-8202 USA

K. Das  
Kobe Steel Inc., Electronic Materials Center, P. O. Box 13608, Research Triangle Park, North Carolina 27709 USA

R. G. Alley, D. P. Malta and J. B. Posthill  
Research Triangle Institute, Research Triangle Park, North Carolina 27709-2194 USA

### A. Introduction

At present, there is a significant scientific and technological interest in the fabrication of stable ohmic and high-temperature rectifying contacts on diamond [1, 2]. To date, several metals, [3, 4] refractory metal silicides [5] and semiconductors [6] have been investigated as appropriate contact materials to semiconducting single crystal diamond substrates. In particular, the authors have demonstrated that the deposition of heteroepitaxial films of Ni on diamond exhibit excellent high-temperature rectifying properties [4]. Indeed, similar studies conducted on post-growth annealed TiSi<sub>2</sub> contacts on diamond have also shown rectification at high-temperature [5]. Moreover, it has also been recently demonstrated by Venkatesan et al. [6] that highly doped polycrystalline Si contacts fabricated on semiconducting diamond substrates form stable high-temperature rectifying diodes. In particular, the Si/diamond heterostructure also affords the potential of fabricating novel heterojunction devices which can be integrated with existing Si-based processing technologies.

In the present study we report initial results pertaining to the growth and characterization of SiGe contacts deposited on natural p-type semiconducting diamond C(001) substrates.

### B. Experimental Procedure

Commercially supplied (D. Drucker & ZN.N.V) low-resistivity ( $\sim 10^4 \Omega \cdot \text{cm}$ , p-type) semiconducting natural diamond (surface orientation (001)) substrates were chemically cleaned. The cleaning procedure included boiling CrO<sub>3</sub>+H<sub>2</sub>SO<sub>4</sub> (heated to 200 °C) for 10 min. followed by immersion in aqua regia (3HCl +1HNO<sub>3</sub>) and standard RCA cleaning solutions. Following cleaning, the samples were mounted on a Mo sample holder and transferred into the

electron-beam evaporation chamber. The base pressure in the system was typically  $2 \times 10^{-10}$  Torr. Prior to deposition, the substrates were heated to 550 °C for 5 minutes to thermally desorb both water vapor and possibly physisorbed gas contaminants. On cooling to room temperature an unreconstructed (1×1) low-energy electron diffraction (LEED) pattern was observed from the C(001) surface. The substrate temperature was maintained at 550 °C and the SiGe films were grown by the co-deposition of Si and Ge using electron beam evaporation. The corresponding Si and Ge fluxes were calibrated to obtain SiGe layers with a 5% Ge composition. By employing a stainless steel shadow mask several SiGe dots of ~200 nm in thickness and  $3 \times 10^{-3}$  cm<sup>2</sup> in area were fabricated. Subsequent post-growth *in-situ* annealing of the samples was performed at a temperature of 850 °C at  $10^{-8}$  Torr for 30 min.

### C. Results and Discussion

Examination of the as-grown films by LEED failed to obtain an ordered surface structure. Indeed, an inspection of the SiGe films by *ex-situ* scanning tunneling microscopy (STM) showed a highly textured surface morphology which indicated that the deposited layers were polycrystalline, as shown in Figure 1. The STM image was obtained in the constant current mode with a tip bias of 2 V. The presence of small polycrystalline grains of ~100 nm is clearly evident. The corresponding rms surface roughness of the deposited layer has been determined to be ~ 5 nm. Also, it was apparent that the SiGe films exhibit excellent adhesion properties with the underlying diamond substrate. In contrast, STM images of the annealed films were much more difficult to obtain due to their higher resistivity. As shown in Figure 2, the surface morphology of the annealed films was significantly smoother with a corresponding rms surface roughness of ~ 3 nm and an apparent increase in grain size.

Shown in Figure 3 is the Raman spectrum of the SiGe films obtained at room temperature using an Ar<sup>+</sup> ion laser (514.5 nm) excitation source. Clearly observed are two distinct phonon peaks pertaining to Si and Ge at 518 cm<sup>-1</sup> and 300 cm<sup>-1</sup>, respectively. It is interesting to note that the corresponding SiGe phonon mode, indicative of alloy formation (near 400 cm<sup>-1</sup>) was not observed. The absence of the SiGe phonon mode would tend to suggest an apparent segregation and clustering of Si and Ge during growth. Differences in the Si and Ge surface mobilities and/or surface energies on the chemically cleaned diamond C(001) surface during the initial stages of growth may account for this behavior [7]. Further studies are currently in progress to study this growth phenomena. Following the high-temperature ultra-high vacuum annealing step only the Si phonon peak was observed in the Raman spectrum. The absence of the Ge phonon mode in the layer was attributed to the evaporation of Ge during thermal annealing.

Current-voltage (I-V) measurements were obtained by mounting the diamond substrates on a Cu plate using Ag paint to form a large area back contact and applying a bias to the SiGe

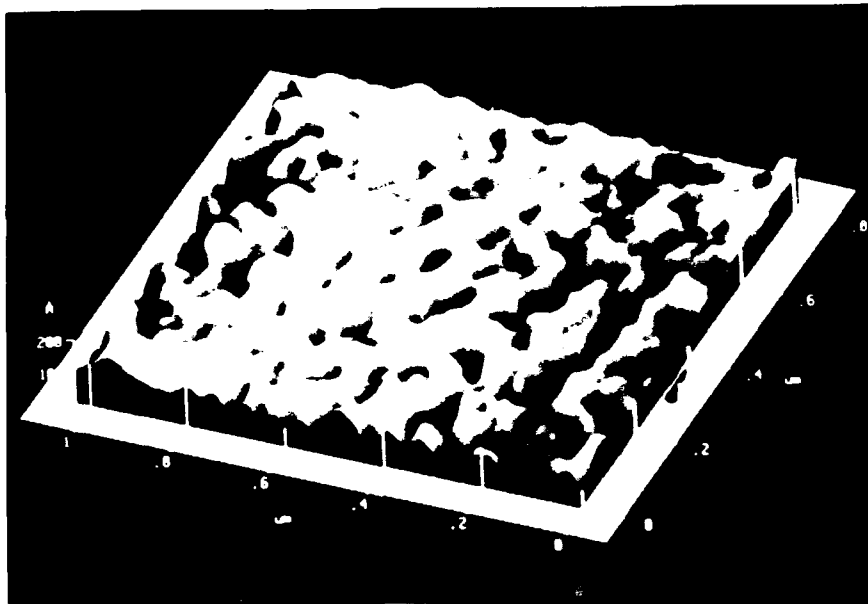


Figure 1. Topographic (constant current) STM micrograph of the surface morphology of the SiGe film deposited on natural diamond C(001) substrates.

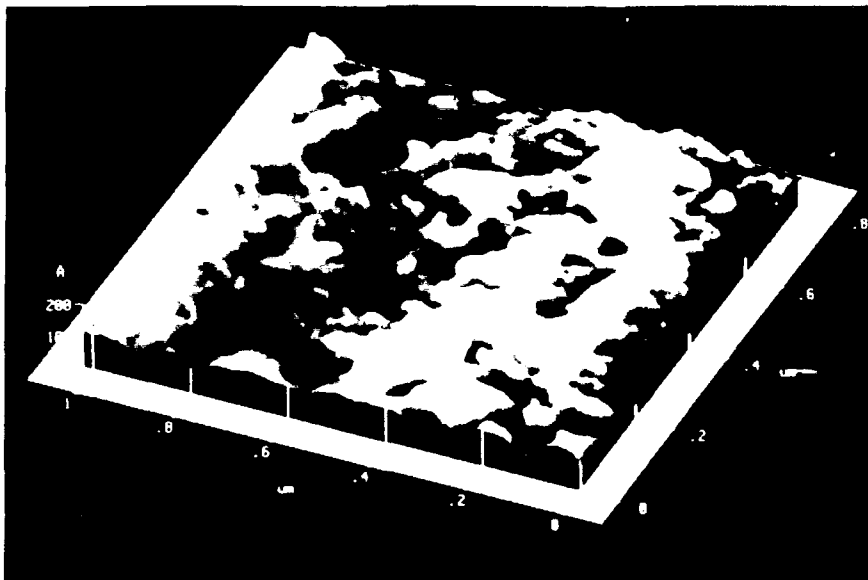


Figure 2. Topographic (constant current) STM micrograph of the surface morphology of the as-deposited SiGe film following a high-temperature anneal at 850 °C in a vacuum of  $10^{-8}$  Torr for 30 min.

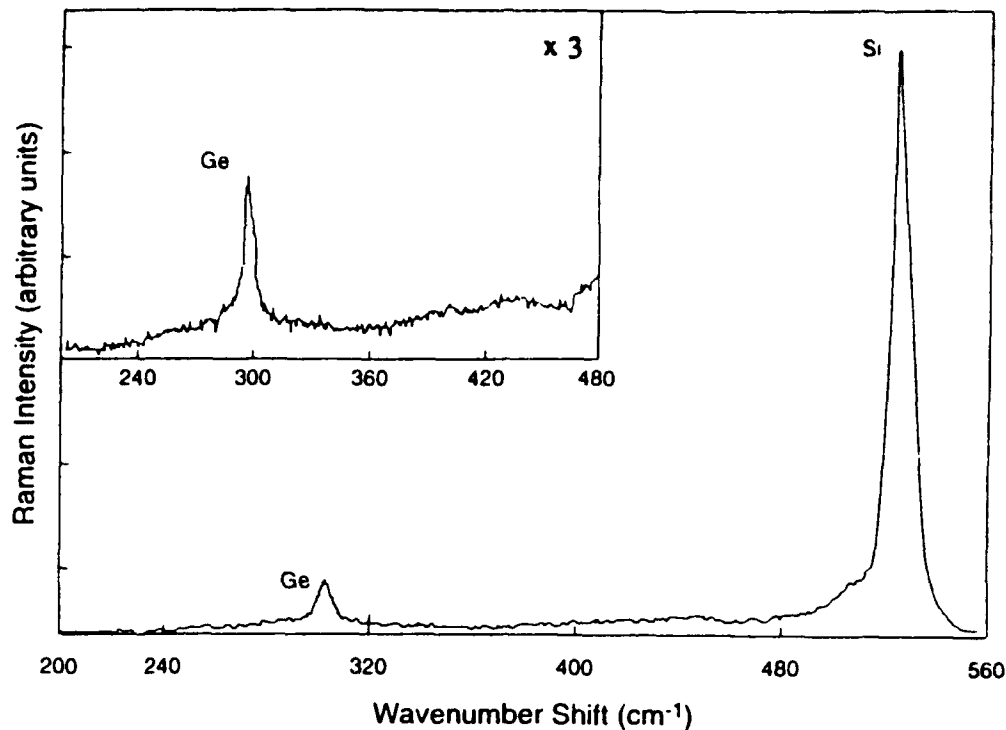


Figure 3. Raman spectrum of the SiGe film deposited on natural C(001) diamond substrates.

contact using a W probe. The room temperature I-V characteristics obtained for the as-deposited SiGe contacts on semiconducting diamond substrates are shown in Figure 4. The rectifying character of the SiGe contact is clearly evident. From the I-V measurements a small forward bias turn-on voltage of  $\sim 0.6$  V was estimated. The corresponding reverse bias leakage current density was measured to be  $\sim 1.56 \times 10^{-6}$  A/cm<sup>2</sup> at 20 V. Moreover, from the apparent linear region of the semilogarithmic plot of the forward characteristics an ideality factor  $n$  of 2.5 was calculated. This high  $n$  value may be an indication that the current conduction at the SiGe/diamond interface is not governed by a thermionic emission mechanism. It is interesting to note that similar observations have also been reported for Ni, TiSi<sub>2</sub> and Si contacts on semiconducting diamond C(001) substrates (4-6). In each of these studies current conduction appeared to be dominated by a space charge limited current (SCLC) mechanism. Consistent with the small turn-on voltage and the relatively high reverse leakage current, the corresponding I-V measurements recorded at 300 °C exhibit ohmic-like behavior.

Shown in Figure 5 is the corresponding I-V characteristics for the high-temperature annealed SiGe contacts recorded at 25 °C. Clearly, in comparison with the as-deposited films, the rectifying behavior of the annealed SiGe contacts has been degraded. In particular, the forward bias turn-on voltage has been significantly reduced. From the I-V measurements a forward bias turn-on voltage of  $\sim 0.2$  V has been estimated. Also, the reverse bias leakage current has increased to  $\sim 22$  nA which corresponds to a current density of  $7.3 \times 10^{-6}$  A/cm<sup>2</sup> at 20 V. In addition, corresponding I-V measurements conducted at 300 °C showed ohmic-like behavior.

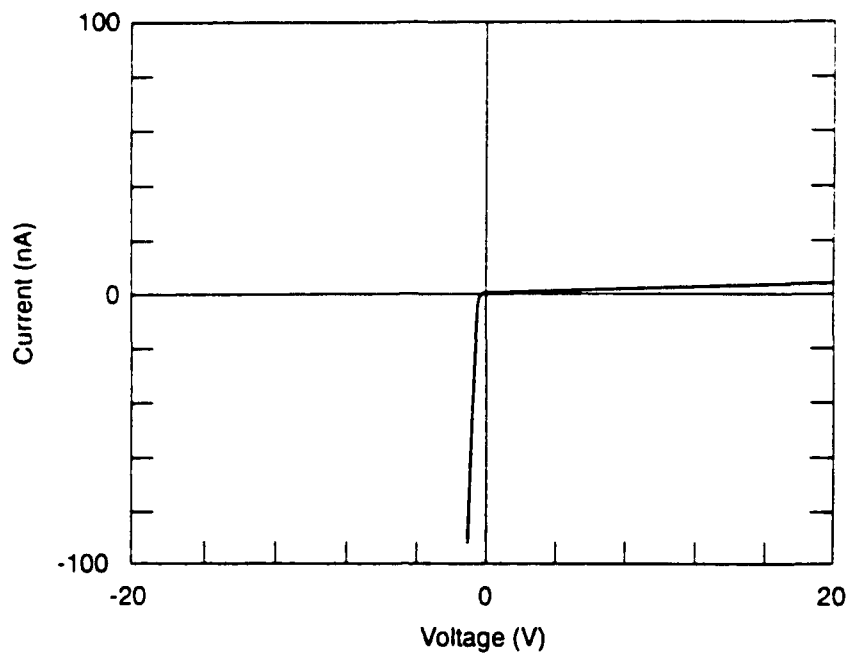


Figure 4. Linear plot of the current-voltage (I-V) characteristics of the SiGe contacts on semiconducting diamond C(001) substrates. Measurements were conducted at 20 °C.

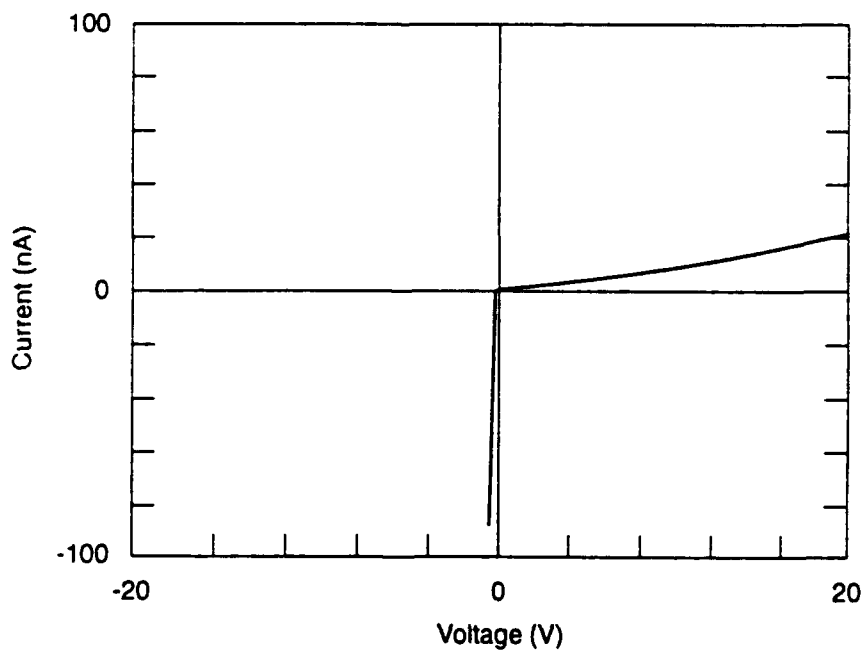


Figure 5. I-V characteristics of the Post-growth high-temperature annealed SiGe contacts at 25 °C.

#### D. Conclusions

In summary SiGe films have been grown by the co-deposition of Si and Ge on natural single crystal diamond C(001) substrates. As evidenced by LEED and STM analysis, the as-deposited films are polycrystalline. The I-V measurements of the SiGe contacts have demonstrated rectifying characteristics at room temperature. However, for measurements conducted at 300 °C the I-V characteristics exhibit ohmic-like behavior. Furthermore, it has also been demonstrated that subsequent post-growth annealing of the contacts has degraded the I-V characteristics.

#### E. Future Research Plans

Optimize the substrate cleaning procedure and growth conditions to achieve epitaxial SiGe films. Measurement of the bandgap offset between the SiGe contacts and the single crystal diamond substrate utilizing ultraviolet photoelectron spectroscopy (UPS).

#### Acknowledgements

TPH and RJN gratefully acknowledge partial support from the Office of Naval Research (Contract No. N00014-92-J-1477) and Kobe Research Laboratories, USA.

#### F. References

1. M. W. Geis, N. N. Efremow and D. D. Rathman, *J. Vac. Sci. Technol.* **6**, 1953 (1988).
2. For a review see K. Das, V. Venkatesan, K. Miyata, D. L. Dreifus and J. T. Glass, *Thin Solid Films*. **212**, 19 (1992).
3. K. L. Moazed, J. R. Zeidler and M. J. Taylor, *J. Appl. Phys.* **68**, 2246 (1990).
4. T. P. Humphreys, J. V. LaBrasca, R. J. Nemanich, K. Das and J. B. Posthill, *Jpn. J. Appl. Phys.* **30**, L1409 (1991).
5. T. P. Humphreys, J. V. LaBrasca, R. J. Nemanich, K. Das and J. B. Posthill, *Electron. Lett.* **27**, 1515 (1991).
6. V. Venkatesan, D.G. Thompson and K. Das, *proceedings of Symp. Mater. Res. Soc.* **270**, 419 (1992).
7. P. C. Kelires and J. Tersoff, *Phys. Rev. B* **63**, 1164 (1989).

### **XIII. Characterization of the Electronic Properties of Diamond**

#### **A. Introduction**

The use of semiconducting diamond for electronic devices is fundamentally affected by the transport properties of the mobile charge carriers. Preliminary measurements and estimates of these properties have resulted in significant interest in the use of diamond to fabricate both high power and high frequency devices. The use of diamond for high power applications is encouraged by the well established high thermal conductivity of diamond, along with a breakdown field that allows high bias to be applied. Although the exact breakdown field for diamond is not yet well established, there is no doubt that it is high (i.e., greater than  $10^6$  V/cm), and at least a factor of two greater than for Si or GaAs. The data available on the transport properties of electrons and holes in semiconducting diamond is not extensive. Preliminary measurements of electron and hole mobility and saturated velocity indicate adequate mobility (for device applications) and high velocity. However, sufficient data to establish the exact values for these parameters have not been reported.

In this work an experimental characterization technique is being developed to determine the electronic properties of semiconducting diamond. A modified Haynes-Shockley experiment is under consideration for use to investigate the mobility, saturated velocity, diffusion coefficient, and lifetime of mobile charge carriers in semiconducting diamond.

#### **B. Haynes-Shockley Experiment**

The Haynes-Shockley experiment allows the transport characteristics of mobile charge carriers in semiconductors to be experimentally determined. In this technique a semiconductor fixture that has the form of a dual-gate MESFET is used. The fixture consists of two relatively large contacts separated by a distance and located on the

surface of the semiconductor to be measured. The contacts are ohmic and are used to apply a bias field to the semiconductor. Located on the same surface between the two outer contacts are two narrow electrode gates. These contacts are reverse biased. One gate electrode is pulsed to inject a supply of mobile charge carriers. These carriers are influenced by the electric field in the semiconductor that results from the applied bias. The charge carriers move under the second gate electrode where they can be detected on an oscilloscope. With knowledge of the time for the charge pulse to move between the electrodes and the distance between the two electrodes, the transport characteristics can be determined. Variation of the bias field allows the v-E characteristics to be investigated. Also, the spread in the pulse allows the diffusion coefficient to be determined and the total area of the pulse allows the carrier lifetime to be measured.

The Haynes-Shockley experiment was originally applied to investigate minority carrier parameters. Since minority carrier lifetimes are relatively long (on the order of mS), the procedure is not difficult to employ. The minority charge pulse can be injected and detected before it has the opportunity to decay and disappear by recombination. Application of the technique to investigate majority carrier properties is much more difficult. Majority carrier lifetimes are effectively equal to the dielectric relaxation time with a magnitude inverse to doping. Typical magnitudes are on the order of nanoseconds for doping densities of interest. The short lifetimes require that very small spacing and fast injection sources and oscilloscopes be used, if the pulse is to be detected before it decays. Injection sources and oscilloscopes must be capable of operating at time intervals in the nsec-psec range. Electrode spacing on the order of 0.5 to 5  $\mu\text{m}$  are readily available using modern lithography techniques, and a Hypres Superconducting Sampling System with a rise time of 5 pS is available. This provides the opportunity to try the technique.

In order to investigate the potential of the technique for use in measuring the transport properties of diamond a model is under development. The purpose of the model is to investigate the fixture dimensions, pulse characteristics, and doping densities that

will allow a measurement to be successfully performed. The model will be used to design the experiment. It will also be used to extract the desired parameter values from the measured data. A preliminary version of the model has been developed and is currently being used to investigate allowed dimensional and parameter values.

### C. Example

The two most critical parameters in the experiment are the minimum electrode spacing and the minimum time interval that can be measured. The first parameter determines the maximum doping density for the semiconductor that can be used. The second factor dominates when the applied field is high. The arrival time for the pulse varies inversely to the magnitude of the electric field. This can, of course, be varied by modification of the electrode spacing.

Preliminary calculations have been performed, assuming a mobility of  $600 \text{ cm}^2/\text{V}\cdot\text{sec}$ . The minimum detectable time is determined by the Hypres oscilloscope and is conservatively estimated to have a magnitude of about 0.05 nsec, including system and fixture time constant effects. The actual value is probably less, but this value is used to perform the initial estimates. The distance between the emitter and collector electrodes is assumed to be  $5 \text{ }\mu\text{m}$ . The calculations were performed for donor concentrations ranging from  $10^{12}$  to  $10^{15} \text{ cm}^{-3}$ . The results of the calculations are presented in Figures 1-8. Figures 1, 3, 5, and 7 show the arrival time as a function of the applied electric field for increasing doping densities. The curve represents the time in nsec for the signal maximum to reach the collector. The straight lines indicate the 0.05 nsec minimum detectable time determined by the oscilloscope. The ratio of the total number of received carriers to the total number of injected carriers for each doping density is shown in Figures 2, 4, 6, and 8, respectively. As indicated, an increase in electric field produces a decrease in the time interval between the injection and collection of the charge carriers, but the ratio of the collected to injected charge density is increased. The limitations of the oscilloscope

indicate that the measurement can only be performed for electric fields less than about 7.5-10 kV/cm. Also, the semiconductor doping for this example is limited to less than about  $10^{15}$  cm<sup>-3</sup>. The range of allowed applied electric field and doping density that can be employed can be increased by reduction in the electrode spacing.

The effect of varying mobility was also investigated. Mobility values ranging from 100 to 1600 cm<sup>2</sup>/V-sec were investigated. The ratio of injected to collected charge density is essentially independent of mobility. An increase in mobility results in a reduction of collection time, but the dielectric relaxation time is also reduced. The net effect is that the ability to perform the experiment is not strongly affected by the magnitude of the mobility.

#### D. Conclusions

A modified Haynes-Shockley experiment is being investigated as a technique for measuring the mobile charge transport characteristics of semiconducting diamond. A preliminary model has been derived and used to investigate dimensional, doping, and time detection limits. Although application of the technique to majority carrier measurement is difficult due to dielectric relaxation time limitations, the calculations indicate that the technique can be successfully applied to measure transport properties over a limited range of doping and electric field. The current calculations were performed assuming electrode spacing of 5  $\mu$ m and a system time constant of 0.05 nsec. This places a limit on allowed doping to less than about  $10^{15}$  cm<sup>-3</sup> and applied electric field to less than about 7.5-10 kV/cm. Electrode spacing can be reduced to the range of 0.5-1  $\mu$ m by making use of modern photolithography. Also, the actual system time constant is probably significantly less than assumed since the oscilloscope has a specified rise time of 5 psec. This should produce significant increases in the allowed doping and applied electric field. The preliminary calculations are encouraging and the work will be continued. It is anticipated that fabrication of a suitable test fixture will begin in the near future.

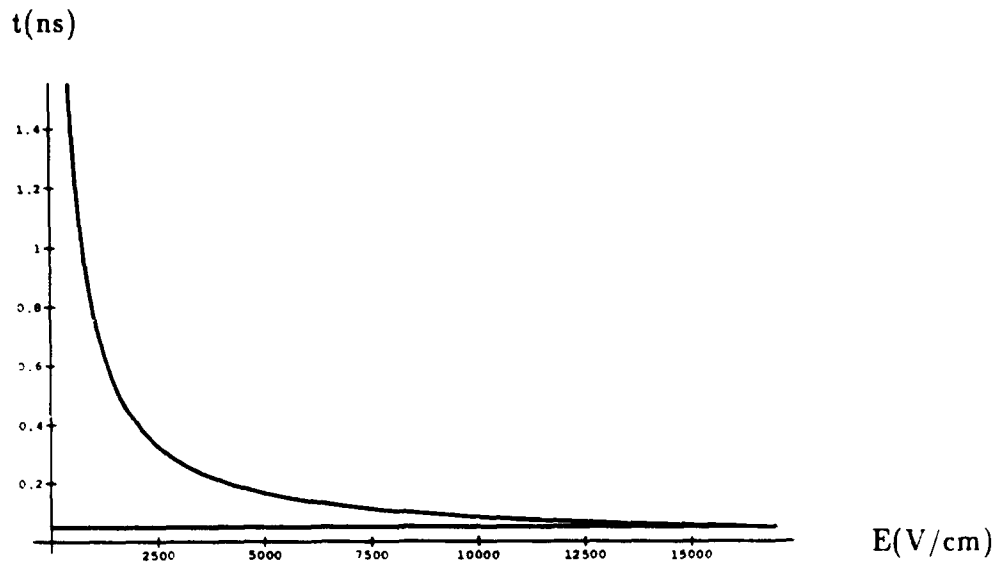


Figure 1. Arrival time for the carriers  $d=5\mu\text{m}$  ( $N_d = 10^{12}$ ).

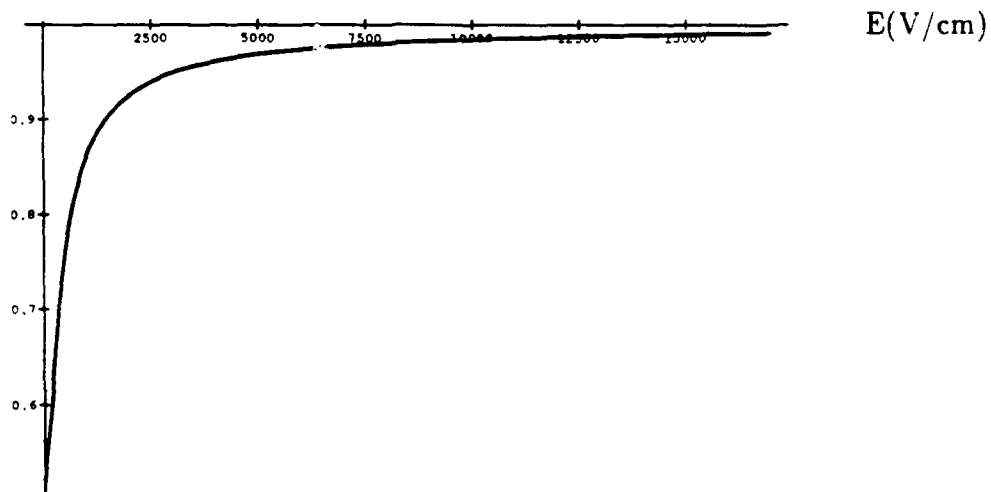


Figure 2. Ratio of the received to injected carriers.

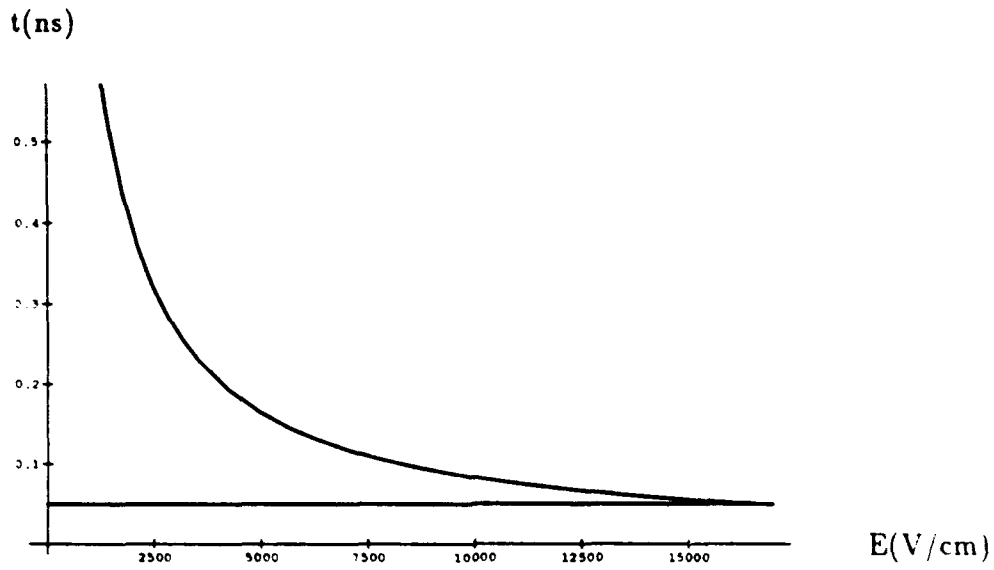


Figure 3. Arrival time for the carriers  $d=5\mu\text{m}$  ( $N_d = 10^{13}$ ).

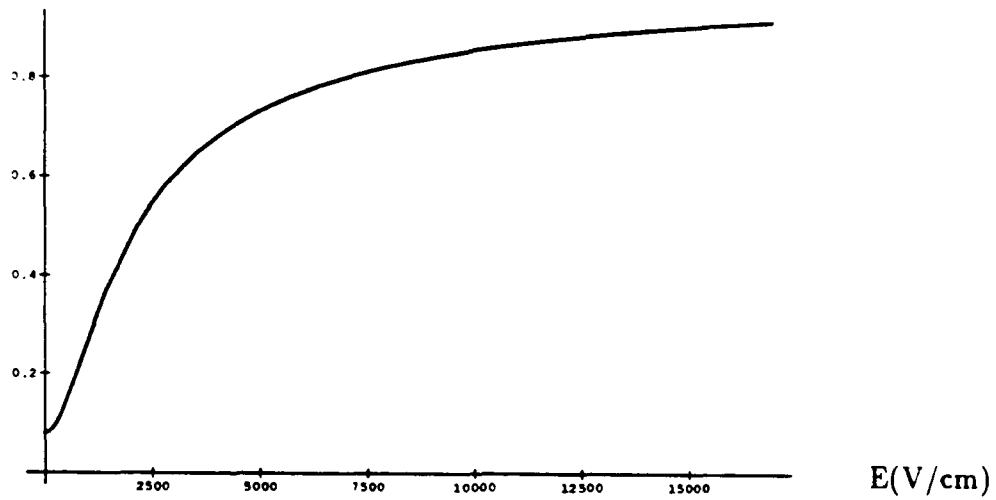


Figure 4. Ratio of the received to injected carriers.

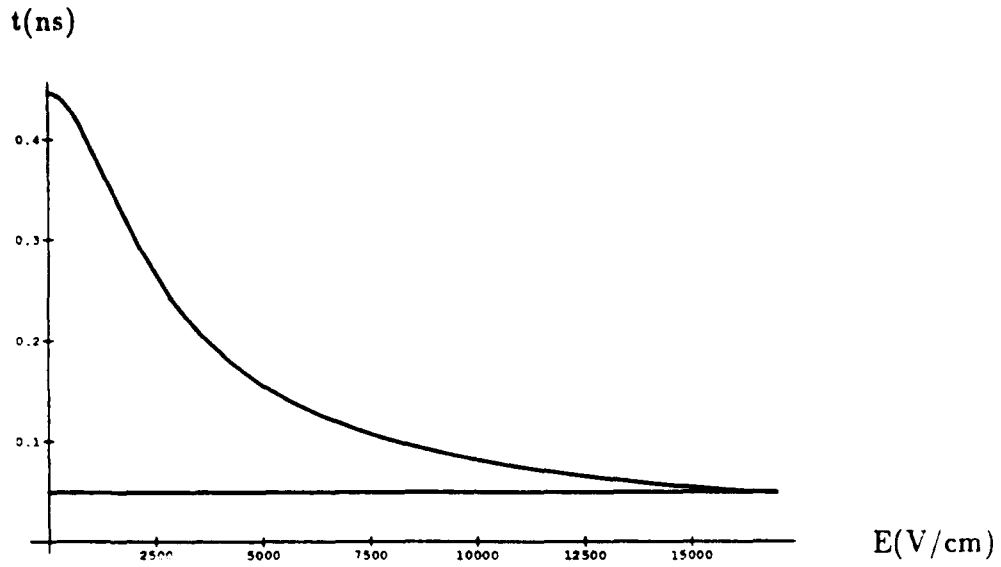


Figure 5. Arrival time for the carriers  $d=5\mu\text{m}$  ( $N_d = 10^{14}$ ).

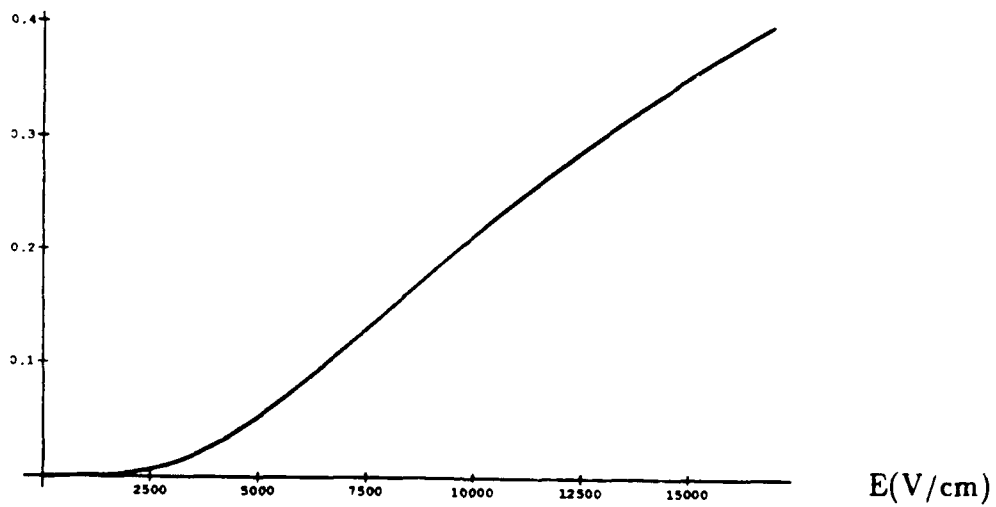


Figure 6. Ratio of the received to injected carriers.

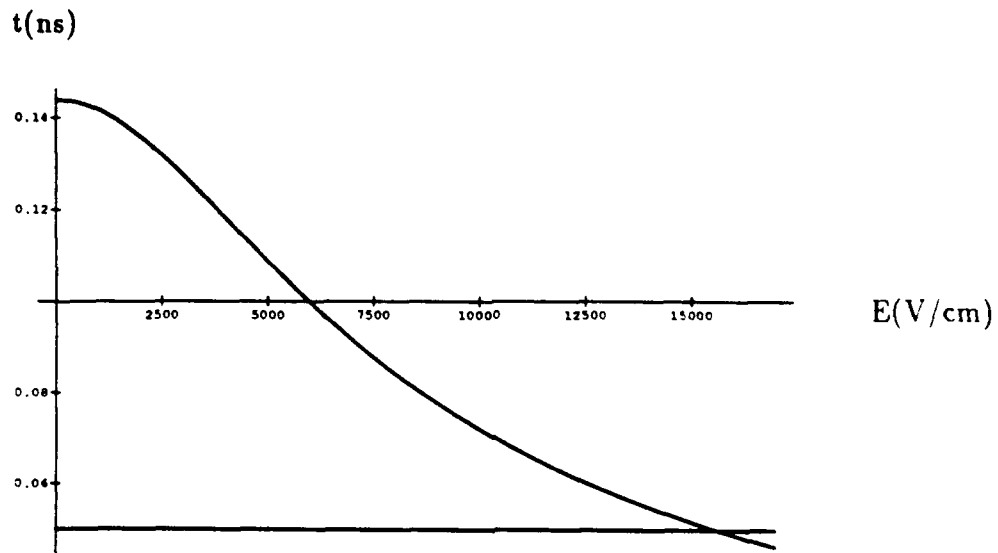


Figure 7. Arrival time for the carriers  $d=5\mu\text{m}$  ( $N_d = 10^{15}$ ).

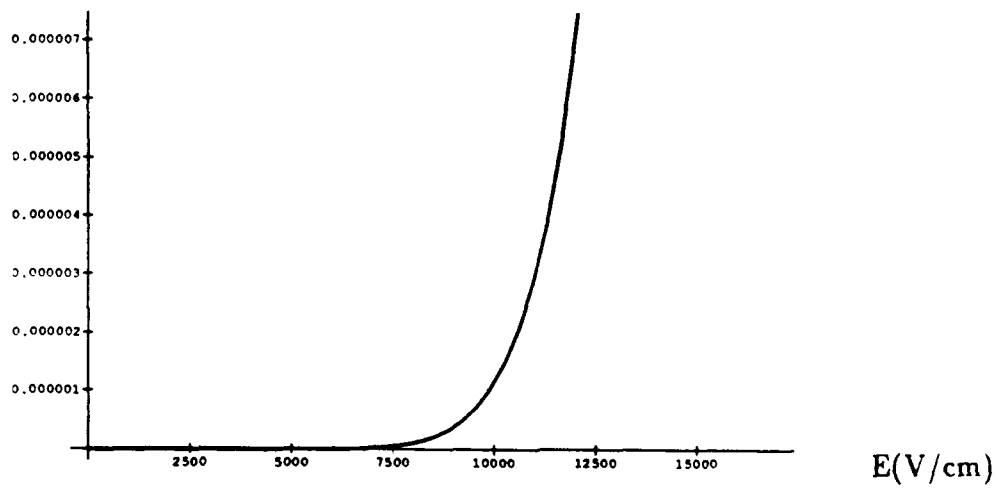


Figure 8. Ratio of the received to injected carriers.

## XIV. Modeling and Characterization of Electronic Devices Fabricated from Semiconducting Diamond Thin Films

### A. Introduction

Wide bandgap semiconductors such as diamond have the potential to be useful for the fabrication of electronic devices that can operate at high temperature and high power levels in corrosive environments. The high saturation velocity of both electrons and holes in semiconducting diamond thin films indicate that this material should be useful for microwave and millimeter-wave devices. The electron and hole mobilities of this material are sufficiently high that it should be possible to design devices with minimum parasitic resistances. Much of the device potential for diamond is predicted by figure-of-merit calculations that indicate the potential for superior performance in comparison with traditional semiconductor materials such as Si and GaAs. The figure-of-merit calculations are generally formulated using some sort of product between the free carrier saturation velocity, critical electric field for avalanche breakdown, and dielectric constant. As such, the figures-of-merit only give a preliminary and approximate indication of the performance potential of devices fabricated from diamond. More detailed information is available from physical device simulators that can predict the dc and RF potential of the devices from material, device design, and operating condition information.

In this report, a physical device simulator for the microwave MESFET is used to examine the microwave and millimeter-wave potential of MESFET devices fabricated from semiconducting p-type diamond. Due to the relatively high activation energy of boron dopants in diamond ( $E_a \sim 0.37$  eV) it may be necessary to operate the device at elevated temperature. For this reason the operation of the device is considered at both room temperature and 500 °C. The RF performance and design tradeoffs are reported. It is found that p-type diamond MESFETs are capable of significant RF output power, even at elevated temperature.

### B. Investigation Procedure

A large-signal, numerical model for the MESFET is used for this investigation. The simulator is based upon solutions to the semiconductor device equations and is, therefore, based upon physical device operation. The simulator has previously been used to predict the microwave performance of GaAs microwave MESFETs and has produced results in excellent agreement with experimental data. For this work the simulator was modified to allow for the investigation of diamond devices.

For the study the charge carriers are assumed to be in equilibrium with the lattice at all times so that the Boltzmann equation reduces to the continuity equations for electrons and holes. All transport processes in the semiconductor can then be represented by drift velocities and diffusion coefficients that are functions of the electric field. Poisson's equation is used to relate the carrier concentrations and doping levels in the structure to the electric field. The continuity equations and Poisson's equation are solved by analytical and table look-up techniques.

The model accepts data about the geometry and doping profile of the diode and with the appropriate material data, produces information about the operating characteristics of the device. Both ac and dc solutions are obtained from the model. The MESFET is embedded in a realistic dc and RF circuit so that impedance tuning considerations are included. The principal output data of the RF simulation are the input and output RF impedances, the RF output power, the power-added efficiency, and the gain. By selecting the operating frequency by means of the period of the applied RF voltage the frequency performance of the device can be investigated. In this work the operation frequency was set to 10 GHz.

### C. P-Type Semiconducting Diamond

One problem that is of concern in research directed towards the development of semiconducting diamond electronic devices is the availability of suitable dopants. Theoretical simulations of possible device structures for implementation in diamond indicate that the best microwave and millimeter-wave performance would be expected from devices fabricated from n-type diamond thin films. Suitable dopants for producing these layers have not yet, however, been identified. Suitable device quality synthetic n-type diamond has not yet been demonstrated. Device quality p-type material, however, can be produced using boron as the impurity. This material also looks attractive for fabrication of electronic devices since holes in diamond have good mobility and saturated velocity, only slightly less than that for electrons. A question concerning the use of p-type material relates to the temperature at which the device must operate. Boron in diamond creates an acceptor level with an activation energy that has been reported to vary from  $E_a = 0.013 \text{ eV}$  when introduced by CVD [15],  $E_a = 0.2-0.35 \text{ eV}$  when introduced during growth by high pressure synthesis [16], and  $E_a = 0.27-0.37 \text{ eV}$  when introduced by ion-implantation [17]. The lower activation energies, however, are believed to involve defects, etc. and the generally accepted activation energy for boron in diamond is  $E_a = 0.37 \text{ eV}$ . There is concern that in order to obtain sufficient charge carriers for device applications high operating temperature may be required.

Operation at elevated temperature, however, creates a problem for p-type material in that the hole mobility demonstrates a temperature dependence of approximately  $T^{-2.8}$ . This is in contrast to that for electrons, which follow approximately a  $T^{-1.1}$  law. Operation at elevated temperature for p-type diamond devices is expected, therefore, to result in significantly degraded RF performance.

#### D. Results

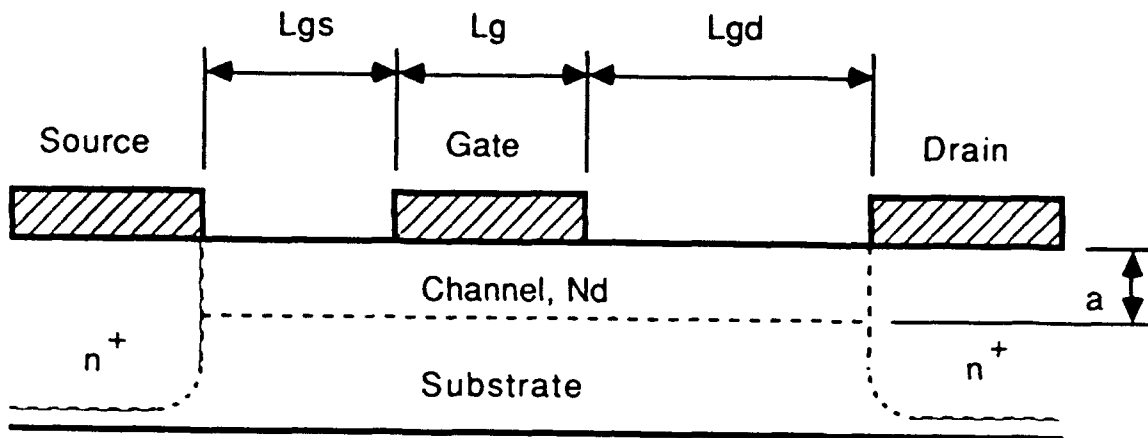
An X-band power MESFET was designed to produce maximum power-added efficiency under class A operating conditions at 10 GHz. The device structure and dimensions and the device and material parameters used in the simulation are shown in Figure 8. The device has a gate length of  $L_g = 0.5 \mu\text{m}$ , and a gate width of  $W = 1 \text{ mm}$ . These dimensions are typical of those used for GaAs power MESFETs. The material parameters used for both the room temperature and 500 °C simulations are listed. Full activation was not assumed and the boron doping level would need to be sufficient to result in a channel hole density of  $4 \times 10^{17} \text{ cm}^{-3}$ . The actual boron density could, therefore, be one to three orders of magnitude greater than the hole density. This difference would diminish as the temperature and activation increased. This issue will be investigated in more detail in future simulations.

The dc I-V characteristics for the device at room temperature are shown in Figure 9. For room temperature operation the hole mobility and saturated velocity were  $600 \text{ cm}^2/\text{V-sec}$  and  $1.08 \text{ cm/sec}$ , respectively. As shown in Figure 9 the device has a pinch-off voltage of about -12 v and a maximum transconductance of  $g_m = 52 \text{ mS/mm}$ .

The RF operation of the device was simulated by embedding the device in an RF circuit and tuning the input and output impedances for maximum power-added efficiency at the one db compressed RF output power point. This is generally accomplished by an iterative procedure in which the input is tuned for maximum RF output power when the output is terminated in a conjugate impedance match. This process can be time consuming, but is consistent with the experimental technique commonly used. The simulation procedure is facilitated with the use of a theoretical load-pull algorithm that has been incorporated into the simulator.

The results of the calculations for the 10 GHz, room temperature operation are shown in Figures 10-12. The RF output power versus input power is shown in Figure 10 for three values of drain bias. As expected, the RF output power increases with drain bias. The maximum RF output power at the one db compression point is 37.7 dbm or 5.9 W/mm. This is significantly greater than can be achieved with GaAs MESFETs, which so far have demonstrated about 1.7 W/mm. The gain is shown in Figure 11. With  $V_{ds} = 40 \text{ v}$  about 12 db of gain is obtained. In addition, the linear (or

## *P-Type Diamond MESFET*



Parameter	Value	
	Room Temp.	500 °C
$L_g$	0.5 $\mu\text{m}$	0.5 $\mu\text{m}$
$W$	1 mm	1 mm
$L_{ds}$	1 $\mu\text{m}$	1 $\mu\text{m}$
$L_{gs}$	1 $\mu\text{m}$	1 $\mu\text{m}$
$N_d$	$4 \times 10^{17} \text{ cm}^{-3}$	$4 \times 10^{17} \text{ cm}^{-3}$
$n^+$	$10^{19} \text{ cm}^{-3}$	$10^{19} \text{ cm}^{-3}$
$a$	0.15 $\mu\text{m}$	0.15 $\mu\text{m}$
$\Phi_{bi}(\text{Au})$	1.71 eV	1.68 eV
$R_c$	$\sim 10^{-4} \Omega\text{-cm}^2$	$\sim 10^{-4} \Omega\text{-cm}^2$
$\mu_p$	600 $\text{cm}^2/\text{V}\text{-sec}$	100 $\text{cm}^2/\text{V}\text{-sec}$
$v_s$	$1.08 \times 10^7 \text{ cm/sec}$	$0.86 \times 10^7 \text{ cm/sec}$
$\Theta$	0.73 °K/W	1.57 °K/W

Figure 8. Device Cross Section and Parameter Values for a P-Type Diamond MESFET.

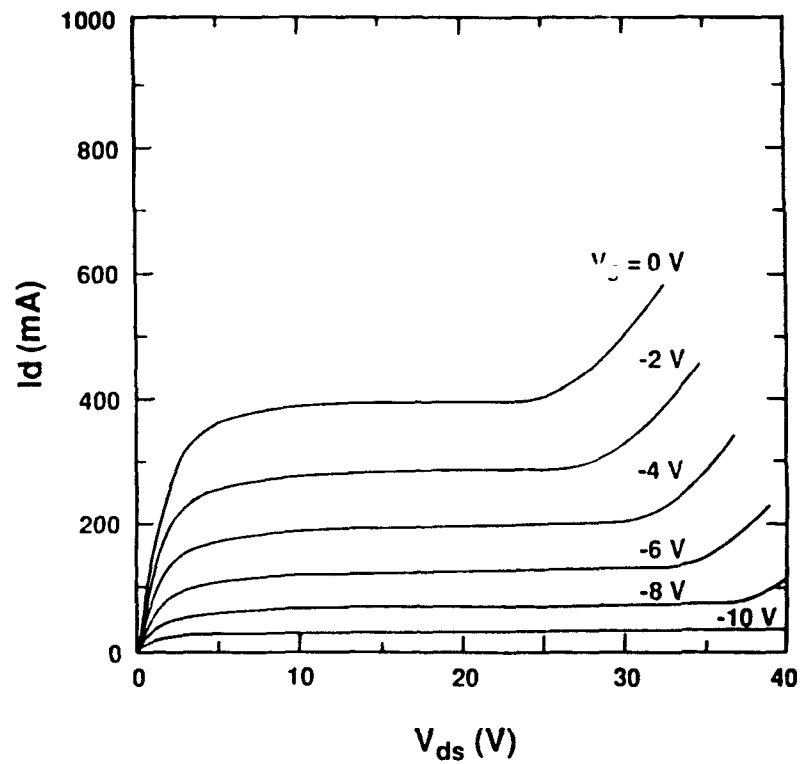


Figure 9. I-V Characteristics for a P-Type Diamond MESFET at Room Temperature.

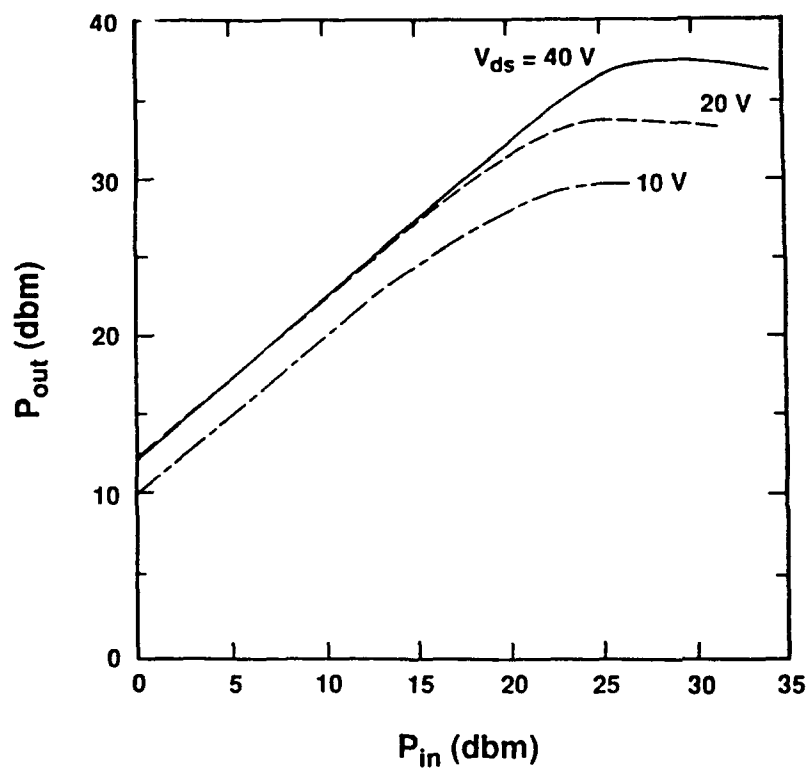


Figure 10. RF Output Power versus Input Power for the P-Type Diamond MESFET at Room Temperature ( $F = 10$  GHz, Class A,  $V_{ds} = 40$  v).

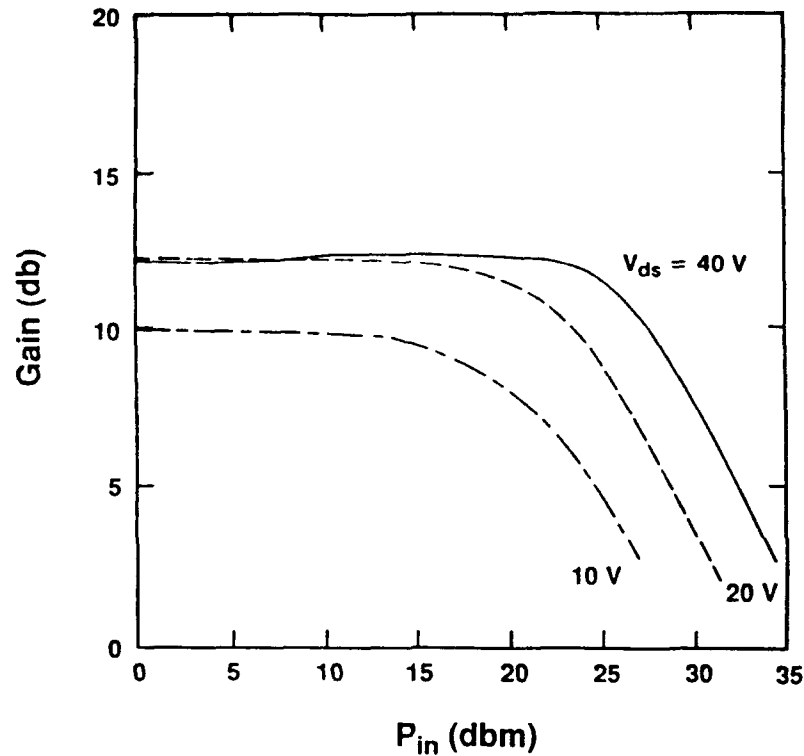


Figure 11. Gain versus Input Power for the P-Type Diamond MESFET at Room Temperature ( $F = 10$  GHz, Class A,  $V_{ds} = 40$  v).

dynamic) range is about 25 db. The power-added efficiency is shown in Figure 12. As indicated, excellent PAE can be obtained and the  $V_{ds} = 40$  v drain bias allows a PAE  $\sim 50\%$  to be achieved. This is at the limit of efficiency expected for class A operation. The excellent performance is obtained due to waveform shaping when the device is driven into saturation. The results are very dependent upon circuit tuning conditions. This process is currently under investigation, but is consistent with both experimental and theoretical calculations obtained with GaAs power devices. The results of the simulations for operation at  $500$  °C are shown in Figures 13–16. For operation at elevated temperature the hole mobility and saturated velocity are  $100$   $cm^2/V\text{-sec}$  and  $0.86 \times 10^7$   $cm/sec$ , respectively. The maximum channel current and transconductance that can be achieved are reduced to slightly over  $200$  mA and about  $30$  mS/mm, respectively. These reductions scale, of course, directly with the velocity-field characteristics. The RF output power versus input power is shown for drain bias voltages of  $V_{ds} = 30, 20,$  and  $10$  v in Figure 14. The one db compressed RF output power for the  $V_{ds} = 30$  v bias is  $P_o = 32.8$  dbm or  $1.9$  W/mm. The gain and PAE versus input power for the device are shown in Figures 15 and 16, respectively. The

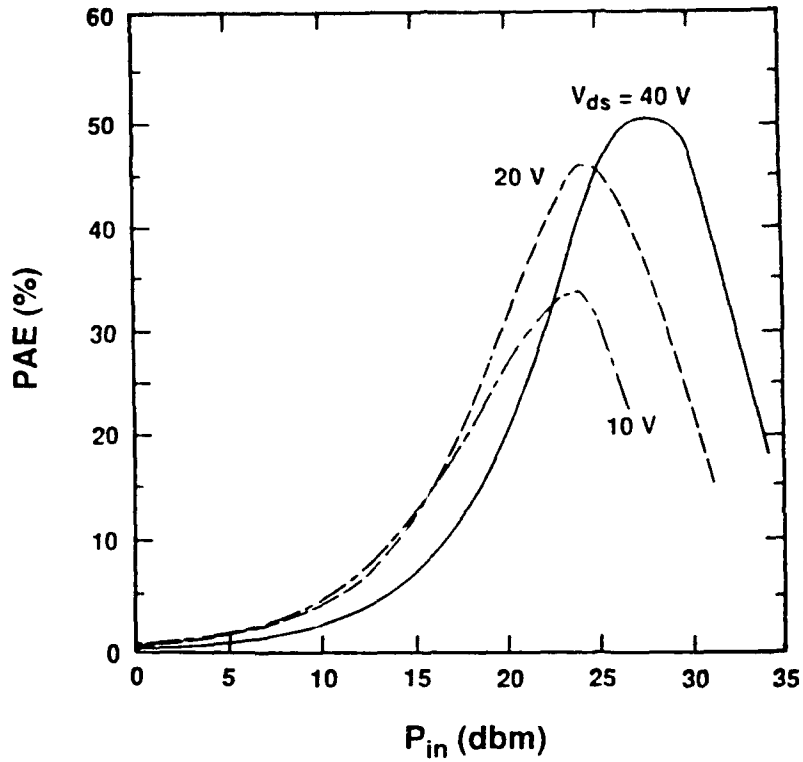


Figure 12. Power-Added Efficiency versus Input Power for the P-Type Diamond MESFET at Room Temperature ( $F = 10\text{ GHz}$ , Class A,  $V_{ds} = 40\text{ v}$ ).

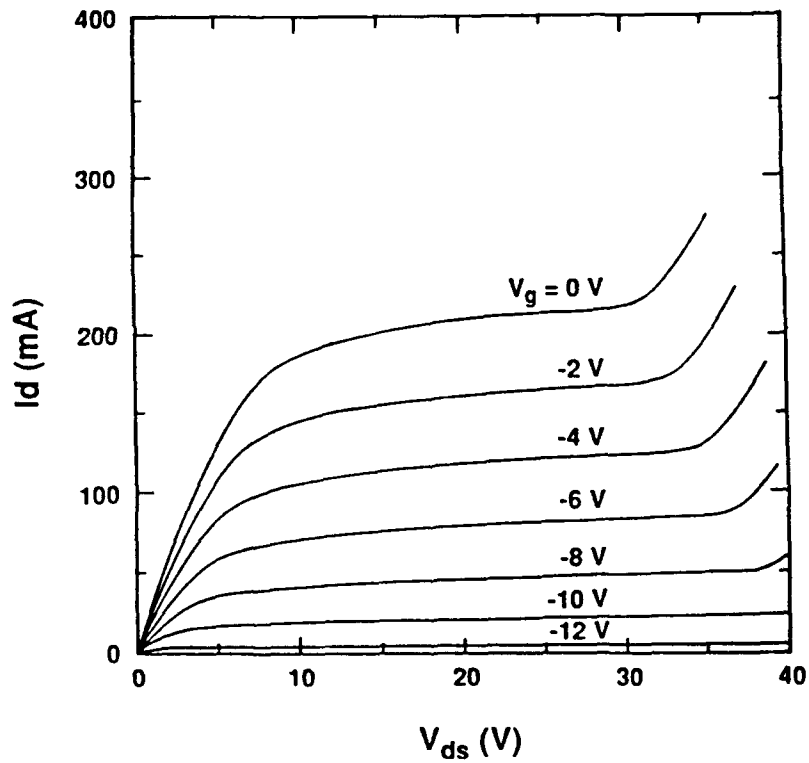


Figure 13. I-V Characteristics for the P-Type Diamond MESFET at  $500\text{ }^{\circ}\text{C}$ .

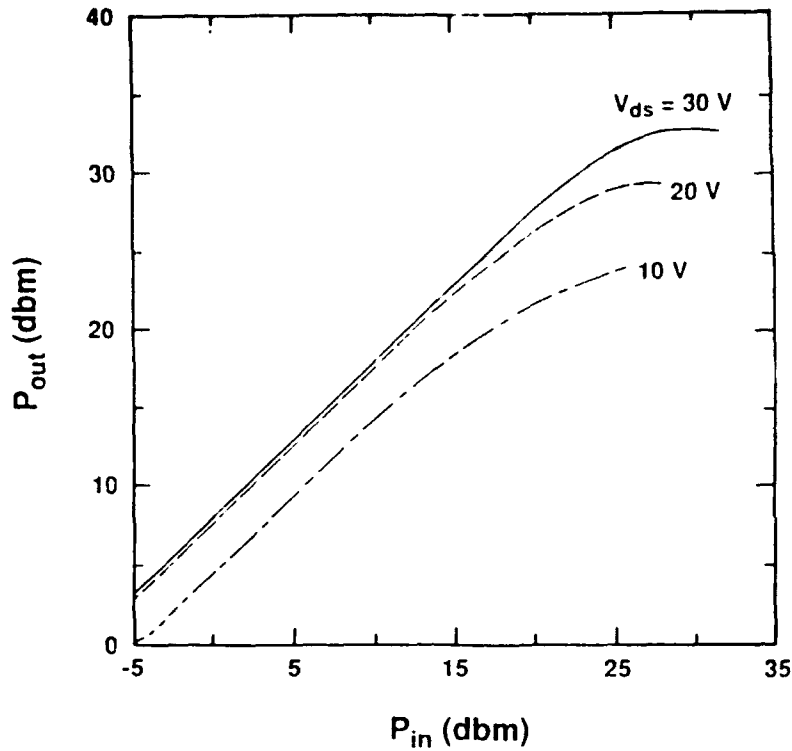


Figure 14. RF Output Power versus Input Power for the P-Type Diamond MESFET at 500 °C ( $F = 10$  GHz, Class A,  $V_{ds} = 30$  v).

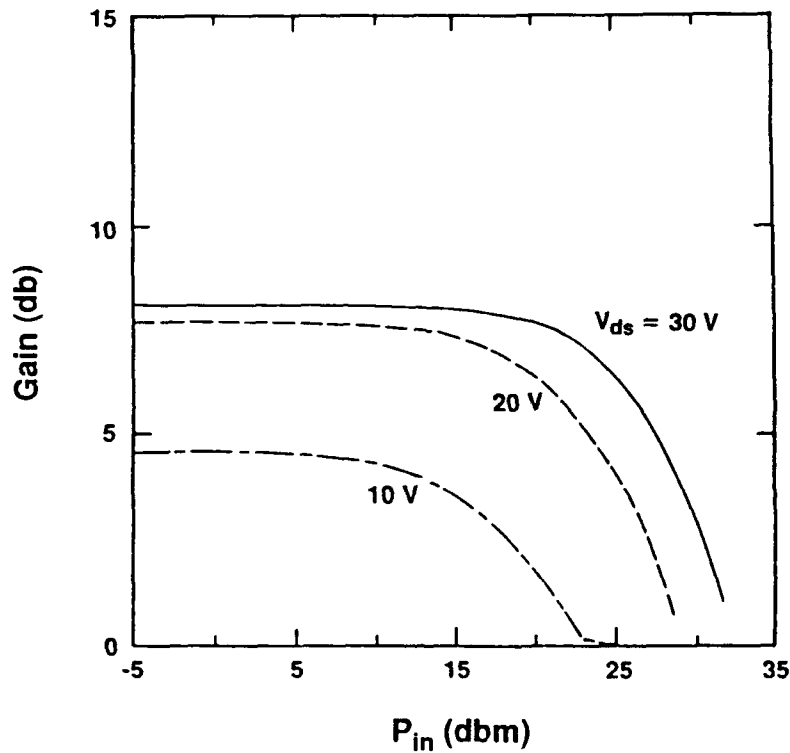


Figure 15. Gain versus Input Power for the P-Type Diamond MESFET at 500 °C ( $F = 10$  GHz, Class A,  $V_{ds} = 30$  v).

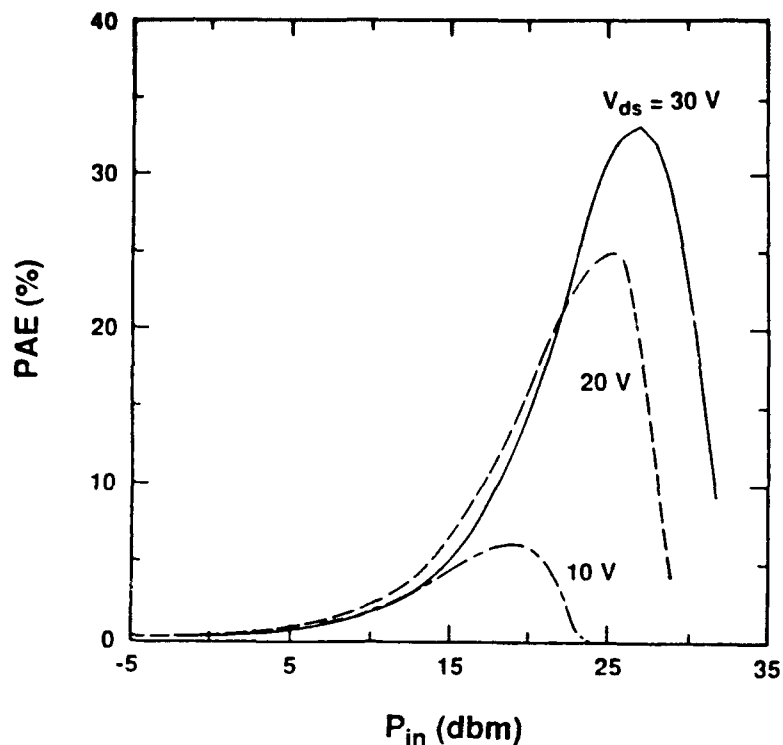


Figure 16. Power-Added Efficiency versus Input Power for the P-Type Diamond MESFET at 500 °C ( $F = 10$  GHz, Class A,  $V_{ds} = 30$  v).

linear gain for the device with the  $V_{ds} = 30$  v bias is about 8 db and the maximum PAE at one db compression is about 33%.

The 500 °C RF performance is significantly reduced from the room temperature results, but is still greater than obtained from GaAs power MESFETs at room temperature. In addition, the GaAs MESFET would not function at 500 °C, but would burn out. This indicates that p-type diamond MESFETs could be used with good RF performance in high temperature applications where currently available devices cannot operate. The room temperature and 500 °C performance are summarized in the following table.

Table I. P-Type Diamond MESFET  
Class A Operation at 10 GHz

Room Temperature	500 °C
$V_{ds} = 40$ v	$V_{ds} = 30$ v
$BV_{gd} = 92$ v	$BV_{gd} = 70$ v
$P_o = 37.7$ dbm	$P_o = 32.8$ dbm
$PAE_{max} = 50.6$ %	$PAE_{max} = 33.2$ %
$G = 12.2$ db	$G = 8.1$ db

### E. Conclusions

The microwave performance of p-type diamond MESFETs operating under class A operation conditions at 10 GHz is investigated. The use of boron dopants allows p-type semiconducting thin films suitable for the fabrication of MESFETs. Boron, however, has a relatively high activation energy and elevated temperature operation may be necessary in order to obtain suitable free charge densities in the MESFET conducting channel. Elevated temperature operation is expected to result in significantly degraded RF performance since holes in diamond demonstrate a  $T^{-2.8}$  temperature dependence. In this study RF operation at room temperature and 500 °C was simulated. The study reveals that although elevated temperature operation results in degradation, the RF performance possible is still significantly superior to that available from GaAs MESFETs operating at room temperature. At 10 GHz and 500 °C the p-type diamond MESFET is capable of producing RF output power, power-added efficiency and gain of 1.9 W/mm, 33 % and 8 db, respectively.

### F. Future Research Plans and Goals

The RF operation of the p-type diamond MESFETs will be investigated in more detail. In particular, the operation of the devices at higher frequencies, up to 100 GHz will be simulated. The dopant activation issue will be investigated in more detail by means of simulations of the density of free charge carriers as a function of temperature. This issue must be addressed, along with the question of gate-drain breakdown voltage in order to obtain a realistic picture of the potential of these devices for microwave and mm-wave applications.

### G. References

15. N. Fujimori, T. Imai and A. Doi, *Vacuum*, vol. 36, no. 1-3, p. 99, 1986
16. R.H. Wentorf, *J. Chemical Phys.*, vol. 36, p. 1987, April 1962.
17. V.S. Vavilov, M.A. Gukasyan, M.I. Guseva, T.A. Karatyginal and E.A. Konorova, *Sov. Phys. Semicond.*, vol. 8, p. 471, Oct. 1974.

## **XV. Modeling of Microwave MESFET Electronic Devices Fabricated from Semiconducting Diamond Thin Films-I**

### **I. Introduction**

The operation of p-type diamond MESFET's is under investigation. It has been observed that these devices are limited in possible applied drain bias by a gate leakage problem. The gate leakage prevents the application of sufficient drain bias to saturate the current flow in the channel. The inability to achieve full channel current saturation limits the gain that can be achieved with the device.

We have proposed a breakdown mechanism for MESFET's that explains the gate leakage and breakdown phenomena observed in experiments. The new gate leakage and breakdown mechanisms have been formulated and are currently being incorporated into the device model. Initial results of this work are encouraging, although simulation time can be large. We are currently refining the model formulation to reduce execution time so that the model can be used for design investigation.

We have also begun formulation of a JFET modification to the program. This work requires development of a pn junction model to replace the Schottky gate model in the current model. This work is anticipated to serve as a stepping stone to formulation of a heterojunction model that can be applied to diamond heterostructures.

### **II. Investigation Procedure**

The formulation of the surface model for the region between the gate and drain electrodes has continued. In this model the surface of the MESFET is a complex physical system where a periodic lattice of diamond atoms terminate into either free space or another material such as gate metals, other semiconductors, or passivating (i.e., insulating) materials. Typical numerical or analytic models for MESFET's neglect surface effects and only include the first order bulk transport properties in the formulation. First order physics

describes MESFET operation in terms of particle conservation equations and particle flux equations which have field, diffusion, and sometimes thermal components. Poisson's equation completes the set by relating the particle and fixed charges within the device to potential. The initial formulation previously reported has been further refined and extended. The model allows for the trapping of negative charge on the surface of the semiconductor in the region between the gate and drain electrodes. The negative charge, in turn, results in a surface depletion region that can penetrate a significant distance into the channel, thereby reducing the cross-sectional area through which current can flow, and reducing the drain current. This phenomenon, although well understood, requires considerable sophistication in the device model, especially when the time dependence of the traps is included. It is necessary to consider the charging/discharging time of the surface traps since the quantitative density of surface charges will determine the degree of surface depletion. The process is frequency dependent and affects the RF operation of the device.

The model has also been extended to include the thermal activation of dopants. This is necessary since the relatively high activation energy of the impurities results in few free charges at room temperature. For example, at room temperature only about 0.01% of the boron atoms in a p-type diamond MESFET structure may be activated. The model predictions are being compared to experimental data provided by Kobe Steel on their recently reported diamond MESFET.

### **III. Results**

The NCSU MESFET model under development incorporates all dominant physical effects simultaneously. Effects such as electric field or energy dependent carrier mobilities, generation and recombination mechanisms, and thermal effects are being included in the formulation. Formulation of the model is continuing and preliminary predictions on the effects of surface depletion have been obtained.

The diamond MESFET reported at the recent Device Research Conference by researchers from Kobe Steel is being simulated. This device is formed from polycrystalline p-type diamond and demonstrates current saturation. The initial simulation results did not provide satisfactory results and the simulation study is continuing. The initial attempts to simulate the structure resulted in predicted drain currents about 3 orders of magnitude larger than measured. The reasons for the large discrepancy are under investigation. Possible reasons for the errors include: (1) underestimation of the surface depletion phenomenon, (2) neglect of possible substrate trapping phenomenon, (3) errors in determining the free charge density from the activation model, (4) underestimation of parasitic resistance effects, and (5) underestimation of the charge transport degradation caused by grain boundaries. Each of these areas have been investigated. The surface depletion phenomena could have a significant effect since the high resistivity of the channel semiconductor results in very significant channel depletion due to surface trapping. Charge transport by space-charge-limited flow is likely. An analogous effect occurs at the interface between the conducting channel and the substrate. The combination of surface and substrate trapping could result in much reduced channel current. The activation mechanism has been investigated and is not thought to be a main problem since the activation is fairly well known. Small deviations would produce slight current variations, but this is easily accounted for by adjustments to the activation energy. The increased scattering due to grain boundaries has also been investigated. The grain boundaries introduce additional scattering locations that can significantly reduce mobility and saturated velocity. The largest effect is upon mobility, which for this device is in the range of 1-10 cm<sup>2</sup>/V-sec. This phenomenon can account for about one order of magnitude of the discrepancy, but not the three orders of magnitude so far observed. Currently, the effects of large parasitic resistance are being investigated. It is possible that the techniques used to measure the contact resistivity of the source and drain contacts significantly underestimate the actual resistivity. The ohmic contact involves generation of a graphite layer between the ohmic metal and the p-type channel material.

Although it was expected that the contact resistivity is in the range of  $10^{-3}$ - $10^{-4}$   $\Omega$ -cm<sup>2</sup>, it is possible that the actual value is significantly larger. If so, a large source resistance could result and this would, in turn, produce a significantly reduced channel current. It is felt that a large source resistance is a likely contributor to the low magnitude of channel current observed in the experimental data. The model is being modified to investigate the low channel current observed. Since the diamond MESFET has a current capability 3 orders of magnitude larger than actually measured, it is felt that significant improvements will result once the reasons for the low current are determined. The model will be fit to the experimental data to determine the parameters responsible for the low current.

A pn junction gate model is also being formulated for inclusion into the device model. The JFET model will allow investigation of these devices, as well as serve as a foundation for development of a heterojunction model. It is believed that heterojunctions of diamond and other semiconductors, such as cBN, may offer improved performance. The goal will be to increase free carrier density by injecting charge across the heterojunction. The injected charge should be able to make use of the excellent transport properties of the diamond to produce a high current structure.

#### **IV. Conclusions**

The operation of a p-type diamond MESFET is under investigation. The investigation is directed towards the development of a physical model for the device. The model is being formulated to include all physical phenomena known to be of significance to device operation. Of particular interest is an accurate simulation of gate breakdown, including both gate tunneling and avalanche breakdown. Also, a thermal activation model has been formulated and included into the model. This model allows calculation of the free charge density in the diamond layers as a function of temperature. Work is under way to simulate the performance of the Kobe p-channel MESFET reported at the recent Device Research Conference. Initial calculations predicted a much larger drain current than actually

measured. The reasons for the discrepancies are under investigation. A pn junction gate model is also being formulated so that the operation of diamond JFET's can be investigated.

## **V. Future Research Plans and Goals**

The surface model will be further expanded and refined. The initial formulation is concentrating upon an electron hopping mechanism in which charge conduction occurs by trap-to-trap transfer. Continuum mechanics are being applied to particles in the surface energy bands. The stochastic transfer of particles to adjacent states appears at the macroscopic level to be continuous, with the effect of the lattice being combined into the effective mass of the particle. Therefore, the particle behaves as if it has an effective mass which is related to the curvature of the appropriate energy band. Charge packets propagate and disperse in a Gaussian shape. The packet moves in time if there is an applied field, and simultaneously disperses due to mutual repulsion of the carriers in the packet. Transport in a disordered medium is markedly different from an ordered semiconductor. The full nature of this is being investigated.

The Kobe diamond MESFET will continue to be investigated in an effort to determine the reasons for the low current measured compared to the simulations. A likely reason for the discrepancy between the simulated and measured data is the source resistance. This phenomenon is under investigation. Also, the effects of surface trapping will be further investigated. It is felt that significant improvements in the drain current may be possible once the reasons for the low value of current measured are understood. Development of the JFET model will also continue.

## **XVI. Modeling of Microwave MESFET Electronic Devices Fabricated from Semiconducting Diamond Thin Films-II**

### **A. Introduction**

The NCSU physics-based MESFET model [3] has been extended to other device structures and materials by interfacing it with PISCES-IIB and an advanced model of breakdown being incorporated into a separate version of the code.

Consideration of insulated-gate FETs and other structures is important for this MESFET project because of the present difficulty producing good metal-semiconductor junctions with diamond. During development of the model, validation requires comparison with experimental measurements and much of the existing diamond device data is for insulated-gate FETs.

Thermal effects are important for devices using diamond as a material because of its potential for high temperature operation and because of the high activation energy of the usual doping, boron. PISCES-IIB [4] is a general two-dimensional device simulator developed at Stanford, as currently enhanced and supported by Silvaco International. This combined system was begun in summer of 1992 and is still under development.

As of March, 1993, the new model is capable of reproducing experimental DC IV curves and predicting RF performance of experimental diamond FETs at a wide range of temperatures with proper treatment of incomplete activation effects.

The combined system successfully reproduced DC IV curves for three experimental FETs fabricated in monocrystalline and polycrystalline diamond. Boron was the acceptor impurity in all three experimental p-type MOSFETs, but the three devices were of diverse origin and structure. The first was fabricated from naturally occurring single-crystal diamond that has been ion-implanted [2]; the second from homo-epitaxially grown single crystal diamond [1]; and the third from epitaxially grown polycrystalline diamond [5]. For all three cases, the new code modeled incomplete activation and extended previous MESFET simulations to monocrystalline and polycrystalline MOSFETs. Previous simulations predicted substantial increase in output power for single crystal MESFETs [6] using the NCSU large-signal MESFET model, but those predictions assumed complete carrier activation. RF predictions were produced somewhat later, but the simulated RF performance was poor for the experimental devices.

Most recently, encouraging DC and RF simulations were performed for a proposed MESFET design. These results will be presented for the first time in this report.

The advanced breakdown model, which includes both surface and avalanche currents, was begun in spring 1992 and has continued. In future work, we will combine thermal effects and breakdown effects.

## B. Investigation Procedure

Our experimental approach was to replace the intrinsic FET model of TEFLON, the NCSU large-signal MESFET simulator [3] with a model of the MOSFET written in Pisces-II [4].

TEFLON combines a sophisticated analytic approximation of the physics in the gate region of a MESFET with harmonic balance to predict large-signal RF performance of realistic microwave circuits.

The physics of the diamond MOSFET channel is similar to the physics currently modeled by TEFLON for the GaAs MESFET. The questions of interest for large-signal or RF applications of diamond MOSFETs are also similar to those addressed by TEFLON, such as predicting gain as a function of input power, estimating power-added efficiency, and calculating output power into saturation. Realistic high-frequency simulation of a FET must include an embedding circuit, which we modeled conventionally as linear, lumped-element input and output microwave circuits. We use the harmonic balance routines of TEFLON to solve the nonlinear FET circuit simultaneously with the linear embedding circuit. In addition, we include realistically adjusted values for parasitic elements around the intrinsic FET.

TEFLON is a quasi-static approximation that used dc values of currents and capacitances  $I_d$ ,  $I_g$ ,  $C_{gs}$ , and  $C_{ds}$  tabulated as function of the biases  $V_{gs}$  and  $V_{ds}$ . These values are computed using Pisces IIB, accounting for incomplete carrier activation.

Pisces is a two-dimensional device modeling and simulation program developed at Stanford [4]. Pisces employs a finite-difference approach which is too slow to be directly interfaced with a harmonic balance routine. However, Pisces is well suited to analysis of dc device behavior, including the estimation of I-V curves and gate capacitances. Pisces supports some RF simulations with simple embedding circuits, but not the rich set of RF circuit simulations that TEFLON supports.

We have developed a combined simulation program including Pisces to simulate dc I-V curves and other relevant dc behavior in the diamond MOSFET gate region, TEFLON to simulate RF behavior from dc I-V curves, and an interface between the two programs.

## C. Results

We have validated on data from three actual devices of diverse origin and structure. Experimental p-type MOSFETs have been fabricated from naturally occurring single-crystal diamond that has been ion-implanted [2], from homo-epitaxially grown single crystal diamond [1], and from epitaxially grown polycrystalline diamond [5]. Boron was the acceptor impurity in all the devices. We are not aware of device quality n-type diamond at this time.

We have validated the PISCES part of the simulator with dc measurements of three different diamond FETs:

1. a boron-doped homoepitaxially grown single-crystal device fabricated at Penn State [1],

2. an ion-implanted homoepitaxially grown single-crystal device fabricated at the Naval Ocean Systems Center (NOSC) [2], and
3. a boron-doped heteroepitaxially grown polycrystalline diamond fabricated at Kobe Steel Electronic Materials Center in North Carolina [5].

We have also considered a diamond JFET device.

The Penn State device reported by Grot, Gildenblat, and Badzian is a recessed gate naturally doped p-type MOSFET [1]. This device was fabricated using ECR plasma etching of an active layer. Most of the parameters required for the simulation were reported: oxide thickness of 100 nm, gate length of 5 micron, gate width of 30 micron, active layer thickness of 0.8 micron, recess depth of 0.2 micron. The doping concentration of the active layer was determined to be about  $1.2 \times 10^{16} \text{ cm}^{-3}$ . This number corresponds to 0.1% hole ionization at room temperature.

The dc simulation was performed at a temperature of 473°K so that a direct comparison with the experimental results could be performed. Because measured hole mobility of 280  $\text{cm}^2/\text{V}\text{-sec}$  was given only at room temperature in the Penn State report, the mobility was adjusted for high temperature operation. Alternative physical models were considered and sensitivity to material parameters was numerically explored.

It was found that an incomplete ionization model was most critical for agreement between simulation and measured data. Good simulation of the diamond single-crystal device required a high value of acceptor energy level ( $E_a=0.37 \text{ eV}$ ). Figure 1 shows the I-V curve simulated at  $V_g=0$  and  $V_g=70 \text{ v}$ . The drain current at  $V_{ds}=-50 \text{ v}$  for zero gate bias and  $V_{ds}=70 \text{ v}$  are about  $5.2 \mu\text{A}/\mu\text{m}$  and  $2.8 \mu\text{A}/\mu\text{m}$ , respectively. These values are in good agreement with the experimental results of  $3.8 \mu\text{A}/\mu\text{m}$  and  $1.0 \mu\text{A}/\mu\text{m}$ , respectively.

The NOSC device reported by Hewett, et. al. is an ion-implanted p-type Insulated-Gate FET fabricated from a single crystal thin film diamond, epitaxially grown on a naturally occurring diamond substrate [2]. A multiple implant scheme was used to provide an approximately uniformly doped active layer of about 210 nm in thickness. The device was fabricated in a concentric ring structure with 1000  $\mu\text{m}$  wide gate in outer diameter (600  $\mu\text{m}$  of inner diameter). The gate length was 1  $\mu\text{m}$ . All the materials parameters and physical model functions were the same as before, except that the room temperature free hole concentration and mobility were taken to be the measured values of  $5 \times 10^{15} \text{ cm}^{-3}$  and 30  $\text{cm}^2/\text{V}\text{-sec}$ , respectively.

The I-V characteristics at room temperature are shown in Figure 2. Current saturation is clearly observed. The simulated I-V curves agree with experiment, except for pinch-off. Pinch-off in the actual device was observed at a gate bias of approximately +12 v, but is harder to obtain in simulation. This may be due to our simple models of free carrier density and mobility in the multiply ion-implanted device. Actual doping profiles are not uniform. In future

PISCES - II 9009R

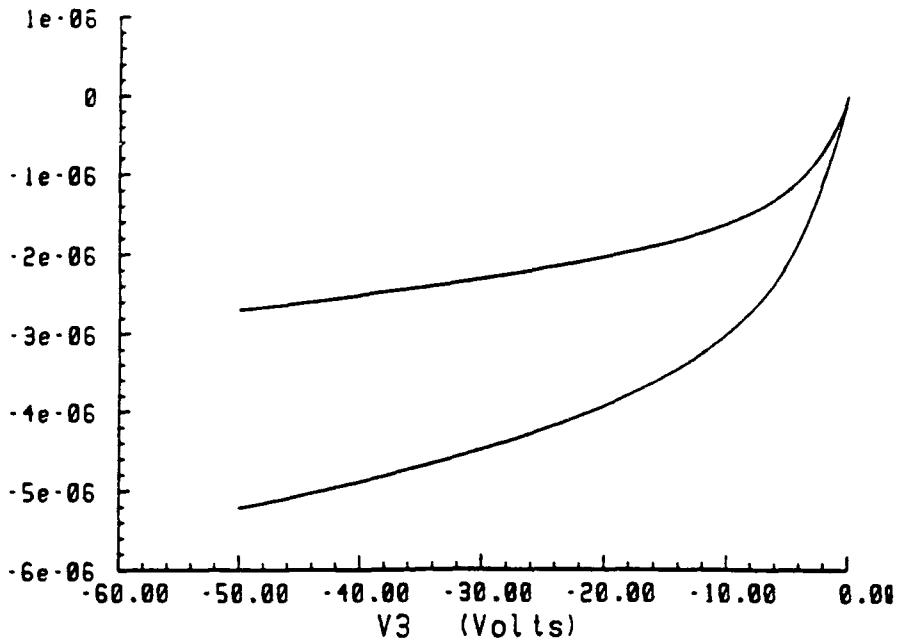


Figure 1. Drain current versus drain voltage for the Penn State device for  $V_g = 70$  v (top curve) and  $V_g = 0$  v (bottom curve).

PISCES - II 9009R

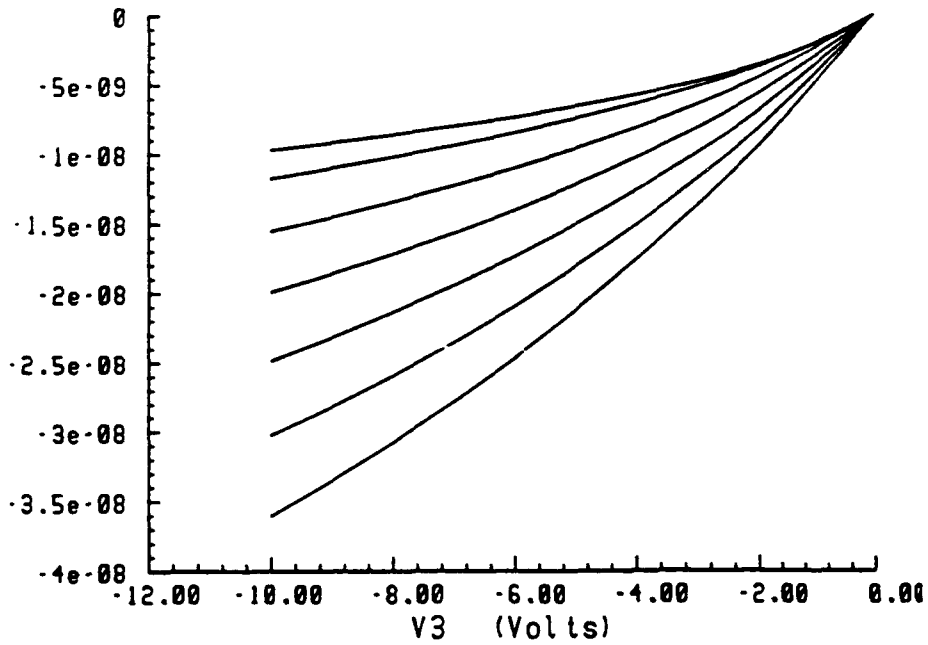


Figure 2. Drain current versus drain voltage for the NOSC device for  $V_g = 12$  v (top curve) to  $V_g = 0$  v (bottom curve) in steps of 2 v.

research, we will use optimization techniques to obtain more accurate and realistic values for the material parameters from the performance of the diamond devices.

The Kobe device reported by Tessmer et. al. is a synthetic device [5]. This was the first device which exhibits saturation and pinch-off in a polycrystalline diamond FET. A 0.5  $\mu\text{m}$  thick active layer of p-type diamond was grown by adding diborane in the gas phase. Boron concentration was measured to be about  $7 \times 10^{16} \text{ cm}^{-3}$ . The device was fabricated in a concentric ring structure with nominal gate length of 2  $\mu\text{m}$  and gate width of 314  $\mu\text{m}$ .

The I-V characteristic at 423  $^{\circ}\text{K}$  shows pentode-like behavior, as indicated in Figure 3. The drain current is very low, about 10 pA/mm at  $V_g=0 \text{ v}$  and  $V_{ds}=-20 \text{ v}$ . The simulated and measured data are in good agreement.

The simulations indicate that polycrystalline diamond may have an effective boron activation energy of about 0.65 eV, rather than the 0.37 eV expected for single crystal material. The increase may be due to the trapping of carriers at the grain boundaries at doping concentrations of around  $7 \times 10^{16} \text{ cm}^{-3}$ . This would indicate a barrier height at the grain boundary of about 0.3 eV in this device (grain size of 3  $\mu\text{m}$ ).

We have also conducted preliminary simulations of a diamond JFET assuming that an n-type dopant may be found. Figure 4 shows that at room temperature, the I-V characteristics of diamond JFETs shown strong space-charge limited behavior. At higher temperature, the behavior may become more pentode-like due to an increased number of free carriers. Also, the shape of the I-V curve is sensitive to the geometry of the channel, i.e., the gate length to the channel width ratio.

#### D. RF Performance Predictions

The RF simulations performed for the NOSC device in the previous section produced disappointing results. This monocrystalline, homoepitaxial, insulated-gate FET fabricated at NOSC and reported by Hewett, et al. has a gate capacitance of about 0.3 pF, which is reasonable for the structure, but is disproportionately large compared to a very low value of  $I_{dss}=45 \text{ mA}$  for a 1000  $\mu\text{m}$  gate width device. This unfortunate condition at room temperature results from low carrier activation and low mobility.

Monocrystalline diamond with high mobility will appear as the technology progresses. With improved materials, better metal-semiconductor junctions may also appear. Much better RF performance is likely for diamond MESFETs with higher mobility and possibly higher operating temperatures. In order to investigate this possibility, the device of Figure 5 was simulated with the parameters at three temperatures as shown in Table I. The DC IV characteristics for operation at 300  $^{\circ}\text{C}$ , 500  $^{\circ}\text{C}$  and 650  $^{\circ}\text{C}$  are shown in Figures 6, 7, and 8, respectively. The increase in channel current and transconductance at elevated temperature is due to the increase in activation. In particular, the performance improvement at 650  $^{\circ}\text{C}$  is most

PISCES - II 9009R

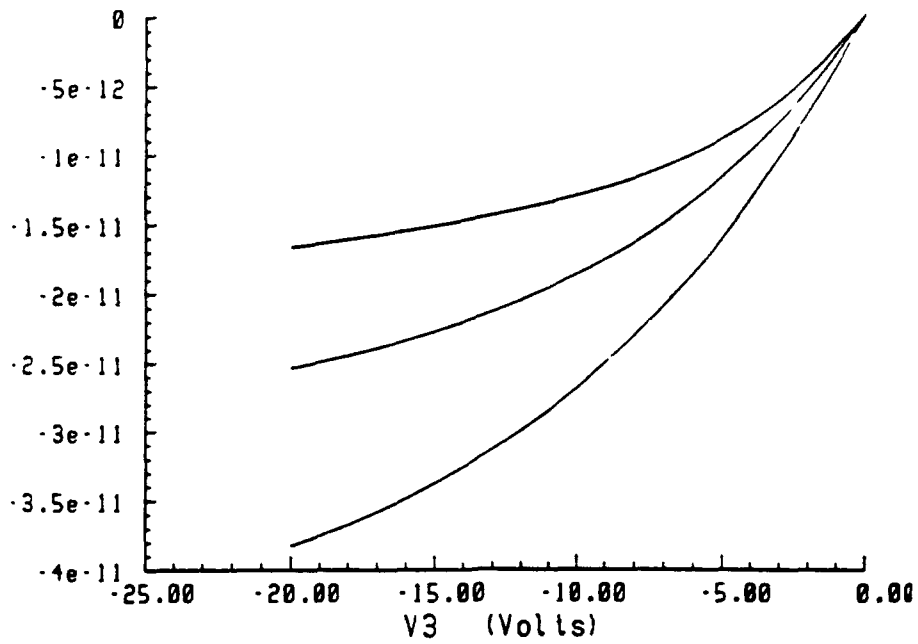


Figure 3. Drain current versus drain voltage for the Kobe Device at  $T=423$  °K for  $V_g=10$  v (top curve) to  $V_g=0$  v (bottom curve) in steps of -5 v.

PISCES - II 9009R

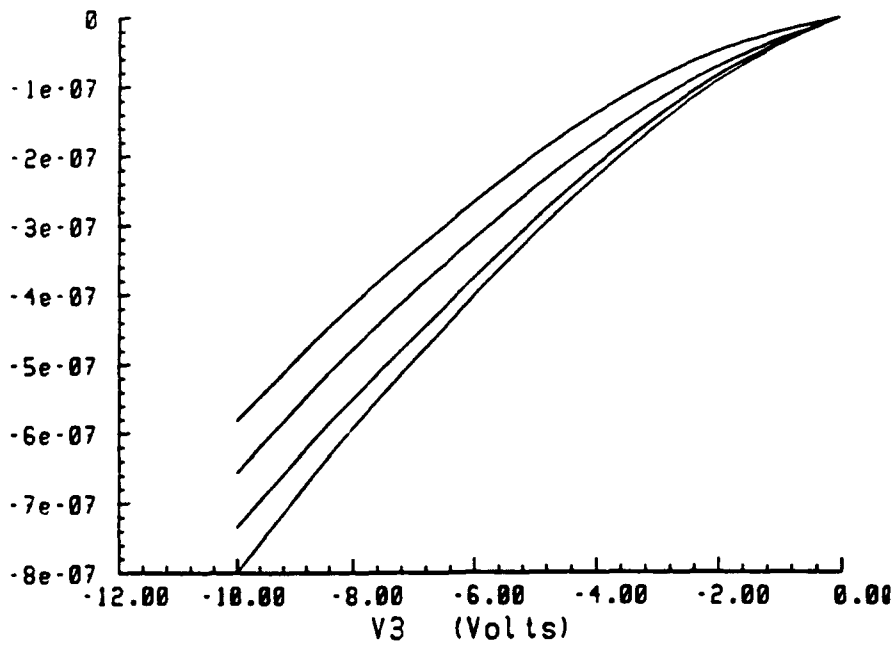


Figure 4. Triode-like drain current versus drain voltage for the diamond JFET for  $V_g=6$  v (top curve) to  $V_g=0$  v (bottom curve) in steps of -2 v.

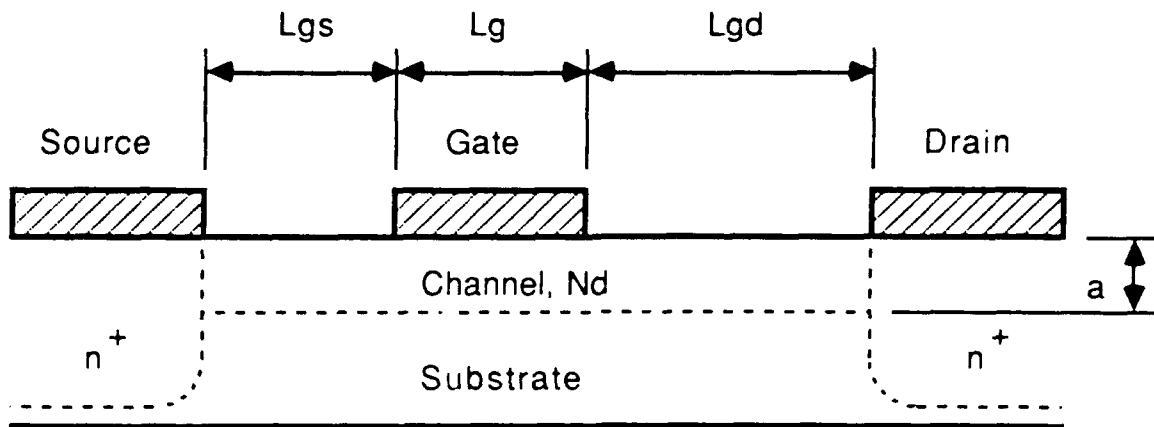


Figure 5. Structure for a proposed P-channel diamond MESFET.

Table I. MESFET Parameter Values

Parameter	Value		
	300°C	500°C	650°C
$L_g$ ( $\mu m$ )	0.5	0.5	0.5
$W$ (mm)	1	1	1
$L_{ds}$ ( $\mu m$ )	1	1	1
$L_{gs}$ ( $\mu m$ )	1	1	1
$N_d$ ( $cm^{-3}$ )	$4 \times 10^{17}$	$4 \times 10^{17}$	$4 \times 10^{17}$
$n^+$ ( $cm^{-3}$ )	$10^{19}$	$10^{19}$	$10^{19}$
$a$ ( $\mu m$ )	0.15	0.15	0.15
$\Phi_{bi}(Au)$ (eV)	1.71	1.68	1.68
$R_c$ ( $\Omega \cdot cm^{-2}$ )	$\sim 10^{-4}$	$\sim 10^{-4}$	$\sim 10^{-4}$
$\mu_p$ ( $cm^2/V \cdot sec$ )	600	100	83
$v_s$ (cm/sec)	$1.08 \times 10^7$	$0.86 \times 10^7$	$0.83 \times 10^7$
$\kappa_{th}$ (W/°K-cm)	30	14	11
$\Theta$ (°K/W)	0.73	1.57	2.03

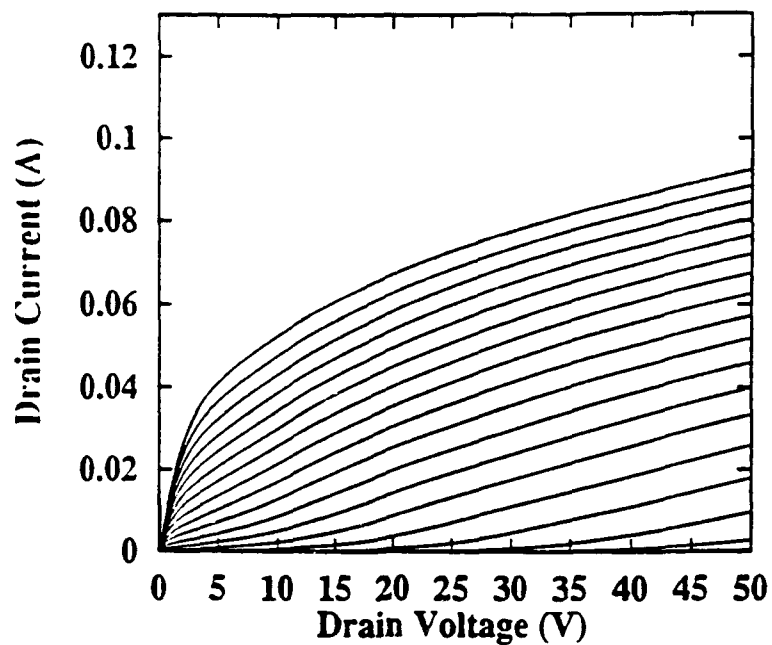


Figure 6. DC I-V Characteristics for the P-Channel MESFET at 300 °C (Gate Bias Voltages start at  $V_g=0$  v and are in 1 v steps).

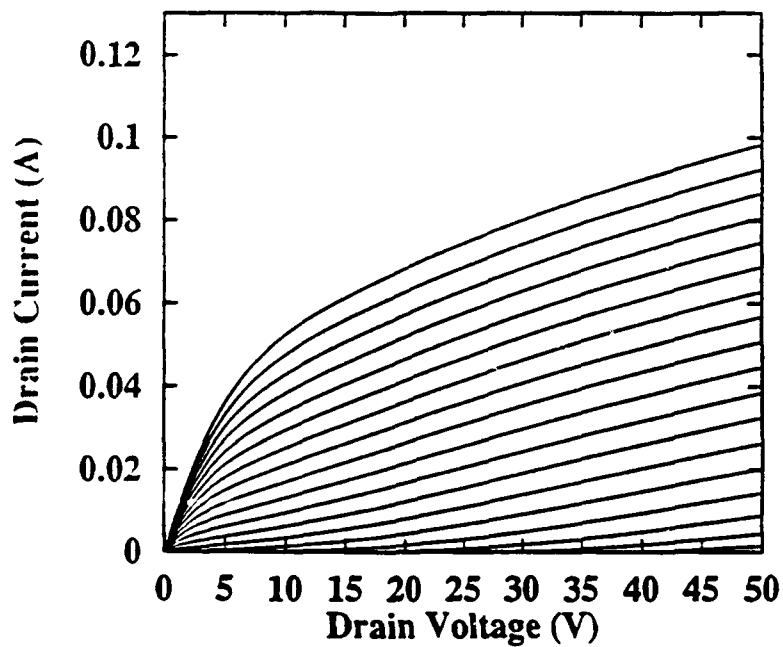


Figure 7. DC I-V Characteristics for the P-Channel MESFET at 500 °C. (Gate Bias Voltages start at  $V_g=0$  v and are in 1 v steps).

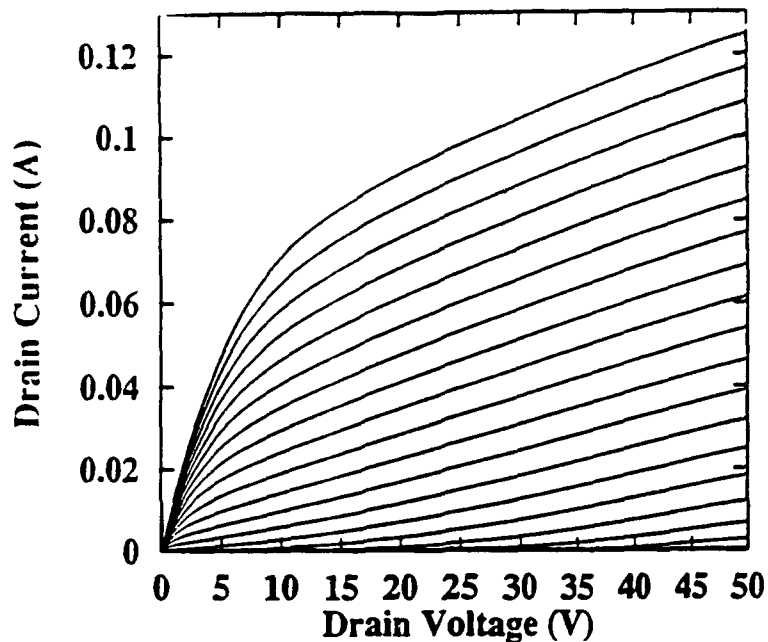


Figure 8. DC I-V characteristics for the P-channel MESFET at 650 °C. (gate bias voltages start at  $V_g=0$  v and are in 1 v steps).

pronounced due to significant activation of charge carriers at this temperature. The increase in free hole density dominates over the decrease in hole transport at the elevated temperature. RF simulations for the device operated in a class A amplifier at 4 GHz are shown in Figures 9, 10, and 11 for operation at the three temperatures. As shown, the diamond MESFET is capable of good RF performance. The device produces about 25.5 dbm of RF output power and about 17% power-added efficiency, essentially independent of operation temperature. Again, this is due to increased activation compensating for reduced hole transport at the elevated temperature. The linear gain increases from about 5 db at 300° C to about 8 db at 650° C. These results are encouraging and indicate that diamond power MESFETs have significant potential, especially for high temperature operation where devices fabricated from conventional semiconductors cannot be operated.

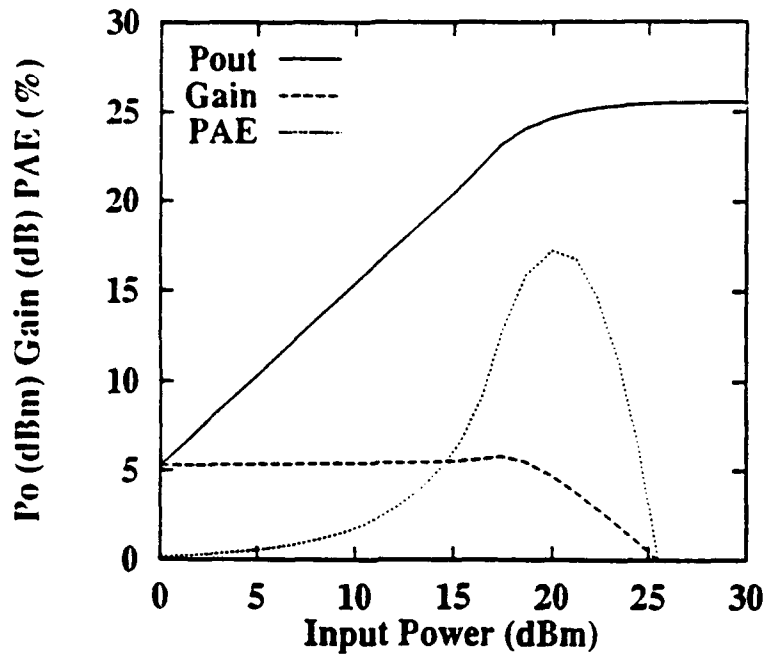


Figure 9. RF Performance for the P-Channel MESFET at 300 °C.

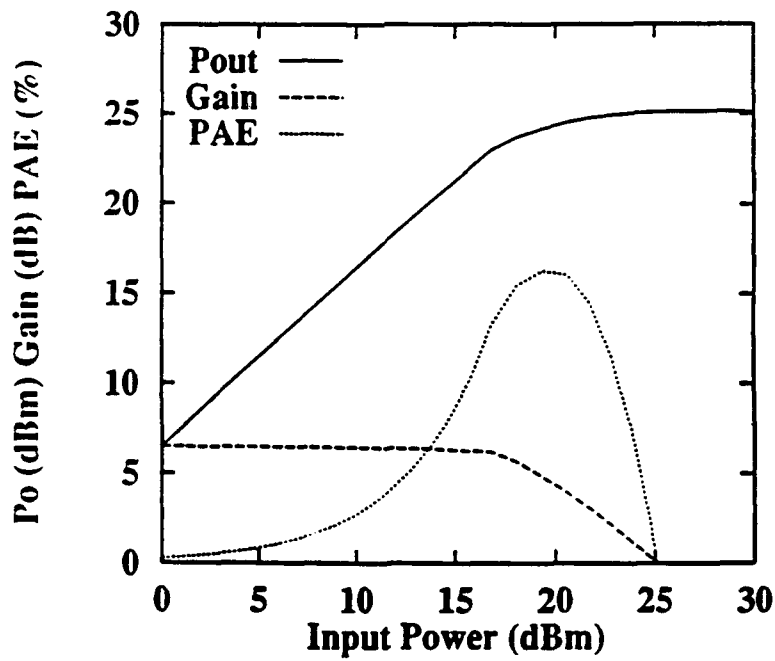


Figure 10. RF Performance for the P-Channel MESFET at 500 °C.

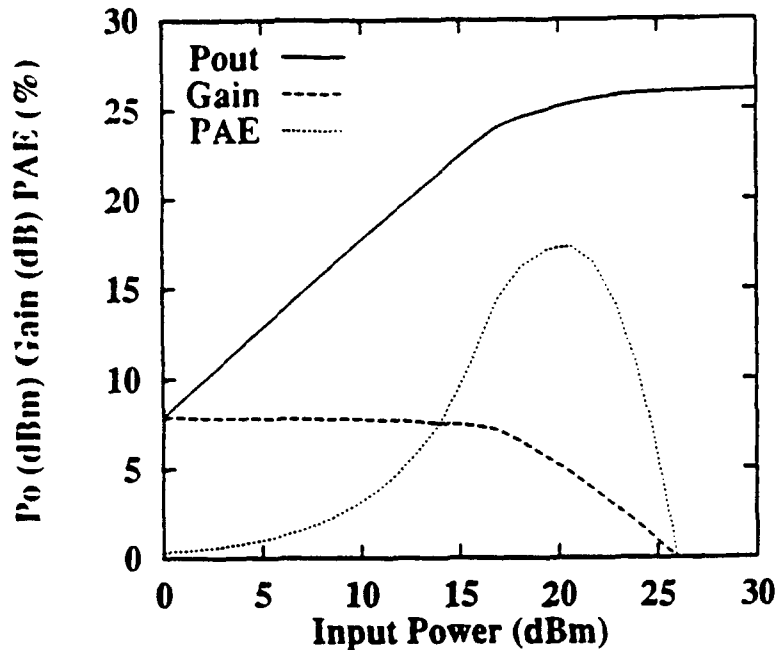


Figure 11. RF performance for the P-channel MESFET at 650 °C.

#### E. Discussion

Our simulated dc I-V curves for each device agree well with the corresponding measurements as shown in the Figures. Pentode-like or triode-like behavior occurs at the appropriate active carrier levels. The active carrier density depends upon doping level and temperature because of the dependence of activation on temperature. There also appears to be significant dependence of the shape of the I-V curves on bound charge at the interface because of backgating. Since bound charge depends upon processing and fabrication technology, the simulations may require recalibration for different fabrication processes.

The DC curves at all three temperatures indicate high currents with the highest currents at the highest temperature (650 °C). As the temperature rises, two antagonistic effects compete. The carrier activation increases and the mobility decreases. It appears that the two effects cancel to large extent, as observed in the essentially temperature independent DC and RF performance.

#### F. Conclusions

Polycrystalline and monocrystalline diamond FETs have been numerically modeled. Agreement with experiment confirms present understanding of the major physical processes in these devices. Allowing for the tradeoff between increased activation and reduced mobility, promising RF performance is predicted for diamond FETs.

### G. Future Research Plans and Goals

Single-crystal diamond MESFETs will be simulated in more detail. The effects of bound charge at the surface and the channel/substrate interface will continue to be investigated. The RF operation of the devices over a range of operating temperatures will be further examined.

### H. References

1. S. A. Grot, G. S. Gildenblat, and A. R. Badzian, "Diamond Thin-Film Recessed Gate Field-Effect Transistors Fabricated by Electron Cyclotron Resonance Plasma Etching," *IEEE Electron Dev. Lett.*, **13**, 462-464, 1992.
2. C. A. Hewett, C. R. Zeisse, R. Nguyen, and J. R. Zeidler, "Fabrication of an Insulated Gate Diamond FET for High Temperature Applications," *First International High Temperature Electronics Conf.*, 168-173, 1991.
3. M. A. Khatibzadeh and R. J. Trew, "A Large-Signal Analytic Model for the GaAs MESFET," *IEEE Trans. Microwave Theory Tech.*, **MTT-36**, 231-238, 1988.
4. M. R. Pinto, C. S. Rafferty, H. R. Yeager, and R. W. Dutton, "Pisces-II Technical Report," Stanford Electronics Laboratory, Stanford University, 1985.
5. A. J. Tessmer, L. S. Plano, and D. L. Dreifus, "Current Voltage Characteristics of In-Situ Doped Polycrystalline Diamond Field Effect Transistors," *Technical Report*, Kobe Steel, USA, Electronics Materials Division, 1992.
6. R. J. Trew, J. B. Yan, and P. M. Mock, "The Potential of Diamond and SiC Electronic Devices for Microwave and Millimeter-Wave Power Applications," *Proc. IEEE*, **79**, 598-620, 1991.

## XVII. The role of geometric considerations in the diamond-cubic boron nitride heteroepitaxial system

M. W. H. Braun,<sup>\*)</sup> H. S. Kong, J. T. Glass, and R. F. Davis  
*Department of Materials Science and Engineering, North Carolina State University,  
 Raleigh, North Carolina 27695*

(Received 20 August 1990; accepted for publication 16 November 1990)

We report the methods and results of a theoretical study of the diamond-cubic boron nitride [BN<sub>cub</sub>] heteroepitaxial system. We introduce a general, geometric reciprocal space technique for evaluating candidate epitaxial configurations, and a novel system of essentially geometric criteria to order them from most to least likely to occur. In the diamond-BN<sub>cub</sub> system, it is found that low index like planes require a relatively small strain of 1.37% from bulk parameters. The unlike epitaxial configuration which pairs diamond{100} with BN<sub>cub</sub>{221} and yields two-dimensional coincidence with the same strain is favored above other low index mixed configurations. The essentially geometric nature of this epitaxial system is highlighted.

Diamond has a unique combination of properties including high thermal conductivity, large breakdown voltage, high electron saturated drift velocity and reasonably high carrier mobilities<sup>1-3</sup> which gives it a significant technological potential. However, the growth of single-crystal diamond films on economically viable nondiamond substrates remains a significant obstacle to exploitation. Currently, only two epitaxial systems are known, specifically diamond deposition on diamond<sup>4,5</sup> and on cubic boron nitride [BN<sub>cub</sub>].<sup>6-8</sup> For the latter, an oriented three-dimensional island growth is observed which leads to a single-crystal film after the islands coalesce, proving the feasibility of heteroepitaxial growth.

The general condition for the formation of an epitaxial monolayer may be formulated as an inequality requiring a free energy reduction, as<sup>9</sup>

$$\gamma_0 - \gamma_s + \gamma_1 < 0 \quad (1)$$

where  $\gamma_0$  and  $\gamma_s$  are the surface free energy of the overgrowth and substrate, respectively, and  $\gamma_1$  is the energy associated with the formation of the interface. In the presence of misfit the last term contains the competing *elastic strain energy* in the monolayer and *misfit energy* of interfacial disregistry, which depend on the interface geometry. To examine the diamond-BN<sub>cub</sub> system we introduce a general geometric method for searching for candidate epitaxial configurations, and essentially geometric conditions with which the candidate configurations may be ordered by how much they potentially lower the interfacial energy,  $\gamma_1$ .

The method is applied to the matching conditions of the low index like faces of diamond and cubic boron nitride as well as the mixed face pairs of diamond {100}, {110}, {111}, {112}, {114}, and {120} on BN {221} and diamond {110} on the BN{120} face, diamond {100} on BN{110}, and diamond {100}, {110}, and {111} on the BN{112} faces. Some unique aspects of the diamond {100}, BN{221} pair are highlighted.

In the van der Merwe-Reiss model<sup>10,11</sup> both components of any bicrystal system are considered rigid, retain their bulk lattice structures and parameters, and are in contact at a single interfacial plane. Each component crystal has unique translational and rotational symmetries, which, in our generalization, are described by the infinite sets of wave vectors forming the surface reciprocal lattices of each crystal face.

From the model<sup>12,13</sup> an expression for the reduction in misfit energy is obtained when the adatom-substrate interaction energy is summed over all the overgrowth atoms, as

$$\sum_{\substack{h,k \\ (h,k) \neq (0,0)}} V_{hk} F_{hk} \frac{\sin \pi(2M+1)p(h,k)}{\sin \pi p(h,k)} \times \frac{\sin \pi(2N+1)q(h,k)}{\sin \pi q(h,k)} \quad (2)$$

with  $h, k$  integer indices of substrate reciprocal lattice vectors.  $V_{hk}$  are Fourier coefficients in an expansion of the overgrowth-substrate interaction energy,  $(2M+1)$  and  $(2N+1)$  are the number of rows and columns of overgrowth lattice points in the overgrowth island respectively,  $F_{hk}$  are structure factors arising from the detailed atomic arrangement in the substrate and overgrowth unit cells, and  $p(h,k)$  and  $q(h,k)$  are the components of the substrate reciprocal lattice vector,  $\mathbf{q}_{hk}$  expressed in the overgrowth reciprocal lattice.

The interaction energy is sharply minimized when  $p$  and  $q$  are integers, which yields a necessary condition for minimum misfit energy. When formulated in reciprocal space<sup>13,14</sup> this means that a *substrate reciprocal lattice vector*  $\mathbf{q}_{hk}$  *must coincide with an overgrowth reciprocal lattice vector*,  $\mathbf{q}^{pq}$  that is,

$$\mathbf{q}_{hk} = \mathbf{q}^{pq} \quad (3)$$

This defines the orientation and associated ratio of lattice constants at which the interfacial misfit energy is minimized without strain. By allowing a system to strain to

<sup>\*)</sup>Permanent address: Department of Physics, University of Pretoria, Pretoria, South Africa.

satisfy Eq. (3) the strain subject to energy minimization may be calculated directly.

Additionally, the model provides useful essentially geometric ordering conditions: (a) a lower energy follows from more resonating terms in the expression (2), and hence the optimum configuration will have a high *relative density of coinciding reciprocal lattice points*, (b) as the magnitude of Fourier coefficients tends to decrease rapidly with order ( $|h| + |k|$ ),<sup>15</sup> shorter resonating reciprocal lattice vectors increase the likelihood of the actual occurrence of the particular epitaxial configuration, (c) the strains to satisfy Eq. (3) may be calculated directly from the reciprocal lattice and configurations with lower *strain energy density* are preferred.

The search method obtained from Eq. (3) is implemented as follows in an interactive computer program ORPHEUS. Briefly, the program produces scaled plots of the substrate and overgrowth reciprocal lattices and interactively leads the user through a construction analogous to the Ewald construction of crystallography. By selecting a substrate reciprocal vector,  $q_{hk}$ , and rotating it 360° about the origin, it constructs a circle. Any overgrowth point lying on this circle describes an overgrowth reciprocal lattice translation vector,  $q^{pq}$  equal in length to  $q_{hk}$ . The angle between  $q^{pq}$  and  $q_{hk}$  determines the angle through which the overgrowth must be rotated to come into epitaxial orientation with the substrate. The strains needed to bring a vector nearly on the circle into coincidence and the associated energy are calculated from the components of the selected vectors. Plots showing the subsequent reciprocal lattices in coincidence are produced by the program, from which quality judgements of the density of points which coincide may be made. Examples are given in the accompanying figures.

To apply the method described above, we have used primitive surface lattices where possible to avoid complications with structure factors due to nonprimitive unit cell constructions. The results of Table I show that the two-dimensional pseudomorphic configuration, "P", [Fig. 1(a) shows diamond{100} on BN<sub>cub</sub>{100}] for like planes requires an isotropic extensive strain of 1.37% with zero misfit energy and a strain energy density of  $2.2 \times 10^9$  erg cm<sup>-3</sup>. This is only twice as high as the one-dimensional matching case, "P<sup>1</sup>" (typically,  $1.09 \times 10^9$  erg cm<sup>-3</sup>), which has potentially higher misfit energy. Second best is the diamond{100} on the BN<sub>cub</sub>{221} case [Fig. 1(b)], identical in strain energy to pseudomorphic cases, but with increased misfit energy, due to coincidence matching, "P<sup>-2</sup>". In this case all overgrowth reciprocal lattice vectors match substrate vectors, but some substrate vectors do not have counterparts in the overgrowth reciprocal lattice. Of other unlike pairs, the diamond{100} on BN<sub>cub</sub>{112} configuration [Fig. 1(c)] has a two-dimensional configuration with a strain energy density of  $1.35 \times 10^9$  erg cm<sup>-3</sup> comparable to the one-dimensional case. However, this is a rather high order coincidence match, "(2)" in which every fifth substrate reciprocal lattice point coincides with every second overgrowth point resulting in an increased misfit energy contribution from surface energy mismatch. The

TABLE I. High-order matched epitaxial configurations with low strain energy for selected planes where diamond forms the overgrowth and cubic boron nitride the substrate. Two-dimensional epitaxial configurations are ranked from pseudomorphic, "P", through coincidence matching, "P<sup>-2</sup>", where all overgrowth reciprocal lattice vectors match substrate vectors, but some substrate vectors do not have counterparts in the overgrowth, to high-order coincidence match, "(2)" where there exist unmatched points in both lattices, with increased misfit energy. In "P<sup>1</sup>" all substrate reciprocal vectors match overgrowth points in one direction but direct lattice positions along equally spaced parallel rows of atom sites are not in coincidence.

Planes		Parallel rows		Energy density ( $\times 10^9$ erg cm <sup>-3</sup> )	Type
BN <sub>cub</sub> diamond	BN <sub>cub</sub>	Diamond	Diamond		
Like planes:					
<i>hkl</i>	<i>hkl</i>	[ <i>uvw</i> ]	[ <i>uvw</i> ]	1.09 <sup>a</sup>	P <sup>1</sup>
		[ <i>UVW</i> ]	[ <i>UVW</i> ] <sup>b</sup>	2.20	P
Unlike planes					
221	100	[ $\bar{1}\bar{1}4$ ]	[ $0\bar{1}1$ ]	1.09	P <sup>1</sup>
		[ $\bar{1}\bar{1}0$ ]	[ $0\bar{1}1$ ] <sup>b</sup>	2.20	P <sup>-2</sup>
112	100	[ $\bar{1}11$ ]	[ $0\bar{1}1$ ]	1.09	P <sup>1</sup>
		[ $\bar{1}\bar{1}0$ ]	[ $0\bar{1}1$ ] <sup>b</sup>	1.35	(2)

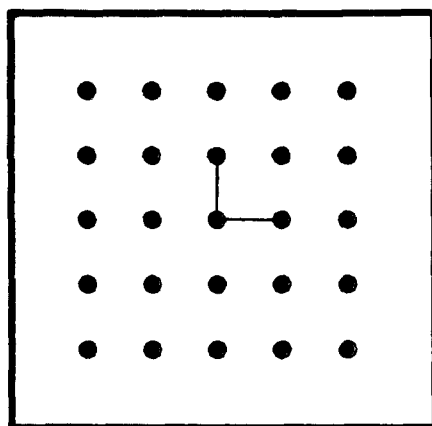
<sup>a</sup>This energy may vary by about 10% due to anisotropy in high order planes.

<sup>b</sup>These rows are parallel and equally spaced in addition to those of the P<sup>1</sup> configuration.

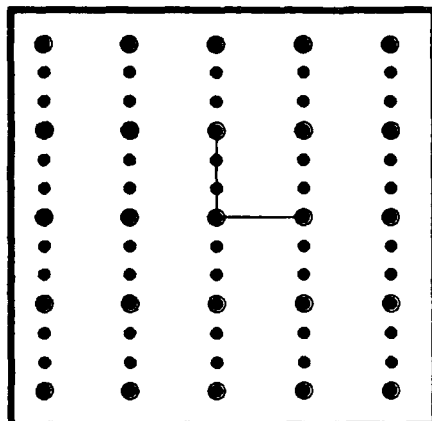
configuration may be better than any one-dimensional case, but compares unfavorably with pseudomorphic diamond{112} on BN<sub>cub</sub>{112}. No other two-dimensional configuration within such a low energy occurs. A similar hierarchy of one-dimensional configurations is listed in the tables (see Table II for additional configurations), where in "P<sup>1</sup>" all substrate reciprocal vectors match overgrowth points in one direction but where lattice positions along equally spaced parallel rows of atom sites are not in coincidence in direct space; in "P<sup>-1</sup>" some substrate vectors do not have partners. However none of these configurations are expected to compete with the like plane pseudomorphy, because of the low strain and zero misfit energies of the latter.

The experiments reported by Koizumi *et al.*,<sup>6</sup> Yoshikawa *et al.*,<sup>7</sup> and Murakami *et al.*<sup>8</sup> indicate results which agree well with the geometric considerations presented here. On the low-index substrates diamond prefers to grow in pseudomorphic arrangement rather than in the alternative but higher index coincidence planes. The experiments are not conclusive due to the limited size of the BN<sub>cub</sub> substrates (on the order of 100 μm) but indicate that diamond grew in a low-index {100} orientation in preference to a pseudomorphic {221} configuration on BN<sub>cub</sub>{221}. Which configuration actually occurs, is expected to depend on the surface energy differences of the growth islands and by kinetic factors such as growth rates of the different directions and planes.

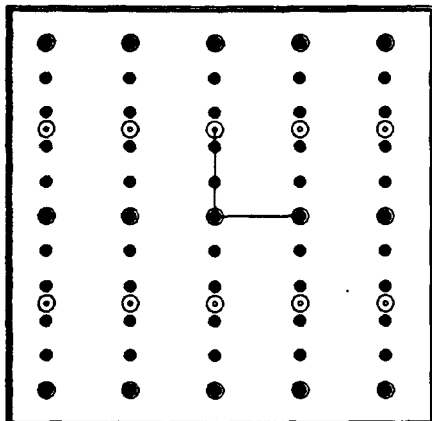
Experimental studies of diamond{100} on BN<sub>cub</sub>{112} configuration have not been reported, and the speculation is triggered whether diamond would tolerate epitaxial configurations only as far as the {100} on {221} P<sup>-2</sup> case. If so, this may indicate a threshold of mismatch beyond which diamond will not grow epitaxially. It should also be noted that a reduced surface energy mismatch might allow further progression down the hierarchy of



(a)



(b)



(c)

FIG. 1. Superimposed reciprocal spaces of the diamond and cubic boron nitride faces after strain. (a) {100} surfaces showing full pseudomorphism after isotropic strain of 1.37%, (b) diamond {100} and cubic boron nitride {221} surfaces, showing the coincidence matching after isotropic strain of 1.37%, (c) superimposed reciprocal lattices of the diamond {100} and cubic boron nitride {112} surfaces, showing the coincidence matching after strain of  $\epsilon_{xx} = 1.37\%$ ,  $\epsilon_{yy} = -0.68\%$ . The symbols having the following meanings:  $\bullet$  indicate matched overgrowth and substrate points,  $\circ$  are substrate reciprocal lattice points which do not have partners in the overgrowth,  $\odot$  are overgrowth points which do not have partners in the substrate.

configurations to one dimensional matching or other two dimensionally coincident cases with low strain energy density, supporting the search for other candidate substrates.

We have introduced a general technique for evaluating candidate epitaxial configurations and extended its useful-

TABLE II. Additional configurations for low-index unlike planes low in the hierarchy. B:  $\text{BN}_{\text{cub}}$  substrate and D: diamond overgrowth.

Planes		Energy density	Type	Planes		Energy density	Type
B	D	( $\times 10^9 \text{ erg cm}^{-3}$ )		B	D	( $\times 10^9 \text{ erg cm}^{-3}$ )	
110	100	1.09	$P^1$	120	110	2.06	$P^1$
112	110	None within 4% strain		112	111	None within 8% strain	
221	110	1.09	$P^1$	221	112	1.13	$P^1$
221	111	1.09	$P^1$	221	112	1.35	(2)
221	120	0.024	$P^1$				

ness by providing a system of essentially geometric selection criteria with which candidate configurations may be ordered by their potential to minimize interfacial energy. Nomenclature for this evaluation has also been developed and presented. When applied to the diamond-cubic boron nitride system, this technique correlates well with published experimental results indicating that this system is well described by the geometric considerations. In this case, heteroepitaxy of like planes has the greatest potential of minimizing interfacial energy, and is also the type of system most observed. The diamond{100}// $\text{BN}_{\text{cub}}$ {221} is next in potential, and appears to have been reported in the literature, although the observations are not conclusive. Diamond{100}/ $\text{BN}_{\text{cub}}$ {112} and one-dimensionally matched configurations are poorer and have not been reported experimentally. It is speculated that these configurations are too far down the hierarchy of configurations for this system.

The geometric considerations have been shown to have utility and potential as a tool for applied physicists for selecting candidates for epitaxial growth.

This work was supported in part by grants from SDIO/IST through ONR and the Office of Naval Research itself. One of us (MWHB) acknowledges the grant of sabbatical leave from the University of Pretoria and the financial burden carried by CEFIM at that university.

<sup>1</sup>These rows are parallel and equally spaced in addition to those of the  $P^1$  configuration.

<sup>2</sup>J. E. Field, *Properties of Diamond*, (Academic, London, 1979).

<sup>3</sup>V. K. Bazhenov, I. M. Vikulin, and A. G. Gontar, *Sov. Phys. Semicond.* **19**, 829, (1985).

<sup>4</sup>M. W. Geis, presented at the Third Annual SDIO-IST/ONR Diamond Technology Initiative Symposium, Cryst. City, VA, 1988.

<sup>5</sup>H. Nakazawa, Y. Kanazawa, M. Kamo, and K. Osumi, *Thin Solid Films* **151**, 451 (1987).

<sup>6</sup>S. Koizumi, T. Murakami, T. Inuzuka, K. Suzuki, *Appl. Phys. Lett.* **57**, 563 (1990).

<sup>7</sup>M. Yoshikawa, H. Ishida, A. Ishitani, T. Murakami, S. Koizumi, and T. Inuzuka, *Appl. Phys. Lett.* **57**, 428 (1990).

<sup>8</sup>T. Murakami, S. Koizumi, K. Suzuki, and T. Inuzuka; Presented at the Fall Meeting of the Japan Society of Applied Physics, Fukuoka, Japan, September 27-28, 1989.

<sup>9</sup>JH. van der Merwe, and E. Bauer, *Phys. Rev. B* **39**, 3632 (1989).

<sup>10</sup>JH. van der Merwe, *Philos. Mag.* **45**, 127, 145, 159 (1982).

<sup>11</sup>H. Reiss, *J. Appl. Phys.* **39**, 5045 (1968).

<sup>12</sup>M. W. H. Braun, DSc. thesis, University of Pretoria (1987).

<sup>13</sup>M. W. H. Braun, and J. H. van der Merwe, *S. African J. Sci.* **84**, 670 (1988).

<sup>14</sup>N. H. Fletcher, and K. W. Lodge, in *Epitaxial Growth, Part B*, edited by J. W. Matthews (Academic, New York, 1975), p. 529.

<sup>15</sup>P. M. Stoop, and J. A. Snyman, *Thin Solid Films* **158**, 51 (1988).

## XVIII. Cubic Boron Nitride Thin Film Growth

### A. Introduction

Cubic boron nitride is a material with potential applications due to both its tribological and electronic properties. It is the hardest material other than diamond, and it is more stable than diamond at higher temperatures. It does not react with the ferrous metals, which makes it an ideal cutting tool material. For electronic applications, it is of interest because it is a wide band gap ( $E_g=6.4$  eV) semiconductor with very high thermal conductivity; yet it also has the potential of being doped as both a p-type and n-type semiconductor. Boron nitride is similar to carbon in having three basic structures, a layered hexagonal structure (h-BN) corresponding to graphite, a cubic structure (c-BN) corresponding to diamond, and a rare hexagonal wurtzite structure (w-BN) which corresponds to Lonsdaleite. The layered hexagonal structure is typically referred to simply as hexagonal BN. There are also variations of these structures, including turbostratic BN (t-BN), which, like hexagonal BN, consists of layers, but in which the layers are randomly oriented to each other [1].

Bulk cubic boron nitride was first synthesized in 1956 using high pressure-high temperature methods [2]. In recent years, cubic boron nitride has been grown in thin film form, using both chemical vapor deposition (CVD) and physical vapor deposition (PVD) methods [3-7].

In this work we are studying the growth of cubic boron nitride thin films, and attempting to grow films which could be used for electronic applications. We have studied the evolution of the films as they grow, and found that the phase of the films changes during growth. On Si substrates an initial amorphous BN layer forms, followed by a hexagonal BN layer, followed by growth of the cubic phase. These results have been written up and submitted to the Journal of Materials Research. A preprint of this article is included as Section VI.

We are also studying how the films grow on various substrates. In addition to growing the films on Si substrates, we have grown them on both single crystal diamonds and on diamond thin films. We have also used the c-BN films grown on Si substrates as substrates for diamond growth.

### B. Experimental Procedure

#### Film Growth

A UHV ion beam assisted deposition (IBAD) system is being used for film deposition. Samples are loaded through a load lock system. Base pressures in the chamber are typically  $< 1 \times 10^{-9}$  Torr. Boron is deposited by evaporating boron metal using an electron beam evaporator. Simultaneously a Kaufman type ion gun is used to bombard the depositing boron with both nitrogen and argon ions. The films are deposited onto heated substrates. A

schematic of the setup is shown in Figure 1. The deposition rate of the boron, the energy and flux of the ions, the ratio of the argon to nitrogen, and the substrate temperature can all be measured, controlled, and varied. The boron is evaporated using a Thermionics HM2 electron gun with an electromagnetic beam sweep. The boron sits in a graphite crucible liner which is in a water cooled 10 cc crucible. It is deposited at a rate of from 0.25 to 1.0 Å/s. The deposition rate is monitored using a quartz crystal monitor.

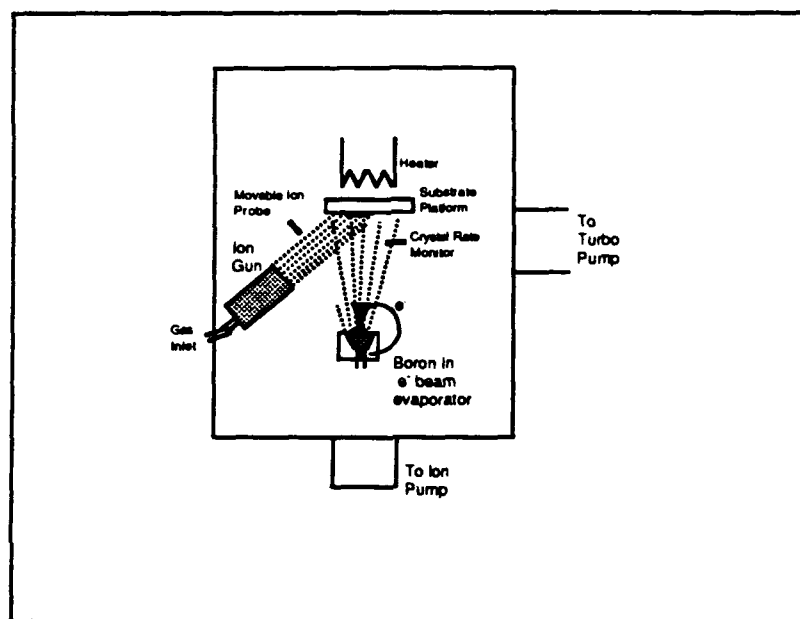


Figure 1. Schematic of deposition system.

The film is bombarded using an Ion Tech 3 cm Kaufman ion source. Bombardment is by nitrogen and argon ions in varied ratios, all at 500 eV. The flux of ions ranges from 0.05 to .30 mA/cm<sup>2</sup> and is measured using a negatively biased ion probe. The gas flow to the ion gun is 1.5 sccm for each of the two gases and is controlled using MKS mass flow controllers. Typical deposition pressures in the chamber are  $1.0 \times 10^{-4}$  Torr.

Substrates are heated from 300 to 700°C. The substrates used are 100 silicon wafers with high resistivity (25-45 W-cm) so as to be transparent for IR spectroscopy. Film thicknesses range from 100Å to 2000Å.

#### Film Characterization

*FTIR.* Fourier transform infrared spectroscopy (FTIR) has been found to be a convenient and reliable method for the purpose of determining whether a deposited film is cubic or hexagonal boron nitride. With FTIR analysis the cubic and hexagonal forms of boron nitride give distinct, independent peaks, due to the sp<sup>3</sup> and sp<sup>2</sup> bonds, respectively. Hexagonal boron

nitride has absorption peaks at  $1367\text{ cm}^{-1}$  and at  $783\text{ cm}^{-1}$  [8], while cubic boron nitride has a transverse optical mode absorption peak at  $1075\text{ cm}^{-1}$  [9].

Transmission FTIR was carried out on an Analect Instruments model fx-6260 spectrometer. Transmission spectra were taken through the BN films and Si substrates. A spectra of an uncoated Si wafer was taken as a background scan, and the spectra of the coated wafer was ratioed against it. The Si wafers used as substrates were high resistivity wafers,  $>50\ \Omega\text{ cm}$ , so as to transmit the IR radiation.

Reflectance FTIR was performed on films coated on substrates which are opaque to IR radiation, specifically Ni and Cu. This work was done on a Nicolet 620 FTIR with a Spectra Tech IR Plan optical microscope.

*Electron microscopy.* Structural characterization was accomplished by scanning electron microscopy (SEM) and transmission electron microscopy (TEM). SEM was performed in an Hitachi S-800 with a field emission gun. The samples were coated with a thin conductive layer of carbon to avoid charging effects. Carbon was deposited on a different area of the sample than that used for preparation of TEM samples. TEM was performed in a TOPCON EM-002B operated at 200 kV and a JEOL 4000EX operated at 400kV. On the JEOL microscope, high resolution images were recorded using a 1mr convergence semi-angle at Scherzer defocus ( $\sim -47\text{nm}$ ). Cross-sectional transmission electron microscopy (XTEM) samples were prepared using standard techniques [10].

*XPS.* X-ray photoelectron spectroscopy (XPS) was used to study the films. A Riber system, consisting of a Mac2 semi-dispersive electron energy analyzer and accessible by UHV transfer from the deposition chamber, was used. A Mg anode was used at 1.2 eV resolution for obtaining valence structure and 0.8 eV resolution for core level data.

*Rutherford Backscattering.* The stoichiometry of the films was measured using Rutherford backscattering (RBS), in which helium nuclei are used to bombard the film. By measuring the energy and angle of the backscattered nuclei, information about the film composition can be determined. RBS is particularly useful in that it gives a depth profile of the film, not only information about the surface layer.

## C. Results

### BN on single crystal diamond

Boron nitride was deposited on single crystal diamond. The diamond was natural diamond which had been cut and polished into substrates, obtained from Dubbledee company. Before loading, the diamonds were etched in a boiling  $\text{H}_2\text{SO}_4:\text{HNO}_3:\text{HClO}_4$  solution in a ratio of 3:4:1 for 45 minutes to remove any graphitic phase.  $1000\ \text{\AA}$  of BN was grown on the diamond, at substrate temperatures of  $400^\circ$  and  $600^\circ\text{C}$ . The FTIR patterns of the films are shown in Figure 2. A sharp c-BN peak is observed at  $\sim 1080\text{ cm}^{-1}$ . The h-BN peak is very

small. This spectra has a sharper c-BN peak, and a better c-BN to h-BN ratio than any films we had previously deposited on Si, and is as good or better than any that have appeared in the literature.

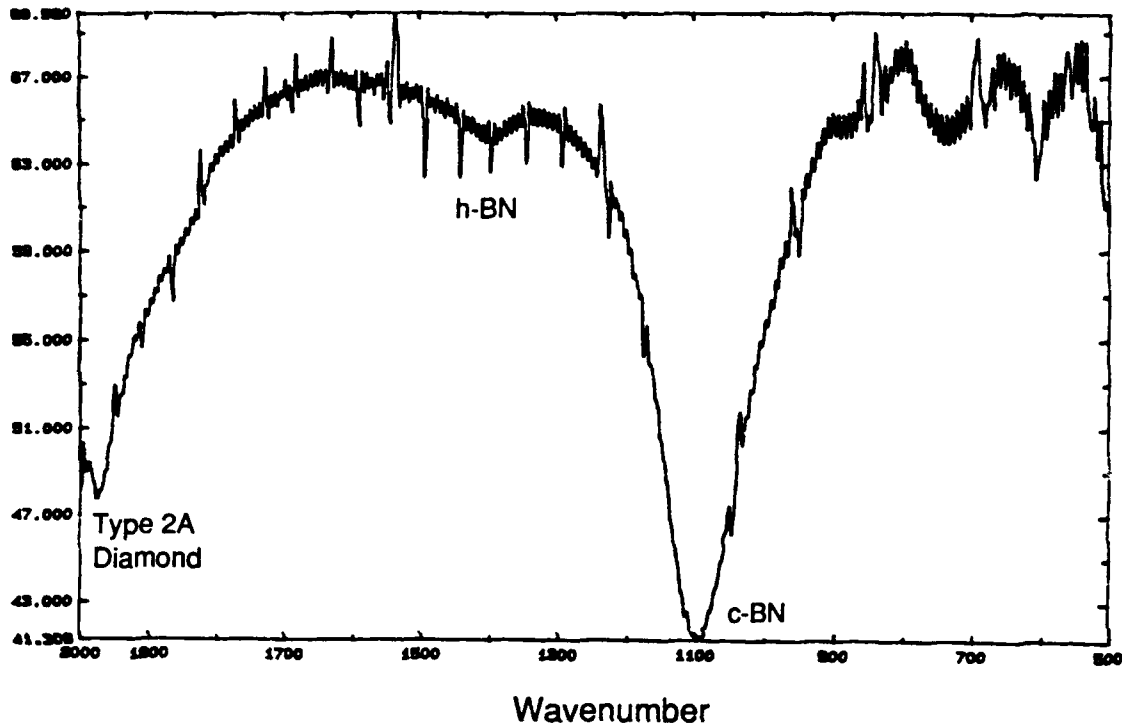


Figure 2. FTIR spectrum of BN film on single crystal diamond.

SEM of the sample deposited at 400°C showed some cracking of the film in spots. The film deposited at 600°C did not show any cracking or delamination. Films deposited at the same deposition conditions and the same thickness on Si are found to have major cracking and delamination of the BN film.

High resolution TEM (HRTEM) was performed on the samples, and the images are shown in Figs. 3 and 4. It can be seen on these two images that the same type of layered structure observed on BN grown on Si is present, if not as pronounced. On the 400° image the hexagonal and cubic regions appear more intermixed.

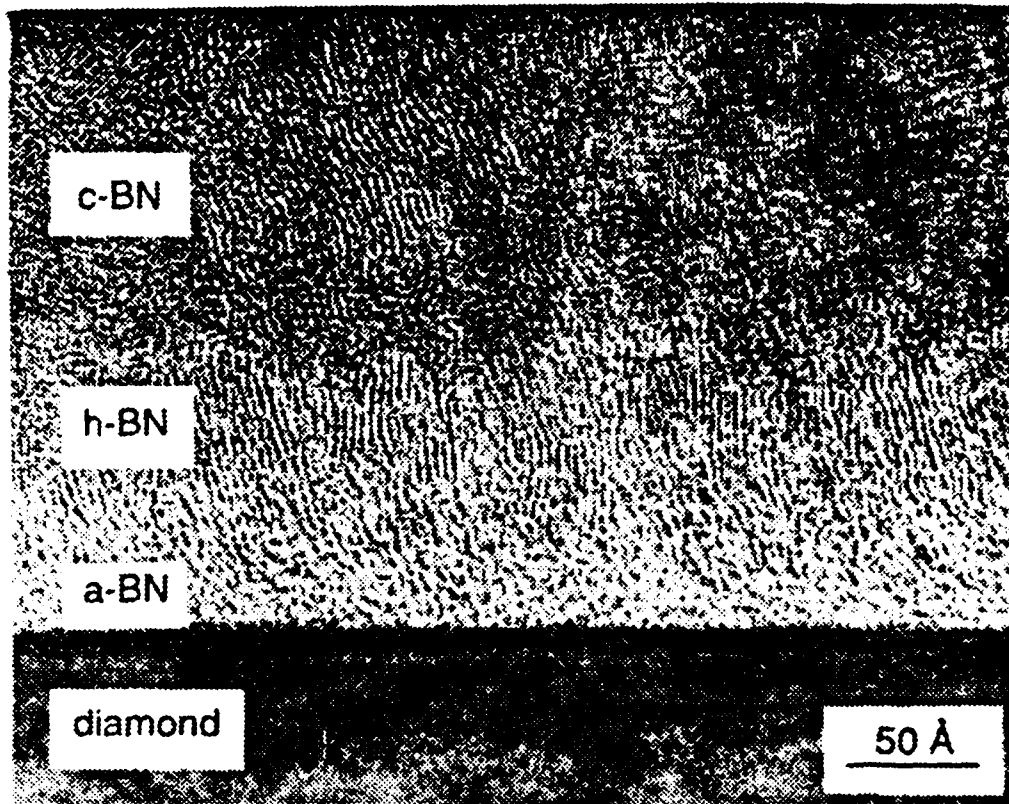


Figure 3. HRTEM of BN on diamond, grown at 400°C

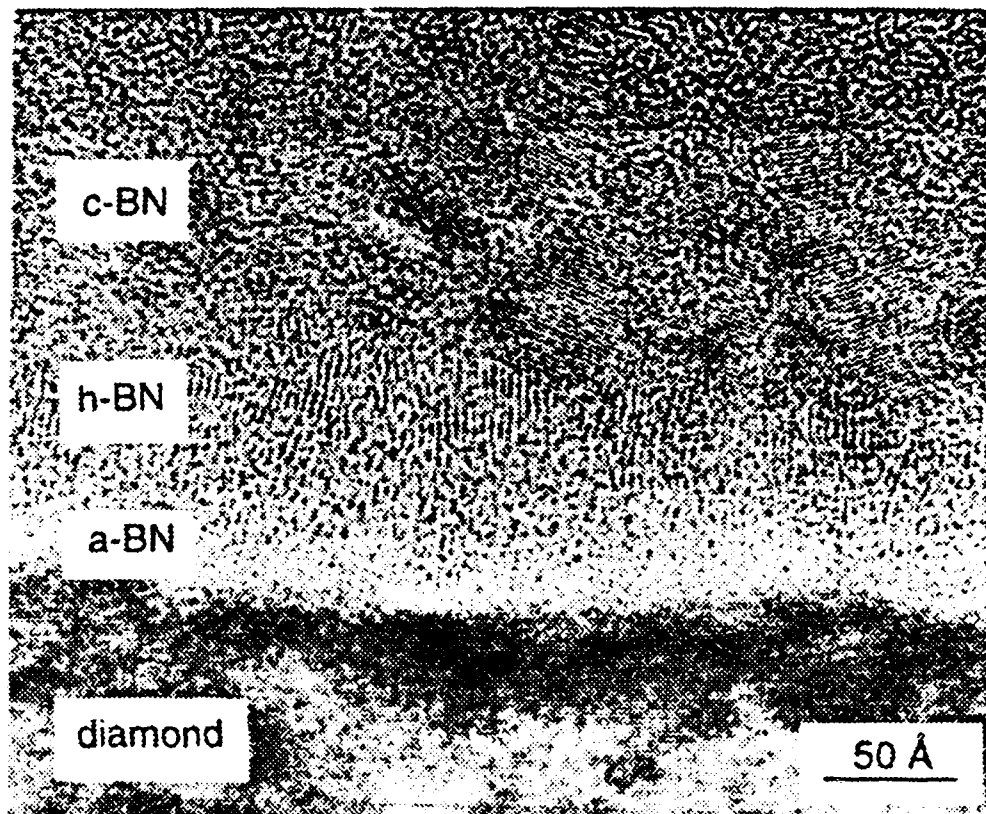


Figure 4. HRTEM of BN on diamond, deposited at 600°C

### BN on diamond films

1000 Å of BN was grown on diamond thin films. The diamond films were grown on Si substrates using a microwave CVD process with 1% CH<sub>4</sub> and were 2-4 μm thick. Before the c-BN deposition the substrates with the diamond films were etched in a boiling acid solution as described above.

HRTEM was performed on the films, however due to the roughness of the diamond surface a clear image could not be obtained. Therefore diamond films on silicon on which the diamond surface had been polished smooth were acquired and 1000 Å BN deposited on those. SEM of the films showed the presence of what appeared as black spots on the surface of the films. It is not yet clear what the source of the spots is, although they may be due to holes in the BN film brought about by the ion bombardment. HRTEM of these films will occur in the near future.

Raman spectroscopy was also performed on these films. The c-BN peak was not observed. This is not unexpected, as getting the raman peak generally requires more crystallinity than we have been able to achieve.

### Diamond films on BN films

Diamond films were grown on BN films which had been deposited on Si substrates. The thickness of the BN films was 150 Å. This was thick enough that the surface of the film would be cubic, but not thick enough for delamination to be a problem. The diamond was grown on these BN films using substrate biasing to help in nucleation of the diamond, as described in Ref. 11. Observation of the plasma during diamond growth showed the plasma to be an unusual color, which may indicate that the BN was being etched during the initial diamond growth, due to bombardment. SEM of the sample showed diamond to have formed on areas of the substrate. It is not clear whether the diamond growth occurred on the BN or on areas where BN had been etched off.

We are presently growing new diamond films on BN films without using the substrate biasing. This is being done on three different thicknesses of BN film: 20 Å, 50 Å, and 150 Å. These thicknesses correspond to the thicknesses at which the BN surface is amorphous, hexagonal, and cubic, respectively. These experiments may give information on how diamond nucleates on the different BN phases.

### BN on Si

XPS. BN films were grown on Si and XPS was performed on them. Films were 20 Å and 100 Å thick. Other than thickness, deposition conditions were identical. The XPS could get data on the top 50 Å of the film, this allowed us to compare the Si-BN interface with the BN material in the film at 50-100 Å. It is seen in Fig. 5 that at the interface there are both Si-Si

(99 eV) and Si-N bonds (101 eV) present. This indicates that there is not an abrupt transition from the Si substrate to the BN film, but that the nitrogen ion bombardment causes the formation of an interfacial silicon nitride ( $\text{Si}_3\text{N}_4$ ) layer.

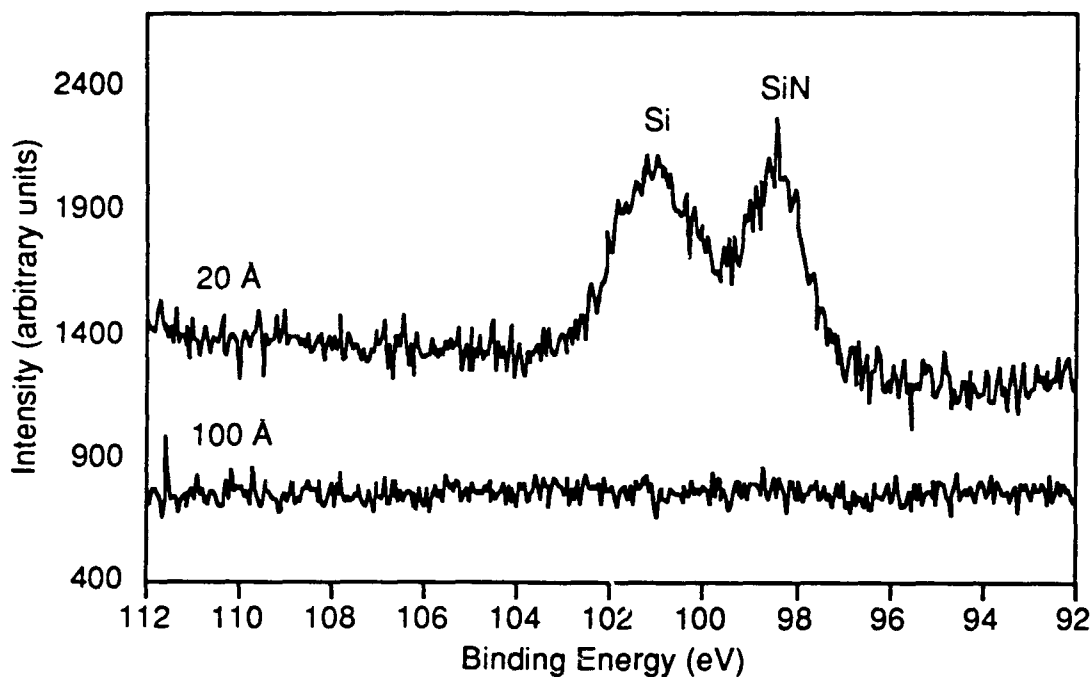


Figure 5. XPS spectra showing Si peaks on 20Å and 100Å thick films.

In Figure 6 the boron XPS peaks for the two films are shown. It is seen that on the 100 Å film the peak due to BN is present. On the 20 Å film there is the BN peak, but also a shoulder that appears to be due to the elemental B peak. This would indicate that near the interface there is both N bonded and B bonded B present.

Figure 7 shows the XPS peaks for Ar. It is seen that there is not much difference between the film at 20 Å and at 100Å. Both contain a detectable amount of Ar.

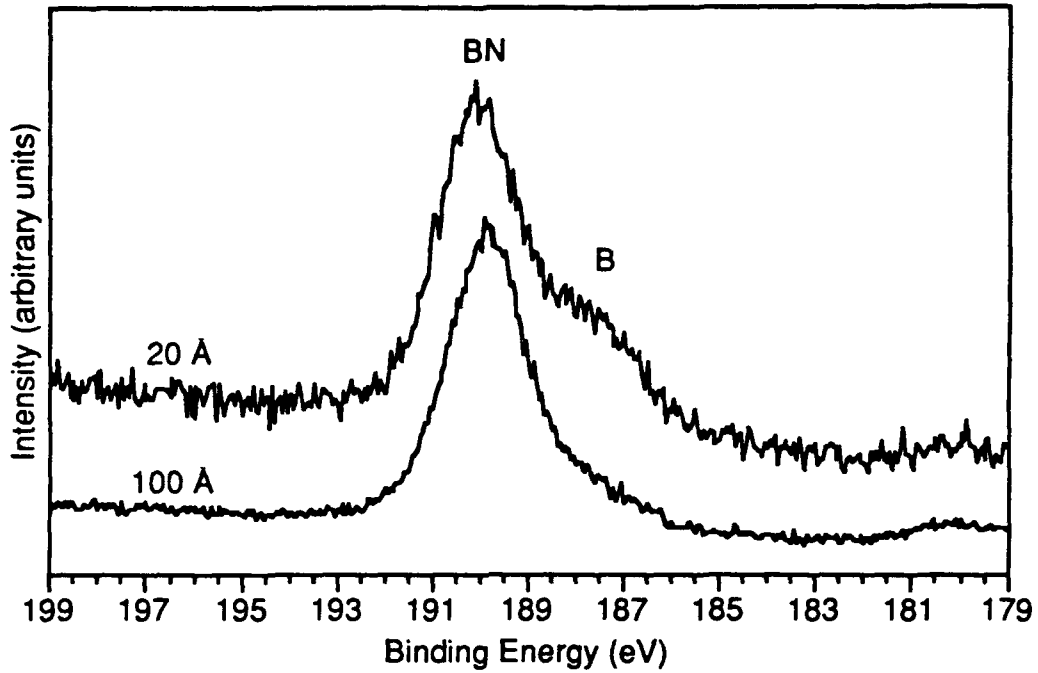


Figure 6. XPS spectra showing B peaks on 20Å and 100Å thick films.

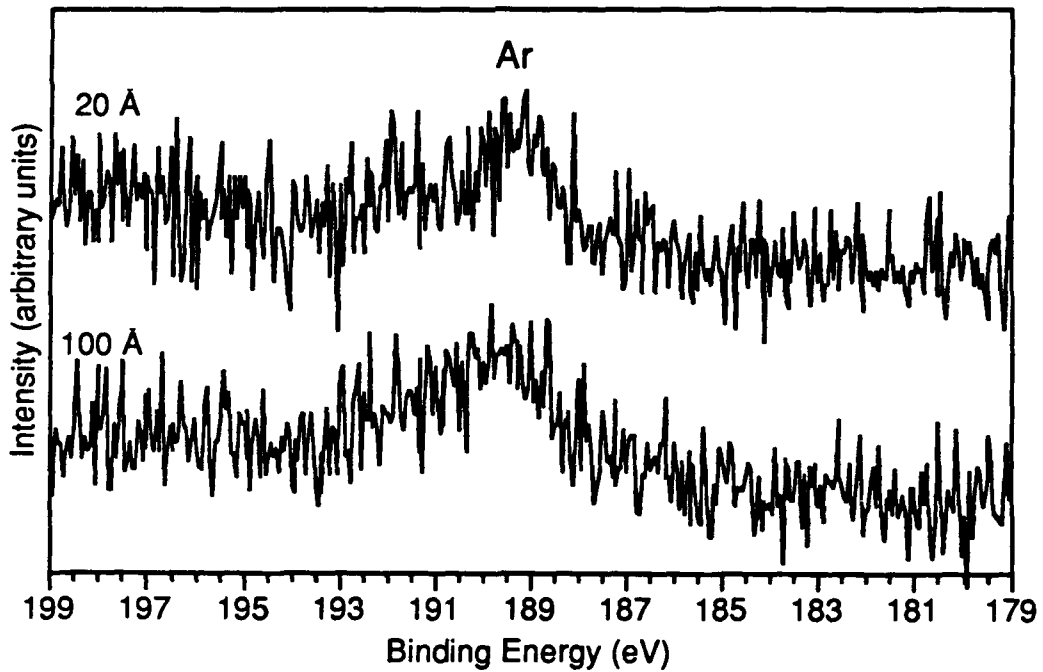


Figure 7. XPS spectra showing Ar peak on 20Å and 100Å thick films.

*RBS.* For RBS it is preferred that the substrate material have a lower atomic number than the film material. Otherwise the spectrum of the substrate will overlap that of the film material, making the film spectra difficult to read. Therefore the film for RBS was deposited on a Be

substrate. Results are shown in Figure 8. RBS is more sensitive to materials of higher atomic numbers, due to their larger nuclear cross sections. Therefore, the size of the peaks of the materials at various channel numbers does not directly show their actual concentration. Computer modeling of the spectra showed that in addition to the expected Be, B, and N, there is also O at the Be surface, and Ar, Fe, and Hf present in the film. The modeling indicates that the O peak is due to a BeO layer between the Be substrate and BN film, and that the atomic percentage of Ar was ~1.5%, of Fe ~0.2%, and of Hf ~0.05%. The source of the Ar would be the Ar ion bombardment during growth, the Fe is probably due to the ion beam bombarding the stainless steel shutter above the substrates, sputtering Fe onto the film. The Hf may be due to the deposition system also being used for Hf film deposition, and previously deposited Hf from the substrate block being sputtered.

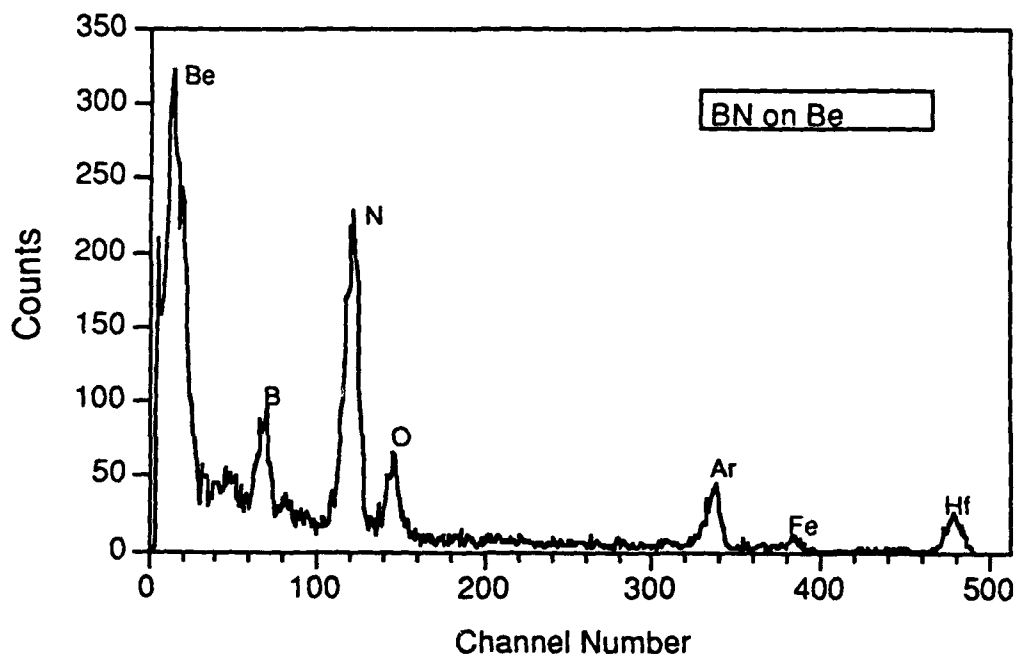


Figure 8. RBS spectra of BN film on Be substrate.

*Growth of initial boron layer.* The XPS analysis showed that an initial  $\text{Si}_3\text{N}_4$  layer was forming at the Si surface. It was thought that the formation of this layer may be inhibiting the epitaxial growth of c-BN. Therefore attempts were made to deposit an initial boron layer before starting the ion bombardment. Boron layers of 20 Å, 50 Å, and 100 Å were deposited under conditions found to lead to cubic growth. FTIR examination of the films showed that all still had a significant h-BN component.

*Other substrates.* Ni and Cu have lattice spacing very close to that of c-BN. Therefore it was thought that they may be better substrates for c-BN than Si which has a lattice mismatch of 34%. Reflectance FTIR was performed on these films.

Films were grown under conditions which had been found to give c-BN films on Si. Films grown on the Ni substrate were found to be mixed h-BN and c-BN (Figure 9); films grown on Cu were h-BN with no evidence of the presence of c-BN (Fig. 10).

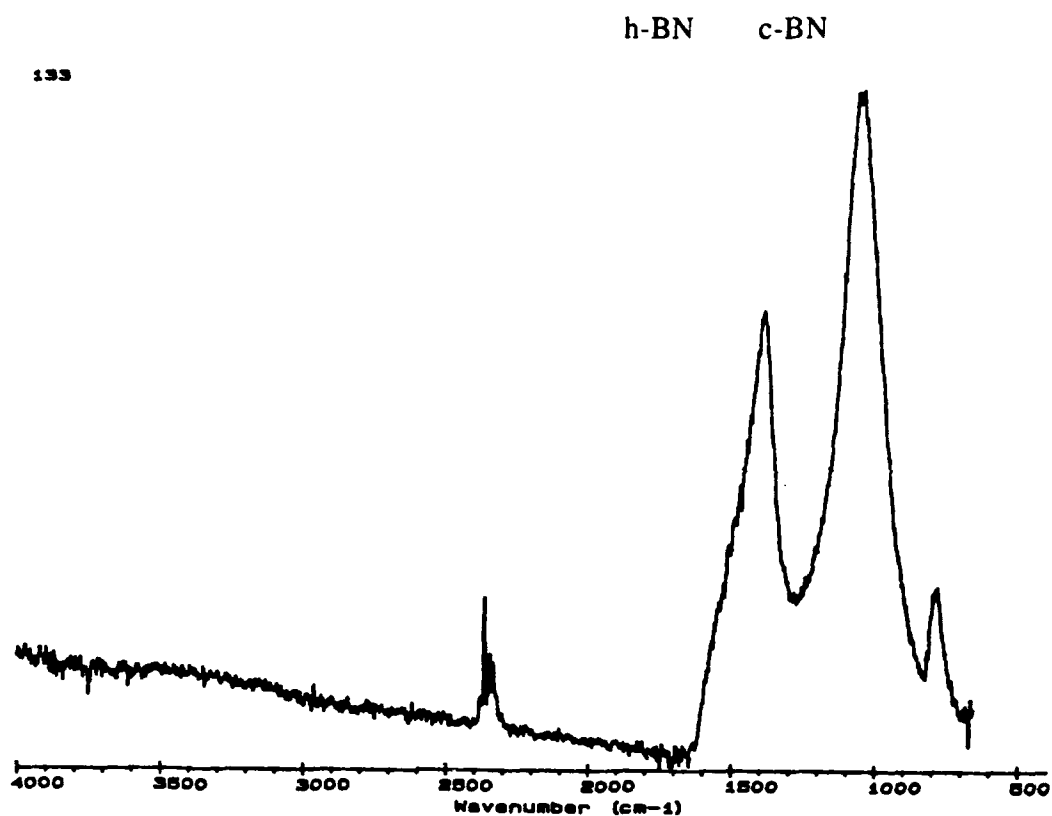


Figure 9. Reflectance FTIR of BN film on Ni substrate.

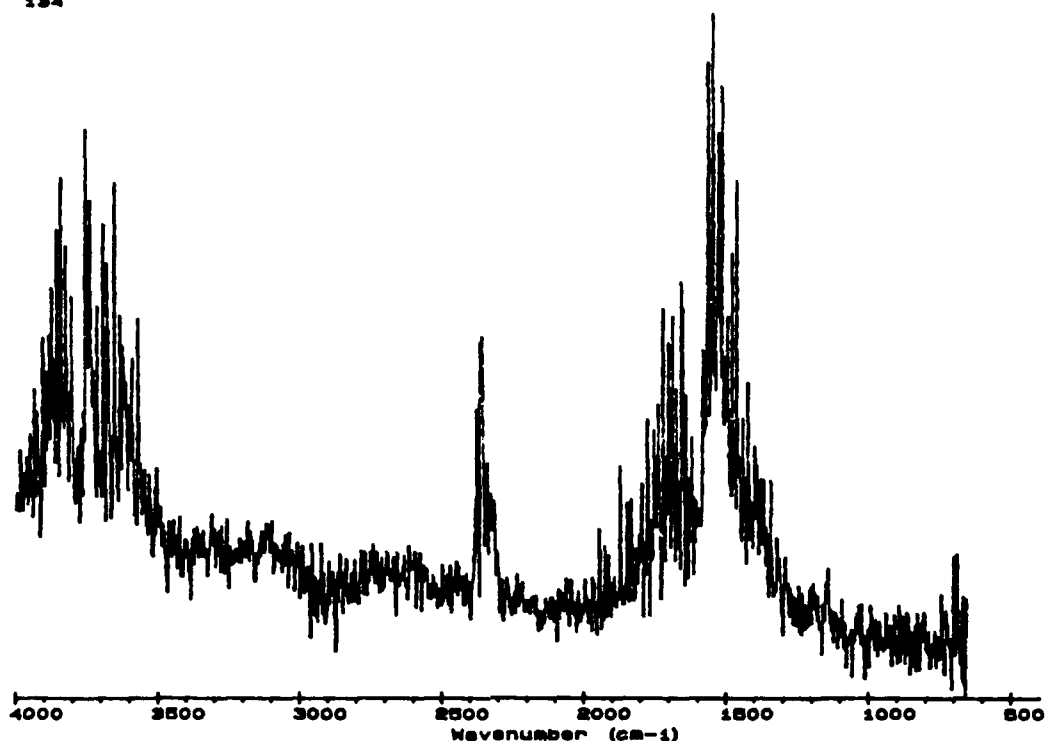


Figure 10. Reflectance FTIR of BN film on Cu substrate.

#### Patterned substrates

Selected area deposition was performed on patterned Si substrates. These consisted of Si wafers which had been coated with an  $\text{SiO}_2$  layer. Holes were etched into the  $\text{SiO}_2$ , to expose the Si in regions of varying diameters. Examination by SEM showed that good adhesion of the BN film on the Si occurred within the etched holes. The material deposited on the  $\text{SiO}_2$  around the holes, had poor adhesion.

#### D. Discussion

The results shown in the paper in Appendix A demonstrate that cubic boron nitride grows on Si with an initial amorphous layer, followed by a hexagonal layer, followed by the growth of cubic material. The fact that the phase changes at some point in the film growth to the metastable cubic phase indicates that at the non-equilibrium deposition conditions used, cubic is the stable phase. This leads to the question of why the film growth is not cubic, but is initially amorphous, and whether it is at all possible to grow epitaxial c-BN. The lack of any repeatable examples of epitaxial c-BN in the literature raises the same question. It was initially thought that the problem was due to the poor lattice mismatch between Si and c-BN. However the results obtained using other substrates with excellent lattice matching showed this not to be the case. It has previously been predicted that c-BN can grow epitaxially on diamond [12]. Yet a

layered structure similar to that observed on Si was also seen on films grown on diamond substrates. Depositions on Cu (with an exact lattice match to c-BN) and on Ni also gave mixed phase films. The fact that depositing an initial layer of boron did not improve the films also indicates that the Si/BN interface itself may not be the problem.

The results presented in Appendix A showed that there is not a sharp change at the interface from Si to cubic BN. The XPS results that there is both  $\text{Si}_3\text{N}_4$  and elemental B (B bonded to other B, not to N) at the interface show that not only is there not a sharp transition to cubic phase BN, but that there is not a sharp transition from Si to BN of any phase. For epitaxial c-BN a sharp Si to BN transition would be the first requirement. The ion bombardment itself, while apparently necessary to grow c-BN [13] may in itself be preventing the growth of epitaxial c-BN by forming a  $\text{Si}_3\text{N}_4$  layer.

Recent work [14] suggests that c-BN forms due to the buildup of stress in the growing films. That study suggests that the onset of the cubic phase will not be initiated until the compressive stress is high enough, which will not occur until a certain film thickness is reached. Our results appear to confirm this.

The actual mechanism causing the stress in the film is not clear. It may be densification due to the ion bombardment. Densification and associated stress has been previously observed in ion bombarded films [15]. The densification occurs through the collapse of the void structure found in non-bombarded films. The stress may also be due to the presence of interstitials in the film. In the case of the c-BN films, the relatively high concentration of Ar (1.5 at.%) as shown by RBS and XPS suggests that the compressive stress may be caused by interstitial Ar atoms.

#### E. Conclusions

HRTEM and FTIR studies have revealed that BN growth on Si(100) substrates occurs as a single sequence of thin amorphous, hexagonal and cubic layers. The c-BN is single phase and does not undergo further transformation to a thickness of  $\approx 1000\text{\AA}$ .

c-BN did not grow epitaxially on any substrate. This may be due to the need for a certain level of compressive stress in the films before the initiation of the cubic phase. This compressive stress would not be reached until the film has grown to a certain thickness (50-100 $\text{\AA}$ ). The cause of the compressive stress may be interstitial Ar in the film.

#### F. Future Research Plans/Goals

Work is continuing on depositing BN on diamond films. We are obtaining a number of oriented 100 diamond films, to use as substrates. This will allow the growth of films at a wider range of deposition conditions than we were able to do on single crystal diamonds. The effect of both substrate temperature and bombardment level will be examined.

BN films on Si have been deposited at different thicknesses which will give different BN phases at the film surface. Diamond films are being grown on these and the effect of the different BN phases on diamond nucleation is being studied.

We are in the process of doing a systematic study of the effect of substrate temperature on the growth of BN on Si. Films are being characterized by FTIR and HRTEM.

Auger electron spectroscopy will be used to examine the first 200 Å of a BN film, to see how the composition varies with thickness. This may give some insight into how the phase evolution of the film develops.

The effect of post-deposition annealing will be studied. It will be seen if this has any effect on the structure of the films.

#### G. References

1. J. Thomas, Jr., N. E. Weston, and T. E. O'Conner, *J. Am. Chem. Soc.* **84**, 4619 (1963).
2. R. H. Wentorf, Jr., *J. Chem. Phys.* **26**, 956 (1957).
3. F. Shimokawa, H. Kuwano, and K. Nagai, *Proc. 9th Symp. on ISIAT 85 Tokyo* (1985).
4. K. Inagawa, K. Watanabe, H. Ohson, K. Saitoh, and A. Itoh, *J. Vac. Sci. Technol.* **A5**, 2696 (1987).
5. Y. Andoh, K. Ogata, and E. Kamijo, *Nucl. Instrum. Methods Phys. Res.* **B33**, 678 (1988).
6. M. Murakawa and S. Watanabe, *Surf. Coat. Technol.* **43/44**, 128 (1990).
7. H. Saitoh, T. Hirose, H. Matsui, Y. Hirotsu, and Y. Ichinose, *Surf. Coat. Technol.* **39/40**, 265 (1989).
8. R. Geick and C. H. Perry, *Phys. Rev.* **146**, 543 (1966).
9. P. J. Gielisse, S. S. Mitra, J. N. Plendl, R. D. Griffis, L. C. Mansur, R. Marshall, and E. A. Pascoe, *Phys. Rev.* **155**, 1039 (1967).
10. C. H. Carter, Jr., J. A. Edmond, J. W. Palmour, J. Ryu, H. J. Kim and R. F. Davis in *Microscopic Identification of Electronic Defects in Semiconductors*, edited by N. M. Johnson, S. G. Bishop, and G. Watkins (*Mater. Res. Soc. Proc.*, **46**, Pittsburgh, PA 1985) pp. 593-598.
11. B. R. Stoner, G.-H. M. Ma, S. D. Wolter, and J. T. Glass, *Phys. Rev. B*, **45**, 11067 (1992).
12. M. W. H. Braun, H. S. Kong, J. T. Glass, and R. F. Davis, *J. Appl. Phys.* **69**, 2679 (1991).
13. D. J. Kester and R. Messier, *J. Appl. Phys.*, **72**, 504 (1992)
14. D. R. McKenzie, talk given at the 1992 American Vacuum Society annual meeting, Chicago, IL, November 1992.
15. R. A. Roy and D. S. Yee, in *Handbook of Ion Beam Processing Technology*, edited by J. J. Cuomo, S. M. Rossnagel, and H. R. Kaufman, (Noyes, Park Ridge, NJ, 1989).

## **XIX. Phase Evolution in Boron Nitride Thin Films\***

D. J. Kester, K. S. Ailey, K. L. More, and R. F. Davis

Department of Materials Science and Engineering, North Carolina State University, Raleigh,  
NC 27695

Boron nitride (BN) thin films were deposited on monocrystalline Si (100) wafers using electron beam evaporation of boron with simultaneous bombardment by nitrogen and argon ions. The effect of film thickness on the phase of BN was investigated using Fourier transform infrared (FTIR) spectroscopy and high resolution transmission electron microscopy (HRTEM). These techniques revealed the consecutive deposition of an initial 20Å thick layer of amorphous BN, 20-50Å of hexagonal BN having a layered structure, and a final layer of the cubic phase. The growth of the non-cubic layers are believed to act as a residual stress relief mechanism and/or to form surface and interface relationships which become favorable for the nucleation of the cubic phase. The presence of the amorphous and hexagonal regions may also explain why there have been no reports of the growth of 100% cubic boron nitride on Si.

\*Submitted for publication to the Journal of Materials Research

Boron nitride is similar to carbon in having three crystalline structures:[1] a layered hexagonal structure (*h*-BN) corresponding to graphite, the cubic structure (*c*-BN) analogous to diamond, and a rare hexagonal wurtzite structure (*w*-BN) corresponding to Lonsdaleite. The last two phases are metastable under normal environmental conditions. An amorphous phase (*a*-BN) is also common in films and coatings.

The extreme mechanical and thermal properties of *c*-BN make it useful for wear-resistant tools for the machining of steels, for corrosion resistant and electrically insulating parts, and for heat sinks for electronic devices. It has also recently been shown that bulk single crystals of this wide bandgap ( $E_g \approx 6.4$  eV) semiconductor can be doped with both n- and p-type impurities and that light emitting p-n junctions can be produced [2]. This phase combined with other BN phases, has also been achieved in thin film form via physical vapor deposition [3-5] and chemical vapor deposition [6] methods.

Most researchers growing BN films use FTIR spectroscopy for phase identification. The cubic phase of BN has a distinct absorption peak at about  $1080\text{ cm}^{-1}$ . The hexagonal, turbostratic (disordered hexagonal), and amorphous phases have primary and secondary absorption peaks at  $1370$  and  $780\text{ cm}^{-1}$ , respectively. Thus, these non-cubic phases cannot be distinguished using FTIR. A commonly reported feature of these spectra obtained from analyses of the total thickness of the films wherein the presence of *c*-BN is apparent is the indication of various amounts of the hexagonal and/or amorphous phases (see, e.g., Refs. 4, 5). The FTIR spectra of the films obtained in the present research showed similar results. However, the unusual evolution of these phases has been determined by HRTEM and has been correlated with the FTIR results.

The Si (100) substrates used in the present study received a standard RCA cleaning [7] which included a 5 min. dip in 10% HF as the final step. This left the surface H-terminated and reduced the rate of reaction of this surface with  $\text{H}_2\text{O}$  and  $\text{O}_2$  in the atmosphere. The substrates were subsequently transferred to the deposition chamber and heated to  $400^\circ\text{C}$  under UHV conditions. Base and deposition pressures were typically  $<10^{-9}$  Torr and  $10^{-4}$  Torr, respectively. The growth method involved the electron beam evaporation of B sufficient to achieve a deposition rate of  $0.25\text{ \AA/s}$ , as measured via a quartz crystal rate monitor. The growing films were simultaneously bombarded with a  $0.12\text{ mA/cm}^2$  ion flux (measured using a biased probe) of 500 eV nitrogen and argon ions produced in a Kaufman source using a 50:50 gas flow ratio of Ar/ $\text{N}_2$ . A shutter was used to cover the substrate prior to film deposition while the boron evaporation and ion bombardment were brought to correct levels for deposition and allowed to stabilize. Conditions during each deposition were maintained constant. The total film thickness ranged from 125-500 $\text{ \AA}$ .

FTIR was performed using an Analect Instruments model fx-6260 spectrometer. Transmission spectra were taken through the BN films and Si substrates. A spectra of an

uncoated Si wafer was taken as a background scan, and the spectra of the coated wafer was ratioed against it. The spectra for films deposited under identical conditions except for growth time are shown in Fig. 1. Peak heights were maximized on each of the spectra, thus only the ratio of peak heights within a single spectra are meaningful; absolute peak heights on different spectra cannot be compared. The relative amount(s) of non-cubic phase(s) was high for very thin films ( $<200\text{\AA}$ ). As the deposition time and resulting thickness increased, the relative percentage of the cubic phase increased. This indicated that the ratio of the concentration of the *c*-BN phase to that of the *a*-BN and *h*-BN phases increased as a function of film thickness rather than being constant regardless of deposition time.

To test this hypothesis, structural characterization of the films as a function of thickness was performed via HRTEM using a TOPCON EM-002B microscope operated at 200kV. Cross-sectional samples of the BN films were prepared using standard techniques [8]. The HRTEM images, an example of which is shown in Fig. 2, supported the above hypothesis in that they revealed that three distinct regions had deposited in the following sequence: an initial layer of about  $20\text{\AA}$  of *a*-BN at the Si (100) interface, a layer of  $20\text{-}50\text{\AA}$  of *h*-BN, and a top layer of polycrystalline, random oriented cubic material. The hexagonal layers grew perpendicular to the Si (100) surface. An optical diffraction pattern was obtained by performing a Fast Fourier Transform on the HRTEM image to obtain the diffraction information shown in Fig. 3. The lattice spacings for the top layer matched that of *c*-BN, while those within the middle layer matched that of *h*-BN.

As noted above, all reported transmission FTIR spectra obtained from analyses of the total thickness of BN films have indicated the presence of some non-cubic phase. Explanations for this phenomenon include: (1) the occurrence of the non-cubic phase(s) on the grain boundaries within the *c*-BN matrix; (2) separate *h*-BN or *a*-BN micro-regions distributed throughout the films; and (3) a layered sequence of these various phases. Microstructures produced by combinations of these three factors may also exist in the films. The results of the present research indicate that sequential layers of *a*-BN and *h*-BN are the sources of the non-cubic phases. The HRTEM image shows that once the growth of the cubic phase is initiated, this layer is single phase. More specifically, even non-cubic grain boundary regions were not observed. Upon nucleation, the cubic phase grows without further transformation, at least to the maximum layer thickness thus far deposited ( $\approx 1000\text{\AA}$ ).

The exact reason(s) for the occurrence and layer sequence within the microstructure shown in Fig. 2 is (are) not known. Previous work on BN film growth [9] has shown that, for a given substrate temperature, the deposition of a particular phase is a function of momentum transferred into the film by the ion bombardment. The deposition conditions used in this study were those that previously resulted in the growth of films containing substantial concentrations of *c*-BN. However, nucleation of this phase is obviously not automatic. The amorphous

phase may occur initially as a transition zone of reduced residual stress relative to that which would develop during *epitaxial* growth of *c*-BN (or *h*-BN) on Si(100) due to the large mismatch in lattice parameter ( $\approx 33.4\%$  for *c*-BN). This constraint may be joined or surmounted by the constraint of surface energy. It may be impossible for *c*-BN (or even *h*-BN) to nucleate and grow *epitaxially* on Si(100) due to the much larger surface energy of the BN crystalline phases.

The transformation of the *a*-BN to the *h*-BN phase is not surprising from the viewpoint of equilibrium thermodynamics under standard conditions. However, as noted above, the experimental parameters favored the nucleation of *c*-BN. The explanation for the nucleation of *h*-BN may be found in the atomic structure of the *a*-BN. X-ray radial distribution curves normally show that stoichiometric amorphous phases are similar in atomic arrangement to their crystalline analogs, especially among nearest neighbors and occasionally to even greater spheres of coordination. The essentially indistinguishable IR spectra between *a*-BN and *h*-BN also indicate similar atomic arrangements in these two phases which may explain the subsequent nucleation of this phase. The reason for the preferred orientation of the basal plane of the *h*-BN perpendicular to the Si(100) surface is not known, though it may also be related to the atomic structure of the *a*-BN surface.

A three dimensional phase transformation only at the growing surface of a thin film phase normally considered to be the equilibrium structure (*h*-BN) to one which is metastable (*c*-BN) is truly an anomaly even under highly nonequilibrium conditions. The experimental conditions coupled with the presence of the high surface energy edges of the *h*-BN which acted as the substrates are believed to be the reasons for this unusual transformation. If this is the case, it would be analogous to the recent findings regarding nucleation of diamond on non-diamond substrates. Williams [10] has investigated personally and via review of the literature the sequence of deposition events leading to the onset of diamond nucleation on carbide- and noncarbide-forming substrates. In all documented cases, the deposition of a particulate amorphous and/or graphitic phase preceded the nucleation of diamond. Davis has argued [11] that the high energy edges of appropriately oriented graphite or other C particles are the likely sites for the onset of diamond nucleation (this scenario may also explain the considerable effectiveness of scratched substrates in that the scratches act to orient the C particles such that diamond nucleation is favored). The research of Angus and his colleagues [12, 13] concerned with the nucleation and growth of diamond on various orientations of pyrolytic graphite support this hypothesis. In this regard, recent research by the present authors involving the deposition and HRTEM of BN films on (100) single crystal diamond substrates under the same conditions noted above resulted in the initial deposition of a very thin *a*-BN layer and a subsequent layer containing a mixture of primarily *c*-BN and a small amount of *h*-BN. The details of this study will be reported in the near future.

Finally, a close examination of Fig. 2 reveals an uneven *h*-BN/*c*-BN interface but a very smooth *c*-BN surface. This indicates that (1) the initial nucleation of the *c*-BN did not occur simultaneously across the *h*-BN surface and (2) the deposition rate of these two phases is essentially the same. These results also show that *c*-BN does not form due to the elimination of the *h*-BN phase by the ion beam. The HRTEM results clearly show that the *h*-BN phase forms under the same conditions used to deposit *c*-BN. To date, it has not been possible to determine the orientation relationship between the *h*-BN and the *c*-BN phases at the site of nucleation.

In summary, HRTEM and FTIR studies have revealed that BN growth on Si(100) substrates occurs as a single sequence of thin amorphous, hexagonal and cubic layers. The *c*-BN is single phase and does not undergo further transformation to a thickness of  $\approx 1000\text{\AA}$ . The non-cubic layers are believed to occur initially to form relatively relaxed transition zones and/or to achieve a surface and interface energy relationship which eventually becomes favorable to the nucleation of the *c*-BN. The preferred orientation of the *h*-BN layers and the exposure of the high surface energy edges of this phase are believed to act in tandem with the highly non-equilibrium growth conditions to achieve the deposition of the *c*-BN.

#### Acknowledgments

The authors express their appreciation to the Electronic Materials Center of Kobe Steel, USA and the Strategic Defense Initiative through the Office of Naval Research and via the contract #N00014-92-J-1720 for support of this research and to Professor J. Angus of Case Western Reserve University for the information regarding the deposition of diamond on pyrolytic graphite and for giving us a preprint of the paper describing this research. A portion of the electron microscopy was supported as part of the Ceramic Technology for Advanced Heat Engines Program of the Advanced Materials Development Program and partially performed in the HTML User Facility, both sponsored by the U. S. Department of Energy, Assistant Secretary for Conservation and Renewable Energy, Office of Transportation Technologies, under contract DE AC0584ORO21400 managed by Martin Marietta Energy Systems, Inc.

#### References

- [1] L. Vel, G. Demazeau and J. Etourneau, *Mater. Sci. and Eng.* **B10**, 149 (1991).
- [2] O. Mishima, K. Era, J. Tanaka, and S. Yamaoka, *Appl. Phys. Lett.*, **53**, 962 (1988).
- [3] K. Inagawa, K. Watanabe, H. Ohson, K. Saitoh, and A. Itoh, *J. Vac. Sci. Technol.* **A5**, 2696 (1987).
- [4] Y. Osaka, M. Okamoto, and Y. Utsumi, *Mater. Res. Soc. Symp. Proc.*, **223**, 81 (1991).

- [5] N. Tanabe, T. Hayashi, and M. Iwaki, *Diamond Relat. Mater.*, **1**, 151 (1992).
- [6] H. Saitoh, T. Hirose, H. Matsui, Y. Hirotsu, and Y. Ichinose, *Surf. Coat. Technol.* **39/40**, 265 (1989).
- [7] W. Kern and D. A. Puo-tinen, *RCA Rev.* **31**, 187 (1970).
- [8] C. H. Carter, Jr., J. A. Edmond, J. W. Palmour, J. Ryu, H. J. Kim and R. F. Davis in *Microscopic Identification of Electronic Defects in Semiconductors*, edited by N. M. Johnson, S. G. Bishop, and G. Watkins (*Mater. Res. Soc. Proc.*, **46**, Pittsburgh, PA 1985) pp. 593 -598.
- [9] D. J. Kester and R. Messier, *J. Appl. Phys.*, **72**, 504 (1992)
- [10] B. E. Williams, Ph. D. Dissertation, North Carolina State University, 1992
- [11] R. F. Davis, Presentation at the 1991 Gordon Conference on Inorganic Thin Films.
- [12] J. Angus (private communication).
- [13] Z. Li, L. Wang, T. Suzuki, P. Pirouz and J. C. Angus, in press.

## FIGURES

1. FTIR spectra of BN films of various thicknesses all deposited on Si (100) substrates under the following conditions: Boron deposition rate:  $0.25 \text{ \AA/s}$ ; ion energy: 500 eV; ion flux:  $0.12 \text{ mA/cm}^2$ ; ion bombardment by 50:50 Ar:N<sub>2</sub>; substrate temperature: 400°C.
2. Cross-sectional HRTEM image of BN film showing Si substrate and regions of amorphous BN (a-BN), hexagonal BN (h-BN), and cubic BN (c-BN).
3. Optical diffraction pattern from the HRTEM image of Fig. 2. (a) From the region labeled as h-BN. (b) From the region labeled as c-BN.

Figure 1

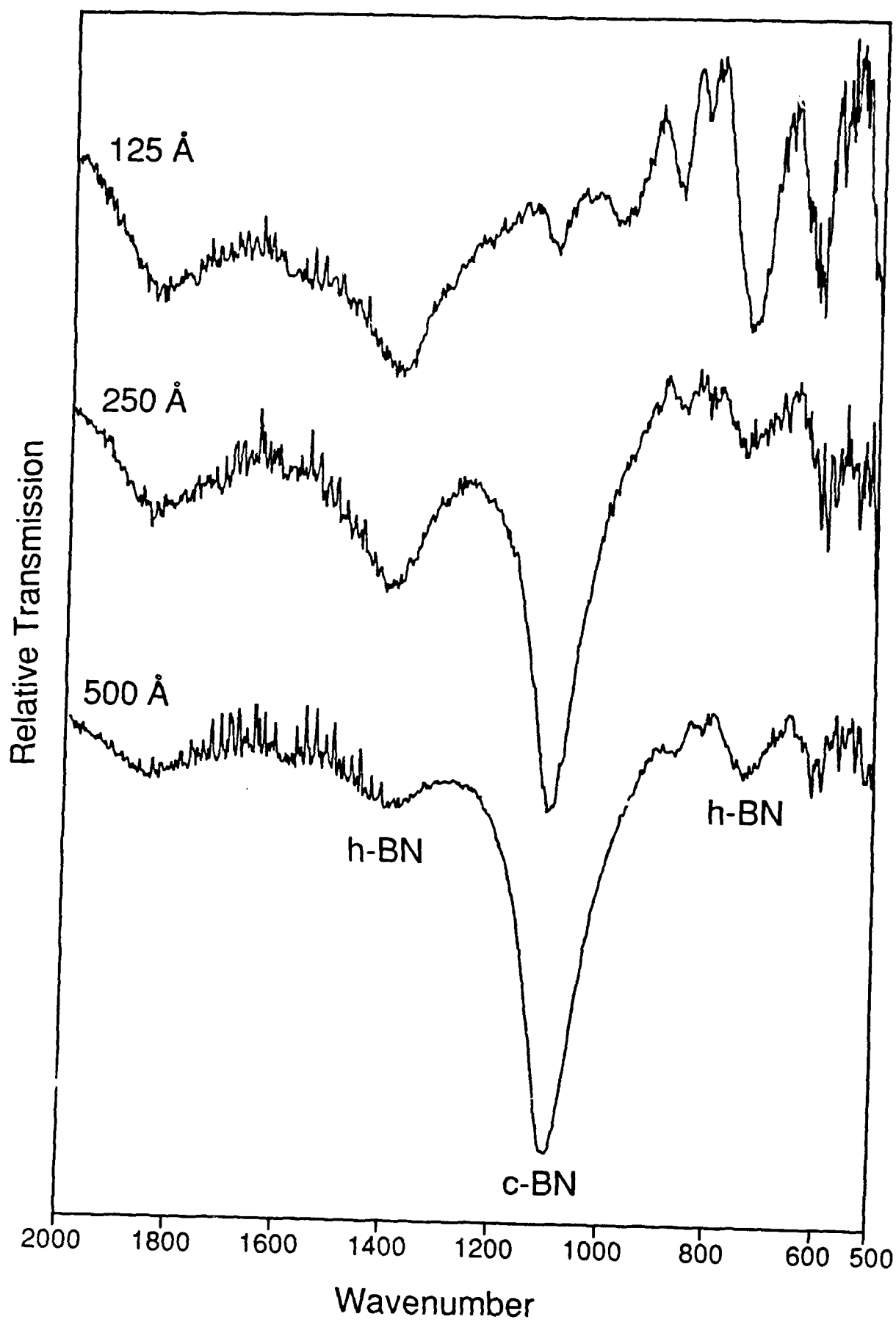
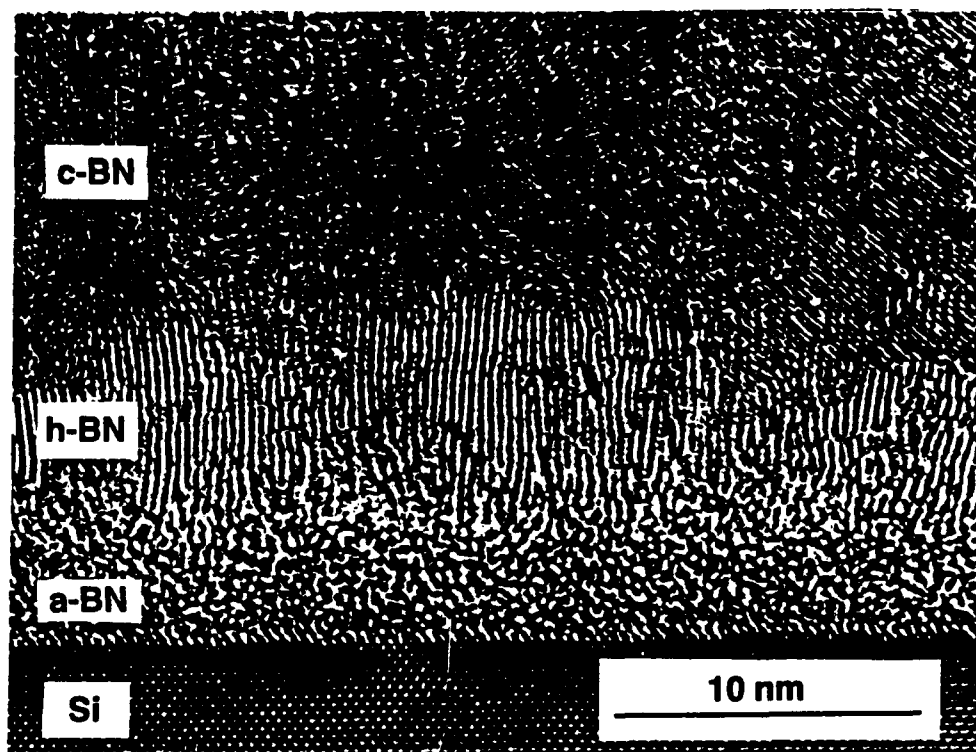


Figure 2



## XX. Distribution List

Mr. Max Yoder Office of Naval Research Electronics Program—Code 1114 800 North Quincy Street Arlington, VA 22217	3
Office of Naval Research Resident Representative The Ohio State Univ. Research Center 1960 Kenny Road Columbus, OH 43210-1063	2
Director Naval Research Laboratory Attention: Code 2627 Washington, DC 20314	1
Defense Technical Information Center Building 5 Cameron Station Alexandria, VA 22314	4